

COMPOSITION – MICROSTRUCTURE – PROPERTY RELATIONSHIPS
IN DUAL PHASE BULK MAGNETOELECTRIC
COMPOSITE

by

RASHED ADNAN ISLAM

Presented to the Faculty of the Graduate School of
The University of Texas at Arlington in Partial Fulfillment
of the Requirements
for the Degree of

DOCTOR OF PHILOSOPHY

THE UNIVERSITY OF TEXAS AT ARLINGTON

MAY 2008

Copyright © by Rashed Adnan Islam 2008

All Rights Reserved

ACKNOWLEDGEMENTS

I would like to express my profound indebtedness and heartfelt gratitude to my dissertation supervisor Dr. Shashank Priya, Associate Professor, Department of Materials Science and Engineering, Virginia Tech, Blacksburg for his valuable suggestions, constant guidance, encouragement and kind help in carrying out the project work as well as in writing this thesis.

I am very much thankful to Dr. E. Meletis, Chair of the Department of Materials Science and Engineering, University of Texas at Arlington and Dr. Pranesh Aswath for their kind inspiration in every step of work. I am grateful to all the committee members Prof. Wen Chan, Dr. J. P Liu for their valuable time during my thesis. I would also like to thank Dr. Choong – Un Kim, Dr. J. C Jiang, Dr. Michael Jin for their constant inspiration and support. I am thankful to Paul Moses from Penn. State for his logistic support.

Thanks are due to all colleagues in my research group specially, Vishwas, Hyunuk, Makarand, Vaneet, Mitesh, Robert and Dr. Kim for their help and encouragement. I am also grateful to all the members of NMMG research group for their continuous help in magnetic characterizations. Thanks are also due to the officers and staff of NanoFab – Teaching and Research Facilities specially Dr. Nasir Basit, Dr. Fatima Amir and Mr. Dennis Bueno.

I am very much grateful to my family member specially my wife Samia, who supported me in very crucial times. I would also like to thank other friends for their continuous encouragement.

Finally I wish to record my gratitude to Allah, the most merciful and the most gracious, for giving him the ability to complete the project.

March 31, 2008

ABSTRACT

COMPOSITION – MICROSTRUCTURE – PROPERTY RELATIONSHIPS IN DUAL PHASE BULK MAGNETOELECTRIC COMPOSITE

Rashed Adnan Islam, PhD.

The University of Texas at Arlington, 2008

Supervising Professor: Shashank Priya

The coexistence of coupled electrical and magnetic properties in the “magnetolectric” material has led to the possibility of developing smarter and smaller electronic components. In order to make this possibility a reality, significant efforts are required to understand the science of magnetolectric (ME) behavior and apply this understanding to develop higher sensitivity material. The primary aims of this thesis are to identify the role of composition, microstructural variables, composite geometry, texturing, post sintering heat treatment, and nanoscale assembly on ME coefficient. The overall objective is to synthesize, characterize and utilize a high ME coefficient composite. The desired range of ME coefficient in the sintered composite is more than 1.5 V/cm.Oe.

At first, a piezoelectric composition in the system of $\text{Pb}(\text{Zr},\text{Ti})\text{O}_3$ - $\text{Pb}[(\text{Zn},\text{Ni})_{1/3}\text{Nb}_{2/3}]\text{O}_3$ was designed and synthesized which has high energy density (d.g) parameter of $18456.2 \times 10^{15} \text{ m}^2/\text{N}$ and high g constant of 83.1 V-m/N in order to use it as the matrix in piezoelectric – magnetostrictive composite. Secondly it was found that soft piezoelectric phase shows much better magnetolectric response. The magnetolectric coefficient for $\text{Pb}(\text{Zr}_{0.52}\text{Ti}_{0.48})\text{O}_3$ - 15%

$\text{Pb}(\text{Zn}_{1/3}\text{Nb}_{2/3})\text{O}_3$ [PZT – 15 PZN] - 20% $\text{Ni}_{0.8}\text{Zn}_{0.2}\text{Fe}_2\text{O}_4$ was found to be around 186 mV/cm.Oe. Thirdly, soft magnetic phase with lower coercivity and higher magnetization was found to be suitable for high ME coefficient. Zinc doped Ni-ferrite has higher resistivity, permeability, magnetization and it was found that with increasing Zn concentration the ME coefficient increases exhibiting maxima near 30 at% Zn (138 mV/cm.Oe).

Fourthly, if the connectivity was changed from (0-3) to (2-2) which is a bilayer geometry, improved piezoelectric ($d_{33} \sim 80$ pC/N), ferroelectric (polarization = $60 \mu\text{C}/\text{cm}^2$), magnetization (25 emu/gm) and lower coercive field (2.8 Oe) were measured. The bilayer shows an enhancement of 67% increase in ME coefficient compared to bulk composite. Finally it was found that the electrical, magnetic and magnetoelectric properties of $(1-x) \text{Pb}(\text{Zr}_{0.52}\text{Ti}_{0.48})\text{O}_3 - x\text{NiFe}_{1.9}\text{Mn}_{0.1}\text{O}_4$ (PZT-NFM) composites were enhanced after post-sinter annealing and aging. The thermal treatment relaxed the strain in the matrix as observed by change in PZT lattice constant from ($a = 3.87 \text{ \AA}$, $c = 4.07 \text{ \AA}$) to ($a = 4.07 \text{ \AA}$, $c = 4.09 \text{ \AA}$). This signifies that strain relaxation helps to enhance the ME coefficient by $\sim 50\%$.

A trilayer composite was synthesized using pressure assisted sintering with soft phase [0.9PZT – 0.1 PZN] having grain size larger than $1 \mu\text{m}$ and soft ferromagnetic phase of composition $\text{Ni}_{0.8}\text{Cu}_{0.2}\text{Zn}_{0.2}\text{Fe}_2\text{O}_4$ [NCZF]. The composite showed a high ME coefficient of 412 and 494 mV/cm.Oe after sintering and annealing respectively. Optimized ferrite to PZT thickness ratio was found to be 5.33, providing ME coefficient of 525 mV/cm.Oe. The ME coefficient exhibited orientation dependence with respect to applied magnetic field. Multilayering the PZT layer increased the magnitude of ME coefficient to 782 mV/cm.Oe. Piezoelectric grain texturing and nano-particulate assembly techniques were incorporated with the layered geometry. It was found that with moderate texturing, d_{33} and ME coefficient reached up to 325 pC/N and 878 mV/cm.Oe respectively. Nano-particulate core shell assembly shows the promise for achieving large ME coefficient in the sintered composites. A systematic relationship between composition, microstructure, geometry and properties is presented which will lead towards development of high performance magnetoelectric materials.

Using the particulate type ME composite developed in thesis, a high sensitivity magnetic field sensor based on piezoelectric transformer principle was fabricated and characterized. This application demonstrates the advantages of ME composites for magnetic field sensing.

TABLE OF CONTENTS

| | |
|--|------|
| ACKNOWLEDGEMENTS..... | iii |
| ABSTRACT..... | iv |
| LIST OF ILLUSTRATIONS..... | xiv |
| LIST OF TABLES..... | xxii |
| Chapter | Page |
| 1. INTRODUCTION..... | 1 |
| 1.1 Magnetoelectric Effect..... | 1 |
| 1.2 Thermodynamic considerations of Magnetoelectricity..... | 1 |
| 1.3 Magnetoelectric single phase materials..... | 5 |
| 1.4 Magnetoelectric composite materials..... | 6 |
| 1.4.1 Properties of composite | 7 |
| 1.4.2 Connectivity of composite | 7 |
| 1.4.3 Types of Magnetoelectric composite..... | 9 |
| 1.4.3.1 Insitu composite using unidirectional solidification..... | 11 |
| 1.4.3.2 Laminated composite..... | 12 |
| 1.4.3.3 ME micro/nanostructures..... | 17 |
| 1.4.3.4 Sintered composite..... | 20 |
| 1.4.4 Problems and shortcoming of sintered composite | 23 |
| 2. OBJECTIVE AND RESEARCH PLAN..... | 25 |
| 2.1 Objective..... | 25 |
| 2.2 Plan of Research..... | 26 |
| 2.2.1 System selection and optimization of | |

| | | |
|----|--|----|
| | composition | 26 |
| | 2.2.2 Effect of matrix grainsize..... | 27 |
| | 2.2.3 Effect of geometry..... | 27 |
| | 2.2.4 Effect of post sinter heat treatment..... | 28 |
| | 2.2.5 Synthesis of cofired composite..... | 28 |
| | 2.2.6 Texturing..... | 28 |
| | 2.2.7 Layered ME composite from bottom-up approach..... | 29 |
| 3. | EXPERIMENTAL PROCEDURE..... | 30 |
| | 3.1 System selection..... | 30 |
| | 3.2 Synthesis | 31 |
| | 3.2.1 Raw material..... | 31 |
| | 3.2.2 Calcination and phase analysis..... | 31 |
| | 3.2.3 Composite powder synthesis and compaction..... | 32 |
| | 3.2.4 Nano size particle synthesis..... | 33 |
| | 3.2.5 Bilayer and trilayer fabrication..... | 33 |
| | 3.2.6 Sintering and post sintering heat treatment..... | 35 |
| | 3.2.7 Texturing..... | 36 |
| | 3.2.8 Synthesis of PZT – NFO core – shell structure..... | 36 |
| | 3.3 Characterization..... | 37 |
| | 3.3.1 Phase and crystal structure analysis..... | 37 |
| | 3.3.2 Microstructural analysis..... | 38 |
| | 3.3.2.1 Scanning electron microscopy..... | 38 |
| | 3.3.2.2 Transmission electron microscopy..... | 38 |
| | 3.4 Physical Properties Characterization..... | 38 |
| | 3.4.1 Electrical properties..... | 39 |
| | 3.4.1.1 Dielectric measurement..... | 39 |
| | 3.4.1.2 Polarization and strain measurement..... | 39 |

| | | |
|----|--|----|
| | 3.4.1.3 Piezoelectric Measurements..... | 39 |
| | 3.4.2 Magnetic properties..... | 40 |
| | 3.4.2.1 Hysteresis loop (M – H) | 40 |
| | 3.4.2.2 Temperature dependent magnetization measurement..... | 41 |
| | 3.4.2 Magnetolectric Properties..... | 41 |
| 4. | HIGH ENERGY DENSITY CERAMIC COMPOSITION IN THE SYSTEM $\text{Pb}(\text{Zr},\text{Ti})\text{O}_3 - \text{Pb}[(\text{Zn},\text{Ni})_{1/3},\text{Nb}_{2/3}]\text{O}_3$ FOR PIEZOELECTRIC – MAGNETOSTRICTIVE COMPOSITES..... | 43 |
| | 4.1 High Energy Density Piezoelectric Phase for ME Composites..... | 43 |
| | 4.2 Design of High 'g' Materials..... | 45 |
| | 4.2.1 Defect Chemistry..... | 46 |
| | 4.3 Structural Studies..... | 49 |
| | 4.3.1 Density measurement of different compositions..... | 49 |
| | 4.3.2 Phase analysis of different Zr/Ti ratio piezoelectric compositions..... | 49 |
| | 4.3.3 Microstructure and grainsize analysis of sintered body using one and two step sintering | 51 |
| | 4.4 Energy Harvesting Parameter and material constant 'n'..... | 55 |
| | 4.5 Piezoelectric Properties..... | 58 |
| | 4.6 Grainsize dependency..... | 62 |
| | 4.7 ChapterSummary..... | 65 |
| 5. | DOPING EFFECT ON MAGNETOELECTRIC COEFFICIENT OF $\text{Pb}(\text{Zr}_{0.52}\text{Ti}_{0.48})\text{O}_3 - \text{Ni}_{(1-x)}\text{Zn}_x\text{Fe}_2\text{O}_4$ PARTICULATE COMPOSITE..... | 67 |
| | 5.1 Effect of Piezoelectric Composition..... | 67 |
| | 5.1.1 Ferroelectric and piezoelectric properties..... | 68 |
| | 5.1.2 Microstructural investigation of doped PZT – 20 NZF composite..... | 69 |
| | 5.1.3 Magnetolectric properties as a function of doping in PZT matrix..... | 71 |

| | | |
|-------|--|-----|
| 5.2 | Effect of Magnetostrictive Composition..... | 72 |
| 5.2.1 | Magnetic properties and structural studies of PZT - Zn doped NFO composites | 73 |
| 5.2.2 | Effect of Zn concentration of NZF on magnetolectric coefficient | 75 |
| 5.3 | Chapter Summary..... | 77 |
| 6. | EFFECT OF GRAIN SIZE ON MAGNETOELECTRIC COEFFICIENT OF $\text{Pb}(\text{Zr}_{0.52}\text{Ti}_{0.48})\text{O}_3 - \text{Ni}_{0.8}\text{Zn}_{0.2}\text{Fe}_2\text{O}_4$ PARTICULATE COMPOSITES..... | 78 |
| 6.1 | Characterization of Starting Particles..... | 78 |
| 6.2 | Characterization of Sintered Composite..... | 79 |
| 6.2.1 | Investigations on microstructure and physical properties for various grainsize | 79 |
| 6.2.2 | Effect of grainsize on piezoelectric and ferroelectric properties of PZT - 20 NZF ME composite..... | 82 |
| 6.2.3 | Variation of magnetization and coercivity for different grain size samples | 92 |
| 6.2.4 | Grainsize dependency of magnetolectric properties of PZT – 20 NZF composite | 92 |
| 6.3 | Chapter Summary..... | 97 |
| 7. | EFFECT OF GEOMETRY ON MAGNETOELECTRIC COEFFICIENT... | 96 |
| 7.1 | Comparison Between Bulk (0 – 3) and Bilayer (2 – 2) Magnetolectric Composites of $\text{Pb}(\text{Zr}_{0.56}\text{Ti}_{0.44})\text{O}_3 - \text{Ni}_{0.6}\text{Zn}_{0.2}\text{Cu}_{0.2}\text{Fe}_2\text{O}_4$ [PZT (H) – NCZF] System | 99 |
| 7.1.1 | Microstructural comparison of PZT(H) – NCZF bulk and bilayer composite | 100 |
| 7.1.2 | Ferroelectric and dielectric properties of PZT(H) – NCZF bulk and bilayer composite | 104 |
| 7.1.3 | Comparison of magnetic moment between bulk and bilayer composite | 108 |
| 7.1.4 | Effect of gradient composite microstructure on magnetolectric properties | 110 |
| 7.2 | Chapter Summary..... | 110 |

| | | |
|----|---|-----|
| 8. | EFFECT OF POST SINTER HEAT TREATMENT ON MAGNETOELECTRIC COEFFICIENT OF SINTERED PARTICULATE COMPOSITE..... | 113 |
| | 8.1 Effect of annealing and aging..... | 113 |
| | 8.1.1 Phase Analysis of sintered, annealed and aged PZT – NFM composites | 114 |
| | 8.1.2 Ferroelectric, piezoelectric and dielectric properties of thermally treated PZT – NFM composites | 117 |
| | 8.1.3 Magnetic moment as a function of magnetic field and temperature for thermally treated PZT – NFM composite | 126 |
| | 8.1.4 Effect of annealing and aging on Magnetolectric properties of PZT – NFM composites | 130 |
| | 8.1.5 Structural characterization for high ME coefficient of PZT – NFM composites | 130 |
| | 8.2 Effect of aging time and temperature..... | 135 |
| | 8.2.1 Phase analysis for variation in aging time and temperature | 135 |
| | 8.2.2 Effect of aging time and temperature on piezoelectric and dielectric properties of PZT – NFM composite | 137 |
| | 8.2.3 Aging time and temperature dependent magnetic properties | 140 |
| | 8.2.4 Effect of aging time and temperature on magnetolectric properties of PZT – NFM composite | 143 |
| | 8.2.5 Microstructural variation for time temperature variation of PZT – NFM composite..... | 144 |
| | 8.3 Chapter Summary..... | 148 |
| 9. | TRILAYER (2 – 2) COMPOSITE SYNTHESIS..... | 149 |
| | 9.1 Trilayer synthesis..... | 149 |
| | 9.1.1 Microstructural characterization of trilayer cross section | 150 |
| | 9.1.2 Piezoelectric and dielectric properties of NCZF – [0.9 PZT – 0.1 PZN] – NCZF trilayer | 154 |
| | 9.1.3 Analysis of NCZF – [0.9 PZT – 0.1 PZN] – NCZF trilayer magnetolectric response..... | 157 |

| | | |
|----------|--|-----|
| 9.2 | Effect of thickness..... | 159 |
| 9.2.1 | Microstructural Investigations of different thickness ratio | 160 |
| 9.2.2 | Effect of [0.9 PZT – 0.1 PZN] thickness and orientation on ME coefficient | 165 |
| 9.3 | Effect of [0.9 PZT – 0.1 PZN] Multilayering..... | 168 |
| 9.3.1 | Design and synthesis of NCZF – PZT (Stack) – NCZF trilayer | 169 |
| 9.3.2 | Piezoelectric and dielectric properties of NCZF – Stack [0.9 PZT – 0.1 PZN] – NCZF trilayer..... | 170 |
| 9.3.3 | Magnetolectric coefficient of stack [0.9 PZT – 0.1 PZN] based trilayer | 173 |
| 9.3.4 | Microstructure of individual phases near interface | 173 |
| 9.4 | Chapter Summary..... | 175 |
| 10. | IMPROVED PROPERTIES OF TRILAYER COMPOSITES THROUGH GRAIN TEXTURING AND NANO PARTICULATES ASSEMBLY..... | 176 |
| 10.1 | Texturing | 176 |
| 10.1.1 | Seed fabrication..... | 176 |
| 10.1.1.1 | Seed Characterization..... | 178 |
| 10.1.2 | Synthesis of trilayer composites with textutred PZT..... | 180 |
| 10.2 | Piezoelectric core – Magnetostrictive shell structure..... | 183 |
| 10.2.1 | Synthesis of PZT core – NFO shell composite powder... | 183 |
| 10.2.2 | Nanosize NiFe ₂ O ₄ Characterization..... | 184 |
| 10.2.3 | Characterization of PZT – NFO core shell structure..... | 185 |
| 10.2.4 | Sintered PZT core – NFO shell structure..... | 185 |
| 10.3 | Chapter Summary..... | 192 |
| 11. | MAGNETOELECTRIC DEVICES..... | 194 |
| 11.1 | Magnetolectric sensor..... | 194 |
| 11.1.1 | Structure and working principle..... | 194 |

| | |
|--|-----|
| 11.1.2 Magnetic sensitivity | 196 |
| 11.2 Sensing mechanism..... | 197 |
| 11.2.1 Voltage gain and magnetic field generation..... | 200 |
| 11.3 Chapter Summary | 204 |
| 12. CONCLUSION | 205 |
| 13. FUTURE WORKS | 209 |
| APPENDIX | |
| A. PUBLICATION RELATED TO THIS RESEARCH..... | 210 |
| REFERENCES..... | 213 |
| BIOGRAPHY..... | 223 |

LIST OF ILLUSTRATIONS

| Figure | Page |
|---|------|
| 1.1 Phase control in multiferroics, interrelation between electric field, magnetic field and stress..... | 2 |
| 1.2 (a) Magnetoelectric coefficient of Cr_2O_3 as a function of temperature and (b) Structural, magnetic and magnetoelectric properties of BiFeO_3 thin film..... | 6 |
| 1.3 Properties of different types of composite system..... | 8 |
| 1.4 Different types of connectivity of the two phase composite system..... | 9 |
| 1.5 (a) simplified diagram of Ba – Ti – Fe – Co system showing the metallic component, (b) micrograph of spine dendrites in matrix of BTO – CFO insitu composite with excess TiO_2 | 10 |
| 1.6 Transverse section of spinel dendrites..... | 11 |
| 1.7 Schematic diagram of laminated composite (a) Terfenol – D sandwich structure with PMN – PT in the middle and (b) Magnetic FeBSiC top and Bottom layer with intermediate layer as piezoelectric fiber..... | 13 |
| 1.8 Different modes of laminated composite (a) longitudinally magnetized – longitudinally polarized (L – L), (b) Transverse magnetized - longitudinally polarized (T – L), (c) longitudinally magnetized - transverse polarized (L – T) and (d) transverse magnetized – transverse polarized (T – T)..... | 15 |
| 1.9 Schematic diagram of magnetoelectric nanostructure, (a) multilayer films, (b) nanopillars structure and (c) magnetoelectric nanowires..... | 16 |
| 1.10 (a) HRTEM of BTO – NFO bilayer thin film structure, (b) HRTEM of PZT – CZFO bilayer thin film structure showing interface, (c) HRTEM of PZT – NFO nanoparticulate composite showing orientation relationship of NFO (110) and PZT (110) and (d) cross sectional TEM image of PZT – CFO bilayer film..... | 17 |
| 1.11 (a) PZT – NZF particulate composite showing ferrite connectivity and (b) Elemental mapping of Zn confirming the connectivity of the ferrite particles..... | 22 |
| 1.12 SEM micrograph of PZT – (Ni, Co, Mn) ferrite showing defects at the interface such as microcracks and porosity..... | 24 |
| 3.1 Schematic diagram of spinel and perovskite crystal structure..... | 32 |
| 3.2 Typical x-ray diffraction pattern of spinel Co ferrite and perovskite BTO..... | 33 |

| | | |
|------|---|----|
| 3.3 | (a) Schematic diagram of trilayer ME composite, (b) sintering set – up of trilayer ME composite and (c) images of sintered trilayer composite (inset: cross section)..... | 34 |
| 3.4 | Heating profile of annealing and aging..... | 36 |
| 3.5 | Magnetolectric measurement setup..... | 41 |
| 4.1 | Variation of density as a function of (a) Mn concentration given in weight percent for 0.9PZT (52:48) – 0.1 PZN + y wt% MnCO ₃ and (b) Mn concentration given in mole percent for 0.9PZT (56:44) – 0.1 PZNN + x mol% MnO ₂ | 50 |
| 4.2 | XRD pattern of different sintered samples synthesized using two step sintering profiles showing single-phase perovskite structure with tetragonal symmetry. (a) 0.9PZT (52: 48) -0.1PZN + 0.7 wt% Mn, and (b) 0.9PZT (56: 44)-0.1PZNN + 2 mol% MnO ₂ and insert of the exploded view of 200/002 peaks..... | 42 |
| 4.3 | SEM micrographs of sintered samples (a) 0.9PZT (52:48) – 0.1PZN + 0.7 wt% Mn, synthesized using one step, (b) 0.9PZT (52:48) – 0.1PZN + 0.7 wt% Mn, synthesized using two step sintering (c) 0.9PZT (56: 44) - 0.1PZNN + 3 mol% MnO ₂ , synthesized using one step sintering and (d) 0.9PZT (56: 44) - 0.1PZNN + 3 mol% MnO ₂ , synthesized using two step sintering..... | 53 |
| 4.4 | SEM micrographs of 0.9PZT-0.1PZN + 0.5%Mn and 0.9PZT-0.1PZN + 0.7%Mn synthesized using the two step sintering at 950 °C for 5 minutes and at 900°C for 4 hours..... | 53 |
| 4.5 | Comparison of the grain size obtained by using the one-step and two-step sintering profile for the case when highest temperature is 1050°C for (a) 0.9PZT (52: 48) – 0.1 PZN + y wt% MnCO ₃ and (b) 0.9PZT (56: 44) - 0.1PZNN + x mol% MnO ₂ | 54 |
| 4.6 | Variation of the material parameter (d_{33} , g_{33}) as a function of grain size for (a) 0.9PZT (52: 48) – 0.1 PZN + y wt% MnCO ₃ and (b) 0.9PZT (56: 44) – 0.1 PZNN + x mol% MnO ₂ | 56 |
| 4.7 | Variation of material constant, n, as a function of (a) grain size for 0.9PZT (52: 48) – 0.1 PZN + y wt% MnCO ₃ , (b) grain size for 0.9PZT (56: 44) – 0.1 PZNN + x mol% MnO ₂ | 57 |
| 4.8 | Variation of material constant, n, as a function of piezoelectric voltage coefficient, g_{33} for 0.9PZT (52: 48) – 0.1 PZN + y wt% MnCO ₃ | 58 |
| 4.9 | Variation of the (a) piezoelectric constant, d_{33} for 0.9PZT (52: 48) – 0.1 PZN + y wt% MnCO ₃ , (b) dielectric constant, ϵ_{33}/ϵ_0 for 0.9PZT (52: 48) – 0.1 PZN + y wt% MnCO ₃ | 60 |
| 4.10 | Variation of the (a) piezoelectric constant, d_{33} for 0.9PZT | |

| | | |
|------|---|----|
| | (56: 44) – 0.1 PZNN + x mol% MnO ₂ and (b) dielectric constant ϵ_{33}/ϵ_0 for 0.9PZT (56: 44) – 0.1 PZNN + x mol% MnO ₂ | 61 |
| 4.11 | (a) Temperature dependence of dielectric constant for 0.9PZT (52: 48) – 0.1 PZN + y wt% MnCO ₃ and (b) temperature dependence of dielectric constant for 0.9PZT (56: 44) – 0.1 PZNN + x mol% MnO ₂ , (c) variation of Curie temperature as a function of the Mn concentration for 0.9PZT (52: 48) – 0.1 PZN + y wt% MnCO ₃ and (d) variation of Curie temperature as a function of the Mn concentration for 0.9PZT (56: 44) – 0.1 PZNN + x mol% MnO ₂ | 63 |
| 4.12 | (a) variation of Curie temperature as a function of the Mn concentration for 0.9PZT (52: 48) – 0.1 PZN + y wt% MnCO ₃ and (b) variation of Curie temperature as a function of the Mn concentration for 0.9PZT (56: 44) – 0.1 PZNN + x mol% MnO ₂ | 64 |
| 5.1 | Polarization vs. electric field loop for different magnetoelectric composite..... | 69 |
| 5.2 | Microstructure of different magnetoelectric composite, (a) PZT – 20 NZF and (b) PZT (soft) – 20 NZF..... | 70 |
| 5.3 | Magnetoelectric coefficient as a function of DC bias field for different compositions of ME composite..... | 71 |
| 5.4 | Magnetic properties of different composite. (a) magnetization and coercive field as a function of Zn% concentration in NZF and (b) magnetization as a function of temperature..... | 74 |
| 5.5 | X-ray diffraction pattern for the hkl : 400 peak for different Zn concentration in NZF showing peak shift..... | 75 |
| 5.6 | Magnetoelectric coefficient as a function of DC bias for different concentration of Zn in NZF..... | 76 |
| 6.1 | Structural characterization of calcined powder (a) XRD patterns of composite powders and (b) Full width half maxima (FWHM) as a function of final grain size in sintered sample..... | 80 |
| 6.2 | Particle size distribution histogram for four different batches of powders..... | 81 |
| 6.3 | Microstructures of ME composites with varying grain size (a) 830nm, (b) 758nm, (c) 556nm, (d) 320nm, (e) 111 nm and (f) 97nm..... | 83 |
| 6.4 | Variation of physical property with grain size (a) Density and densification, and (b) resistivity..... | 84 |
| 6.5 | XRD patterns of the sintered composite showing perovskite (P) and spinel (S) peaks..... | 85 |
| 6.6 | Piezoelectric properties as a function of grain size (a) Longitudinal piezoelectric and dielectric constant and (b) piezoelectric voltage constant..... | 86 |
| 6.7 | Polarization vs. electric field loop as a function of grainsize..... | 88 |

| | | |
|------|---|-----|
| 6.8 | Dielectric properties as a function of temperature (a) dielectric constant for 111 nm, (b) loss factor for 111 nm,..... | 89 |
| 6.9 | Dielectric properties as a function of temperature (a) dielectric constant for 320 nm, (b) loss factor for 320 nm,..... | 90 |
| 6.10 | Dielectric properties as a function of temperature (a) dielectric constant for 830 nm, and (b) loss factor for 830 nm..... | 91 |
| 6.11 | Magnetolectric coefficient as a function of (a) DC bias field and (b) grain size..... | 94 |
| 6.12 | Magnetolectric coefficient as a function of (a) piezoelectric strain constant and (b) dielectric constant..... | 95 |
| 6.13 | Comparison of the measured ME coefficient with that predicted from theory..... | 97 |
| 7.1 | Microstructure of bilayer and bulk composites, (a) bilayer composite and (b) bulk composite..... | 101 |
| 7.2 | Microstructure of bilayer bulk composites using (a) Inlens detector, (inset: magnified view and EDS pattern) and (b) quadrant back scattering detector..... | 102 |
| 7.3 | Cu elemental mapping in the vicinity of the interface..... | 103 |
| 7.4 | Ferroelectric loop of PZT – NCZF composite, (a) cofired bilayer composite and (b) bulk composite..... | 105 |
| 7.5 | Dielectric properties of bulk and bilayer as a function of temperature, (a) dielectric constant (inset: dielectric constant vs. temperature of PZT – NF and PZT – NZF bilayer) and (b) dielectric loss..... | 106 |
| 7.6 | Ferromagnetic property of two types of composite. (a) Moment vs. Field (hysteresis loop) and (b) magnetization as a function of temperature..... | 107 |
| 7.7 | ME coefficient of PZT – NCZF bilayer and bulk composite. (a) ME coefficient as a function of DC bias in T – T mode, (b) ME coefficient as a function of frequency..... | 111 |
| 8.1 | X-ray diffraction patterns of calcined PZT and NFM..... | 114 |
| 8.2 | X-ray diffraction patterns of (b) as-sintered (1-x) PZT-x NFM samples for 2 hrs at 1125°C..... | 115 |
| 8.3 | X-ray diffraction patterns of (1-x) PZT-x NFM composite - sintering followed by annealing at 800°C for 10 hrs and then aging at 400°C for 5 hrs..... | 116 |
| 8.4 | Polarization – electric field (P-E) and strain – electric field (S-E) bipolar loops for all the three composition before and after the thermal treatment for the samples sintered at 1100 °C. | |

| | |
|---|-----|
| (a) and (b) PZT – 3 NFM, | 118 |
| 8.5 Polarization – electric field (P-E) and strain – electric field (S-E) bipolar loops for all the three composition before and after the thermal treatment for the samples sintered at 1100 °C. (c) and (d) PZT – 5NFM,..... | 119 |
| 8.6 Polarization – electric field (P-E) and strain – electric field (S-E) bipolar loops for all the three composition before and after the thermal treatment for the samples sintered at 1100 °C. (e) and (f) PZT – 10NFM..... | 120 |
| 8.7 Variation of piezoelectric and dielectric constant with NFM mol% before and after thermal treatment for the samples sintered at 1100 and 1125 °C. (a) Piezoelectric constant (b) Dielectric constant, and (c) Dielectric loss factor..... | 122 |
| 8.8 Variation of dielectric loss factor with NFM mol% before and after thermal treatment for the samples sintered at 1100 and 1125 °C..... | 123 |
| 8.9 Dielectric constant and dielectric loss as a function of temperature..... | 124 |
| 8.10 Dielectric constant as a function of the temperature at 1 kHz for PZT – 5 NFM at three different conditions..... | 125 |
| 8.11 Variation of the ferromagnetic properties for three compositions before and after thermal treatment (a) PZT – 3NFM and (b) PZT – 5NFM, | 128 |
| 8.12 Variation of the ferromagnetic properties for three compositions before and after thermal treatment (c) PZT – 10NFM..... | 129 |
| 8.13 Temperature dependent ferromagnetic property (saturation magnetization) of PZT – 5 NFM composite..... | 129 |
| 8.14 Magnetolectric coefficient for different composites at three different conditions, (a) PZT – 3 NFM and(b) PZT – 5 NFM..... | 131 |
| 8.15 Magnetolectric coefficient for different composites at three different conditions for PZT 10 – NFM..... | 132 |
| 8.16 Bright field TEM images PZT – 5 NFM composites after (a) sintering, and (b) annealing. Selected area electron diffraction (SAED) pattern of PZT phase after sintering for (c) [101], (d) [001] zone axis and NFM phase after sintering (e) [211], (f) [110] zone axis..... | 133 |
| 8.17 Bright field TEM images PZT – 5 NFM composites after (a) sintering, (b) annealing and (c) aging..... | 134 |
| 8.18 XRD patterns of PZT -10 NFM at different aging condition showing variation of spinel peaks. (a) function of aging temperature, and (b) function of aging time..... | 136 |
| 8.19 Variation of piezoelectric and dielectric constant with aging time and | |

| | |
|--|-----|
| temperature. (a) Piezoelectric constant as a function of aging temperature, (b) Piezoelectric constant as a function of aging time..... | 138 |
| 8.20 Variation of piezoelectric and dielectric constant with aging time and temperature, (c) Dielectric constant as a function of aging temperature and (d) dielectric constant as a function of aging time..... | 139 |
| 8.21 Variation of piezoelectric voltage constant (g_{33}) as a function of aging temperature and time. (a) Aging temperature dependence of g_{33} and (b) aging time dependence of g_{33} | 141 |
| 8.22 Variation of ferromagnetic property as a function % (mole) NFM at different aging temperature and time. (a) Saturation magnetization M_s and (b) Remnant magnetization M_r | 142 |
| 8.23 Magnetolectric Coefficient (dE/dH) as a function of mole% NFM at different aging condition..... | 143 |
| 8.24 SEM microstructure of PZT – 5 NFM at different conditions and different magnifications. (a) Sintered sample at 5kX magnification, (b) sintered sample at 20kX magnification, | 145 |
| 8.25 SEM microstructure of PZT – 5 NFM at different conditions and different magnifications. (c) sintered, annealed and aged sample at 5kX magnification and (d) sintered, annealed and aged sample at 20kX magnification..... | 146 |
| 8.26 PFM images of PZT – 5 NFM after (a) sintering and (b) annealing/aging..... | 147 |
| 9.1 Optical image of sintered sample (inset – cross section)..... | 150 |
| 9.2 SEM micrographs. (a) low magnification image of sintered trilayer sample, (b) interface microstructure,..... | 151 |
| 9.3 SEM micrographs. (a) low magnification image of sintered and annealed sample, (b) interface microstructure of sintered and annealed trilayer sample,..... | 152 |
| 9.4 SEM micrographs. (e) grain structure of PZT side and (f) grain structure of ferrite side..... | 153 |
| 9.5 Impedance spectrum of the trilayer composite..... | 155 |
| 9.6 Dielectric properties as function of temperature of (a) sintered sample and (b) sintered and annealed sample..... | 156 |
| 9.7 Magnetolectric coefficient as a function of dc bias field..... | 159 |
| 9.8 Composite of different PZT thicknesses, (a) 0.38 mm, (b) 0.45 mm..... | 161 |
| 9.9 Composite of different PZT thicknesses, (c) 0.55 mm, (d) 0.85 mm | 162 |

| | | |
|------|---|-----|
| 9.10 | Composite of different PZT thicknesses, (e) 0.95 mm and (f) 1.2 mm | 163 |
| 9.11 | Interface microstructure of trilayer sample showing NCZF, electrode and PZT layer..... | 164 |
| 9.12 | X-ray elemental mapping of trilayer sample, (a) image of trilayer sample, (b) Pb map, (b) Ag map and (d) Fe map..... | 165 |
| 9.13 | Magnetoelectric Coefficient as a function of DC bias field for different thickness of PZT..... | 166 |
| 9.14 | Comparison between theoretical and experimental magnetoelectric coefficient for different thickness ratio of magnetic to piezoelectric layer..... | 167 |
| 9.15 | Effect of orientation on ME coefficient of NCZF-[PZT-0.1 PZN]-NCZF Trilayer composite with two different PZT thickness..... | 169 |
| 9.16 | Schematic diagram for NCZF-Stack PZT-NCZF trilayer ME composite..... | 170 |
| 9.17 | Cross sectional optical image of NCZF – stack PZT – NCZF trilayer..... | 171 |
| 9.18 | Impedance spectrum of NCZF – stack PZT – NCZF trilayer..... | 172 |
| 9.19 | Magnetoelectric coefficient of stack PZT based trilayer composite..... | 172 |
| 9.20 | TEM micrograph and SAED pattern for (a) PZT – PZN and (b) NCZF near the interface..... | 174 |
| 10.1 | Optical images of large size BTO seed crystal, (inset: facets or growth marks)..... | 177 |
| 10.2 | X-ray diffraction pattern of BTO seed showing (001) orientation | 177 |
| 10.3 | X – ray diffraction pattern of textured PZT – PZN compared to randomly oriented PZT - PZN | 178 |
| 10.4 | SEM micrographs of PZT – PZN with textured grains, (a) low magnification and (b) high magnification..... | 179 |
| 10.5 | (a) Optical images of NCZF – (Textured PZT – PZN) – NCZF trilayer and (b) ME coefficient of this trilayer composite..... | 181 |
| 10.6 | TEM image of NFO Nanoparticles..... | 185 |
| 10.7 | (a) X-ray diffraction pattern and (b) magnetic properties of NFO nano particles | 186 |
| 10.8 | Micrographs for PZT – NFO core shell structure, (a) SEM and (b)TEM..... | 187 |
| 10.9 | Microstructure of sintered PZT – NFO core shell structure (a) SEM and (b) TEM..... | 188 |

| | |
|---|-----|
| 10.10 TEM images of sintered core shell structure..... | 189 |
| 10.11 Comparison of magnetic hysteresis property of NF nano particles and PZT – NFO core – shell structure..... | 190 |
| 10.12 Magnetoelectric coefficient as a function of DC bias field..... | 192 |
| 11.1 Structure of the piezoelectric transformer based magnetic field sensor..... | 194 |
| 11.2 Sensor characterization showing the variation of the output voltage as a function of frequency with and without applied magnetic field: (a) input voltage = 10 V_{rms} and (b) input voltage = 20 V_{rms} | 195 |
| 11.3 Sensor characterization showing the variation of the output voltage as a function of frequency with and without applied magnetic field: input voltage = 30 V_{rms} | 196 |
| 11.4 Electrical and magnetic data from the fully electroded sample. (a) Schematic description of the sample shape and magnetic field measurement technique, (b) impedance spectrum of the fully electroded sample..... | 198 |
| 11.5 Electrical and magnetic data from the fully electroded sample. (a) input driving condition variation as a function of the frequency at constant voltage of 30 V_{rms} , and (b) magnetic field wave form from the sample as a function of driving voltage at the resonance frequency..... | 199 |
| 11.6 Electrical and magnetic data from the sample with ring-dot electrode pattern. (a) Schematic representation of the sample and the voltage gain as a function of frequency. The maximum in the voltage gain corresponds to the resonance frequency of the dot section, (b) variation of the output magnetic field from the dot section as a function of the frequency..... | 202 |
| 11.7 Electrical and magnetic data from the sample with ring-dot electrode pattern. (a) output magnetic field wave form as a function of the input voltage in the ring section at the resonance frequency, and (b) change in voltage gain of the dot section in the frequency range of 132–134 kHz with and without the external dc magnetic field..... | 203 |
| 13.1 Flowchart of the thesis..... | 208 |

LIST OF TABLES

| Table | | Page |
|-------|--|------|
| 1.1 | List of some reported laminated composites and their ME response..... | 14 |
| 1.2 | List of some reported magnetoelectric thin film and nanostructures | 18 |
| 1.3 | List of some reported insitu and particulate/sintered composite..... | 20 |
| 4.1 | Properties of the modified $0.9 \text{Pb}(\text{Zr}_{0.5}\text{Ti}_{0.5})\text{O}_3 - 0.1 \text{Pb}(\text{Zn}_{1/3}\text{Nb}_{2/3})\text{O}_3$ ceramics..... | 48 |
| 5.1 | Piezoelectric properties of different compositions of PZT – 20 NZF Composite..... | 68 |
| 6.1 | Magnetic Properties of the composite as a function of average grain size..... | 93 |
| 8.1 | Variation of the density for two different sintering temperatures..... | 117 |
| 8.2 | Magnetic Properties of PZT-NFM powders..... | 127 |
| 9.1 | Piezoelectric properties of NCZF – (0.9PZT – 0.1 PZN) – NCZF trilayer after different thermal treatment | 154 |
| 9.2 | Piezoelectric and dielectric properties of NCZF – stack (0.9PZT – 0.1 PZN) – NCZF trilayer | 171 |
| 9.3 | Comparison between bulk, bilayer and trilayer ME composite..... | 173 |

CHAPTER 1

INTRODUCTION

1.1 Magnetoelectric Effect

Magnetoelectric effect is the combination of two types of materials property such as magnetostriction and piezoelectricity [1-3]. Magnetoelectric effect can be described as the induced electrical polarization under magnetic field or induced magnetization under electric field. Under applied alternating magnetic field, the magnetostrictive phase produces strain which is transferred to the piezoelectric phase that converts strain into electric charge. On the other hand, under applied electric field piezoelectric phase produces strain which is transferred on to the magnetostrictive phase that converts it into magnetic field. The former is called the direct magnetoelectric effect and the later is called the converse magnetoelectric effect [4 - 5]. These materials are extremely promising for applications such as sensors, actuator, transducer, storage devices and many more interesting applications [6 – 8]. The interrelation between ferroelectricity and magnetism allows the magnetic control of ferroelectric properties and vice versa [9 – 12]. Figure 1.1 shows the interrelation between electric field, magnetic field and stress. A ferromagnetic and ferroelectric phase can be combined in several different ways, including naturally occurring composites, artificially designed composites, and in-situ sintered composites [13 – 14].

1.2 Thermodynamic considerations of Magnetoelectricity

The thermodynamic consideration of magnetoelectric effect is obtained from the expansion of free energy of the system in terms of magnetic and electric field, such as

$$G(\vec{E}, \vec{H}) = G_o - P_s \bar{E} - M_s \bar{H} - \frac{1}{2} \chi_{ij}(E) \bar{E}_i \bar{E}_j - \frac{1}{2} \chi_{ij}(H) \bar{H}_i \bar{H}_j - \alpha_{ij} \bar{E}_i \bar{H}_j \quad (1.1)$$

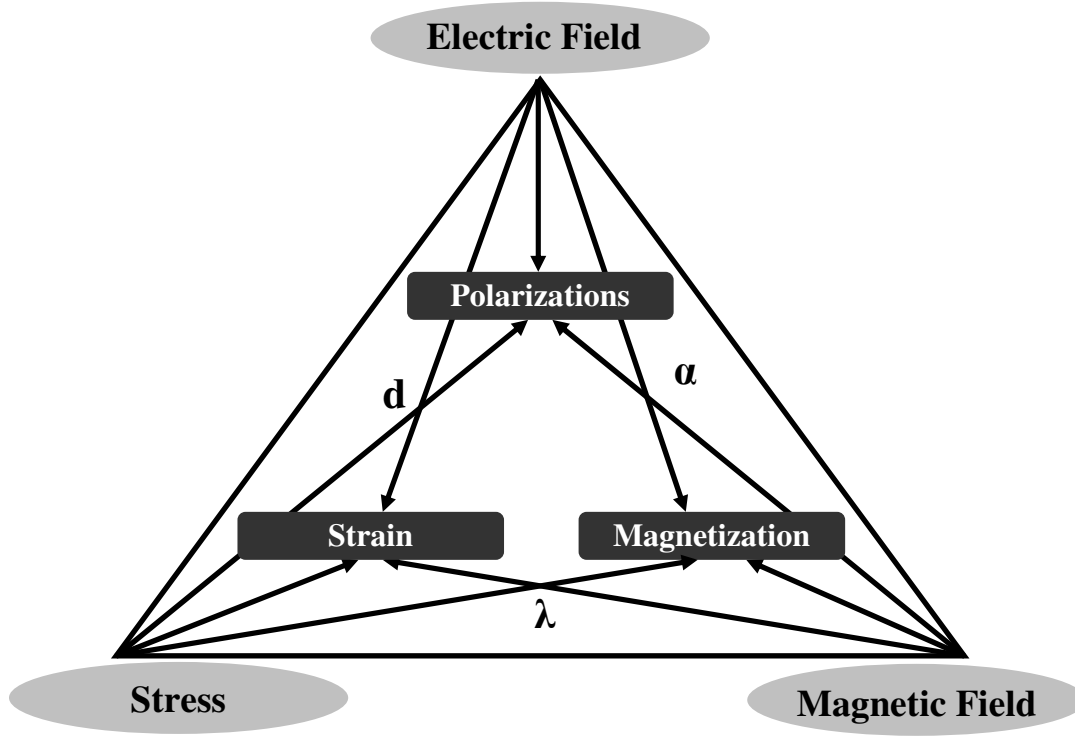


Figure 1.1: Phase control in multiferroics, interrelation between electric field, magnetic field and stress.

where \bar{E} and \bar{H} are the electric field and magnetic field respectively [15]. Differentiation of equation (1.1) gives us polarization and magnetization as following:

$$P_i = -\left(\frac{\partial G}{\partial E}\right) = P_s + \chi_{ij} E_j + \alpha_{ij} H_j \quad (1.2)$$

$$M_i = -\left(\frac{\partial G}{\partial H}\right) = M_s + \chi_{ij} H_j + \alpha_{ij} E_j \quad (1.3)$$

Here α_{ij} is the magnetoelectric tensor. Magnetoelectric effect combines two important materials property, permittivity and permeability, and for a single phase material they define the upper limit of α_{ij} as following [15]

$$\alpha_{ij} < \sqrt{\epsilon_{ij}\mu_{ij}} \quad (1.4)$$

Many of the single phase materials posses either low permittivity or low permeability or both, as a consequence of which the magnetoelectric coupling is small. For magnetoelectric composite materials, an indirect coupling between ferroelectric and ferromagnetic phase can be established via strain.

Piezoelectricity defines the materials property that converts applied stress in to proportional electric charge. The linear constitutive equations for a piezoelectric material are given as:

$$D_3 = \epsilon_{33}^T E_3 + d_{33} T_3 \quad (1.5)$$

$$S_3 = d_{33} E_3 + s_{33}^E T_3 \quad (1.6)$$

where D, E, T and S are the dielectric displacement, electric field, stress and strain, ϵ is the permittivity, s is elastic compliance and d is piezoelectric charge constant. The constitutive equations for magnetostriction are given as [16]:

$$S = s^H T + qH \quad (1.7)$$

$$B = qT + \mu^T H \quad (1.8)$$

where B, q, μ and H are magnetic induction, piezo magnetic coefficient, permeability and magnetic field.

Magnetoelectric coefficient of a composite can be described in direct notation of tensors as:

$$T = cS - e^T E - \alpha S^{ms} \quad (1.9)$$

$$D = eS + \varepsilon E + \alpha H \quad (1.10)$$

$$B = \mu(\varepsilon, E, H)H \quad (1.11)$$

where σ , ε , D , E , B , H , c and K are the stress, strain, electric displacement, electric field, magnetic induction, magnetic field, stiffness constant at constant field and dielectric constant at constant strain and magnetic field respectively [17].

The models proposed in literature show variation of ME coefficient with piezoelectric coefficient, piezomagnetic coefficient, and elastic compliances of piezoelectric and magnetostrictive phases. Srinivasan et al. have proposed the ME coefficient as:

$$\frac{\delta E_3}{\delta H_1} = \frac{-2d_{31}^p q_{11}^m v^m}{(s_{11}^m + s_{12}^m)\varepsilon_{33}^{T,P} v^p + (s_{11}^p + s_{12}^p)\varepsilon_{33}^{T,P} v^m - 2(d_{31}^p)^2 v_m} \quad (1.12)$$

where d_{31}^p is the piezoelectric coefficient, v^m and v^p are the volume of magnetic and piezoelectric phase, t^m and t^p are the thickness of magnetic and piezoelectric phase, s_{11}^p, s_{12}^p are the elastic compliances for piezoelectric phase, s_{11}^m, s_{12}^m are the elastic compliances for magnetostrictive phase, q_{11} is the piezomagnetic coefficient of the magnetic phase and $\varepsilon_{33}^{T,P}$ is the permittivity of the piezoelectric phase.

Dong et al. have derived the expression for the magnetoelectric coefficient in T – T mode as:

$$\left. \frac{dV}{dH} \right|_{T-T} = \beta \frac{n(1-n)Ad_{33,m}d_{31,p}g_{31,p}}{S_{11}^E[nS_{11}^E(1-k_{31}^2) + (1-n)S_{11}^H]} \quad (1.13)$$

where β is a constant related to DC magnetic field with a maximum value of 1, n is the thickness ratio of magnetostrictive layer to composite thickness, d is the piezoelectric strain constant, s is the elastic constant, g is the piezoelectric voltage constant, A is the cross-sectional area of the laminate and k is the electromechanical coupling factor. The relevance of the constant β was not explained in this model.

Clearly the ME coefficient is directly related to piezoelectric constant which is related to dielectric permittivity [$d_{31}^2 = k_{31}^2 (s_{11}^E \epsilon_{33}^T)$] and piezomagnetic coefficient which is related to permeability [$q_{11,m} = \mu_{33} \cdot s_{33} \cdot \lambda_{33}$].

1.3 Magnetoelectric single phase materials

The history of the magnetoelectric effect dates back to 1894 when Pierre Curie observed that a body with asymmetric molecules gets electrically polarized under magnetic field and vice versa. In 1958, Landau and Lifshitz conducted the feasibility study on presence of magnetoelectric effect in crystals of specific symmetry. Later Dzyaloshinskii showed the violation of time-reversal symmetry explicitly for a single phase antiferromagnetic system (Cr_2O_3). In 1960, Astrov presented the experimental evidence of ME effect in Cr_2O_3 in a wide temperature range of 80 – 330 K [18 -19]. Figure 1.2(a) shows the magnetoelectric coefficient of Cr_2O_3 exhibiting peak at sub ambient temperature. Smolensky and Ioffe synthesized the antiferromagnetic ferroelectric perovskite ceramic $\text{Pb}(\text{Fe}_{1/2}\text{Nb}_{1/2})\text{O}_3$ (PFN). Later single crystals of PFN were grown and the presence of weak spontaneous magnetic moment in the ferroelectric phase below 9K was confirmed [20]. Recently single phase thin film multiferroic system such as perovskite type BiFeO_3 or BiMnO_3 , the boracite family, BaMF_4 families where M is the divalent transition metal, hexagonal RMnO_3 where R is rare earth metals, are of interest to understand the magnetoelectric coupling between two types of dipoles [21 – 24]. These single phase materials show two transitions, one corresponding to paraelectric to ferroelectric phase and another corresponding to ferro / ferri / antiferromagnetic to paramagnetic phase. The mechanism for the observance of magnetoelectric effect in single phase materials is specific to a family. For example – stereochemical activity of Bi lone pair for BiFeO_3 , frustrated spin resulting from magnetoelastic lattice modulations for TbMnO_3 , and charge ordering in doped perovskite [14].

Single phase magnetoelectric (ME) materials suffer from the drawback that the ME effect is considerably weak. They can be used only at very low temperature and involve expensive materials and processing technique, and have disadvantage of degradation under cyclic conditions. The reason behind this is that the single phase materials have two order parameters: polarization and magnetization. One of the order parameters is generally large and the other is small, which results in minor ME exchange between the two subsystems.

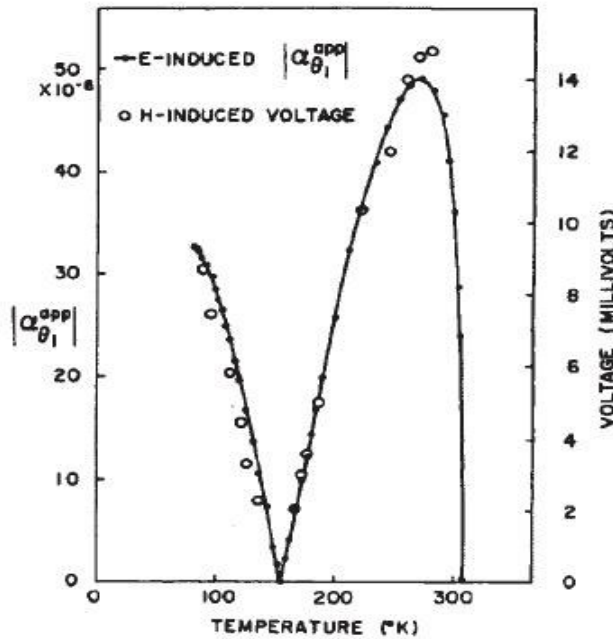


Figure 1.2: Magnetoelectric coefficient of Cr_2O_3 as a function of temperature [Ref: 18 -19]

1.4 Magnetoelectric composite materials

Better alternatives are ME composites that have large magnitudes of ME voltage coefficient. The ME effect can be realized by using composites of piezomagnetic and piezoelectric phases or magnetostrictive and piezoelectric phases. Moreover these composites are easy to fabricate compared to the single phase materials, cost effective, and have higher working temperature range [25 -27].

1.4.1 Properties of composite

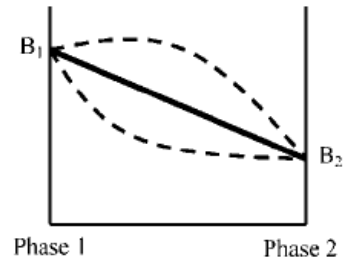
Composite properties can be divided into three categories; sum properties, product properties and combination properties. A sum property is average of the contribution from individual phases present in the composite such as density, resistivity etc. Product property can be explained as following: If one phase shows the property $A \rightarrow B$ and the other shows $B \rightarrow C$, then the composite will show new property $A \rightarrow C$. Magnetolectric effect is product property of the composite. Other examples of product property are piezoresistance (piezoelectric and magnetoresistance), magnetoresistance (magnetostriction and piezoresistance), photostriction (photoconductivity and electrostriction), and piezoluminescence (piezoelectricity and electroluminescence) [28]. If the average magnitude of the property in composite exceeds the value of the end components then it's an example of combination properties. If two phases show convex and concave type of sum properties then the combination of these two will produce a maximum at an intermediate phase composition. Figure 1.1 schematically describes the various configurations [29].

1.4.2 Connectivity of composite

Composite geometry can be designed based on the connectivity. For two phase system, there are ten types of connectivity. For three and four phase system there are 20 and 35 types of connectivity. The connectivity in general can be given by the ratio $\frac{(n+3)!}{3!n!}$, where n is number of phases. Figure 1.4 shows the geometry for different connectivities (1 – 0, 2 – 0, 3 – 0, 1 – 1, 2 – 1, 3 – 1, 2 – 2, 2 – 3 and 3 – 3) in two phase composite.

(a) Sum Properties

Phase 1 : $A \rightarrow B_1$
 Phase 2 : $A \rightarrow B_2$ \int $A \rightarrow B^*$



(b) Product Properties

Phase 1 : $A \rightarrow B$
 Phase 2 : $B \rightarrow C$ \int $A \rightarrow C$ New Function

(c) Combination Properties

Phase 1 : $A \rightarrow B_1/C_1$
 Phase 2 : $A \rightarrow B_2/C_2$ \int $A \rightarrow (B/C)^*$

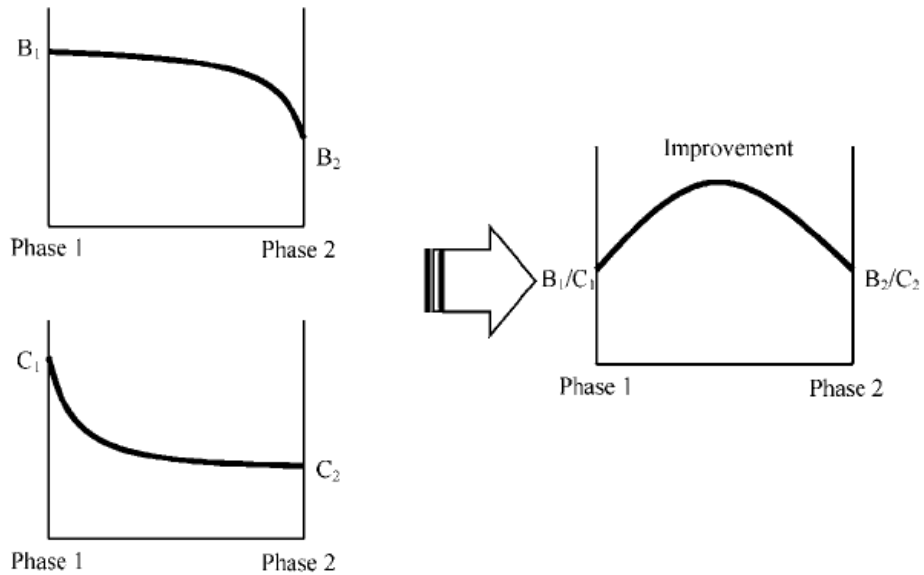


Figure 1.3: Properties of different types of composite system [Ref: 36].

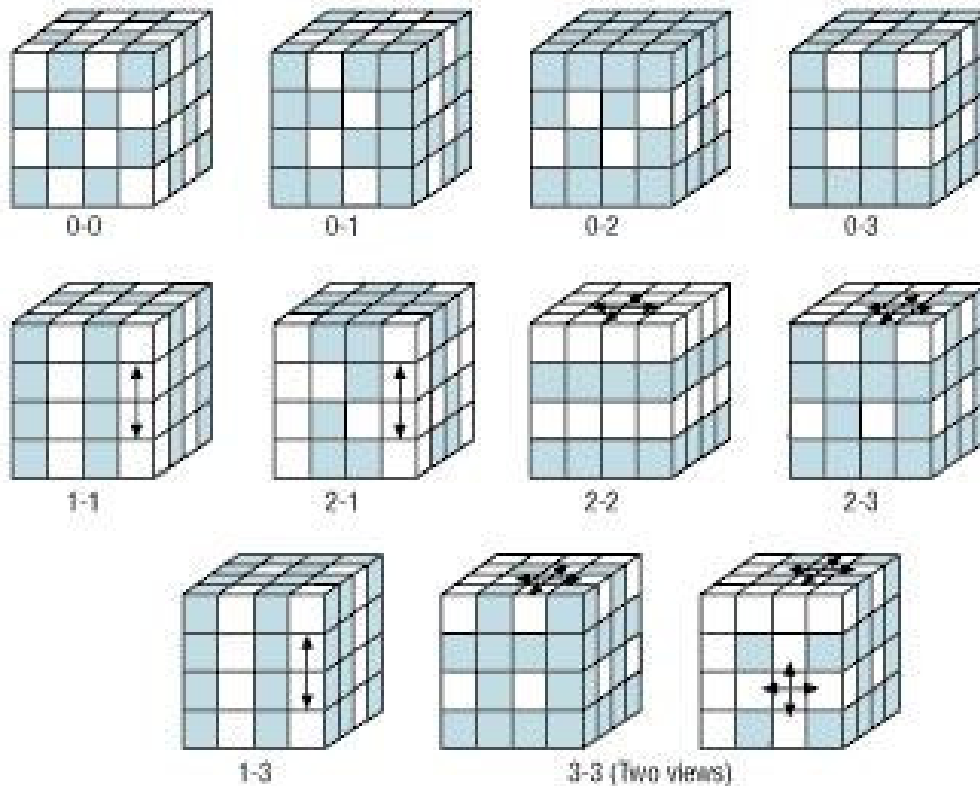


Figure 1.4: Different types of connectivity of the two phase composite system. [Ref. 29, 30]

A 3 – 0 connectivity implies particulate type of composite where one phase will be the matrix and the other phase will be dispersed in the matrix. A 2 – 2 connectivity represents the layered geometry which can be bilayer, trilayer or multilayer. The phases are connected in plane but not out of plane. This connectivity is most commonly used for multilayer capacitors and laminated magnetoelectric composite [30].

1.4.3 Types of magnetoelectric composites

Among various possibilities for magnetoelectric composites, insitu, sintered particulate and nano particulate composites are of 0 – 3 connectivity whereas laminate and multilayer composites are mainly of 2 – 2 type and the nanopillars are 1 – 3 composites. In the following subsection each of the composite system will be discussed separately with list of different reported values for ME coefficient.

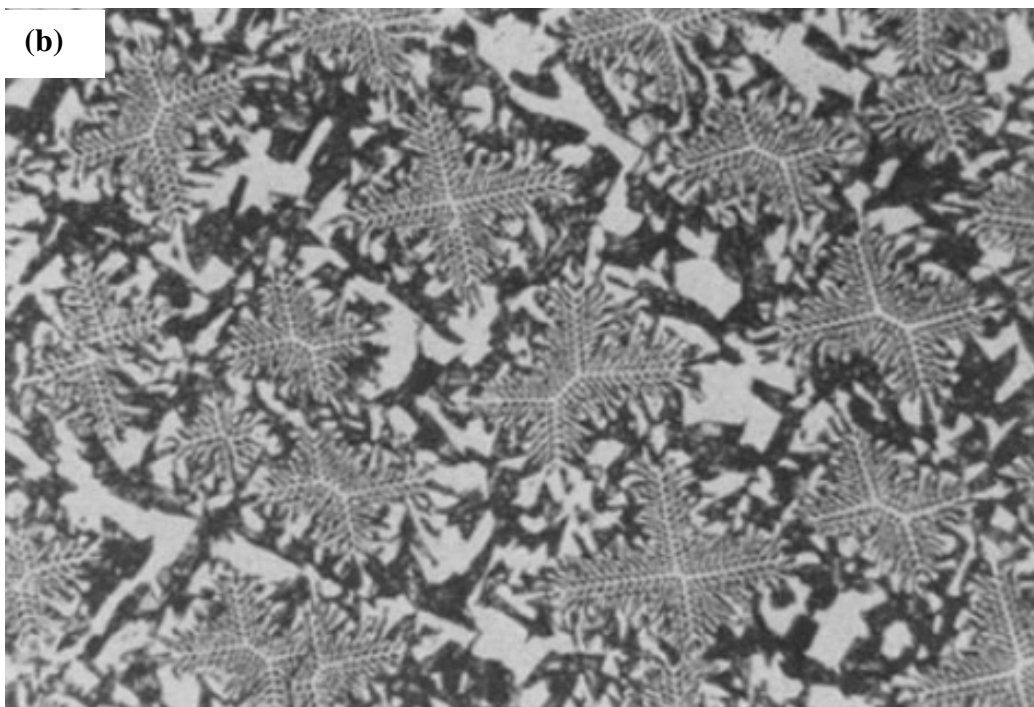
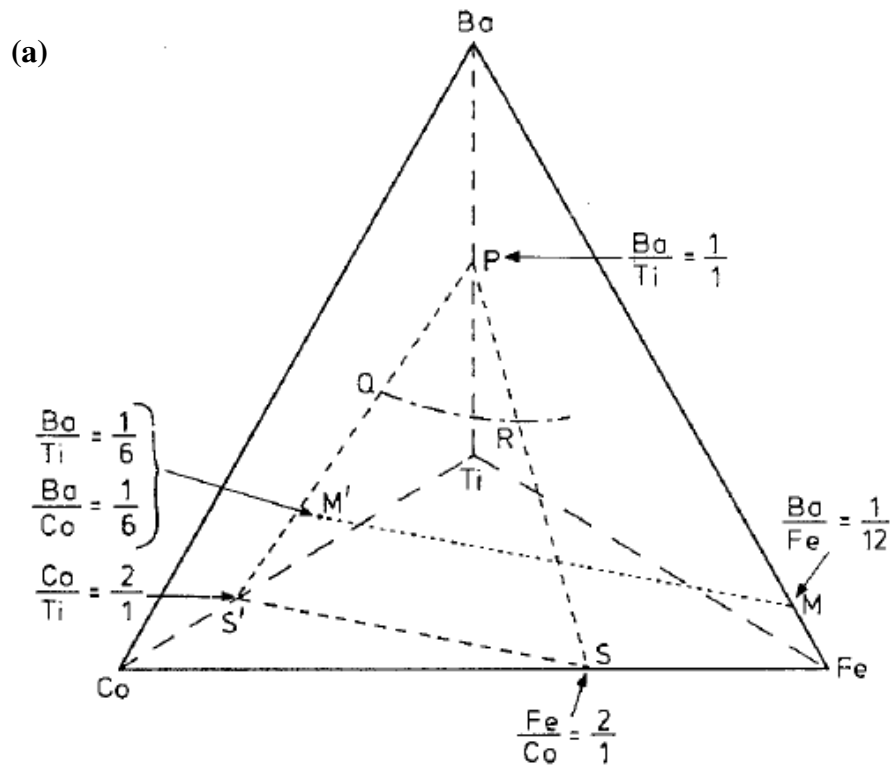


Figure 1.5: (a) simplified diagram of Ba – Ti – Fe – Co system showing the metallic component, (b) micrograph of spinel dendrites in matrix of BTO – CFO insitu composite with excess TiO_2 [Ref: 31].

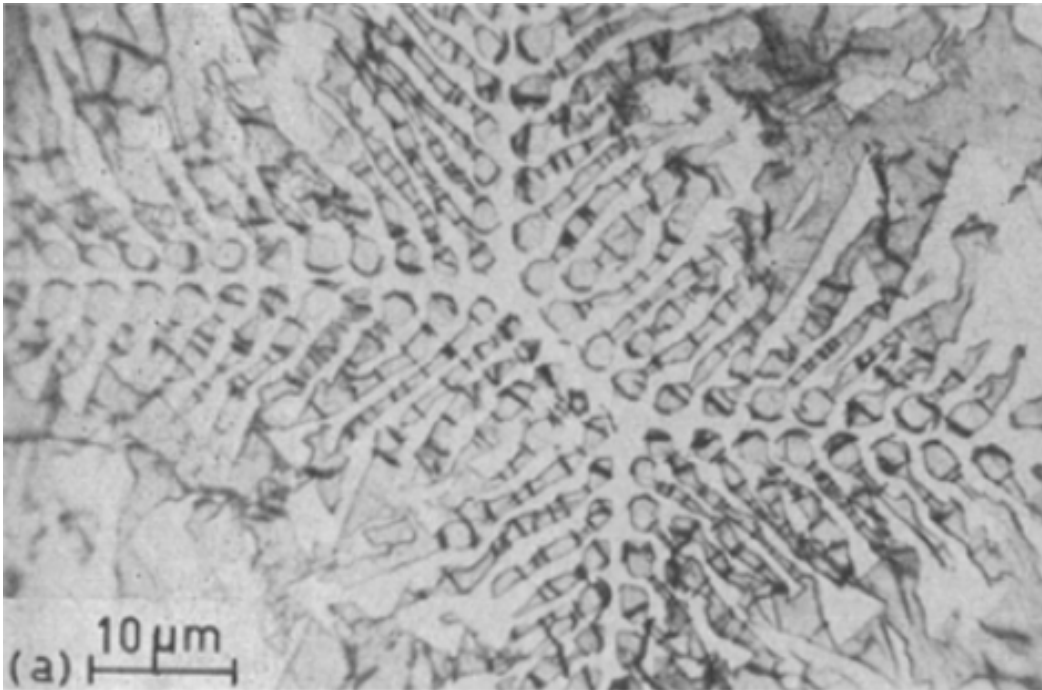


Figure 1.6: Transverse section of spinel dendrites. [Ref: 33]

1.4.3.1 Insitu composite using unidirectional solidification

The original work on ME composites was done at Philips Laboratories [31 -35]. The ME composites were synthesized by unidirectional solidification of eutectic composition in quinary system Fe-Co-Ti-Ba-O. Figure 1.5 (a) shows the phase diagram for Ba – Ti – Co – Fe quinary system. The unidirectional solidification results in decomposition of eutectic liquid into alternate layers of the constituent phases; a piezoelectric perovskite phase (P) and a piezomagnetic spinel phase (S) ($L \rightarrow P + S$). The results showed that presence of excess TiO_2 (1.5 wt %) gives a high ME voltage coefficient of $dE/dH = 50 \text{ mV/cm.Oe}$ [32]. However, other compositions showed a lower dE/dH in the range of 1-4 mV/cm.Oe . In subsequent work, a high ME coefficient of 130 $\text{mV/cm}\cdot\text{Oe}$ was obtained for eutectic composition of $\text{BaTiO}_3\text{-CoFe}_2\text{O}_4$ by unidirectional solidification [34]. This value is about an order of magnitude higher than that of single phase Cr_2O_3 ($dE/dH = 20 \text{ mV/cm.Oe}$). However, unidirectional solidification has several complications for implementing in practical applications such as long duration, and requires critical control

over the composition [33]. Figure 1.5 (b) shows the spinel dendrites in perovskite matrix. Figure 1.6 shows transverse section of spinel dendrites which are detrimental for obtaining large piezoelectric and magnetoelectric effect. The resistivity of these insitu composites is very low of the order of $10^8 - 10^9 \Omega - \text{cm}$, which presents difficulty in electrical poling.

1.4.3.2 Laminated composite

Recently, giant ME response has been reported for laminate composites, fabricated by bonding piezoelectric plate/disk/fibers between two layers of magnetostrictive plates/disks/foils [35 – 38]. Figure 1.7 (a) and (b) shows the piezoelectric plates or fiber sandwiched between two magnetostrictive plates or foils respectively. In these designs, the external magnetic field creates strain in the magnetostrictive layers which is transferred on to the piezoelectric material through bonding layer thereby producing electrical charge across the electrodes. The electrical charge is amplified and converted into voltage using a capacitive circuit. A magnetic DC bias of varying magnitude is essential to obtain the magnetostrictive strain. The magnetoelectric laminate composite, embedding piezoelectric PMN-PT single crystal between magnetostrictive Terfenol-D single crystal, exhibited the ME coefficient of 10.30 V/cm.Oe, which is ~80 times higher than that previously reported in either naturally occurring magnetoelectrics or Artificially-Designed Composites (ADC). Srinivasan et al. have investigated the bilayer and multi-layer structure of PZT and ferromagnetic ferrites. It was shown that multilayer structures can provide ME coefficient as high as 1500 mV/cm.Oe [39 – 40]. Laminated structures of Ni – PZT – Ni were found to exhibit ME coefficient of 400 – 450 mV/cm.Oe [41]. Three phase composites of PZT/epoxy/Terfenol-D or PZT/PVDF/Terfenol-D have been reported to possess the ME coefficient in the range of 50 – 150 mV/cm.Oe [44]. Dong et al. have reported composite structures consisting of piezofiber laminated between two Three phase composites of PZT/epoxy/Terfenol-D or

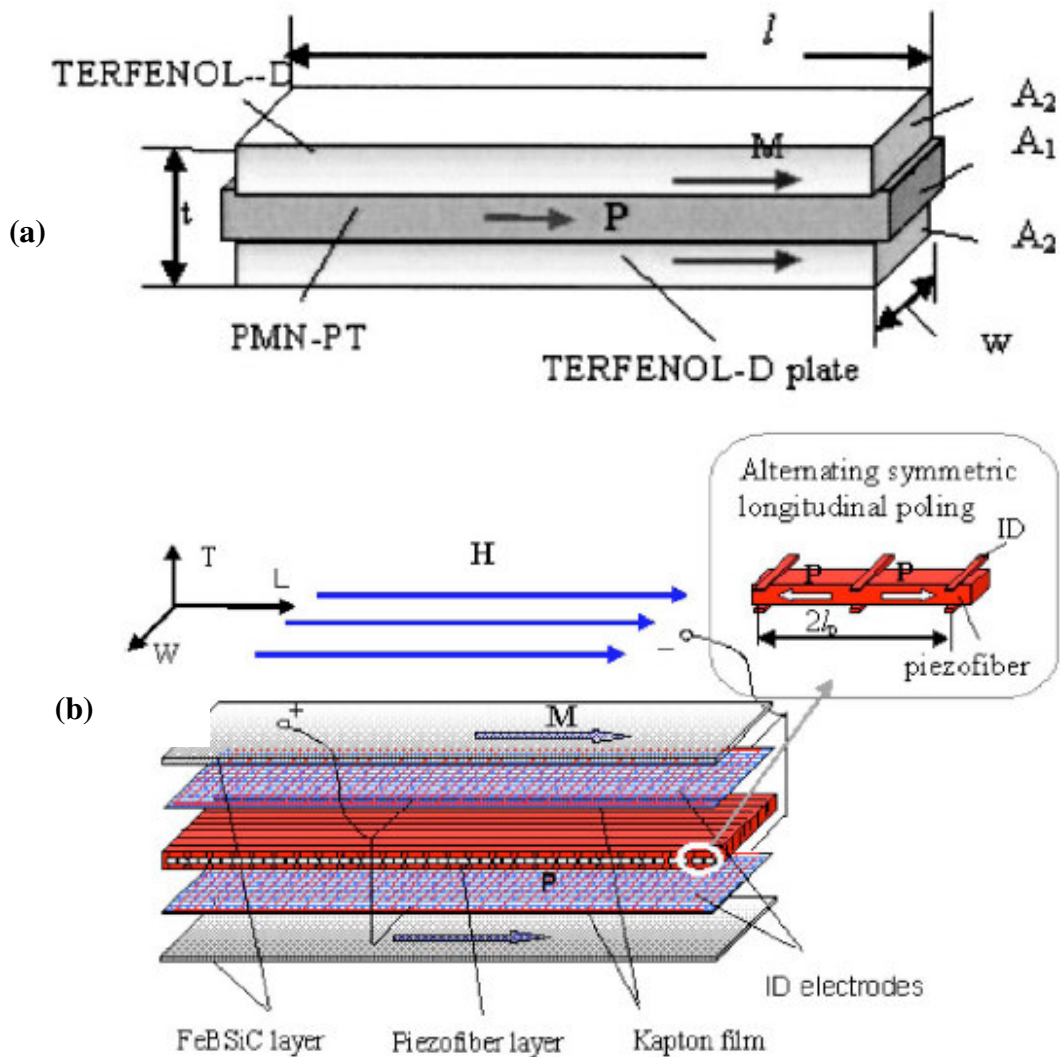


Figure 1.7: Schematic diagram of laminated composite (a) Terfenol – D sandwich structure with PMN – PT in the middle and (b) Magnetic FeBSiC top and Bottom layer with intermediate layer as piezoelectric fiber. [Ref: 47, 51]

PZT/PVDF/Terfenol-D have been reported and the magnitude of ME coefficient was found to be in the range of 50 – 150 mV/cm.Oe [44]. Dong et al. have reported composite structure consisting of piezofiber laminated between two sheets of high-permeability magnetostrictive FeBSiC alloys [51]. This structure shows a giant response of 22 V/cm.Oe at 1 Hz. Table 1.1

Table 1.1: List of reported laminated composites and their ME response.

| Composition | Type | Coupling mode | DC Bias and Frequency | dE/dH (mV/cm.Oe) |
|--|-------------------------|---------------|-----------------------|------------------|
| PZT-Terfenol D | Laminate | T - T | 4 kOe 1 KHz | 5900 [36] |
| PMN-PT and Terfenol D | Laminate | T - T | 4 kOe 1 KHz | 10390 [36] |
| PZT – 0.4 CZFO | Laminate | T - T | 100 Hz | 280 [39] |
| PZT – Ni ₂ MnGa | Bilayer Composite | T – T | 216 Oe | 170 [42] |
| PZT and Fe- (20 at%)Ga | Laminate | L - L | 800 Oe 1 KHz | 3450 [43] |
| Terfenol D + PVDF and PZT + PVDF | Laminate | T - T | 1 KHz | 400 [44] |
| Terfenol –D + Stainless steel sheet and PZT | Laminate | L – L | 5 kHz Resonance | 40000 [45] |
| Terfenol –D + PZT and μ metal | Laminate | L – L | 1 kHz 240 Oe | 1400 [46] |
| Terfenol –D + PMN – PT | Laminate Push – pull | L - L | 1 kHz 400 Oe | 4300 [47] |
| Metglas and PVDF | Laminate Flexible | L – T | 1 kHz 8 Oe | 7200 [48] |
| PMN – PT and Fe- (20 at%)Ga | Laminate | L – L | 750 Oe 1 kHz | 1010 [49] |
| Terfenol – D + MZF and PZT | Laminate | L – L | 56 Oe 1 kHz | 3000 [50] |
| Metglass + Piezo fiber | Laminate | L – L | 2 Oe 10 Hz | 22000 [51] |
| Co _{0.6} Zn _{0.4} Fe ₂ O ₄ + PZT | Laminate | L - T | 500 Oe 1 kHz | 156 [52] |
| Ni – PZT – Ni | Laminate | L - T | 80 Oe 1 kHz | 450 [41] |
| NiFe ₂ O ₄ – PZT | Laminate | L – T | 120 Oe 1 kHz | 410 [53] |
| Terfenol –D + Epoxy + PZT | Laminate | L – T | 700 Oe 1 kHz | 7000 [54] |

Table 1.1 – Continued

| | | | | |
|--|--------------------------------------|-------|------------------|------------|
| NiFe ₂ O ₄ – PZT | Laminate bilayer | T – T | 70 Oe 1 kHz | 460 [40] |
| NiFe ₂ O ₄ – PZT | Laminate multilayer | T – T | 400 Oe 1 kHz | 410 [40] |
| NiFe ₂ O ₄ – PZT | Laminate multilayer ratio = 2.2:1 | T – T | 40 Oe 1 kHz | 1500 [40] |
| Terfenol – D – BaTiO ₃ | Laminate | T – T | 350 Oe 1 kHz | 2100 [55] |
| PZT Disk CFO ring | Laminate Disk ring | T – T | 3400 Oe 1 kHz | 102.6 [56] |

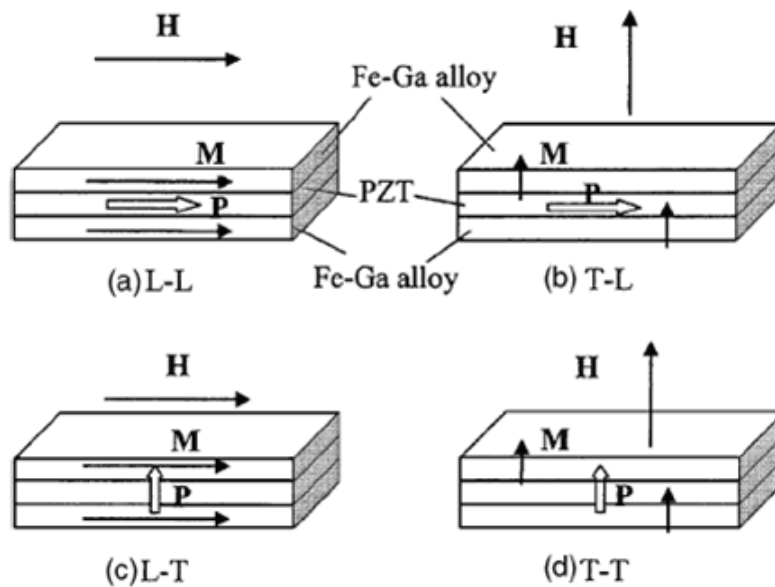


Figure 1.8: Different modes of laminated composite (a) longitudinally magnetized – longitudinally polarized (L – L), (b) Transverse magnetized - longitudinally polarized (T – L), (c) longitudinally magnetized - transverse polarized (L – T) and (d) transverse magnetized – transverse polarized (T – T). [Ref: 43]

summarizes the data reported in literature. Laminated composites offer various advantages [45 – 51] that includes:

- (i) high resistivity due to no inter-diffusion between the individual piezoelectric and magnetostrictive phase

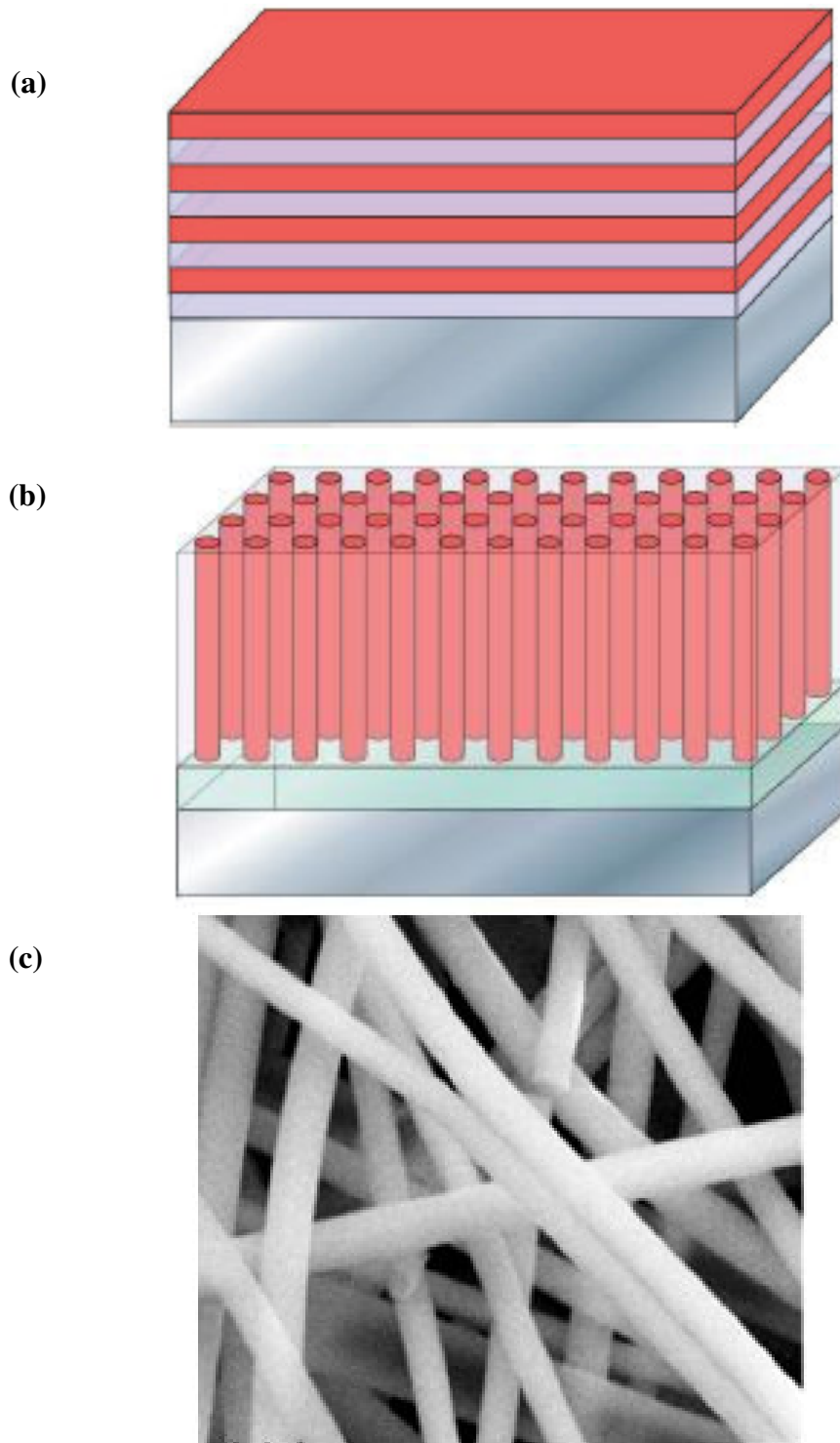


Figure 1.9: Schematic diagram of magnetolectric nanostructure, (a) multilayer films, (b) nanopillars structure and (c) magnetolectric nanowires. [Ref: 8, 65]

- (ii) Different modes of ME composite can be designed. Dong et al. have shown the design of four different modes depending upon the polarity of piezoelectric and magnetostrictive layer as shown in Fig. 1.8.

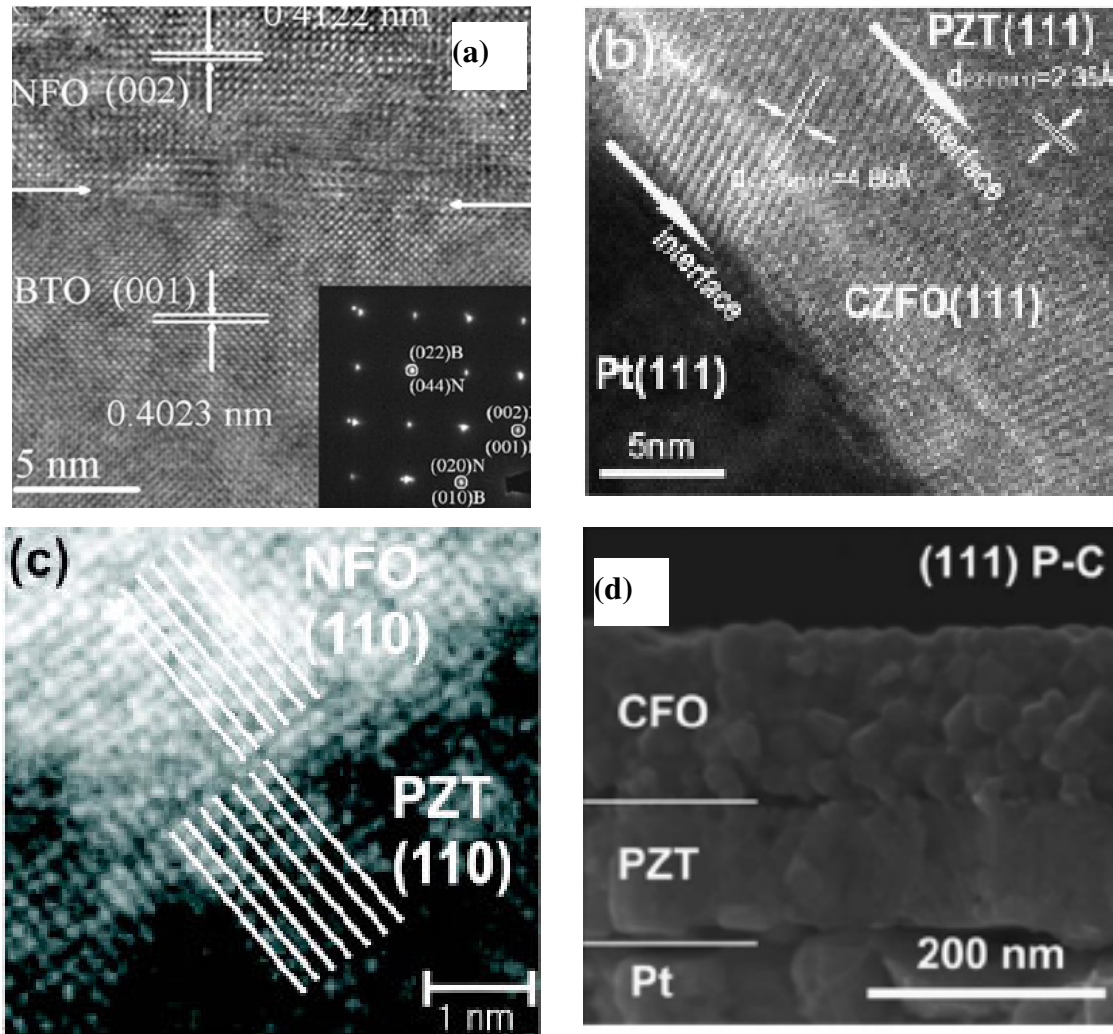


Figure 1.10: (a) HRTEM of BTO – NFO bilayer thin film structure, (b) HRTEM of PZT – CZFO bilayer thin film structure showing interface, (c) HRTEM of PZT – NFO nanoparticulate composite showing orientation relationship of NFO (110) and PZT (110) and (d) cross sectional TEM image of PZT – CFO bilayer film.[Ref: 58, 61, 62, 66]

1.4.3.3 ME micro/nanostructures:

Recently magnetoelectric composite based nanostructure have been synthesized using thin film deposition techniques such as sol - gel deposition, PLD, and RF

Table 1.2: List of reported ME coefficients in magnetoelectric thin film and nanostructures

| Composite geometry | Synthesis technique | Polarization ($\mu\text{C}/\text{cm}^2$) | Magnetization | Reported ME Coefficient |
|-------------------------------|------------------------------------|--|---------------------------|--------------------------------|
| BTO – CFO Nano pillars | PLD | 23 | 350 emu /cm ³ | - [8] |
| BTO – CFO Epitaxial | PLD | - | 225 emu /cm ³ | -[57] |
| BTO – NFO Heterostructures | PLD | 29 | 80 emu /cm ³ | 12.1 mV/cm.Oe[58] |
| BTO – CFO Nanocomposite | RF magnetron sputtering | ~ 30 | ~ 280 emu/cm ³ | 167 mV/cm.Oe[59] |
| BTO – CFO Heterostructures | PLD | 34 | 35 | 104 mV/cm.Oe[60] |
| PZT – NFO Nanoparticulate | PLD | 60 | 35 emu /cm ² | 16 mV/cm.Oe[61] |
| PZT – LSMO Epitaxial | PLD | 27 | 8 emu | 4.2 mV/cm.Oe[62] |
| PZT – CFO Bilayer | PLD | 1.25 | 0.35 T | 1.3 pC/cm ² [63] |
| PZT – CFO Bilayer | Sol – gel | 50 | 108 emu /cm ² | ~ 15 mV/cm.Oe [64] |
| PZT – CFO Nanowires | Sol – gel & electrospinning | - | 30 emu/gm | -[65] |
| PZT – CZF | Sol – gel Spin coating | 12.8 | 250 emu /cm ² | -[66] |
| PZT – (Tb – Fe) | Low Energy Cluster Beam | 51 | 47 emu /cm ² | 140 mV/cm.Oe[67] |
| PZT – SRO – CFO | PLD | 35 | 170 emu /cm ² | -[68] |
| PT – CFO Epitaxial | PLD | - | 220 emu/cm ³ | -[69] |
| PZT – CFO Nanostructure | PLD | 45 | 10 emu/cm ³ | 390 mV/cm.Oe[70] |
| BNTO – CFO Nanocomposite | Chemical Solution Deposition | - | - | 52.8 mV/cm.Oe[71] |

magnetron sputtering. The commonly experimented geometries are bilayers, heterostructures, self-assembled structures, and nanowires. Figure 1.9 shows the common nanostructures based

on thin film fabrication technique. Zheng et al. have synthesized the self-assembled nanostructure in $\text{BaTiO}_3 - \text{CoFe}_2\text{O}_4$ [BTO - CFO] composite system consisting of CFO nanopillars embedded in BTO matrix [8]. TEM investigation of self assembled nanopillars show 20 – 30 nm CFO pillars embedded in BTO matrix. Compared to bulk ME composites, nanostructures offer the possibility of much higher interlayer interaction. The disadvantage of nanopillars is high leakage current due to continuous path of low resistance ferrite pillars. The multilayer geometry has a disadvantage of clamping effect of the substrate. ME nanoscale heterostructures of PZT – CFO double layer thin films, PZT – NFO nanoparticulate composites, and PZT – CFO nano wires have also been reported [63]. Table 1.2 briefly summarizes the results on magnetoelectric thin films, multilayers and nanostructures. Figure 1.10 shows the HRTEM and cross sectional TEM of 4 different systems. Figure 1.10 (a) shows the HRTEM image of BTO – NFO heterostructure with sharp SAED pattern in the inset. The misfit strain is around – 0.8 % which is smaller than that for bulk ceramics. The lattice constant calculated from SAED pattern was 3.943 and 4.023 Å for BTO and 8.244 Å for NFO [58]. Figure 1.10 (b) shows the cross sectional HRTEM for PZT – CZFO composite thin film. Clear interface between PZT and CZFO was observed as well as the interface between the CZFO and the substrate. No evidence of 2nd phase was found in these kinds of layered film by HRTEM. In the same literature, it was found that if the PZT was deposited earlier, then it has a preferential growth along the (100) crystallographic orientation [66]. Figure 1.10 (c) shows the HRTEM image of PZT – NFO nanoparticulate composite thin film. Clearly a well defined boundary with different atomic arrangements was observed in this kind of composite which indicates good dispersion of NFO particles in PZT matrix [61]. The cross sectional TEM image shown in 1.10 (d) corresponds to PZT (440 nm) – LSMO (330 nm) bilayer deposited on top of (001) LaAlO_3 substrate. There were large amounts of void grain boundaries observed in LSMO phase, which may help to release the magnetostrictive strain along the normal of the plain direction [62].

1.4.3.4 Sintered composites:

Magnetolectric (ME) effect in particulate sintered composites has generally been obtained by combining magnetostrictive and piezoelectric phases. Sintered composites fabricated by mixing of piezoelectric and ferromagnetic phases have been widely

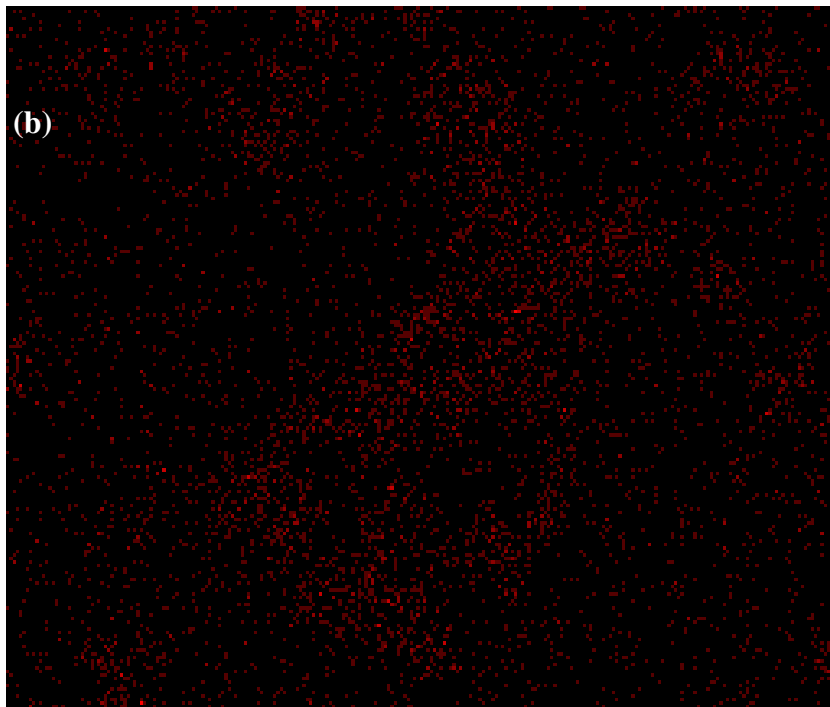
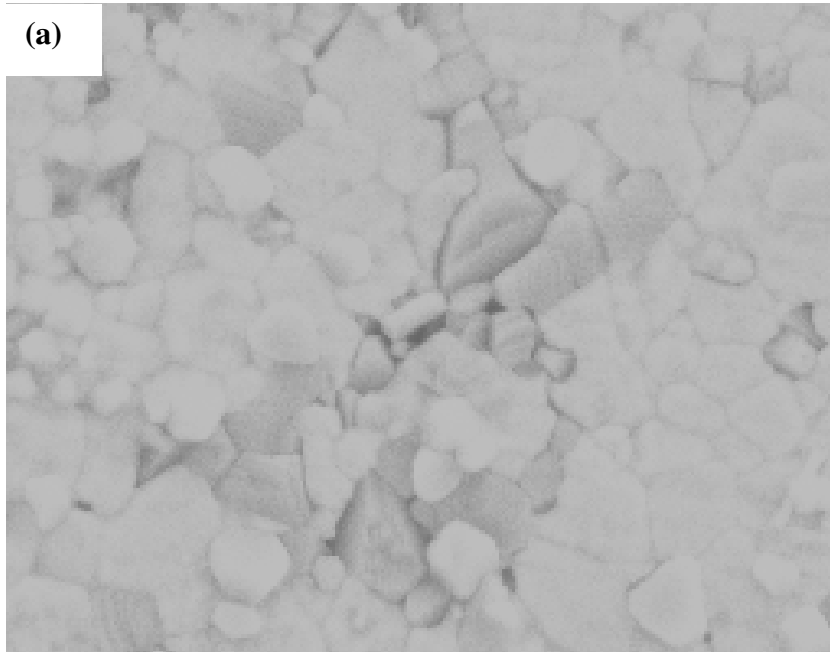
Table 1.3: List of some reported insitu and particulate/sintered composite.

| Composition | Type | Sintering Condition | DC Bias and Frequency | dE/dH (mV/cm.Oe) |
|--|-------------------------------|------------------------------|-----------------------|------------------|
| BaTiO₃- CoFe₂O₄ | Unidirectional solidification | With excess TiO ₂ | | 50 [31] |
| BaTiO₃ – Ni(Co, Mn)Fe₂O₄ | Particulate | | 1kHz | 80 [32] |
| PZT – 20 (wt%) NiCo_{0.02}Cu_{0.02}Mn_{0.1} Fe_{1.8}O₄ | Particulate | 1250°C | 1.25 kOe 1 kHz | 115 [1] |
| PZT – 30 % CuFe₂O₄ | Particulate | 950° C, 2 Hrs | 460 Oe 100 kHz | 421[72] |
| PZT – 59% Ni_{0.8}Zn_{0.2}Fe₂O₄ | Particulate | Hot Pressed 1000° C | 250 Oe 100 Hz | 45 [73] |
| BTO – 25% CuFe₂O₄ | Particulate | 1200° C 12 Hrs | 1000 Oe | 0.52[74] |
| BTO – 45% CuFe_{1.6}Cr_{0.4}O₄ | Particulate | 1100° C 24 Hrs | 1500 Oe | 0.0956[75] |
| PZT – PVDF – Terfenol – D | Particulate | 190° C 10 MPa | 2000 Oe 100 Hz | 45[76] |
| PZT – 32 NiFe₂O₄ | Particulate | 1150° C 2 Hrs | 1000 Oe 1 kHz | 80 [77] |
| BTO – 20% CoFe₂O₄ | One Pot Process | 1180°C 2 Hrs | 270 Oe 170 Hz | 2540 [78] |
| BTO – 30% Ni_{0.94}Co_{0.01}Cu_{0.05}Fe₂O₄ | Particulate | 1150° C 12 Hrs | 1000 Oe 1 kHz | 0.637[79] |
| BTO – 40% CoFe₂O₄ | Particulate Core shell | 1200°C 12 hrs | 1 kHz | 1.48 [2] |
| PZT – 35 NiFe₂O₄ | Particulate Sol-gel | 1150°C 2 Hrs | 1000 Oe 287 kHz | 28500 [80] |
| (Sr, Ba)Nb₂O₆ – 30% Ni_{0.8}Zn_{0.2}Fe₂O₄ | Particulate | 1250°C 3 Hrs | 1000 Oe 100 kHz | 26.6 [81] |

studied because of its simplicity in synthesis using well-established conventional ceramic processing technique. Various particulate composites of piezoelectric (BaTiO_3 or $\text{Pb}(\text{Zr,Ti})\text{O}_3$) and magnetostrictive (LiFe_5O_8 , $\text{Ni}_{1-x}\text{Zn}_x\text{Fe}_2\text{O}_4$, CoFe_2O_4 , or CuFe_2O_4) phases with different dimensional connectivities have been reported as summarized in Table 1.3. Although the ME effect is known in various binary systems, little information is available on structure – property relationship. Sintered particulate composites have inferior properties compared to laminated ones because of drawbacks of low resistivity, interface defects, interface diffusion and mismatch of elastic compliances. To enhance the ME coefficient of sintered composite, it is necessary to optimize the composition, microstructural features (grain size, grain orientation), and sintering parameters.

In particulate composites, higher ME coefficient implies higher elastic coupling between the magnetic and piezoelectric phases. The elastic coupling can be maximized by having coherent response from the magnetostrictive phase under dc bias, so that the stress on the piezoelectric lattice across the grains is in phase with each other. This is only possible if there is uniform distribution of the magnetostrictive phase with soft piezoelectric phase. If the particles are crystallographically aligned with the matrix, more benefits can be obtained because of the built-in directionality. However, this is quite difficult to obtain in practice. An attempt has been made in this thesis to synthesize the textured composites.

In addition to conventional ceramic processing and sol-gel route, one pot [78] is a process where the two phases are simultaneously synthesized in the same pot in order to get better homogenization, and dispersion of magnetic phase. Heterocoagulation has been demonstrated to synthesize the core shell structures of ferroelectric and ferromagnetic composite particles [reference]. Heterocoagulation process consists of coagulation of particles with opposite surface charges dispersed in a solution. At some specific pH value one species has a positive surface charge density whereas other has a negative one.



1.11: (a) PZT – NZF particulate composite showing ferrite connectivity and (b) Elemental mapping of Zn confirming the connectivity of the ferrite particles.

1.4.4 Problems and shortcoming of sintered composite:

The trend of the ME research since 2002 is to use a high magnetostriction material (Terfenol-D) or a high permeability material (Metglas) and use epoxy to bond with a PZT plate, rod, disk, fiber, etc. Different piezoelectric vibration modes such as bending, longitudinal, radial, push-pull etc. have been utilized in laminated geometries. However, these reported structures have so far failed to identify the synthesis process that can eliminate the need for epoxy. Practically, industry would like to have a ceramic composition with relatively simple processing technique that can provide high sensitivity. In order to get high ME coefficient following problems need to be addressed:

1. How can the ME coefficient be enhanced in the bulk sintered composites?
2. What are the microstructural variables that make significant contribution towards ME coefficient?
3. Define a composition space that allows identification of specific elements providing enhanced ME coefficient.
4. Define the geometry of the sintered composite that will lead to better coupling in dual phase structures.
5. Establish the composition – microstructure – property relationships for dual phase sintered composites.

In order to solve these problems several factors need to be investigated [1, 32].

1. Effect of the piezoelectric and magnetostrictive composition.
2. New microstructures that can provide enhanced resistivity (reduce interconnectivity as shown in Figure 1.11),
3. Processing steps that can provide equilibrium between the two phases,
4. Removal of defects at the piezoelectric – magnetostrictive interface formed due to mismatch in shrinkage rate and sintering temperatures of individual phases (Figure 1.12).

5. Control of grainsize and orientation,
6. Periodic distribution of two phases.
7. Geometry of the phase distribution

A significant effort is required to address the above mentioned factors. Realization of sintered composite with large ME coefficient will provide an adequate energy conversion device from magnetic to electric. In addition to magnetic field sensing and current probes, various other commercial application are possible such as gyrator, read only memory device, transducers, filters, recording heads and sensors.

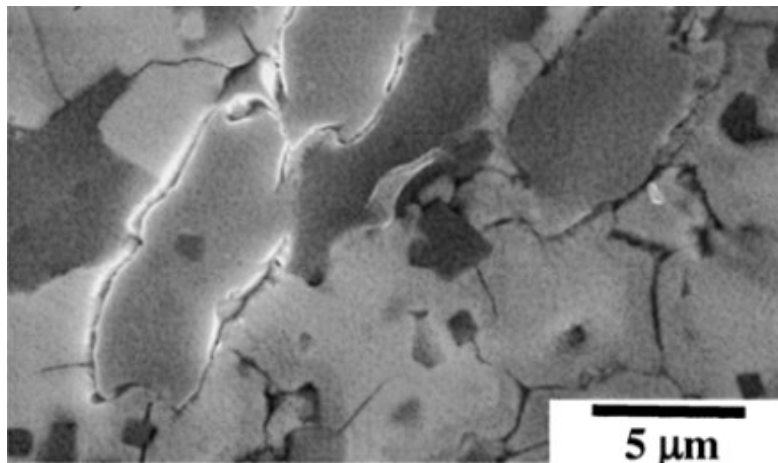


Figure 1.12: SEM micrograph of PZT – (Ni, Co, Mn) ferrite showing defects at the interface such as microcracks and porosity. [1]

CHAPTER 2

OBJECTIVE AND RESEARCH PLAN

2.1 Objective

There are several fundamental challenges in realization of high ME coefficient bulk sintered composites. For 25 years, since the pioneering work at Phillips laboratories, ME coefficients did not change much until Ryu et al. reported results on laminates in 2001. In order to achieve similar breakthrough in the field of sintered ME composite a new vision is required. This thesis is a step in that direction. To improve the performance of sintered composites, comprehensive understanding of each parameter that controls the magnetoelectric coefficient is necessary. An effort has been made here to correlate these parameters with the magnitude of ME coupling. Some of these controlling parameters are identified as: composition, microstructure, geometry, orientation, post-sinter heat treatment, and nanoscale assembly.

In this work, emphasis was placed on basic understanding of magnetoelectric phenomenon in sintered composites to clearly delineate the effect of each parameter. Several experiments were designed and implemented such that magnetoelectric coupling is dependent on only specific set of variables. It is imperative that each experiment should be followed by thorough electrical, magnetic, and microstructural investigation to correlate the physical properties with the changes occurring in synthesized composite. This process was the underlying theme in this study.

The major goal of this proposed research is to synthesize a ME composite which has a high ME coefficient of 1.0 – 1.5 V/cm.Oe.

2.2 Plan of Research

The selection of appropriate composition and tenability of the composition with suitable doping is the primary step towards the goal of high ME coupling. Next, the effect of microstructural features, sintering parameters and heat treatment on the ME response should be analyzed. The tasks conducted in this thesis are summarized as following:

2.2.1 System selection and optimization of composition

The figure of merit for large magnetoelectric coefficient in a ferromagnetic – ferroelectric composite is given as:

$$\text{Figure of merit} = \sqrt{\mu\epsilon} \quad (1)$$

where μ is the magnetic permeability and ϵ is the dielectric permittivity. Thus, the primary criterion for selection of individual phases in the composite is to identify materials having similar crystallographic symmetry and possessing large magnetic permeability and dielectric permittivity. BaTiO₃ (BT), Pb (Zr,Ti)O₃ [PZT], Pb(Mg_{1/3}Nb_{2/3})O₃ – PbTiO₃ [PMN – PT] have high piezoelectric and dielectric properties, Curie temperature, and resistivity. Nickel based ferrite have been found to be suitable second phase as they exhibit high stability in doped-PZT matrix. Ni based ferrites are soft compared to cobalt ferrite and have higher permeability. It has been shown that addition of Zn in ferrite structure improves the permeability, magnetization and reduces Curie temperature. The composition for ferromagnetic phase can be varied to change the magnetic properties such as magnetization, permeability, and coercivity.

PZT composition can be varied using acceptor or donor dopant. To improve the resistivity of the PZT based ceramic Mn, and Nb can be used as the dopants. The combined studies of Ni based ferrites with that of piezoelectric phase in sintered composites has not been conducted and is required in order to choose the proper material system. By this compositional optimization it can be understood, which type of dopant really contributes to the enhancement of magnetoelectric coefficient.

2.2.2 Effect of matrix grainsize

The dependence of piezoelectric, ferroelectric and dielectric properties on grainsize is well – known but the grain size effects in a composite system has not been studied. One of the reasons for this can be difficulty in achieving systematic changes in the grain structure. The contribution of grainsize will come from the grain boundary pinning mechanism for large and small grains. SEM analysis combined with surface tension measurements indicates that the surface bond contraction due to small size induces a compressive stress on the inner part of a grain and this effect plays an important role in ferroelectric materials in the nanometer size range. The induced stress causes decrease of Curie temperature and spontaneous polarization with decreasing grain size. The domain wall contribution has an opposite effect as compared with the surface bond contraction induced effect. When the grain size decreases to a value comparable to the width of domain walls, pinning points develop inside the grains and the domain wall motion is inhibited. The reduced wall mobility causes a decrease in the relative permittivity. The measured value is a competition between the increase of relative permittivity by the surface bond contraction effect and its decrease by the domain wall pinning effect. It will be very important to understand these effects in ME composites.

2.2.3 Effect of geometry

In bulk composite, the resistivity of the composite drops rapidly as the connectivity of the ferrite particles forms a conductive path along the sample dimension. This leads to charge leakage through the ferrite. This problem can be addressed by adopting the layered geometry. However, the challenge lies in the synthesis of the sintered layered structures with buried electrodes. The diffusion of the elements from the magnetic phase into piezoelectric and vice versa can be prevented by incorporating the electrode layer however the interface between the metallic electrode and ceramic may reduce the overall resistivity. Thus, a synthesis process needs to be designed such that there is sharp interface between the ceramic and electrode layer and there is no cross – diffusion of the elements.

2.2.4 Effect of post sinter heat treatment

For high magnetoelectric coefficient, homogenized large piezoelectric grain, even distribution of magnetic phase in the matrix, reduced defects, and internal strain – free composite is desired. Internal strains arise due to difference in shrinkage rates and crystal structure. A post sintering treatment will help in reducing the defects such as porosity and chemical heterogeneity at the boundary, compositional gradients across the matrix, and elastic softening [82 – 84]. Optimized post sinter heat treatment condition may improve the individual piezoelectric and ferromagnetic properties, consequently affecting the magnetoelectric properties.

2.2.5 Synthesis of cofired composites

The next step in this study will be to combine all the above mentioned parameters in a co-fired sintered composite. This is challenging as it requires control on the microstructure development along with mechanical integrity. The poling process for piezoelectric layer requires intermediate electrodes which presents additional constraint on sintering temperature and time.

2.2.6 Texturing

Crystallographic texturing of piezoelectric grains can improve the piezoelectric and ferroelectric response because better spontaneous polarization can be achieved as compared to randomly oriented grain. The goal in this study will be to texture the piezoelectric layer in co-fired laminate composite. The challenge of cofiring the textured piezoelectric phase with magnetostrictive phase is related to diffusion. For texturing the grains, the samples needs to be soaked for long periods of time (~ 50 – 100 hrs) at high temperature (>1000 °C), which may cause diffusion of elements from magnetostrictive phase into PZT and hinder the grain texturing process. In order to achieve the grain texturing in trilayer, lower sintering temperature phases needs to be identified. Another problem which may arise is the delamination at the interface. In order to prevent delamination pressure-assisted sintering process will be developed.

2.2.7 Layered ME composite from bottom-up approach

A strong magnetoelectric coupling requires a strong interphase elastic interaction. Thus, this chapter plans to investigate the particle-by-particle synthesis approach for building a three-dimensional composite. Synthesis of core-shell particles of $\text{Pb}(\text{Zr,Ti})\text{O}_3$ (PZT) and NiFe_2O_4 (NFO), where PZT is core and nanosize NF is shell, will be conducted. The core-shell structure of PZT and NFO will be pressed and sintered together to form a layered geometry. It is expected that this composite will provide the most effective inter-phase exchange coupling, originating from the maximized inter-phase contact. This bottom-up approach, where single core – shell particles are compacted into a three dimensional network will also enhance the surface area contact for the ME composite.

CHAPTER 3

EXPERIMENTAL PROCEDURE

3.1 System Selection

In addition to equilibrium between phases, there are some other important fabrication issues associated with the sintered ME particulate composites. These are: (i) chemical reaction should not occur between the piezoelectric and magnetostrictive materials during sintering, (ii) resistivity of magnetostrictive phase should be as high as possible, and (iii) mechanical defects, such as pores at the interface between two phases should not exist in the composite for good elasto-mechanical coupling. If the resistivity of magnetostrictive phase is low, the electric poling becomes very difficult due to leakage current which reduces the ME properties of the composites. If the ferrite particles with low resistivity make connected chains, the electric resistivity of composites will reduce significantly. Thus, good dispersion of the ferrite particles in the matrix is essential for high electric resistivity of the composite.

As is well known that compared to BaTiO₃, PZT has stronger piezoelectric and dielectric properties, higher Curie temperature, higher resistivity and lower sintering temperature. Investigations have shown that nickel ferrite particles are very stable in the doped-PZT matrix and do not react even at high sintering temperatures of 1250°C [85]. Further, as the resistivity of NiFe₂O₄ sintered in air is lower than that of BaTiO₃, nickel ferrite has to be doped with Mn or Co to enhance the resistivity. However, because of the cross doping the presence of Mn in BaTiO₃ phase results in the decrement of the cubic (BaTiO₃) → hexagonal (BaTiO₃) transition temperature (cubic being the low temperature phase). Thus, a modifier needs to be added to increase the transition temperature which has negative effect on ME coefficient. On the other

hand, there is no high temperature phase transition in the PZT system. PZT also satisfies the phase equilibrium criterion for large ME effect [1].

3.2 Synthesis

3.2.1 Raw Materials

Reagent-grade powders of BaCO₃, PbO, ZrO₂, TiO₂, ZnO, CoCO₃, NiO, CuO, MgO, Nb₂O₅, Fe₂O₃, MnCO₃ were obtained from Alfa Aesar, Co. MA, USA. Stoichiometric ratios of powders corresponding to composition of BaTiO₃, Pb(Zr_{0.52}Ti_{0.48})O₃ (PZT), NiFe_{1.9}Mn_{0.1}O₄ (NFM), Ni_(1-x)Zn_xFe₂O₄ (NZF, x varies from 0 to 0.5), Ni_{0.6}Zn_{0.2}Cu_{0.2}Fe₂O₄, CoFe₂O₄, Co_{0.6}Zn_{0.4}Fe₂O₄ etc. were separately ball-milled with ethyl alcohol and YSZ grinding media (5mm diameter, Tosoh Co. Tokyo, Japan) in a polyethylene jar. After 24 hours of ball milling the powders were dried at 80°C crushed and grinded for the next step.

3.2.2 Calcination and phase analysis

The powders were then shaped into a disc in 1 inch hardened steel die and kept it in alumina crucible for calcination. Calcination was done at different temperatures for different phase. BaTiO₃ and Pb(Zr_{0.52}Ti_{0.48})O₃ (PZT) were calcined at 900°C for 3 hours and 750°C for 2 hours respectively. Ferrites such as NiFe_{1.9}Mn_{0.1}O₄ (NFM), Ni_(1-x)Zn_xFe₂O₄ (NZF, x varies from 0 to 0.5), CoFe₂O₄ (CFO), Co_{0.6}Zn_{0.4}Fe₂O₄ (CZF) were calcined at 1000°C for 5 hours and Ni_{0.6}Zn_{0.2}Cu_{0.2}Fe₂O₄ was calcined at 750°C for 5 hours. After calcination, the calcined powders were crushed and sieved. Small amount of powder was used for phase analysis in order to confirm single phase formation. X-ray powder diffraction techniques were used to determine the crystal structure and phase identification. Figure 3.1 shows the schematic diagram of perovskite (BTO and PZT) and spinel (ferrite) phase structure. Figure 3.2 shows the typical X-ray powder diffraction pattern for perovskite and spinel structure.

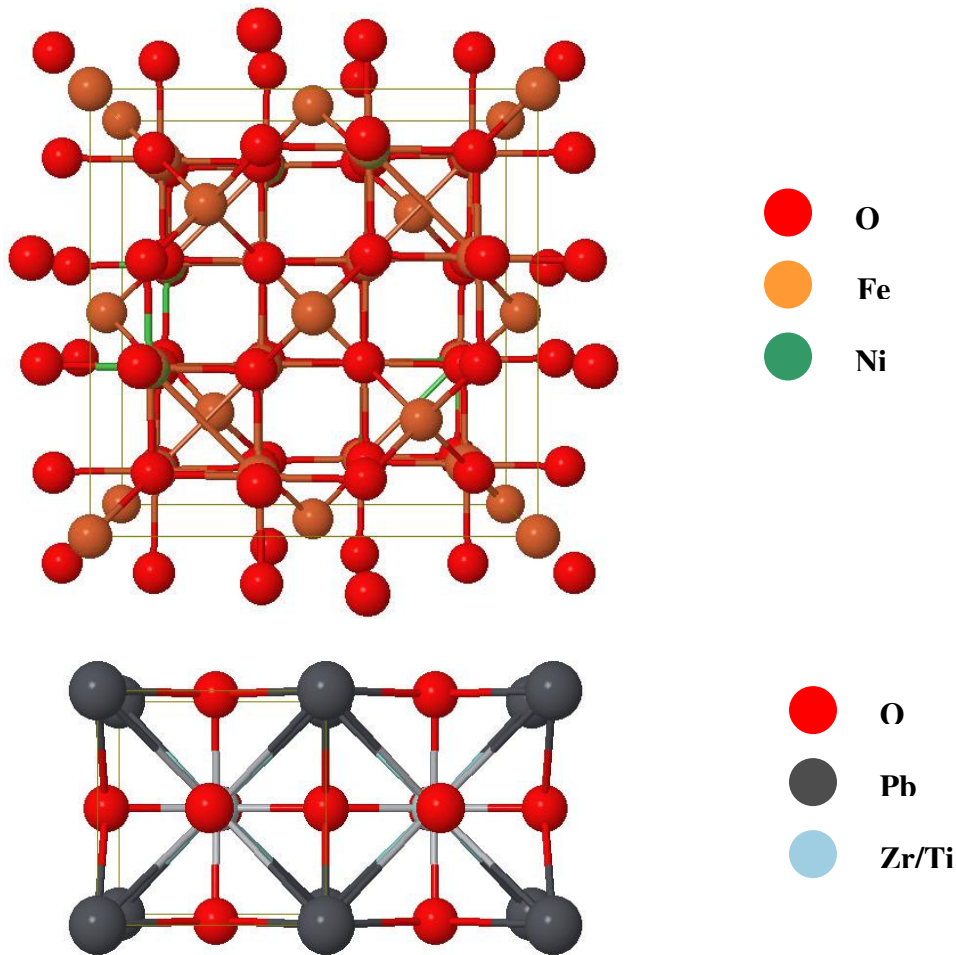


Figure 3.1: Schematic diagram of spinel and perovskite crystal structure

3.2.3 Composite powder synthesis and compaction

Calcined powders of piezoelectric phase (BTO, PZT) and ferrite phase (NFM, NZF, CFO, CZF) were crushed, sieved using a sieve of US mesh # 270, mixed stoichiometrically as $(1-x)$ PZT – x (ferrite) where x varies from 0.03 to 0.2. BTO – CFO powders were mixed as 30 and 35% CFO. The composite powders were ball milled with alcohol and grinding media for 24 hours and dried at 80°C . Dried powder was sieved using a stainless steel sieve of US mesh #170. Sieved powders were pressed in to pellets of different sizes ($12.7 \times 1.5 \text{ mm}^2$, $25.4 \times 1.5 \text{ mm}^2$, $12.7 \times 12.7 \times 1.5 \text{ mm}^3$) in hardened steel die using a hydraulic press under a pressure of 15 MPa. Then the pellets were sealed in a vacuum bag and pressed isostatically in a laboratory cold isostatic press (CIP) under a pressure of 207 MPa.

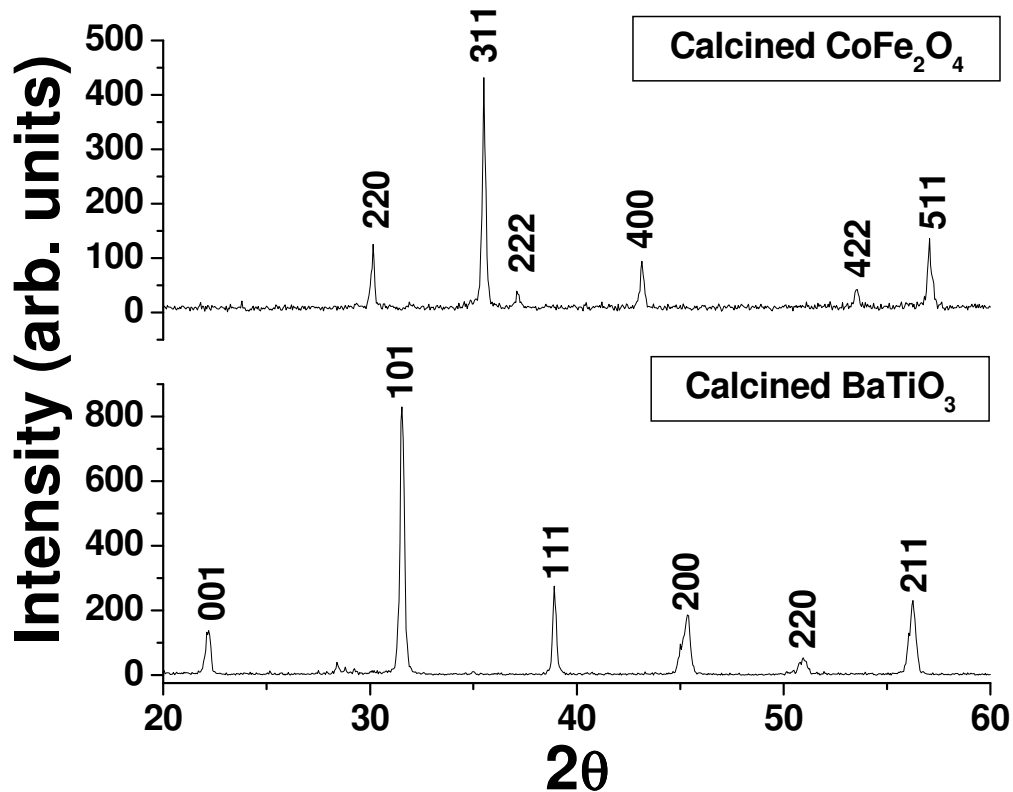


Figure 3.2: Typical x-ray diffraction pattern of spinel Co ferrite and perovskite BTO.

3.2.4 Nano size powder synthesis

Small amount of composite powders (10 gm) was taken in stainless steel vial and mixed with alcohol and YSZ grinding media (3, 5 or 10mm) and milled in high energy 3-D planetary milling machine (Spex 8000M mixer mill) for 3 to 15 hrs. The slurries were again dried at 80°C , crushed and sieved with a stainless steel sieve of US mesh #170.

3.2.5 Bilayer and trilayer structure fabrication

For bilayer composite, first PZT / BTO powders were pressed under 5 MPa pressure inside the die mentioned above and then the NCZF / CFO powders were added on top of PZT / BTO powders and pressed under 15 MPa pressure using hydraulic press. To fabricate a

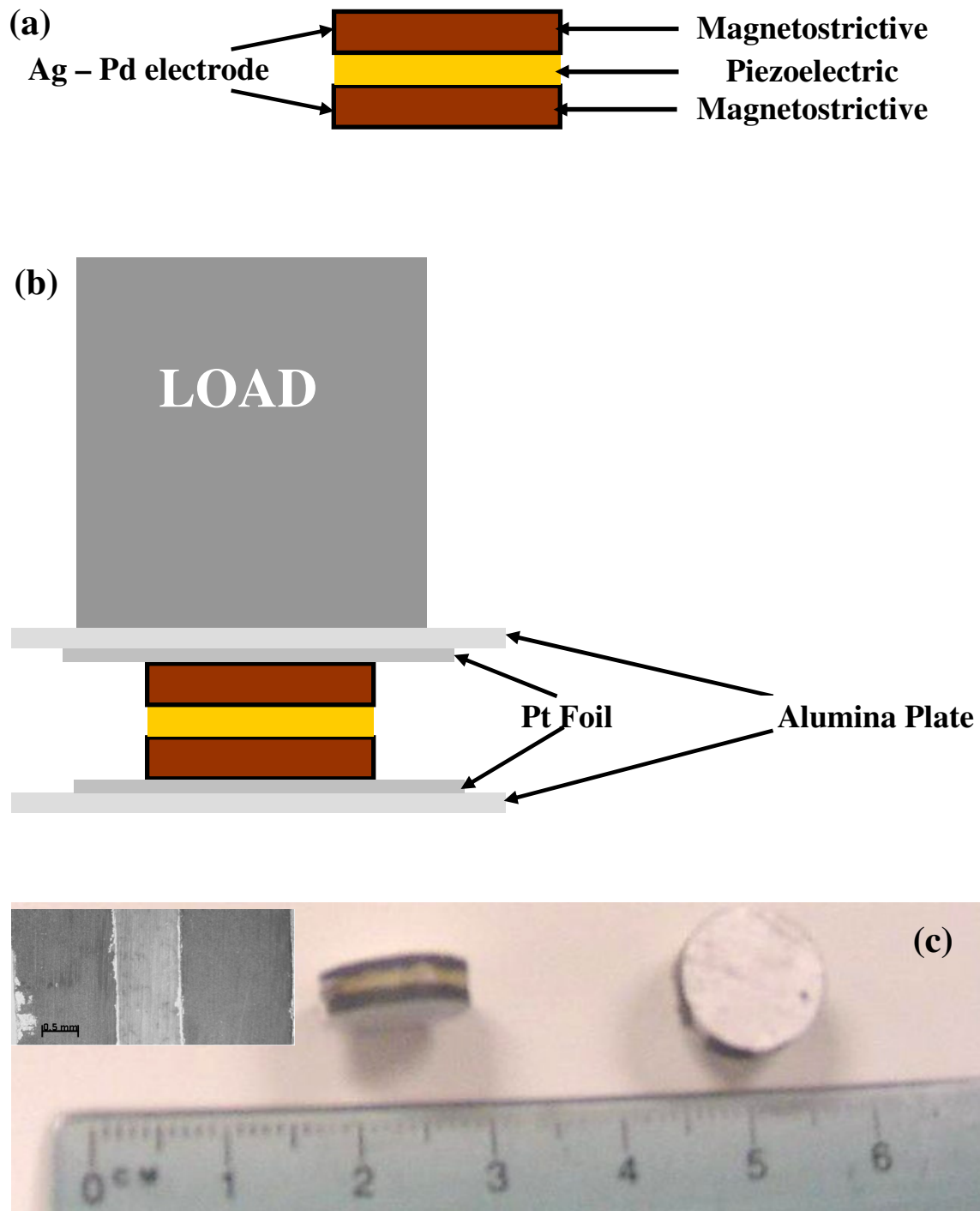


Figure 3.3: (a) Schematic diagram of trilayer ME composite, (b) sintering set – up of trilayer ME composite and (c) images of sintered trilayer composite (inset: cross section).

trilayer sample, initially single layer of NCZF was pressed at 5 MPa and then Ag-Pd (DuPont 6160 conductor paste) electrode was printed. The second layer of 0.9 Pb (Zr_{0.52}Ti_{0.48})O₃ – 0.1 Pb (Zn_{1/3}Nb_{2/3})O₃ [0.9 PZT – 0.1 PZN] was pressed on top of Ag-Pd and then the electrode was applied again. The third and the final layer of NCZF layer was pressed on top of electrode. The five layer structure NCZF/Ag- Pd/PZT-PZN/Ag-Pd/NCZF was than pressed under 20 MPa using hydraulic press. Both the bilayer and trilayer samples were sealed in a vacuum bag and pressed isostatically in a laboratory cold isostatic press (CIP) under a pressure of 207 MPa. After pressing the trilayer samples were dried at 100°C for 10 minutes in order to dry the electrodes.

3.2.6 Sintering and post sintering heat treatment

Pressureless sintering of the particulate composites was performed in air using a Lindberg BlueM furnace in the favorable temperature range. PZT based composites were sintered at a temperature range of 1100 – 1150°C for 2 - 4 hours whereas BTO based particulate composites were sintered at around 1200 – 1250° C for 3 – 5 hours. For PZT – NCZF bilayer composite, before the final sintering at 1000°C, the composites were annealed at 950°C for 1 hr and then slowly heated to 1000°C. Final sintering was done at 1000° C for 4 - 5 hours. For trilayer, pressure assisted sintering was used. The pressed and dried pellets were placed inside a Lyndberg BlueM furnace according to the set up shown in Figure 3.3 (b). The sintering was done at 900°C under a pressure of 30 KPa with very slow heating and cooling rate (~ 1°C / min). The thermal treatment on the sintered samples constituted of annealing followed by rapid air cooling and subsequent aging at lower temperatures. The thermal treatment profile is shown in Figure 3.4. The annealing temperature was selected as 800°C for 10 hours. This temperature is just above the calcination temperature of PZT. At first aging temperature was fixed at 400°C and the time was varied from 3 to 15 hours. Once the optimized time was selected, the temperature was varied from 300 to 400° C.

3.2.7 Texturing

The processing of textured samples consisted of two important steps: seed crystal synthesis and texturing the grains. The seed crystal synthesis technique constituted the

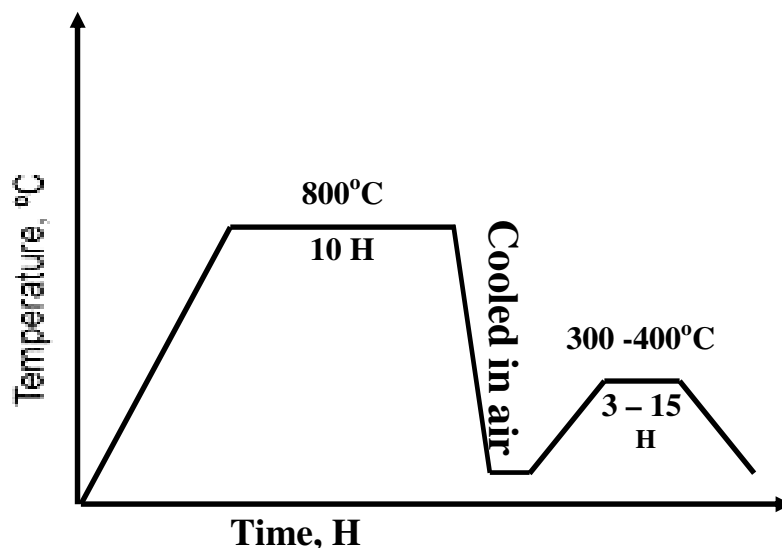


Figure 3.4: Heating profile of annealing and aging.

following steps: heating up the BTO covered with KF salt in Pt crucible in furnace (1225°C) and holding for 8-12 hours, cooling down to the room temperature and dissolving the salt in hot water to separate the crystal. For fabricating oriented grain, small amount (1 – 5 wt. %) of seed (~ 75 - 300 μm dia.) was mixed with the piezoelectric powder (e.g. PZT – PZN). The seed embedded powder was mixed thoroughly, dried, pressed as an intermediate layer of trilayer ME composite and fired at desired temperature for long time (50 – 100 hrs).

3.2.8 Synthesis of PZT – NFO core – shell structure

A mixture of 256 mg of $\text{Ni}(\text{acac})_2$, 500 mg of 1,2- hexadecanediol was added to a 125 mL european flask containing a magnetic stir bar. Benzyl ether 20 mL was then transferred into the flask and the contents were stirred while purging with N_2 for 20 min at room temperature. The flask was then heated to 120°C and the temperature was held for 20 min. During this time, 0.2 mmol of $\text{Fe}(\text{CO})_5$ was injected into the flask while the N_2 purge continued. After one minute,

1 mL of oleic acid and 1 mL of oleylamine were injected and the mixture was maintained under N₂ blanket and heated to 160°C at the rate of 5°C per minute. The mixture was held at high temperature for 10 minutes. The flask was maintained at the refluxing temperature of 295°C for 30 min before cooling down to room temperature under the N₂ blanket. Coating of NiFe₂O₄ nanoparticles on PZT was done using similar recipe for synthesizing the NiFe₂O₄ nanoparticles. PZT particles were added in the beginning of synthesis keeping the other parameters constant. Amount of PZT particles was varied from 2 g to 500 mg to vary the coating thickness and obtain different ratio of NiFe₂O₄ to PZT ratio in the final product. Size of NiFe₂O₄ was controlled by varying the amount of surfactants and heating rates. When faster heating rate and more surfactants were used bigger NiFe₂O₄ nanoparticles were obtained.

3.3 Characterization

3.3.1 Phase and crystal structure analysis

X-ray diffraction analysis was performed using Siemens Krystalloflex 810 D500 x-ray diffractometer on samples after each steps of calcination, sintering and thermal treatment. The fraction of the spinel phase present was computed using the expression:

$$\% \text{ spinel} = \frac{\text{Area under the spinel peak (311)}}{\text{Area under the perovskite peak } \{(110) + (101)\} + \text{Area under the spinel peak (311)}} \times 100 \quad (3.1)$$

The lattice parameter of each phase was calculated using Bragg's law: $\lambda = 2d \sin\theta$, where θ is the Brag angle, d is the interplanar distance and λ is the wavelength of the x-ray (Cu K α = 1.54 Å). The change in lattice parameter can be identified by the peak shift and can be characterized by the calculation of lattice constant (a). For different starting particle size, peak broadening was

investigated using the following formula $B = \frac{0.9\lambda}{t \cdot \cos\theta}$, where B is the full width half maxima (FWHM), λ is the wavelength of the x-ray, t is the particle size.

3.3.2 Microstructural Investigation

3.3.2.1 Scanning Electron Microscopy

Scanning electron microscopy was done using Leo Supra 55 VP scanning electron microscope using secondary electron, backscattered electron, and Inlens detectors. For elemental analysis energy dispersive x-ray spectroscopy was used to identify and quantify the elements present inside the sample. Grain size was measured using linear intercept method from the thermally etched microstructures. Thermal etching consists of heating the sample at a temperature 100° C below the sintering temperature and holding it for an hour and then cooling down. After thermal etching the samples were coated with Ag or C to have a conductive layer and then mounted on SEM stub. X-ray elemental mapping was done for phase identification and interface diffusion.

3.3.2.2 Transmission Electron Microscopy

TEM analysis was performed in a JEOL 1200EX transmission electron microscope. Investigations were done in order to characterize the particle size, shape, grain size of the sintered sample and confirm the lattice parameter variation across the interfaces using selected area electron diffraction pattern. The interface between the piezoelectric and magnetostrictive grains was also investigated to quantify strain fields, domain size, defects and also the domain patterns. For TEM sample preparation, samples were cut into 3 x 3 x 1 mm³ and then glued on a circular Cu TEM grit. Using mechanical polishing, the samples were thinned down to ~ 100µm and then dimple grinded so that the center of sample reached thickness less than 10 µm. This wedge shaped sample was then ion milled. Argon ions were bombarded onto the samples to thin even more near the center region.

3.4 Physical Properties Characterization

After phase analysis and microstructural characterizations, samples were polished to 3 µm finish by using silicon carbide and alumina polishing powders. DuPont 6160 and 7713 (Ag-

Pd) conductor pastes were applied and dried at 100 - 110°C. For DuPont 6160 the firing was done at 850°C and for DuPont 7713 the samples were fired at 650°C. The PZT based samples were poled under high DC field of 2 – 3 kV/mm at a temperature of 120°C. BT samples were poled under 5 kV/mm electric field at a temperature which is cooled from 80°C to room temperature. PMN – PT samples were poled under 4 kV/mm at room temperature.

3.4.1 Electrical properties

3.4.1.1 Dielectric measurement

Dielectric properties were measured using HP 4274 multi frequency LCR meter. The measurements were performed before and 24 hours after poling. Temperature dependent dielectric constant measurement was performed using a computer controlled furnace connected with the LCR meter. The furnace used for this purpose was Thermolene 6000 series furnace. Dielectric constant and loss was measured in the temperature range of 25 to 400°C and frequency range of 100 Hz to 100 KHz.

3.4.1.2 Polarization and strain measurement

P – E (polarization vs. electric field) measurements were made using homemade Sawyer – Tower circuit. The same system was capable of measuring strain using a linear variable differential transformer (LVDT) sensor. The sample was held in place at the bottom while the top electrode was free to move. The resolution of the measurement system was 5 nm.

3.4.1.3 Piezoelectric Measurements

The piezoelectric charge coefficients (d_{33}) were measured using a Berlincourt APC YE 2730A d_{33} meter. Resonance characteristics were determined by HP 4194A impedance analyzer (Hewlett Packard Co. USA). Electromechanical properties were measured using the resonance method using HP 4194A impedance analyzer. The electromechanical coupling factor, mechanical quality factor, piezoelectric voltage constants, and elastic stiffness were calculated from these measured parameters. For a radial mode disk, s_{11}^p can be calculated as following:

$$s_{11}^p = \frac{\eta_1^2}{\rho(2\pi f_s a)^2 [1 - (\sigma^p)^2]} \quad (3.2)$$

where η_1 is the frequency constant, σ^p is the planar Poisson's ratio, f_s is the resonance frequency, a is the radius and ρ is the density. The coefficients η_1 and σ^p can be found by measuring ratio of 1st overtone to fundamental resonance frequency. For any fixed ratio, corresponding η_1 and σ^p values were found from IEEE standards. The transverse mode coupling constant k_{31} can be calculated by using the following expression [86]:

$$k_{31}^2 = k_p^2 \frac{(1 - \sigma_p)}{2} \quad (3.3)$$

where k_p is the planar coupling constant. If k_{31} and s_{11}^E are known, then d_{31} can be calculated as following

$$k_{31}^2 = \frac{d_{31}^2}{(s_{11}^E \epsilon_{33}^T)} \quad (3.4)$$

3.4.2 Magnetic properties

3.4.2.1 Hysteresis loop (M – H)

Magnetic hysteresis loop (magnetic moment vs. field) was measured using quantum design alternating gradient magnetometer (AGM). For this measurement sample size was kept below $2 \times 2 \times 0.5 \text{ mm}^3$ and total weight below 70 mg. The samples were loaded at the end of the tuning fork resonator and positioned between two poles of the magnetometer. The field from outside magnet magnetizes the sample. An alternating force was applied at the resonance frequency of the resonator, which results in increased vibration and voltage. This voltage was detected by lock in method.

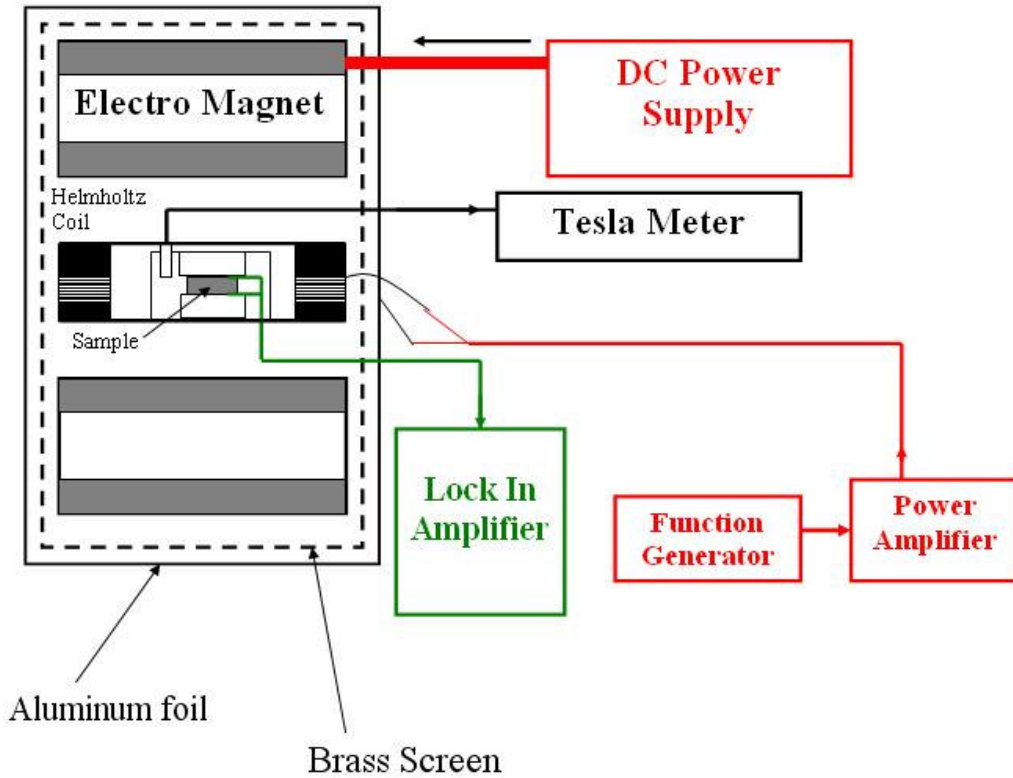


Figure 3.5: Magnetolectric measurement setup.

3.4.2.2 Temperature dependent magnetization measurement

Temperature dependent magnetization was measured using quantum design physical properties measurement system (PPMS) and super conducting quantum interference device (SQUID). The temperature range in PPMS was 10 – 1000 K whereas in SQUID it was 10 – 400 K. The temperature dependent magnetization was measured in order to identify the Neel temperature (T_n) and Curie temperature (T_c).

3.4.2 Magnetolectric properties

The magnetolectric measurement setup is shown in Figure 2. Magnetolectric coefficient (dE/dH) was determined by applying an A.C. magnetic field at 1 kHz and 10e amplitude (H) under varying DC magnetic bias. The AC magnetic field was generated by a

Helmholtz coil powered by Agilent 3320 function generator. The output voltage generated from the composite was measured using a SRS DSP lock-in amplifier (model SR 830). The ME coefficient (mV/cm.Oe) can be calculated by dividing the measured output voltage by thickness of the sample and applied AC field. For frequency dependent magnetoelectric coefficient measurement, the Helmholtz coil was powered by the above mentioned function generator from 1 kHz to 1 MHz and the output voltage was recorded using lock-in amplifier.

CHAPTER 4

HIGH ENERGY DENSITY CERAMIC COMPOSITION In THE SYSTEM $\text{Pb}(\text{Zr},\text{Ti})\text{O}_3 - \text{Pb}[(\text{Zn},\text{Ni})_{1/3}\text{Nb}_{2/3}]\text{O}_3$ FOR PIEZOELECTRIC – MAGNETOSTRICTIVE COMPOSITES

Magnetolectricity in two phase (piezoelectric – magnetostrictive) composite is a strain mediated effect where magnetostrictive strain produced by applied magnetic field is transferred on to the piezoelectric phase. In order to achieve efficient strain transfer, piezoelectric materials with matching elastic properties and higher piezoelectric voltage constant (g) are suitable. The mechanical properties of PZT based ceramics are nearly similar for various compositional modifications. However, the electrical properties can be changed to a large extent by tailoring the microstructure, defect concentration, and domain states. Thus, in this chapter we attempt to design a high piezoelectric voltage constant material that can serve as an optimum phase in the magnetolectric composites. This goal correlates with the design of high energy density material as it will be shown here that the coefficients for energy are dependent on ' g ' constant.

4.1 High Energy Density Piezoelectric Phase for ME Composites

The magnitude of the transduction is governed by the effective piezoelectric strain constant, d , and the effective piezoelectric voltage constant, g . Using the linear constitutive piezoelectric equations a relation between the energy density of the piezoelectric material and the transduction coefficient ($d \cdot g$) under an applied stress X can be derived. Under an applied force ($F = X \cdot A$, where A is the area), the open circuit output voltage (V) of the ceramic is given as:

$$V = E \cdot t = -g \cdot X \cdot t = -\frac{g \cdot F \cdot t}{A} \quad (4.1)$$

where t is the thickness of the ceramic, E is the electric field, and g is the piezoelectric voltage coefficient given as:

$$g = \frac{d}{\epsilon_o \epsilon^x} \quad (4.2)$$

where ϵ^x is the dielectric constant under constant stress condition. The charge (Q) generated on the piezoelectric ceramic is given by the relation:

$$D = \frac{Q}{A} = \frac{E}{\beta^x} = \frac{V \cdot \epsilon_o \epsilon^x}{t} \quad (4.3)$$

or

$$\frac{Q}{V} = \frac{\epsilon^x \epsilon_o A}{t} = C \quad (4.4)$$

where D is the dielectric displacement, C is the capacitance and β^x is the dielectric susceptibility of the material under constant stress condition. Dielectric susceptibility is equal to the inverse of dielectric permittivity tensor component and can be defined from the constitutive equation for a linear piezoelectric material as:

$$E = -g X + \beta^x D \quad (4.5)$$

Equation (4.4) shows that at low frequencies a piezoelectric plate can be assumed to behave like a parallel plate capacitor. Hence, electric energy available under ac stress excitation is given as:

$$U = \frac{1}{2} CV^2$$

or energy per unit volume, $u = \frac{1}{2} (d \cdot g) \cdot \left(\frac{F}{A} \right)^2 \quad (4.6)$

Equation (4.1) and (4.6) shows that for a given material of fixed area and thickness, a material with high $(d \cdot g)$ product and high g constant will generate high voltage and power when the piezoelectric ceramic is directly employed for mechanical to electrical energy conversion. Since, in the case of magnetoelectric composites the magnetostrictive phase applies the stress on the piezoelectric phase through elastic coupling the high energy density material will lead to higher response.

4.2 Design of High 'g' Materials

Enhancement in the magnitude of the piezoelectric voltage constant requires an optimization in the magnitude of the piezoelectric stress constant and dielectric constant. In general, the variation in the magnitude of piezoelectric stress constant and dielectric constant is similar and they increase or decrease simultaneously upon modification with dopants or processing technique resulting in minor changes in the magnitude of their ratio. A novel theoretical model and processing strategy is required to obtain large g constants [90]

The criterion for maximization of the product (d.g) with respect to the microstructure variable x (such as grain size) can be determined as following:

$$\frac{\partial}{\partial x}(d.g) = d \cdot \left(\frac{\partial g}{\partial x} \right) + g \cdot \left(\frac{\partial d}{\partial x} \right) = 2 \cdot \left(\frac{d}{\epsilon} \right) \cdot \left(\frac{\partial d}{\partial x} \right) - \left(\frac{d}{\epsilon} \right)^2 \left(\frac{\partial \epsilon}{\partial x} \right) = 0 \quad (4.7)$$

or
$$\frac{\partial(\ln d^2)}{\partial x} = \frac{\partial(\ln \epsilon)}{\partial x} \Rightarrow d = \epsilon^{0.5} \quad \text{where } \epsilon = \epsilon^x \epsilon_o \quad (4.8)$$

Once again differentiating Eq. (4.7) with respect to x and substituting the condition given by Eq. (4.8) it can be shown that:

$$\left(\frac{\partial^2}{\partial x^2} \right) (d.g) = \left(\frac{\partial \epsilon}{\partial x} \right)^2 \frac{1}{\epsilon^{1.5}} \left(1 - \frac{1}{\epsilon^{0.5}} \right) < 0 \quad (4.9)$$

Thus, the condition given by Eq. (4.8) represents the maximum magnitude of the product (d.g). In general, the condition given by Eq. (4.8) can be expressed as:[90]

$$|d| = \epsilon^n \quad (4.10)$$

Using Eq.(4.10) the maximum magnitude of the product (d.g) is given as:

$$\text{Max}(d.g) = \epsilon^{2n-1} \quad (4.11)$$

where n is the material constant which is fixed by the magnitude of the piezoelectric and dielectric constants. It has been shown that for all the commercial polycrystalline ceramic materials the magnitude of n lies in the range of 1.1 to 1.3. Equation (4.10) represents a deterministic rule for realizing the high energy density piezoelectric materials. According to this equation a giant enhancement in the magnitude of the g constant will be obtained by reducing the magnitude of the n. As the magnitude of n decreases and approaches the theoretically

minimum possible value of 0.5 the magnitude of product (d.g) reaches the maximum possible magnitude of unity. In order to obtain large magnitude of the product (d.g), the piezoelectric compositions can be tailored by modifying with the dopant or processing technique such that the change in piezoelectric and dielectric constant leads to a decrement in the magnitude of constant n.

The piezoelectric constant, d, can be written in terms of the electromechanical coupling factor, k, and the elastic compliance, s, as following:

$$d = k\sqrt{\epsilon \cdot s} \quad (4.12)$$

Substituting Eq.(4.10) into Eq. (4.12), it can be shown that:

$$n - \frac{1}{2} = \frac{\ln(k)}{\ln(\epsilon)} + \frac{1}{2} \frac{\ln(s)}{\ln(\epsilon)} \quad (4.13)$$

Eq.(4.13) indicates that a material with low magnitude of n will require low magnitude of coupling coefficient and elastic compliance. However, large coupling factor and low losses are important for efficient energy conversion.

4.2.1 Defect chemistry

Defects and substituents are known to affect the electromechanical properties of the normal ferroelectrics in both poled and unpoled conditions [91 - 96] Generally, acceptor doping (Fe, Mn, Ni, Co) in the PZT based ceramics results in (i) decreased dielectric constant and loss, (ii) lower elastic compliance, (iii) lower electromechanical coupling factor, and (iv) lower electromechanical losses. In contrast, donor doping (La, Sb, Bi, W) results in (i) increased dielectric constant and loss, (ii) increased elastic compliance, (iii) increased electromechanical coupling factor, and (iv) increased electromechanical losses. Thus, an acceptor modified material seems to be appropriate for obtaining low value of n.

In acceptor modified materials, oxygen vacancies are created for charge compensation, which are frozen into the ceramic during quenching from high temperature. The electroneutrality

reaction representing the equilibrium between acceptor ions (A) and oxygen vacancies is expressed as:

$$n + 2[A'] = p + [V_o^{**}] \quad (4.14)$$

Assuming a constant lead activity, the formation of oxygen vacancy can be expressed as:



The rate constant for this reaction can be expressed as:

$$K = [V_o^{**}] P_{O_2}^{1/2} e^{-2} \quad (4.16)$$

where P_{O_2} is the partial pressure of the oxygen. If P_{O_2} is constant, then the formation of

V_o^{**} can be expressed as:



These oxygen vacancies can reside in the material in many possible ways: (i) associated defect dipole structure with acceptor (ii) diffuse to domain walls or (iii) compensate the local charge fluctuation at domain walls. The mechanism for introduction of “hard” properties depends on the way in which oxygen vacancies distribute themselves. In Mn-modified PZT ceramics, it is believed that hardening occurs due to the pinning of domain boundaries by Mn - oxygen vacancy defect structure [96]. Further, it is believed that Mn^{+3} attaches strongly to oxygen vacancies due to Jahn Teller effect. This prevents conduction and reduces the domain wall mobility resulting in reduced losses [91].

The MPB (Zr: Ti = 52: 48) composition in PZT shows the highest piezoelectric properties such as high piezoelectric constant d_{33} , coupling factor k and dielectric constant. These properties drop on either side of the MPB. The compositions on tetragonal side (Zr: Ti ratio of 56: 44) have less variation in the dielectric and piezoelectric properties as compared to composition on the rhombohedral side with reference to MPB [97]. Thus, by selecting a composition on the tetragonal side and doping with suitable donor (Nb^{+5} etc.) and acceptor

(Zn⁺², Ni⁺² etc.) ions, it is possible to formulate a composition, which has relatively higher piezoelectric constant d_{33} but lower dielectric constant.

The aim in this chapter is to identify a high energy density piezoelectric polycrystalline ceramic material. For this purpose, $\text{Pb}(\text{Zr}_{1-x}\text{Ti}_x)\text{O}_3 - \text{Pb}[(\text{Zn}_{1-y}\text{Ni}_y)_{1/3}\text{Nb}_{2/3}]\text{O}_3$ ($y = 0$ and 0.2) system was selected as the piezoelectric material and was modified with Mn to obtain the low magnitude of material constant, n . Previously, Priya et al. have conducted extensive studies on the Mn-modified PZT – PZN system. Table I lists the data for the 0.5 wt% Mn-modified compositions along with the calculated magnitude of the n parameter [96]. It can be seen from this table that increase in the magnitude of the d_{33} is accompanied by a proportional increase in ϵ_{33} , thus limiting the magnitude g_{33} . Further, a correlation between the magnitude of ‘ n ’ and g_{33} can be seen in this table.

Table 4.1: Properties of the modified $0.9 \text{Pb}(\text{Zr}_{0.5}\text{Ti}_{0.5})\text{O}_3 - 0.1 \text{Pb}(\text{Zn}_{1/3}\text{Nb}_{2/3})\text{O}_3$ ceramics.

| Sample | d_{33} (pC/N) | ϵ_{33}/ϵ_0 | g_{33} ($\times 10^{-3}$ V-m/N) | $d_{33}\cdot g_{33}$ ($\times 10^{-15}$ m ² /N) | n |
|--------|-----------------|----------------------------|------------------------------------|---|-------|
| PZT1 | 135 | 754 | 20.22 | 2729.96 | 1.207 |
| PZT2 | 277 | 946 | 33.07 | 9160.7 | 1.183 |
| PZT3 | 265 | 1011 | 29.60 | 7845.15 | 1.189 |
| PZT4 | 300 | 1173 | 28.88 | 8665.73 | 1.192 |

PZT1: $\text{Pb}(\text{Zr}_{0.5}\text{Ti}_{0.5})\text{O}_3 + 0.5 \text{ wt}\% \text{ MnO}_2$

PZT2: $\text{Pb}(\text{Zn}_{1/3}\text{Nb}_{2/3})_{0.2}(\text{Zr}_{0.5}\text{Ti}_{0.5})_{0.8}\text{O}_3 + 0.5 \text{ wt}\% \text{ MnO}_2$

PZT3: $\text{Pb}(\text{Zn}_{1/3}\text{Nb}_{2/3})_{0.16}(\text{Ni}_{1/3}\text{Nb}_{2/3})_{0.04}(\text{Zr}_{0.5}\text{Ti}_{0.5})_{0.8}\text{O}_3 + 0.5 \text{ wt}\% \text{ MnO}_2$

PZT4: $\text{Pb}(\text{Zn}_{1/3}\text{Nb}_{2/3})_{0.12}(\text{Ni}_{1/3}\text{Nb}_{2/3})_{0.04}(\text{Sb}_{1/2}\text{Nb}_{1/2})_{0.04}(\text{Zr}_{0.5}\text{Ti}_{0.5})_{0.8}\text{O}_3 + 0.5 \text{ wt}\% \text{ MnO}_2$

4.3 Structural Studies

4.3.1 Density measurement of different compositions

The density of 0.9PZT (52:48) - 0.1PZN + y wt% Mn ceramics as a function of the Mn weight percent is plotted in Fig 4.1 (a). The samples sintered at 1050°C using one step sintering had the density of 7.9 gm/cm³ which is approximately 98% of the theoretical density (8.02gm/cm³). The density decreased with the decreasing sintering temperature in one step process. Using the two step sintering process the maximum density was found to be around 7.85 gm/cm³ for the sintering profile of 1000-925°C. It was noticed that the compositions with 0.5wt% Mn were difficult to sinter at lower temperatures both in one-step and two-step process. The composition with 0.7 wt% Mn provided density in the range of 7.8 – 7.9 gm/cm³ in both one step and two steps sintering indicating the optimum magnitude of doping for 0.9PZT-0.1PZN. For 0.9PZT (56: 44) - 0.1PZNN + x mol% MnO₂, the density increases with sintering temperature for low concentration of MnO₂ but as the concentration of MnO₂ increases, high density can be obtained at low sintering temperature. The composition 0.9PZT (56: 44) - 0.1PZNN + 1 mol% MnO₂ showed high density of 7.92 gm/cm³ at 1100-1000 °C sintering profile while 0.9PZT (56: 44) - 0.1PZNN + 3 mol% MnO₂ showed the high density of 7.98 gm/cc at 1000 – 925 °C as shown in Figure 4.1 (b).

4.3.2 Phase analysis of different Zr/Ti ratio piezoelectric compositions

Figure 4.2(a) and (b) shows the XRD patterns for the sintered samples of composition 0.9PZT (52: 48) - 0.1PZN + 0.7 wt% Mn and 0.9PZT (56: 44) - 0.1PZNN + 2 mol% MnO₂ respectively using different two step sintering profiles. It can be seen from these figures that all the samples have perovskite structure and no sign of pyrochlore phase formation was detected. In case of 0.9PZT (52: 48) - 0.1PZN + 0.7 wt% Mn, samples at all the three sintering temperatures were found to have tetragonal symmetry as the splitting of the (200) / (002) peaks was clearly observed in Figure 4.2 (a). For 0.9PZT (56: 44) - 0.1PZNN + 2 mol% Mn samples as the sintering temperature increases tetragonality increases for observed in Figure 4.2 (b).

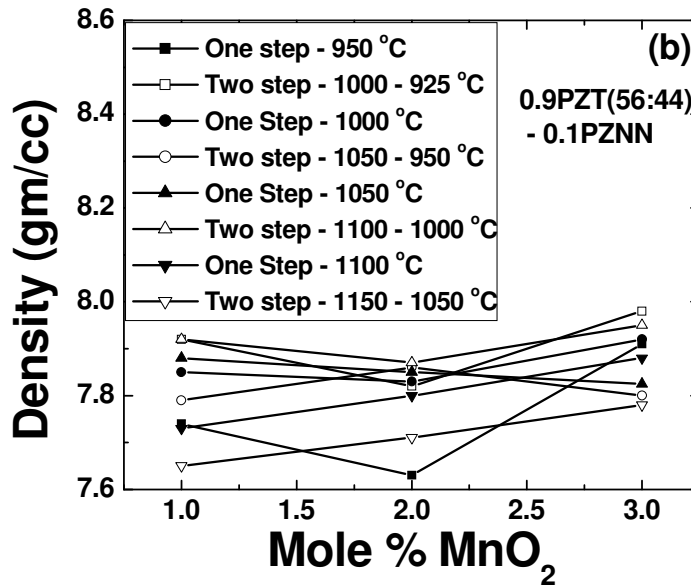
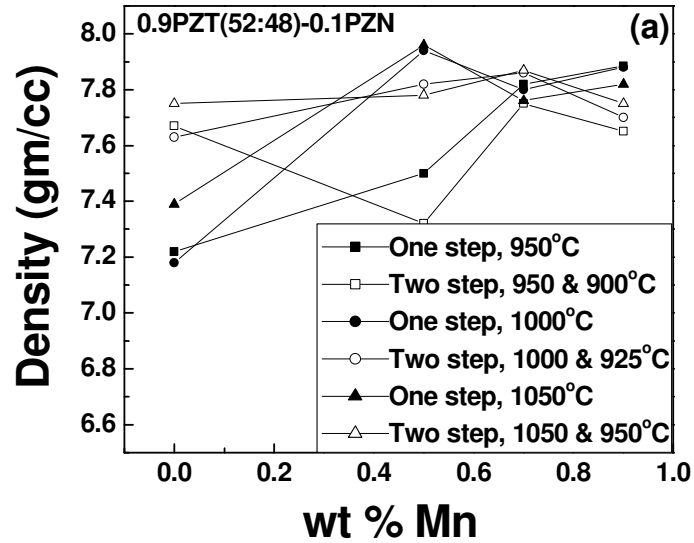


Figure 4.1: Variation of density as a function of (a) Mn concentration given in weight percent for 0.9PZT (52:48) – 0.1 PZN + y wt% MnCO₃ and (b) Mn concentration given in mole percent for 0.9PZT (56:44) – 0.1 PZNN + x mol% MnO₂.

The inserts show the magnified image of splitting for 200/002 peaks at different two step sintering condition.

4.3.3 Microstructure and grain size analysis of sintered body using one and two step sintering

Figure 4.3 (a) and (b) compares the microstructure of the samples sintered in one step (1050°C for 2 hours) and two-step (1050°C for 5 minutes and 950°C for 4 hours) respectively for the composition 0.9PZT (52:48) -0.1PZN + 0.7 wt% Mn. The microstructures of the sintered samples are dense, consistent with the measured density value. The reduction in the magnitude of the grain size by using the two step sintering can be clearly seen from these figures. In Fig. 4.3 (c) and (d), the microstructure of 0.9PZT (56:44) -0.1PZNN + 3 mol% MnO₂ sintered in one step (950°C for 2 hours) and two step (1000°C for 5 minutes and 925°C for 4 hours) have been compared. One step sintering at 950°C results in the grain size of 1.06µm, whereas two step sintering at 1000 – 925°C provides average grain size of 0.95µm. Figure 4.4 shows the SEM images of 0.9PZT (52: 48) - 0.1PZN + 0.5 wt% Mn and 0.9PZT (52: 48) - 0.1PZN + 0.7 wt% Mn sintered samples using two step profiles at 950° and 900°C. From these micrographs (Fig. 4.3 and Fig. 4.4) it can be seen that there is pronounced increase in the grain size with the increase in the sintering temperature. A considerable increase in grain size was also recorded when the concentration of Mn is increased to 0.9 wt% and the maximum sintering temperature increases to 1050°C for 0.9PZT (52: 48) - 0.1PZN system.

Figure 4.5 compares the grain size obtained by using the one-step and two-step sintering for the case when highest sintering temperature is 1050°C for all the compositions. There is a significant reduction in grain size, from 3.36 to 2.4 µm for the composition 0.9PZT (52: 48) - 0.1PZN + 0.7 wt% Mn as the sintering temperature was decreased to 950°C from 1050°C as shown in Fig. 4.6(a). In case of the compositions represented as 0.9PZT (56:44) - 0.1PZNN + x mol% MnO₂, the grain size was found to decrease with increasing Mn

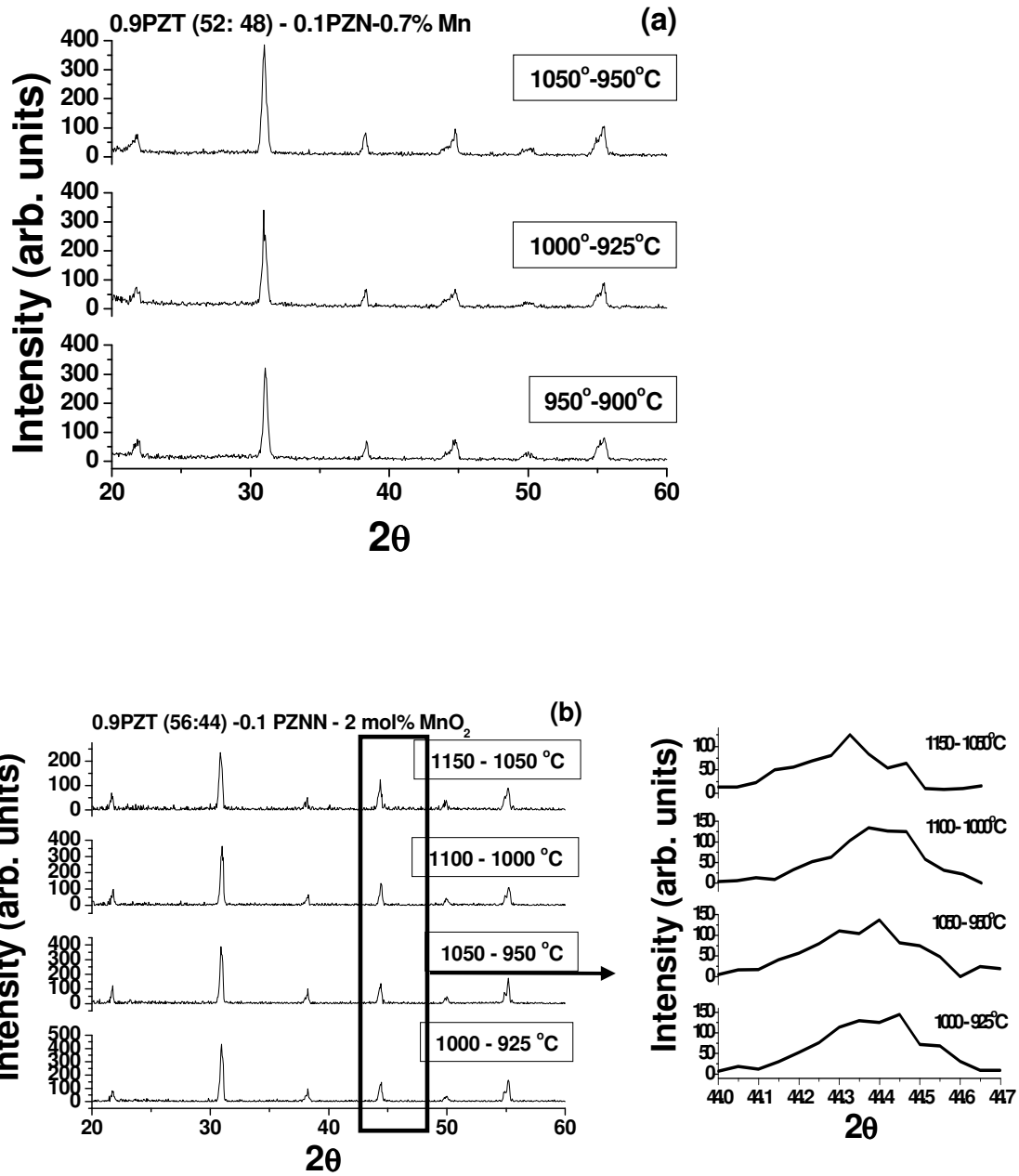


Figure 4.2: XRD pattern of different sintered samples synthesized using two step sintering profiles showing single-phase perovskite structure with tetragonal symmetry. (a) 0.9PZT (52:48) -0.1PZN + 0.7 wt% Mn, and (b) 0.9PZT (56:44)-0.1PZNN + 2 mol% MnO₂ and insert of the exploded view of 200/002 peaks.

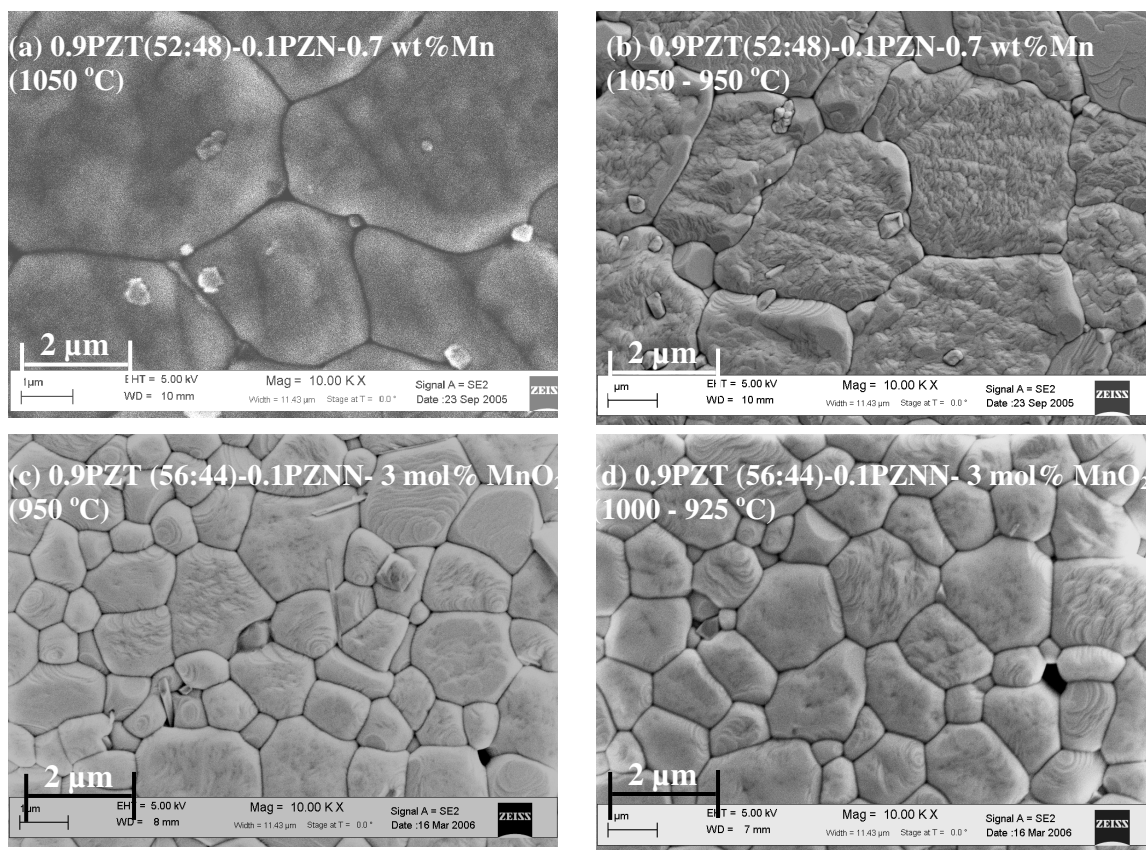


Figure 4.3: SEM micrographs of sintered samples (a) 0.9PZT (52:48) - 0.1PZN + 0.7 wt% Mn, synthesized using one step, (b) 0.9PZT (52:48) - 0.1PZN + 0.7 wt% Mn, synthesized using two step sintering (c) 0.9PZT (56: 44) - 0.1PZNN + 3 mol% MnO₂, synthesized using one step sintering and (d) 0.9PZT (56: 44) - 0.1PZNN + 3 mol% MnO₂, synthesized using two step sintering.

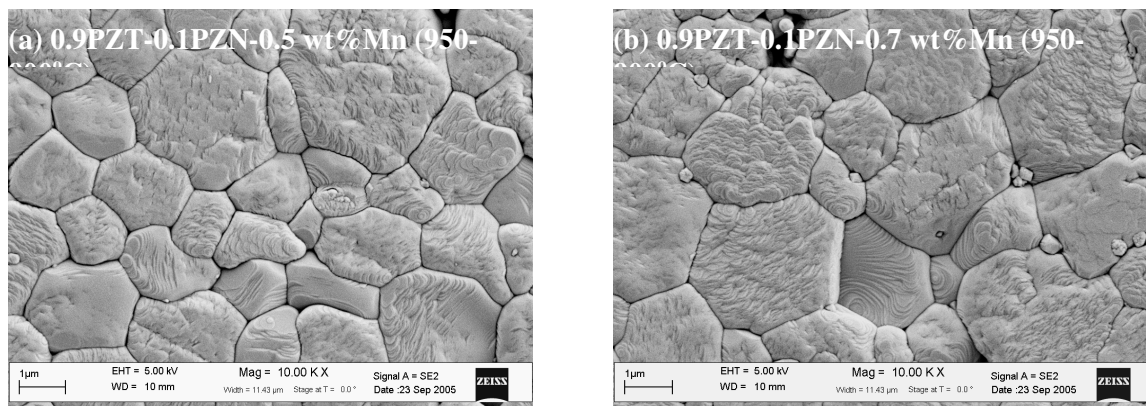


Figure 4.4: SEM micrographs of 0.9PZT-0.1PZN + 0.5%Mn and 0.9PZT-0.1PZN + 0.7%Mn synthesized using the two step sintering at 950 °C for 5 minutes and at 900°C for 4 hours.

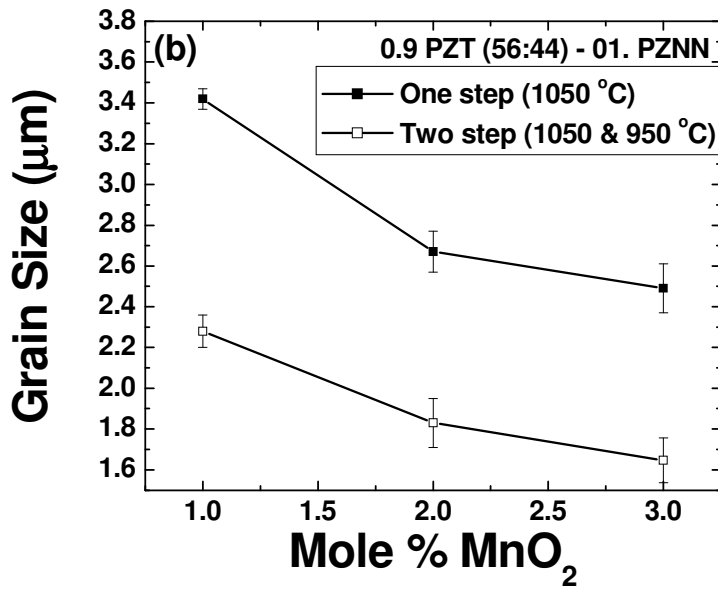
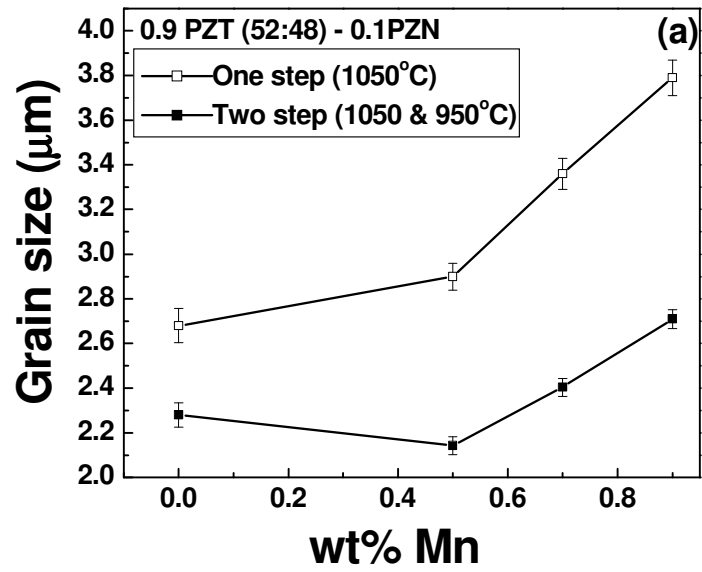


Figure 4.5: Comparison of the grain size obtained by using the one-step and two-step sintering profile for the case when highest temperature is 1050°C for (a) 0.9PZT (52: 48) – 0.1 PZN + y wt% MnCO₃ and (b) 0.9PZT (56: 44) - 0.1PZNN + x mol% MnO₂.

concentration as shown in Fig 4.5 (b). Again in this figure a significant difference in the grain size can be noted between the one step and two step sintering.

4.4 Energy Harvesting Parameter and material constant 'n'

The variation of the energy density parameter ($d_{33}\cdot g_{33}$, in the longitudinal mode) as a function of grain size for 0.9PZT (52:48) -0.1PZN + y wt% Mn and 0.9PZT (56:44) -0.1PZNN + x mol% MnO₂ using various two step sintering profiles is shown in Fig. 4.6 (a) and (b) respectively. It can be seen from these figures that for a certain Mn concentration $d_{33}\cdot g_{33}$ exhibit a maximum value with varying grain size. The composition given as 0.9PZT-0.1PZN + 0.7 wt% Mn sintered at 1000-925°C and having a grain size of 1.75 μm exhibited the magnitude of $d_{33}\cdot g_{33}$ as $16168 \times 10^{-15} \text{ m}^2/\text{N}$. The composition given as 0.9PZT (56:44) -0.1PZNN + 2 mol% MnO₂ sintered at 1100 – 1000°C exhibited the $d_{33}\cdot g_{33}$ magnitude of $18456.2 \times 10^{-15} \text{ m}^2/\text{N}$ at the grain size of 2.98μm, which in the knowledge of authors is the highest value reported for the polycrystalline ceramics.

Figure 4.7 (a) and (b) show the variation of material constant, n, as a function of the grain size for 0.9PZT (52:48) -0.1PZN + y wt% Mn and 0.9PZT (56:44) -0.1PZNN + x mol% MnO₂ respectively using two step sintering profile. The magnitude of the n varies significantly with the change in the Zr/Ti ratio and grain size and the lowest value of n (1.126) was found for the composition 0.9PZT (56:44) -0.1PZNN + 2mol% MnO₂. Figure 4.8 shows the relationship between the magnitude of n and the piezoelectric voltage coefficient for 0.9PZT (52:48) - 0.1PZN + y wt% Mn. Based on the data it can be hypothesized that as the magnitude of the n approaches towards unity a giant enhancement in the magnitude of g constant is obtained. This is further evident from the data shown in the Fig. 4.7(b). The solid line in this figure was plotted using the expression:

$$n = 1 + \left[\frac{\ln(g)}{\ln(\epsilon)} \right] \quad (4.18)$$

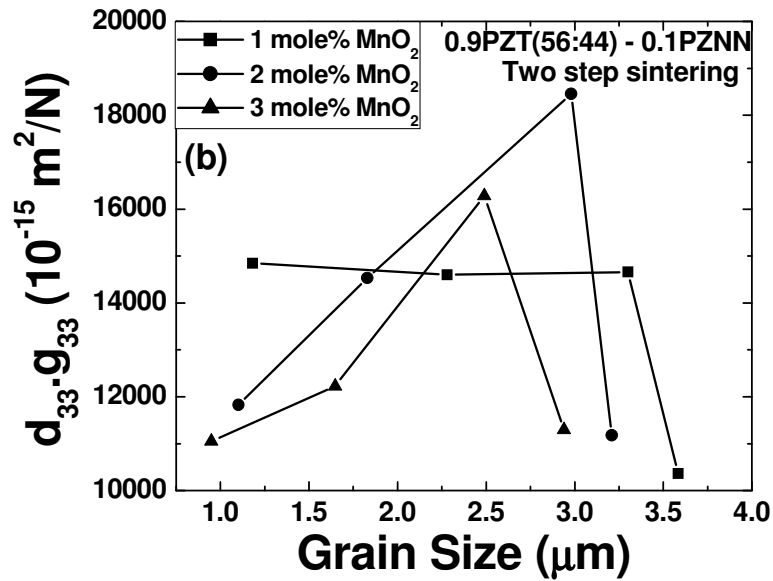
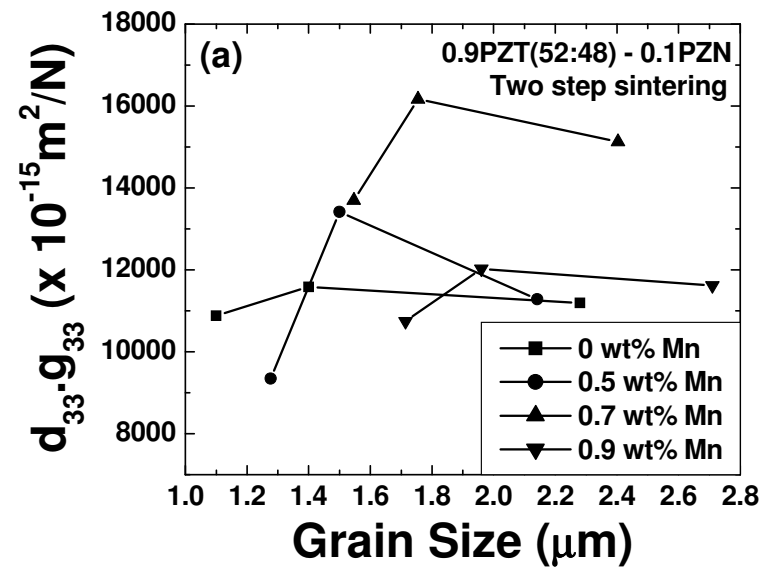


Figure 4.6: Variation of the material parameter ($d_{33}\cdot g_{33}$) as a function of grain size for (a) 0.9PZT (52: 48) – 0.1 PZN + y wt% MnCO_3 and (b) 0.9PZT (56: 44) – 0.1 PZNN + x mol% MnO_2 .

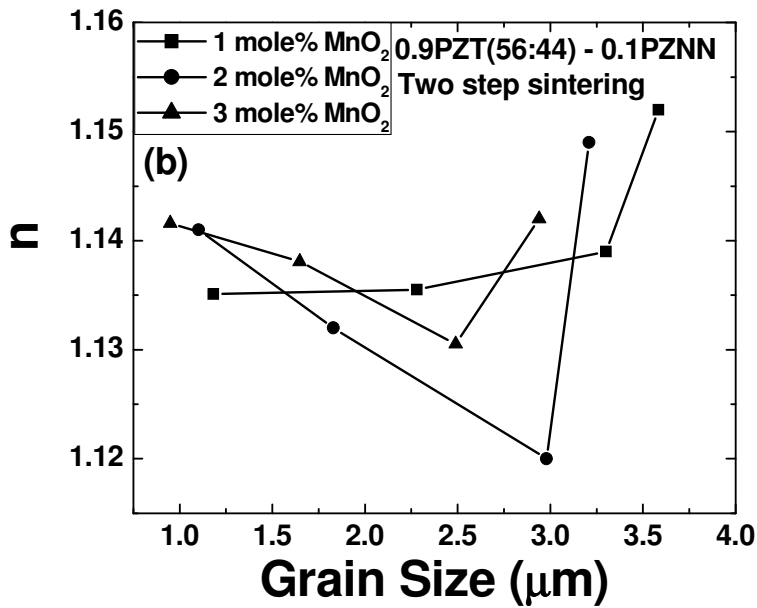
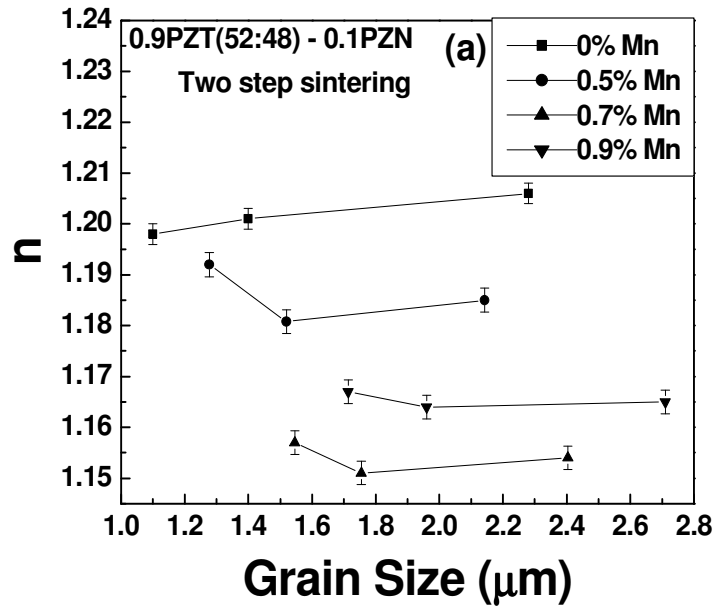


Figure 4.7(a) and (b): Variation of material constant, n , as a function of (a) grain size for 0.9PZT (52: 48) – 0.1 PZN + y wt% MnCO_3 , (b) grain size for 0.9PZT (56: 44) – 0.1 PZNN + x mol% MnO_2

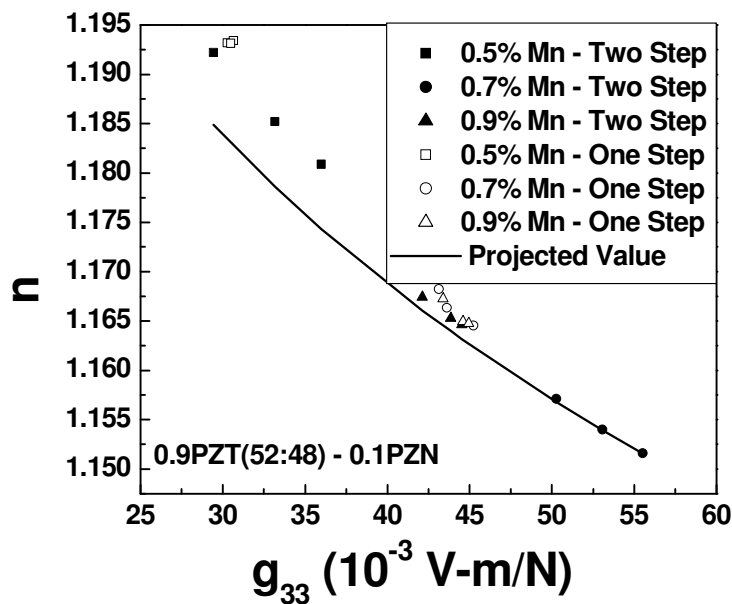


Figure 4.8: Piezoelectric voltage coefficient, g_{33} for 0.9PZT (52: 48) – 0.1 PZN + y wt% $MnCO_3$.

This logarithmic relationship was found to be obeyed by all the synthesized samples as shown in Fig. 4.7 (c). Composition of 0.9PZT (56: 44) - 0.1PZNN + 2 mol% MnO_2 corresponds to the highest value of the g_{33} of 83.136 ± 0.84 ($\times 10^{-3}$ Vm/N) and lowest n value of 1.126 ± 0.0019 as shown in Fig. 4.7(b). From the data shown in Fig. 4.7 a clear correlation between the magnitude of n and the g constant can be seen.

4.5 Piezoelectric Properties:

Figure 4.9(a) & (b) and 4.10 (a) & (b) show the effect of the grain size on the magnitude of piezoelectric and dielectric properties for the 0.9PZT (52:48) -0.1PZN + y wt% Mn and 0.9PZT (56:44) - 0.1PZNN + x mol% MnO_2 samples synthesized using two step sintering profiles. Smaller grain sizes correspond to lower sintering temperature and the grain size increases as the maximum sintering temperature increases. With increase in Mn concentration the magnitude of d_{33} decreases. Mn is an acceptor dopant and as the Mn concentration

increases domain pinning increases. As a result there is a considerable restriction in domain wall movement, which reduces the piezoelectric charge constant. The variation of dielectric constant as a function of grain size is shown in Fig. 4.9(b) and 4.10 (b) for these two compositions. For 0.9PZT (52:48) -0.1PZN + y wt% Mn, as the grain size increases, dielectric constant slightly decreases but becomes flat as the Mn concentration increases. For the composition with 0.9 wt% Mn, almost no change in dielectric constant with grain size was found. The results reported in this figure are consistent with the results reported in literature [96, 99 - 103].

For 0.9PZT (56:44) -0.1PZN + x mol% MnO₂, the dielectric constant decreases with the grain size. The minimum was observed between 2.25 and 3 μm grain size for all the composition (1-3 mol% MnO₂). The lowest dielectric constant magnitude of 305.8 was recorded for the composition of 0.9PZT (56:44) -0.1PZNN + 2 mol% MnO₂ sintered in two steps at 1100 – 1000°C. The corresponding average d₃₃ value for this composition was 222pC/N which provides average g₃₃ of 83.1 x 10⁻³ V-m/N, n of 1.126 and d₃₃-g₃₃ of 18456.2 x 10⁻¹⁵ m²/N. This result indicates that an optimized microstructure and defect chemistry provides the lowest magnitude of n and highest magnitude of the piezoelectric voltage constant, g.

Figure 4.11 (a) and (b) shows the variation of the dielectric constant measured from room temperature to 400°C for 0.9PZT (52:48) -0.1PZN + y wt% Mn and 0.9PZT (56:44) -0.1PZNN + x wt% MnO₂ respectively. All the composition exhibited high Curie temperature above ~305°C. As the Mn doping amount increases the Curie temperature was found to decrease from 340 °C (± 2 °C) for 0.5 wt% Mn to 329°C (± 2 °C) for 0.9 wt% Mn for 0.9PZT (52:48) -0.1PZN + y wt% Mn as shown in Figure 4.12(a). Similar trend was observed for 0.9PZT (56:44) -0.1PZNN + x mol% MnO₂ as shown in Figure 4.12 (b). As the Mn concentration increases from 1 to 3 mol% Curie temperature drops from 326 °C (± 2 °C) to 306 °C (± 2 °C).

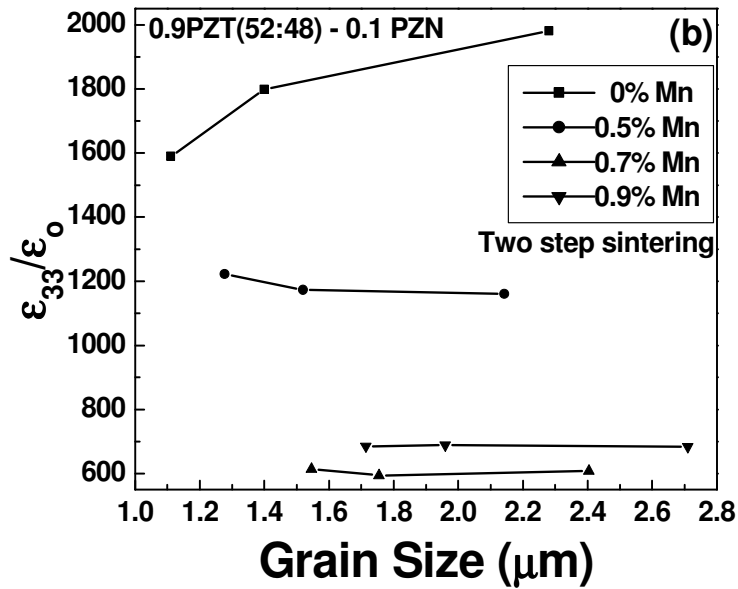
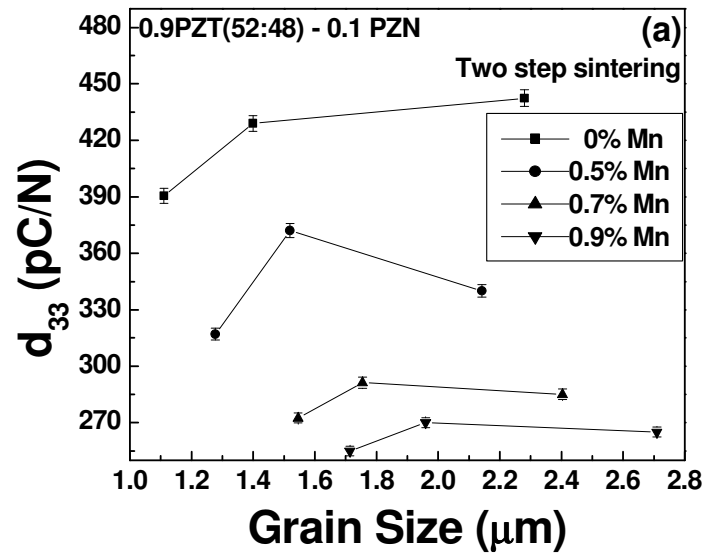


Figure 4.9: Variation of the (a) piezoelectric constant, d_{33} for 0.9PZT (52: 48) – 0.1 PZN + y wt% MnCO_3 , (b) dielectric constant, ϵ_{33}/ϵ_0 for 0.9PZT (52: 48) – 0.1 PZN + y wt% MnCO_3 .

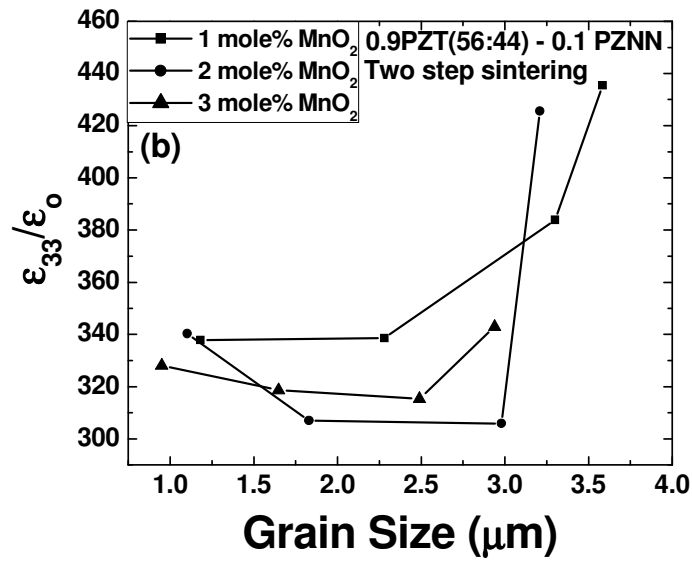
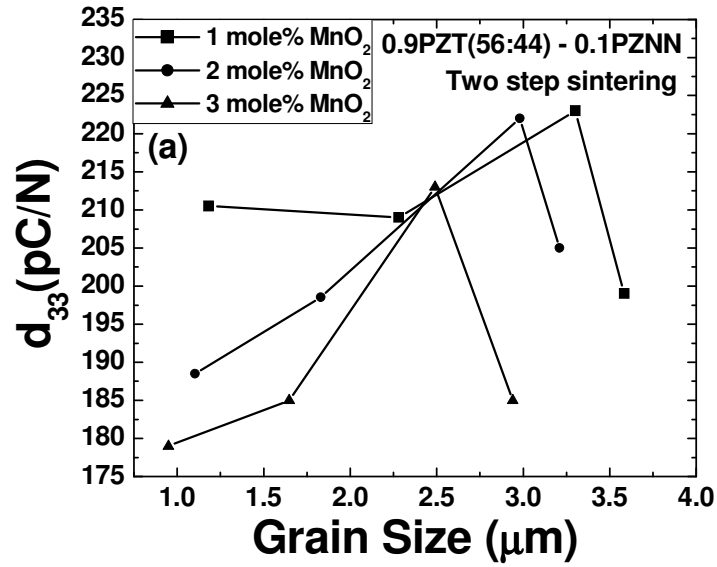


Figure 4.10: Variation of the (a) piezoelectric constant, d_{33} for 0.9PZT (56: 44) – 0.1 PZNN + x mol% MnO_2 and (b) dielectric constant ϵ_{33}/ϵ_0 for 0.9PZT (56: 44) – 0.1 PZNN + x mol% MnO_2 .

4.6 Grain size dependency

The variation of the piezoelectric and dielectric properties with Mn modification can be explained in terms of hardening effect and grain growth. In general, charge compensation for acceptor-type modifications (lower valence ion on Zr^{+4} or Ti^{+4} site) in PZT is achieved by oxygen vacancies or hole generation. If the oxygen vacancies are generated then there are several mechanisms through which domain pinning can occur. These are: (i) associated defect dipole formed by oxygen vacancies and acceptor which aligns with the spontaneous polarization creating an internal bias field; (ii) oxygen vacancies diffuse to domain walls and pin them and (iii) defects in the domain wall regions adjust in position to compensate local polarization fluctuations. The reason for domain pinning by oxygen vacancies in perovskite structure lies in the fact that distance between neighboring oxygen atoms (2.8 Å) is much smaller than the A-site or B-site separation (4 Å). Oxygen atoms form the octahedron and are interconnected to each other. Hence, defect dipoles formed by acceptor ions and oxygen vacancies can realign with spontaneous more easily than the corresponding dipoles formed by point dipoles in donor-doped material. Previously, Priya et al. have conducted extensive investigations on Mn-modified PZN – PT single crystals and shown that hardening occurs due the pinning of the domains by dipolar defects at domain boundaries [91 – 94] It is believed that similar mechanism is operating in the Mn-modified PZT-PZN ceramics [96]. Hardening results in decrement in the magnitude of the piezoelectric constants, dielectric constants, and losses. The grain size has strong effect on the magnitude of the dielectric and piezoelectric properties. As the grains become finer, under the same electric field, the absolute value of the strain decreases and the hysteresis becomes smaller [104] This is explained by the increase in coercive field for 90° domain rotation with decreasing grain size. The grain boundaries (with many dislocations on the grain boundary) "pin" the domain walls and do not allow them to move easily. Takasu et al. [105] have studied

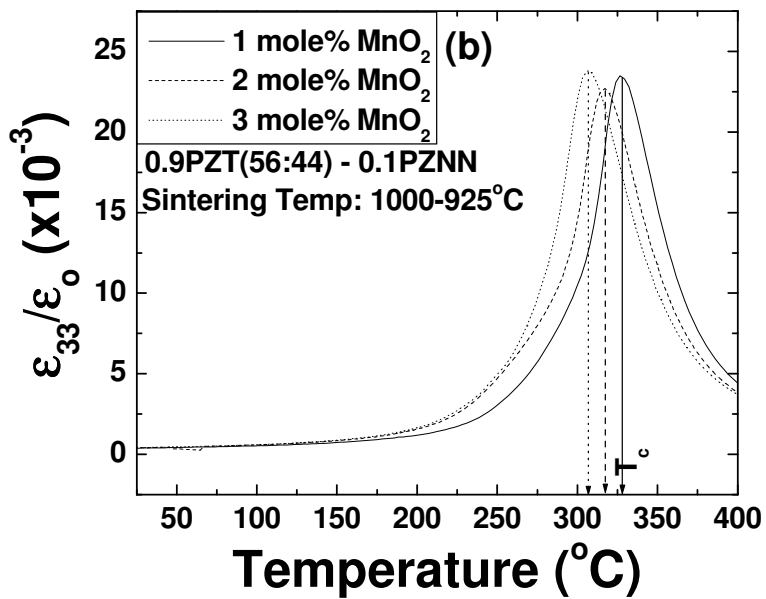
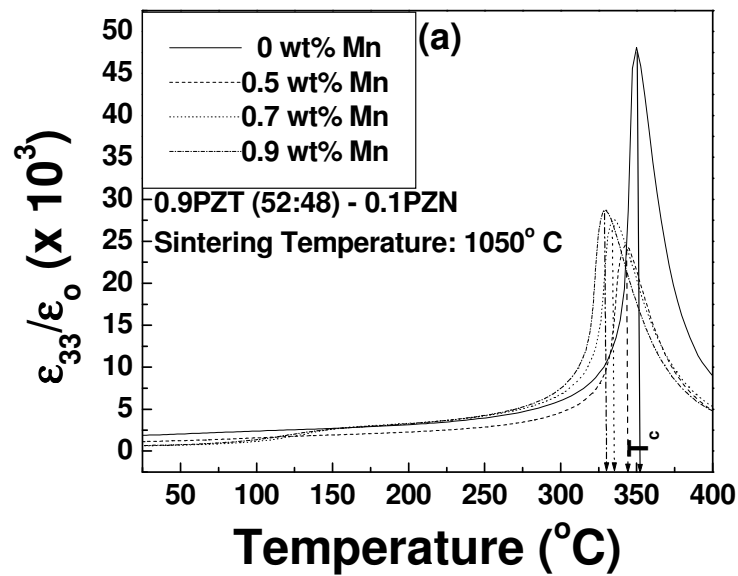


Figure 4.11: (a) Temperature dependence of dielectric constant for 0.9PZT (52: 48) – 0.1 PZN + y wt% MnCO₃ and (b) temperature dependence of dielectric constant for 0.9PZT (56: 44) – 0.1 PZNN + x mol% MnO₂.

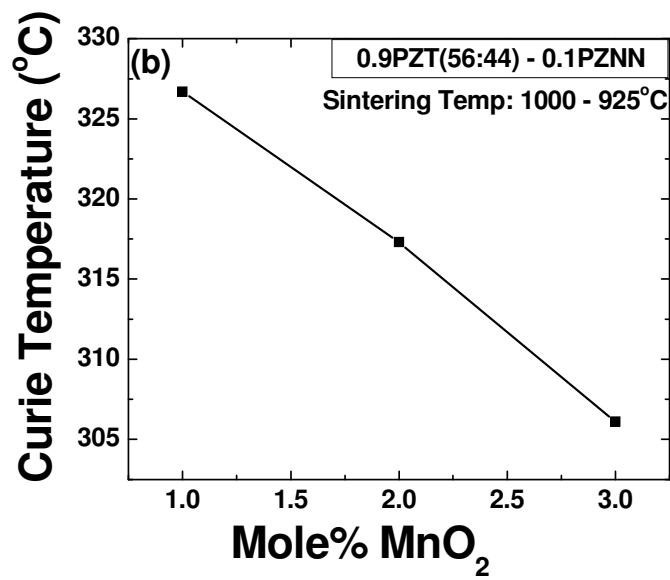
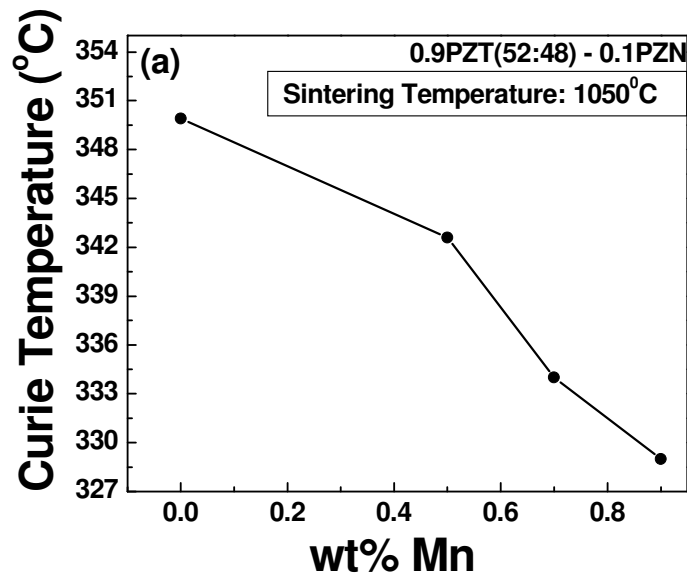


Figure 4.12: (a) Variation of Curie temperature as a function of the Mn concentration for 0.9PZT (52: 48) – 0.1 PZN + y wt% MnCO₃ and (b) variation of Curie temperature as a function of the Mn concentration for 0.9PZT (56: 44) – 0.1 PZNN + x mol% MnO₂.

the effects of grain size on PLZT (9/65/35) and showed that for grain size larger than 1.7 μm , the dielectric constant increases with increasing grain size. Similar trend was also observed for the strain measured as a function of the electric field. Below 1.7 μm , the dielectric constant increases with decreasing grain size. This behavior can be explained as follows: with decreasing grain size, ferroelectric domain walls become difficult to form in the grain, and the domain rotation contribution to the strain becomes smaller. Thus, for the Mn-modified PZT – PZN it can be expected that the dielectric constant and losses increase with the Mn concentration as there is pronounced increase in the grain size (Figure 4.6) for compositions given by 0.9PZT (52:48) -0.1PZN + y wt% Mn.

The data in the Fig. 4.9 and 4.10 is the average of the changes in piezoelectric and dielectric properties of two compositions occurring due to acceptor modification and grain size increase, both being complementary to each other. The dielectric and piezoelectric properties show decrement with Mn concentration. The decrement could be explained on the basis of conventional hardening effect. This argument is supported by the fact that a large decrease in the d_{33} and ϵ_{33} was obtained in the case of 0.9PZT (52:48) - 0.1PZN + 0.7 wt% Mn. On further increase of Mn concentration the grain size effect is more dominant as a result of which the change in dielectric and piezoelectric constant is minimal. For the compositions given by 0.9PZT (56:44) -0.1PZNN + x mol% MnO_2 , the changes in piezoelectric and dielectric properties can be also explained on the basis of averaging effect due to grain size and oxygen vacancy concentration.

4.7 Chapter Summary

This chapter discusses a high energy density piezoelectric polycrystalline ceramic composition in the system $\text{Pb}(\text{Zr}_{1-x}\text{Ti}_x)\text{O}_3 - \text{Pb}[(\text{Zn}_{1-y}\text{Ni}_y)_{1/3}\text{Nb}_{2/3}]\text{O}_3$ (PZT – PZNN). Two different Zr/Ti ratios in the PZT system were investigated, 52/48 corresponding to morphotropic phase boundary (MPB) and 56/44 corresponding to the tetragonal phase. The compositions

investigated in this study are represented as: $0.9 \text{ Pb}(\text{Zr}_{0.52}\text{Ti}_{0.48})\text{O}_3 - 0.1 \text{ Pb}(\text{Zn}_{1/3}\text{Nb}_{2/3})\text{O}_3$ [0.9PZT (52:48) - 0.1PZN] + y wt% MnCO_3 , where y varies from 0 wt% to 0.9 wt% and $0.9 \text{ Pb}(\text{Zr}_{0.56}\text{Ti}_{0.44})\text{O}_3 - 0.1 \text{ Pb}[(\text{Zn}_{0.8}\text{Ni}_{0.2})_{1/3}\text{Nb}_{2/3}]\text{O}_3$ [0.9PZT (56: 44) – 0.1PZNN] + y mol% MnO_2 , where y varies from 1 to 3 mol%. A high energy density material is characterized by the large magnitude of the product of the piezoelectric voltage constant (g) and the piezoelectric strain constant (d) given as (d.g). The condition for obtaining large magnitude of d.g was derived to be as $|d| = \epsilon^n$, where ϵ is permittivity of the material and n is a material constant having lower limit of 0.5. The $d_{33} \cdot g_{33}$ values of the samples having composition 0.9 PZT (56: 44) – 0.1 PZNN + 2 mol% MnO_2 (sintered in two steps at 1100 – 1000°C) was found to be as $18456.2 \times 10^{-15} \text{ m}^2/\text{N}$, which in the knowledge of the authors is the highest value reported for polycrystalline ceramics. This composition was also found to exhibit a high magnitude of g_{33} as 83.1 V-m/N, corresponding to the magnitude of n as 1.126.

Once the high performance piezoelectric composition is known, the next goal will be to understand the role of dopants in the composite structure. It will be interesting to quantify the variation in ME properties with changes in the piezoelectric phase. A clear tendency with modification of piezoelectric composition will indicate that the composite properties are influenced by the characteristics of the individual phases. This implies that by selecting high performance individual phases better coupling can be obtained.

CHAPTER 5

DOPING EFFECT ON MAGNETOELECTRIC COEFFICIENT OF $\text{Pb}(\text{Zr}_{0.52}\text{Ti}_{0.48})\text{O}_3$ - $\text{Ni}_{(1-x)}\text{Zn}_x\text{Fe}_2\text{O}_4$ PARTICULATE COMPOSITES.

Magnetolectric [ME] particulate composites combine the magnetostrictive and piezoelectric properties of materials through product tensor properties. Sintered particulate composites have inferior properties compared to laminated ones mainly due to low resistivity, interface defects, interface diffusion, and mismatch of elastic compliances. In order to overcome these drawbacks we propose to study the effect of dopants in this chapter. In the previous chapter, a piezoelectric composition was derived that can provide high magnitude of piezoelectric voltage constant 'g'. In this chapter we will start with MPB PZT and introduce dopants systematically to identify the variation in properties.

Doping can also be done on the Ni ferrite composition in order to improve the resistivity, permeability, magnetization, and coercive field. Investigations have shown that the nickel based ferrite particles are chemically stable in doped-PZT matrix and do not react at high sintering temperatures of 1250°C. Besides Mn / Ni based ferrites are soft compared to cobalt ferrite, and they offer higher permeabilities. The advantage of Ni based ferrite over Mn-ferrite is that it has a higher electric resistivity and lower dielectric loss.

5.1 Effect of Piezoelectric Composition

Doping of PZT can be done to make it soft or hard [107]. Generally, acceptor doping (Fe, Mn, Ni, Co) in the PZT based ceramics results in (i) decreased dielectric constant and loss, (ii) lower elastic compliance, (iii) lower electromechanical coupling factor, and (iv) lower electromechanical losses. In contrast, donor doping (La, Sb, Bi, W, Nb) results in (i) increased

dielectric constant and loss, (ii) increased elastic compliance, (iii) increased electromechanical coupling factor, and (iv) increased electromechanical losses [108].

We used both soft and hard PZT for the fabrication of 0.8 PZT – 0.2 NZF magnetolectric composite. Ceramic compositions with stoichiometric ratios of $\text{Pb}(\text{Zr}_{0.52}\text{Ti}_{0.48})\text{O}_3$ (PZT), $0.85[\text{Pb}(\text{Zr}_{0.52}\text{Ti}_{0.48})\text{O}_3] - 0.15[\text{Pb}(\text{Zn}_{1/3}\text{Nb}_{2/3})\text{O}_3]$ [PZT (soft)], $\text{Pb}(\text{Zr}_{0.56}\text{Ti}_{0.44})\text{O}_3 - 0.1 \text{Pb}[(\text{Zn}_{0.8/3} \text{Ni}_{0.2/3})\text{Nb}_{2/3}]\text{O}_3 + 2$ (mol %) MnO_2 [PZT (hard)] were synthesized. To understand the effect of doping on piezoelectric properties in ME composites, magnetostrictive composition was fixed at $\text{Ni}_{0.8}\text{Zn}_{0.2}\text{Fe}_2\text{O}_4$ [NZF].

5.1.1 Ferroelectric and piezoelectric properties

Figure 5.1 shows the polarization – electric field behavior of undoped PZT, hard PZT and soft PZT. The magnitude of polarization under the electric field of 4.5 kV/mm was found to be 14.61, 23.54 and 31.65 $\mu\text{C}/\text{cm}^2$ for the unmodified, hard and soft PZTs respectively. It is well known that soft PZT's have higher polarization magnitudes resulting in enhancement of both the dielectric and piezoelectric susceptibilities. In our samples, the piezoelectric constant (d_{33}) increased from 75 to 105 pC/N, dielectric constant increased from 642 to 914, dielectric loss increased from 1.26% to 2.7% and Q_m dropped from 613 to 142 between undoped and soft

Table 5.1: Piezoelectric properties of different compositions of PZT – 20 NZF composite.

| | PZT – 20 NZF | PZT (hard) – 20 NZF | PZT (soft) – 20 NZF |
|------------------------------------|---------------------|----------------------------|----------------------------|
| d_{33} (pC/N) | 75 | 85 | 105 |
| Dielectric Constant | 642 | 771 | 914 |
| Tan δ (%) | 1.26 | 0.82 | 2.7 |
| Q_m | 613 | 656 | 142 |

PZT. Table 5.1 lists the piezoelectric and dielectric properties of these three composites with different piezoelectric matrix (undoped, soft and hard). Corresponding elastic compliance (S_{11}) of these three compositions are 1.74×10^{-11} (soft), 1.37×10^{-11} (hard) and 1.11×10^{-11} (undoped)

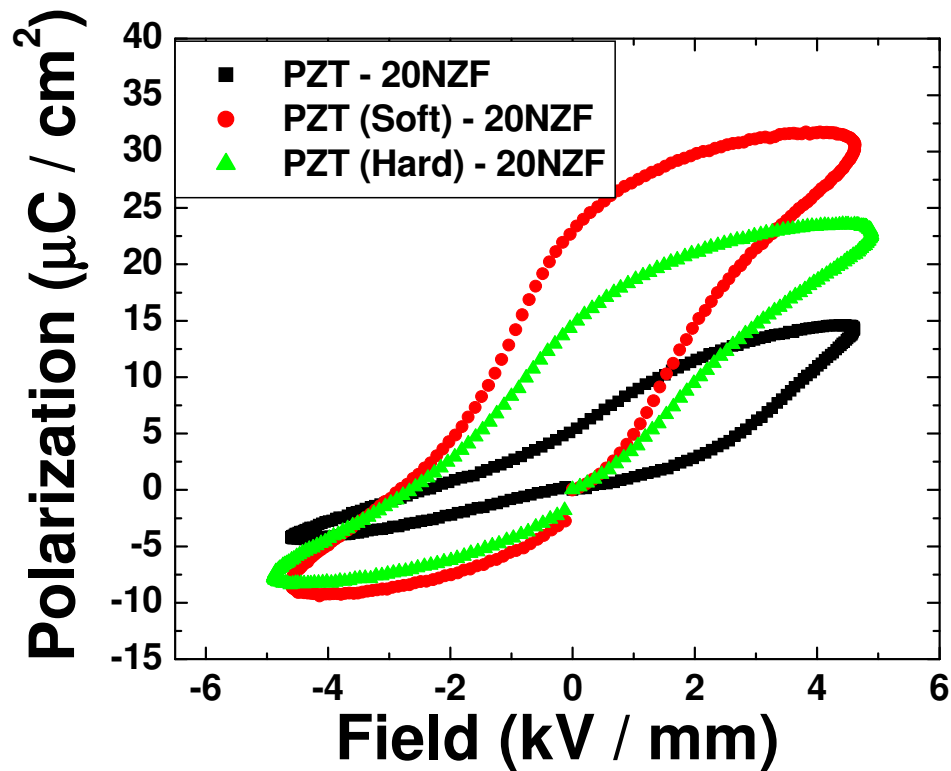


Figure 5.1: Polarization vs. electric field loop for different magnetolectric composite

5.1.2 Microstructural investigations of doped PZT – 20 NZF composite

Figures 5.2 (a) and (b) show the microstructures of PZT – 20NZF and PZT (soft) – 20NZF composites. Both microstructures were dense with the measured densities of $\geq 95\%$. The average grainsize of PZT – 20NZF composite was about 800 - 850 nm, whereas that of PZT (soft) – 20 NZF was smaller and ranges between 650 – 700 nm. Doping of PZN in PZT reduces the grainsize. Other than lower grain size, some other notable differences between

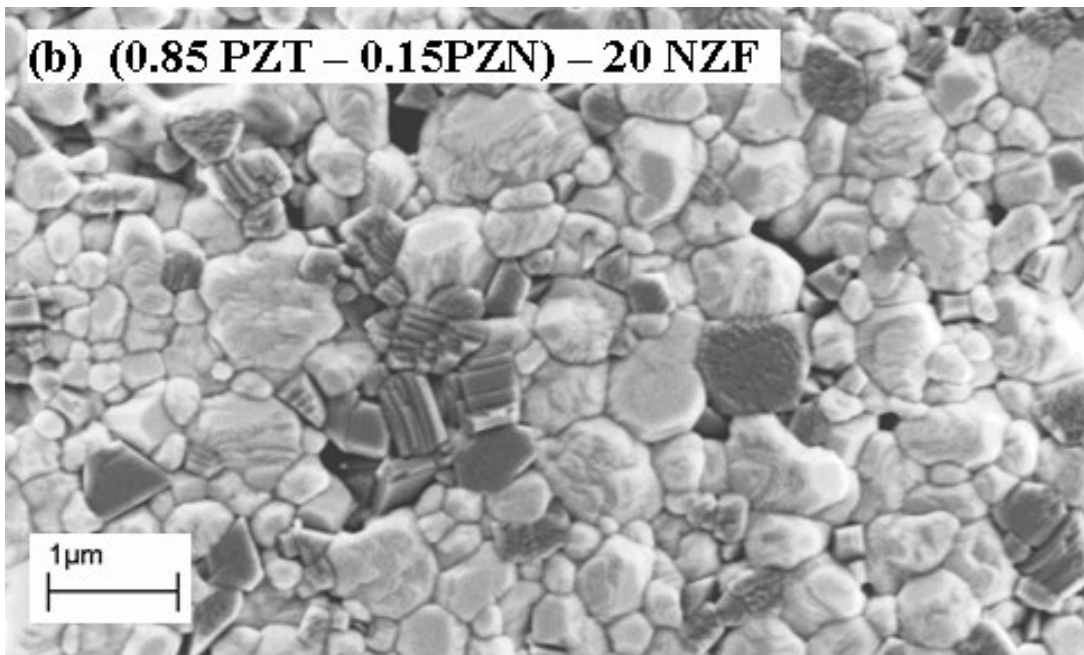
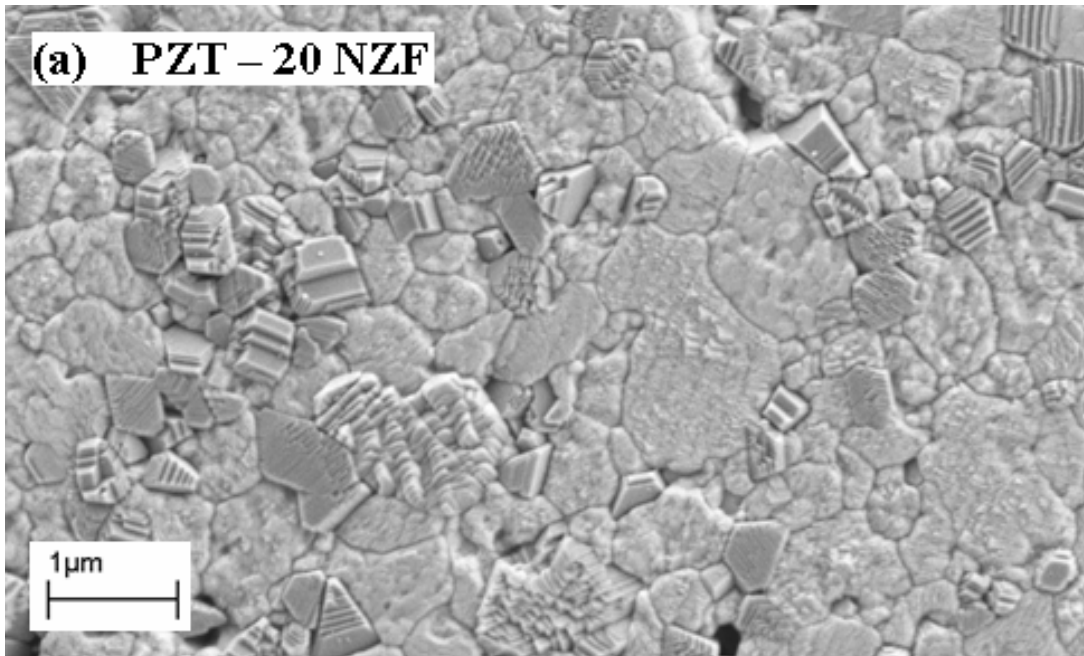


Figure 5.2: Microstructure of different magnetolectric composite, (a) PZT – 20 NZF and (b) PZT (soft) – 20 NZF.

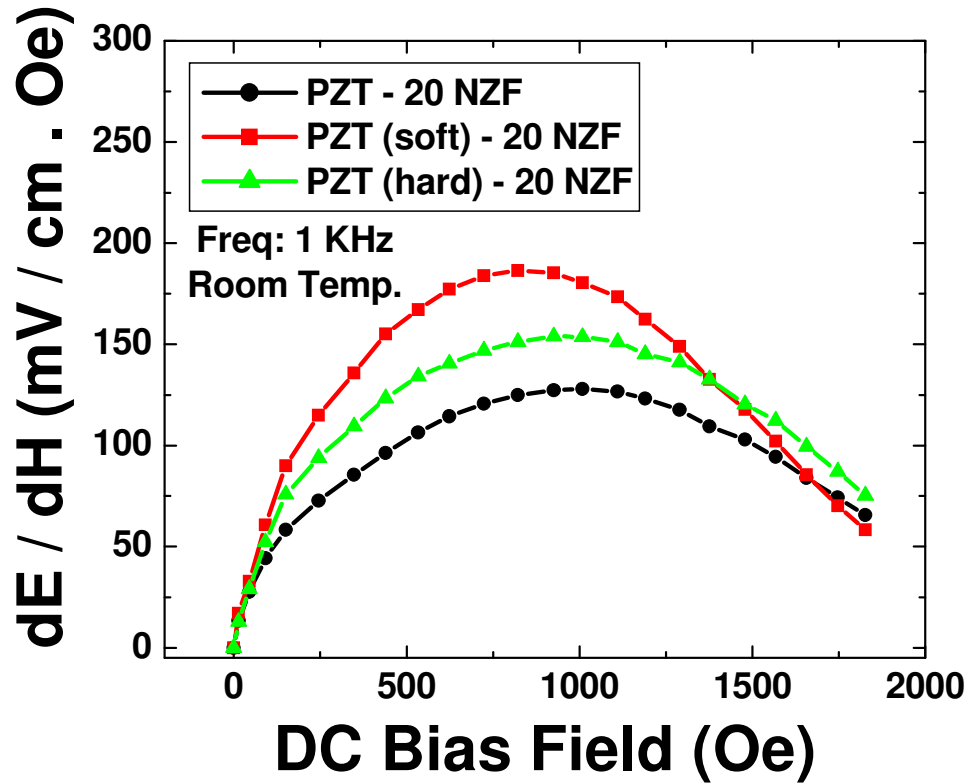


Figure 5.3: Magnetolectric coefficient as a function of DC bias field for different compositions of ME composite.

these two micrographs are the thick grain boundaries observed in the PZT (soft) matrix and better ferrite dispersion. The resistivity of PZT increases upon doping with PZN and also due to better dispersion. The increase in resistivity allowed better poling.

5.1.3 Magnetolectric properties as a function of doping in PZT matrix

Figure 4.3 shows the ME voltage coefficient of a PZT (soft) – 20 NZF composite $\frac{\delta E}{\delta H} =$

186.5 mV/cm.Oe. In this figure, the magnitudes of $\frac{\delta E}{\delta H}$ can be found to be as 154 and 128 mV/cm.Oe for composites made of hard and undoped PZT respectively. In this case, the magnetic field was perpendicular to the surface of the sample or parallel to the poling direction.

The DC bias field at which the magnetoelectric coefficient showed maxima for all three composition was in the range of 800 – 950 Oe. This data coincides with the polarization data of these three composites where PZT (soft) – 20 NZF also shows higher polarization. Since, ME coefficient is the directly proportional to the $\sqrt{\epsilon}$ considering the permeability (μ) is constant, the observed data scales with the basic approximation. Higher piezoelectric (d_{33}), dielectric, coupling constant, and polarization of soft PZT phase contribute towards higher magnetoelectric coefficient. The ME coefficient of 186 mV/cm.Oe was measured for PZT (soft) – 20 NZF. The elastic constant (in this case s_{11}) has a significant effect on magnitude of ME coefficient as d_{31} is directly related to s_{11} by following relationship:

$$d_{31} = k_{31} \sqrt{S_{11}^E \epsilon_{33}^T} \quad (5.1)$$

ME coefficient depends on d_{31} according to the following expression,

$$\left. \frac{dV}{dH} \right|_{T-T} = \beta \frac{n(1-n) A d_{33,m} d_{33,p} g_{33,p}}{S_{11}^E [n S_{11}^E (1 - k_{31}^2) + (1 - n) S_{11}^H]} \quad (5.2)$$

which can be simplified as:

$$\left. \frac{dV}{dH} \right|_{T-T} \propto d_{33,p} g_{33,p} \quad (5.3)$$

The magnitude of $d_{33,p} g_{33,p}$ were found to be as: 0.989×10^{-12} , 1.058×10^{-12} and 1.36×10^{-12} m^2/N for undoped PZT, hard PZT and soft PZT respectively. Thus, higher magnitude of product (d.g) leads to higher ME coefficient, justifying our predictions from the previous chapter.

5.2 Effect of Magnetostrictive Composition

Doping experiments on Ni ferrite has been conducted previously in order to improve the resistivity, permeability, magnetization and coercive field [79, 109]. An addition of Zn in the ferrite structure improves the resistivity, permeability, and magnetization; but reduces its Curie temperature. It was found that as the Zn is added to the spinel structure, Zn^{+2} usually replaces

the Fe^{+3} in the tetrahedral site and the replaced Fe^{+3} take the vacant octahedral site, emptied by Ni^{+2} . In that way divalent Zn has no unpaired electron, divalent Ni has one and trivalent Fe has 5 unpaired electrons [109].

5.2.1 Magnetic properties and structural studies of PZT - Zn doped NFO composites

Figure 5.4 (a) shows the saturation magnetization (M_s) and coercive field (H_c) of the PZT – 20NZF composite as a function of Zn concentration in NZF. It can be seen from this figure that with increase of Zn concentration coercivity (H_c) decreases. A maximum in the magnetization (0.72 emu/gm) can be seen near 30% Zn doping, which had a coercivity of 49.6 Oe. Figure 5.4(b) shows the magnetization as a function of temperature. The Curie temperature dropped from 850 K to 549 K as the Zn concentration was increased from 0 to 50 mole %. As Zn concentration is increased, it replaces Fe^{+3} in the tetrahedral site and the formation of ZnFe_2O_4 becomes more prominent which will decrease the Curie temperature as it is paramagnetic at room temperature. Further, as we increase the Zn substitution in NFO, permeability starts to increase. Due to the change in position of Fe^{+3} from tetrahedral site to the octahedral site magnetization is higher in 30% Zn doped NZF. For the same reason the Curie temperature starts to drop as the Zn concentration is increased. As the Zn concentration is further increased magnetization starts to drop as there are very few Fe^{+3} left for the tetrahedral site. The coercivity has direct relationship with Zn concentration because as more Zn is doped the structure shifts towards paramagnetic Zn ferrite. That's why observed a drop in coercivity with Zn concentration. Figure 5.5 shows the diffraction peak for (hkl: 400) plane for various NZF composites ranging from pure Ni-ferrite to 50 mole% Zn doped Ni-ferrite. As the Zn concentration was increased a systematic shift was observed in the XRD peaks. Figure 5.5(a) shows the peak shift for (400) towards lower Bragg angles as we increase the Zn concentration. This shift is an indication of increased magnitudes of the lattice parameters. Using Bragg's law, the lattice parameter was found to be 8.32 Å for NiFe_2O_4 and 8.394 Å for $\text{Ni}_{0.5}\text{Zn}_{0.5}\text{Fe}_2\text{O}_4$, a 0.9% lattice expansion.

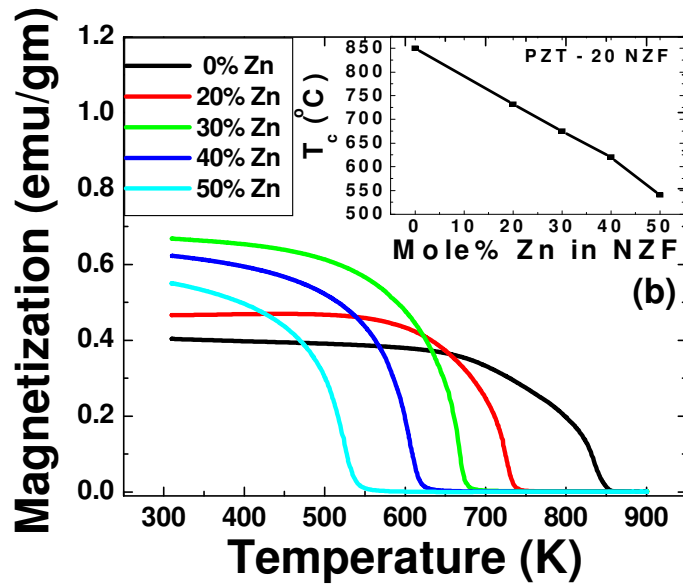
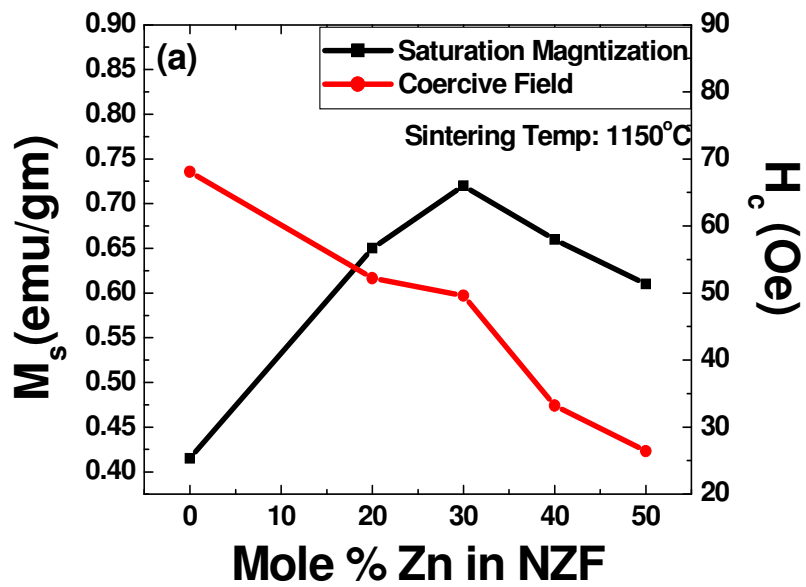


Figure 5.4: Magnetic properties of different composite. (a) magnetization and coercive field as a function of Zn% concentration in NZF and (b) magnetization as a function of temperature.

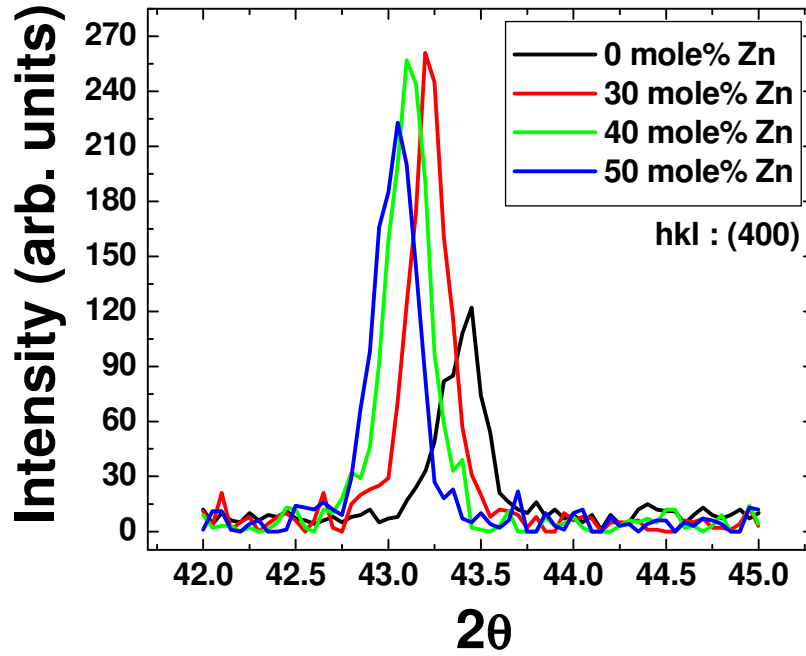


Figure 5.5: X-ray diffraction pattern for the hkl : 400 peak for different Zn doping concentration in NZF showing peak shift.

5.2.3 Effect of Zn concentration of NZF on magnetoelectric coefficient

Figure 5.6 shows the ME voltage coefficient as a function of DC bias for different Zn concentration in PZT – 20 NZF. It was found that as the Zn concentration was increased, ME coefficient also increases and shows a maxima near 30 mole% Zn. The magnitude of $\frac{\delta E}{\delta H}$ was found to be 138 mV/cm.Oe at the maximum. With further increase in Zn concentration, the ME coefficient dropped to ~60 mV/cm.Oe at 50 at%. The inset in this figure shows the ME coefficient as a function of Zn concentration. The variation of ME coefficient with Zn concentration is similar to that for the saturation magnetization. This is expected, as the permeability μ is directly related to magnetization M via $\mu = 1 + 4\pi \frac{M}{H}$. The piezomagnetic

coefficient is directly related to permeability through the expression $d_{33,m} = \mu_{33} \cdot s_{33} \cdot \lambda_{33}$ [51], where s and λ are the elastic compliance and magnetostriction coefficient. Clearly the changes in ME coefficient with Zn concentration depends on the effective change in piezomagnetic coefficient and of magnetization values. The coercivity plays an important role in magnetoelectric coefficient along with magnetostriction as it relates the field

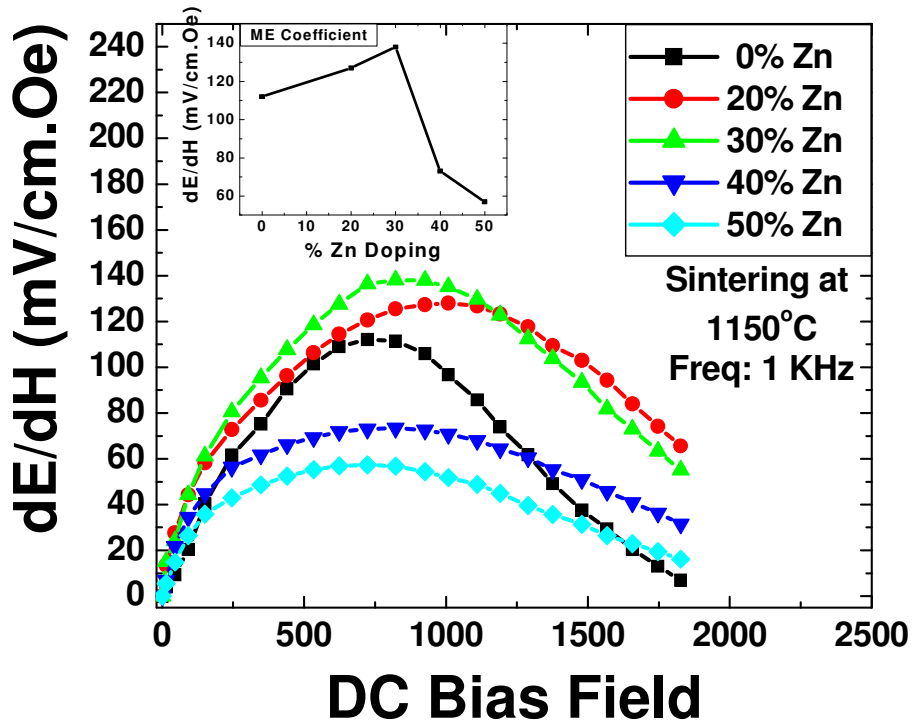


Figure 5.6: Magnetoelectric coefficient as a function of DC bias for different concentration of Zn in NZF (Inset: ME coefficient vs. Zn doping)

required for domain rotation. The composition with 30% Zn doping had lower coercive field (49.6 Oe) compared to pure NFO (68 Oe), which contributes towards higher ME coefficient at low bias values. Although 50% Zn doped NFO has even lower coercivity (26 Oe), it has lower magnetization which reduces the magnitude of ME coefficient.

5.3 Chapter summary

In this chapter, doping effect in the piezoelectric and magnetostrictive phases was investigated to understand their effect on ME coefficient. It was found that 15at% doping of $\text{Pb}(\text{Zn}_{1/3}\text{Nb}_{2/3})\text{O}_3$ [PZN] in $\text{Pb}(\text{Zr}_{0.52}\text{Ti}_{0.48})\text{O}_3$ [PZT] enhances the piezoelectric and magnetoelectric properties of a PZT – 20 at% $\text{Ni}_{0.8}\text{Zn}_{0.2}\text{Fe}_2\text{O}_4$ [NZF] composite. The piezoelectric constant, dielectric constant, and magnetoelectric coefficient increases from 75 pC/N, 642 and 127 mV/cm.Oe to 105 pC/N, 914 and 187 mV/cm.Oe, respectively. The effect of doping in the ferromagnetic phase was also investigated. With increase in Zn concentration, it was found that the coercive field and Curie temperature of $\text{Ni}_{(1-x)}\text{Zn}_x\text{Fe}_2\text{O}_4$ [NZF] decreases, while its saturation magnetization shows a maxima at 30 mole% Zn doping. X-ray diffraction revealed that the lattice constant of NZF increases from 8.32 Å for 0 at% Zn doping to 8.39 Å for 50 at%. The magnetoelectric coefficient was found to have maxima of 144 mV/cm.Oe at 30 at% Zn. The ME composites of soft piezoelectric phase [0.85 PZT – 0.15 PZN] and soft ferromagnetic phase [NZF] exhibited high ME voltage coefficient of 187 mV/cm.Oe.

CHAPTER 6

EFFECT OF GRAIN SIZE ON MAGNETOELECTRIC COEFFICIENT OF $\text{Pb}(\text{Zr}_{0.52}\text{Ti}_{0.48})\text{O}_3 - \text{Ni}_{0.8}\text{Zn}_{0.2}\text{Fe}_2\text{O}_4$ PARTICULATE COMPOSITES

Composition, microstructure, and geometry play important role on the magnitude of the ME coefficient [77 – 81]. In the previous two chapters, effect of composition and doping concentration was investigated for the PZT and ferrites. In this chapter, effect of microstructural variable, grain size, on magnetoelectric properties will be investigated. The effect of grain size on piezoelectric, dielectric, and ferroelectric properties has been widely studied in literature [110 – 114]. It is well known that piezoelectric and dielectric properties drop rapidly below critical grain size (~100 nm) [115 – 116]. SEM analysis combined with surface tension measurement indicate that the surface bond contraction due to small size induces a compressive stress on the inner part of a grain and this effect plays an important role in ferroelectric materials in the nanometer size range. The induced stress causes decrease of Curie temperature and spontaneous polarization with decreasing grain size. The domain wall contribution has an opposite effect as compared with the surface bond contraction induced effect. When the grain size decreases to a value comparable to the width of domain walls, pinning points develop inside the grains and the domain wall motion is inhibited. The reduced wall mobility causes a decrease in the relative permittivity. The measured value is a competition between the increase of relative permittivity by the surface bond contraction effect and its decrease by the domain wall pinning effect [117 – 120].

6.1 Characterization of Starting Particles

Figure 6.1(a) shows the XRD patterns of starting powder as a function of final grain size. No secondary peaks were found other than perovskite (P) and spinel (S). As the grain size

decreases the intensity of the peaks also decreases. Also as the particles size decreases, the background noise increases. This is due to the large extent of diffraction occurring from smaller particle sizes. Another important feature that can be noted is that with decreasing grain size the peak width increases and intensity of the diffraction peaks is decreased. The full width half maximum (FWHM) was quantified from the XRD pattern and is plotted as a function of grain size in Fig. 6.1(b). The 101/110 peaks were chosen for the FWHM measurement, shown by a set of arrows in Fig. 6.1(a). For a final grain size of 97nm the FWHM for 101/110 peak was recorded as 0.772° , whereas the FWHM for the 627nm grain size was found to be as 0.401° . Figure 6.2 shows the histogram patterns of particle size distribution of four different batches of powders. It was found that the starting average particles size of 76nm produces a final grain size of 97nm whereas the average particle size of 486nm produces ~556nm grain size. Grain growth in the range of 15 to 25% was observed during sintering. For smaller particle size (76 and 84 nm) a narrow distribution was observed whereas for larger particles sizes (486 nm and above) a relatively wider distributions was notable. TEM investigations of the particles were conducted as shown in Figure 6.2 and the results are consistent with the particle size data. Most of the particles observed were spherical but there is variation in the geometry.

6.2 Characterization of Sintered Composite

6.2.1 Investigations on microstructure and physical properties for various grainsize

Figure 6.3 (a) – (f) shows the SEM microstructure of ME composite with 830, 758, 556, 320, 111 and 97nm average grain size respectively. For larger particles size (545 nm and above) higher sintering temperatures were required whereas around 50 – 75 °C less sintering temperature were used for lower particle size (84 nm or less). Optimization of the sintering temperatures was done for each batch and only the samples with optimum densities were reported in figure 6.3. All the microstructures were found to be dense and well sintered. The

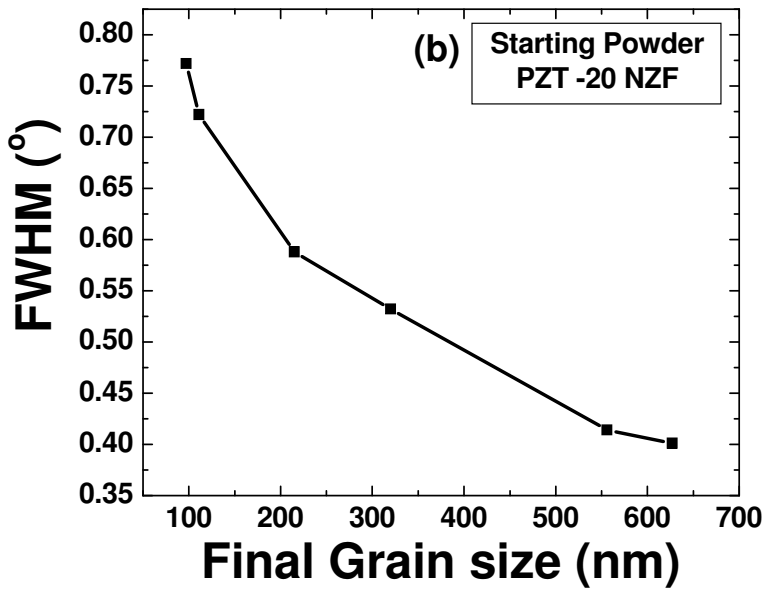
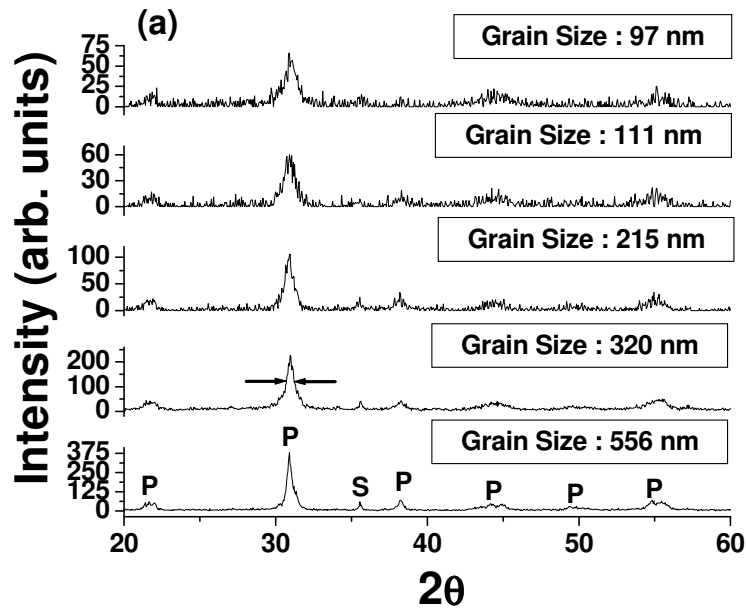


Figure 6.1: Structural characterization of calcined powder (a) XRD patterns of composite powders and (b) Full width half maxima (FWHM) as a function of final grain size in sintered sample.

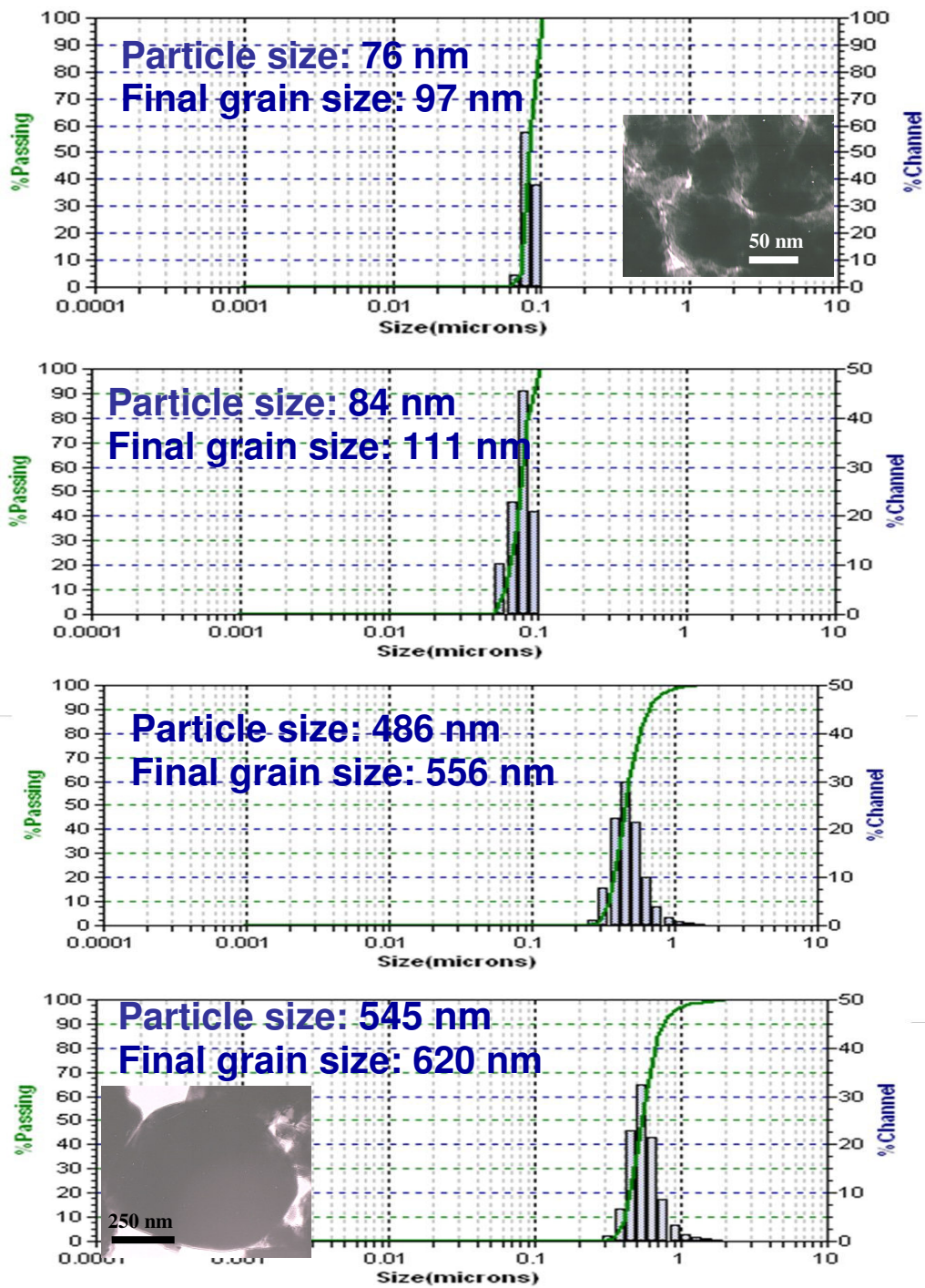


Figure 6.2: Particle size distribution histogram for four different batches of powders.

amount of porosity increases as the grainsize increases but the connectivity of the ferrite particles was less in the larger grainsize samples. The density data shown in Figure 6.4(a) illustrates that as the grain size of the composite decreases the density increases and at grain size of 97 nm the densification reaches about 98%. The densification decreases to 93% as the grain size increases to 750nm. This is consistent with the amount of porosity observed in SEM investigations as higher porosity was found for larger grainsize samples. Figure 6.4(b) shows the variation of resistivity as a function of grain size. For a small grain size of 97nm the resistivity exhibited a magnitude of $1.23 \times 10^{10} \Omega\text{-cm}$ whereas for the large grain size of 600nm the value increased to $7.15 \times 10^{10} \Omega\text{-cm}$. The increase in resistivity at higher grain size indicates that ferrite grain size and distribution is affected by growth of piezoelectric phase. Figure 6.5 shows the sintered composite XRD patterns for different grain sizes. Major peaks of perovskite (marked as P) and spinel (marked as S) were observed with no trace of any other intermediate phase. The peak width (FWHM) also follows the same trend; with increasing grainsize from 97 nm to 758 nm, FWHM decreases from 0.411 to 0.245 deg. Intensity of the peaks increases as the grainsize increases, which was also observed with the particle size data. Tetragonality (c/a) was measured for all these samples and it was found that as the grainsize increases the c/a ratio increases. For smaller grain size of near 100 nm, the c/a ratio was calculated to be around 1.07 where as for larger grain size (830 nm) the c/a ratio increases to 1.018. This data gives an idea about increased piezoelectricity for larger grainsize samples. A transition from pseudo cubic to tetragonal was noticeable as the grainsize increases from below 100 nm to close to $1\mu\text{m}$.

6.2.2 Effect of grainsize on piezoelectric and ferroelectric properties of PZT - 20 NZF ME composite

Figure 6.6(a) and (b) shows the variation of longitudinal piezoelectric strain constant (d_{33}), dielectric constant (ϵ_r/ϵ_0) and longitudinal piezoelectric voltage constant (g_{33}) with grain

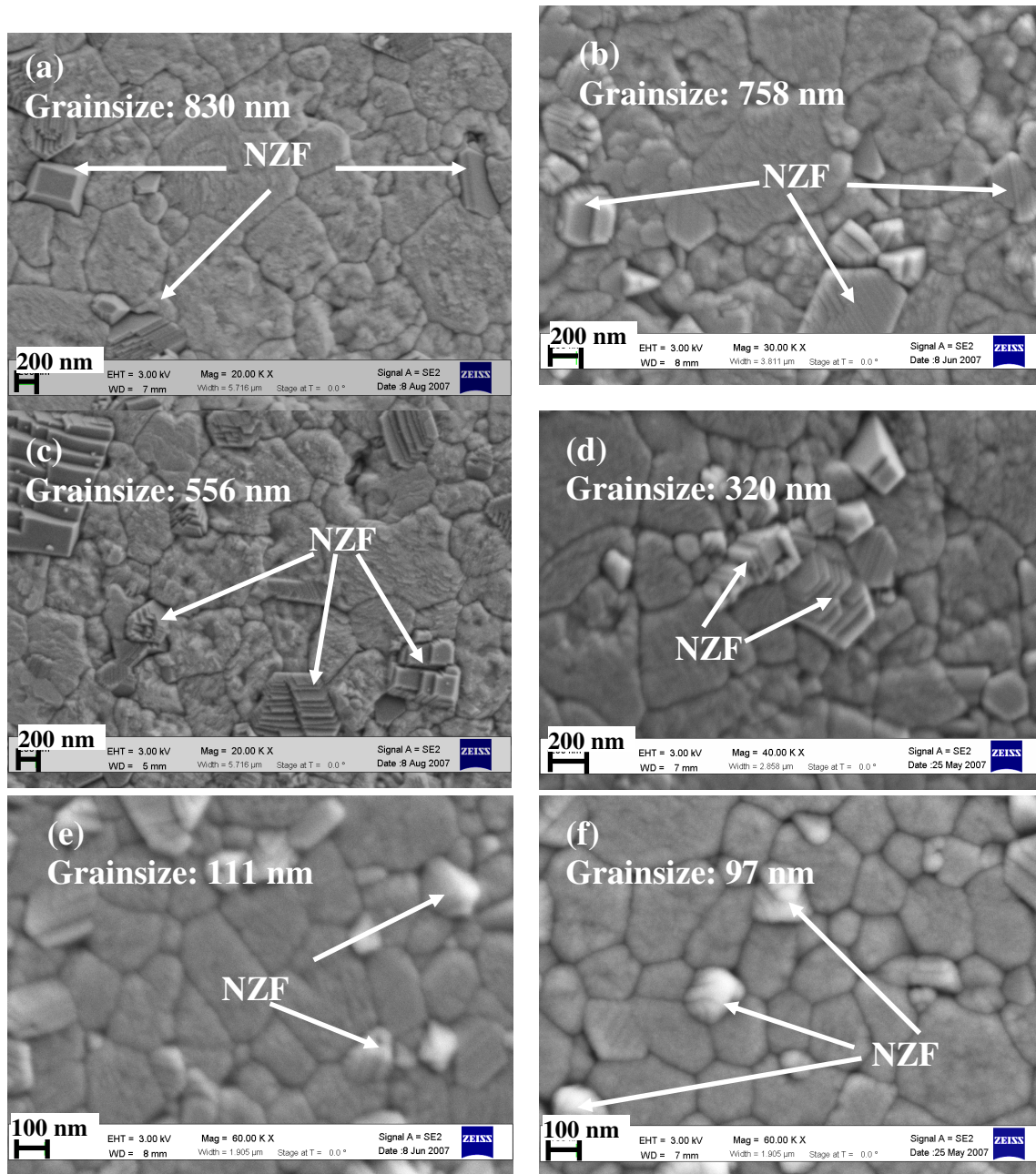


Figure 6.3: Microstructures of ME composites with varying grain size (a) 830nm, (b) 758nm, (c) 556nm, (d) 320nm, (e) 111nm and (f) 97nm.

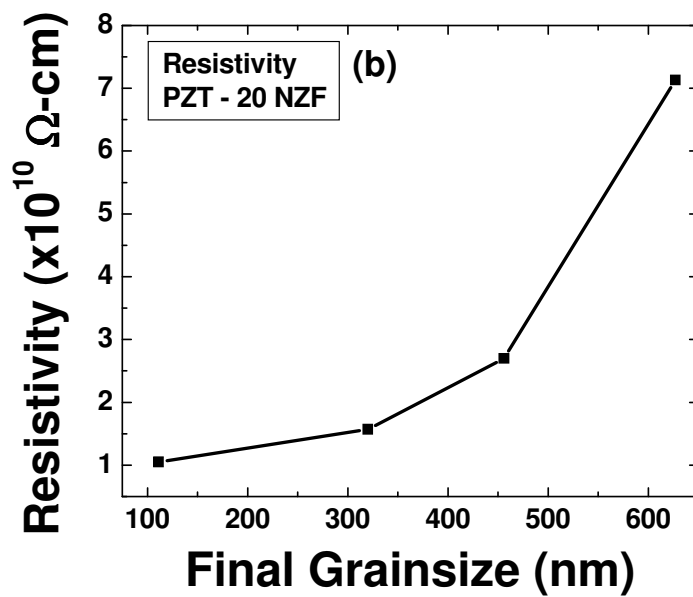
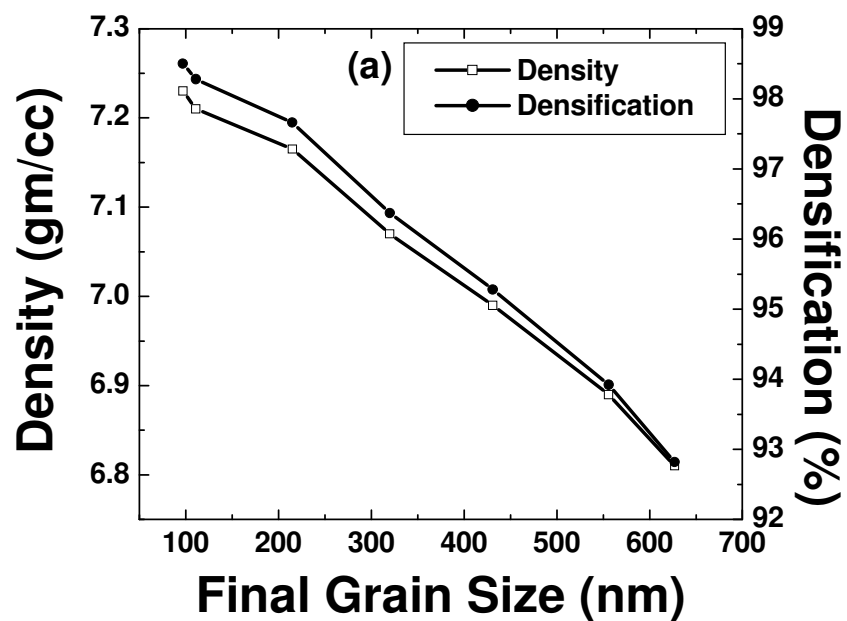


Figure 6.4: Variation of physical property with grain size (a) Density and densification, and (b) resistivity.

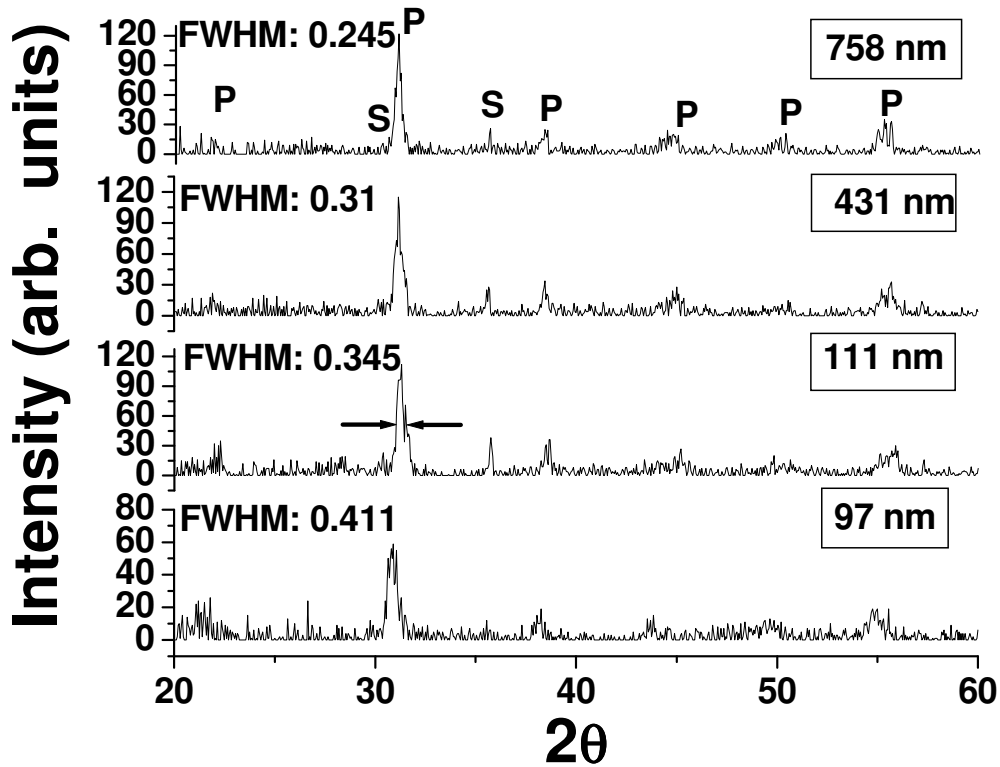


Figure 6.5: XRD patterns of the sintered composite showing perovskite (P) and spinel (S) peaks.

size. It can be noticed in this figure that there is a critical grain size below which the piezoelectric properties drop rapidly. This critical grain size is in the range of 100 – 150nm. Above 200nm the piezoelectric properties increases slowly and saturates at 600nm. The magnitude of d_{33} , ϵ_r/ϵ_0 , and g_{33} for ME composite with grain size of 97nm were 44 pC/N, 659 and 7.5×10^{-3} V-m/N. This magnitude increases rapidly to 65 pC/N, 746 and 9.9×10^{-3} V-m/N at grain size of 215nm. Above 600nm the piezoelectric and dielectric properties saturate at the magnitude of 72 pC/N, 781 and 10.4×10^{-3} V-m/N. The increase in the piezoelectric and dielectric properties can be explained in terms of domain wall motion. For larger grains, where

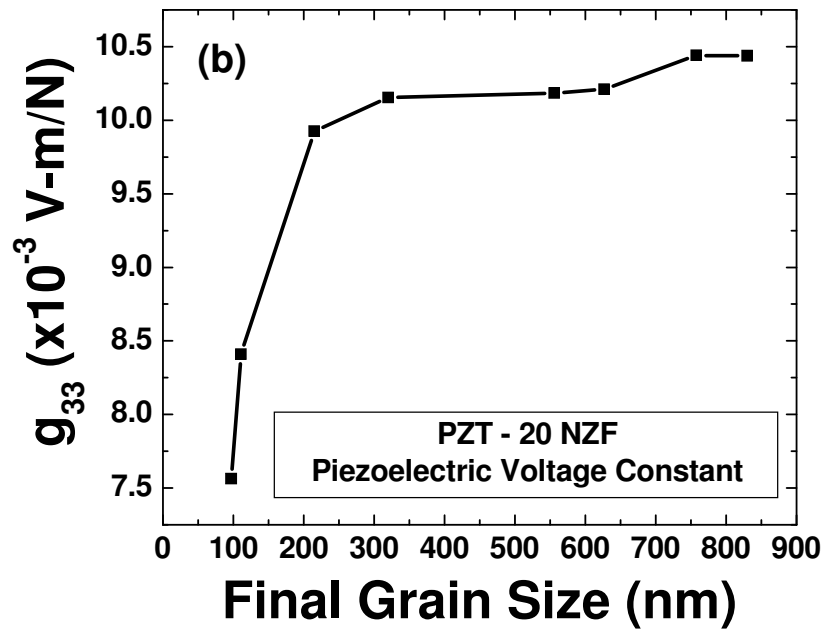
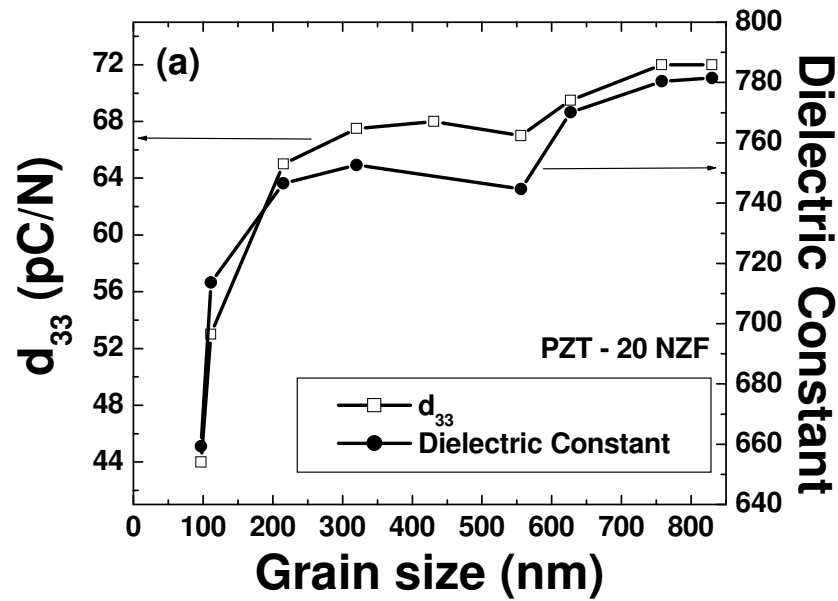


Figure 6.6: Piezoelectric properties as a function of grain size (a) Longitudinal piezoelectric and dielectric constant and (b) piezoelectric voltage constant.

the size of the domain is smaller than the size of the grains, the movement of the domain walls is easier. On the other hand, in small grains the movement of domain walls is restricted by the grain boundary. As a result during poling the domain switching will be difficult which reduces the piezoelectric properties [111]. The decrease in the magnitude of the piezoelectric constant (72 pC/N for 600nm grain size) compared to the original PZT composition (~220 pC/N) does indicate that there is interdiffusion of ions. However, we have not studied nature of diffusing species and diffusion distances. There is a minimum in d_{33} and dielectric constant at around 500 - 600 nm grainsize in Fig. 6.6 (a), which can be described as a transition region where the domain changes its structure. Above this critical grainsize, 90° domain starts to switch. Poling efficiency (degree of 90° domain switching) also improves as the grainsize increases. Previously, Uchino has reported for PLZT (9/65/35) ceramics a drop in relative dielectric constant near the critical grainsize where domain changes its structure. Arlt showed that transition region where domain structure changes depends on grainsize and below this transition region the grains consist of a simple lamella domain structure whereas above this critical grainsize microstructure changes to complex banded domain structure. Figure 6.7 shows the polarization vs. electric field loop for PZT – 20 NZF for four different average grain sizes. It was found that as the grain size increases the squareness of the loop increases. Saturation polarization (P_s) and coercive field (E_c) increases with the increase in grain size, and P_s and E_c values of $7.68\mu\text{C}/\text{cm}^2$ and 1.7 kV/mm were measured at 627nm grain size. These values were found to be $5.79\mu\text{C}/\text{cm}^2$ and 1.2 kV/mm for 111nm grain size. The low values of saturation polarization and coercivity at smaller grain sizes can be explained in terms of nucleation sites density. The number of nucleation sites for new domains are more in smaller grain size during polarization switching thus resulting in smaller coercive field. Similar behavior was observed in the dielectric constant vs. temperature plot as shown in Figure 6.8 (a), (c) and (e). It was found that as the grain size increases the dielectric constant and Curie temperature slightly increases. From the dielectric data at 100 kHz it can be seen that at grain size of 111nm the dielectric

maximum occurs at 355.8°C while at grain size of 830 nm the dielectric maximum occurs at 368.5°C. Figure 6.8 (b), (d) and (f) shows the variation of dielectric loss factor ($\tan \delta$) as a function of temperature. The loss factor increases rapidly at high temperatures indicating the space charge conduction and is significantly smaller at high frequency of 100 kHz. Space charge conduction is related to the transport of defects such as oxygen vacancies to the dielectric – electrode interface [121, 122]. In general, for smaller grain size the loss factor is lower because the grain boundary acts as pinning site for the domain wall movement [111 - 113]. From the data in Figure 6.8, the loss factor at 100 kHz and 30°C was found to be 0.0113 for 111 nm grain size while 0.00696 for 830 nm grain size. At the temperature of dielectric maximum and 100 kHz frequency the loss factor for 111 nm grain sizes was found to be 0.232 while that for 830 nm it was found to be 0.297.

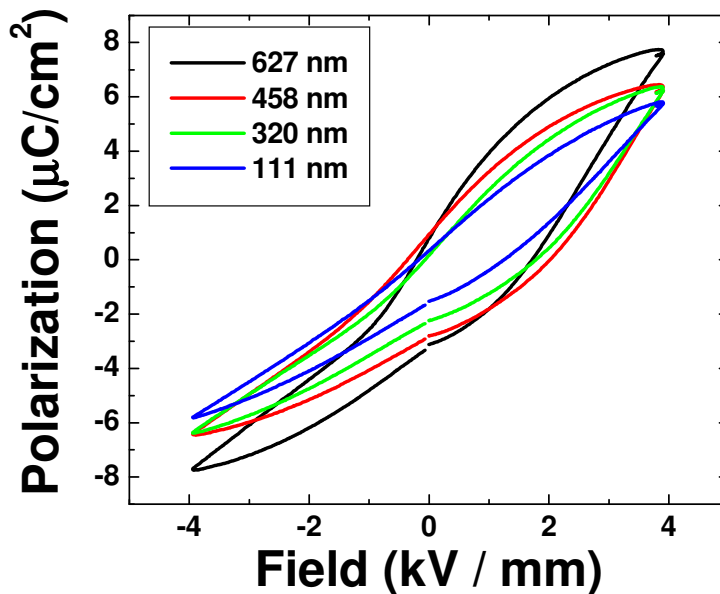


Figure 6.7: Polarization vs. electric field loop as a function of grainsize.

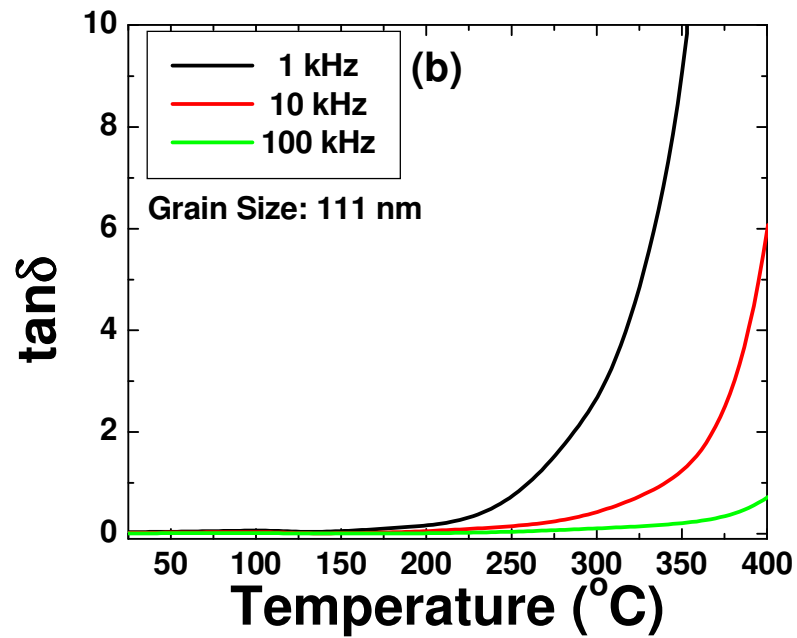
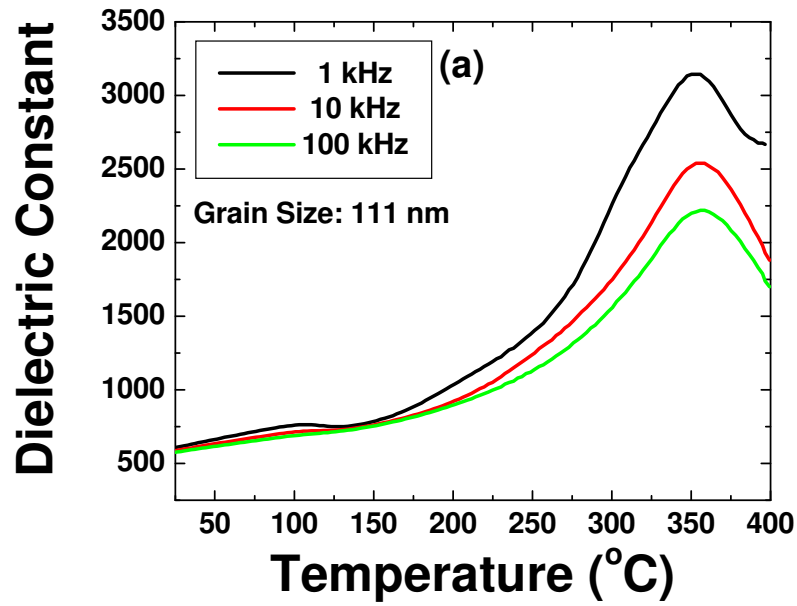


Figure 6.8: Dielectric properties as a function of temperature (a) dielectric constant for 111 nm, (b) loss factor for 111 nm

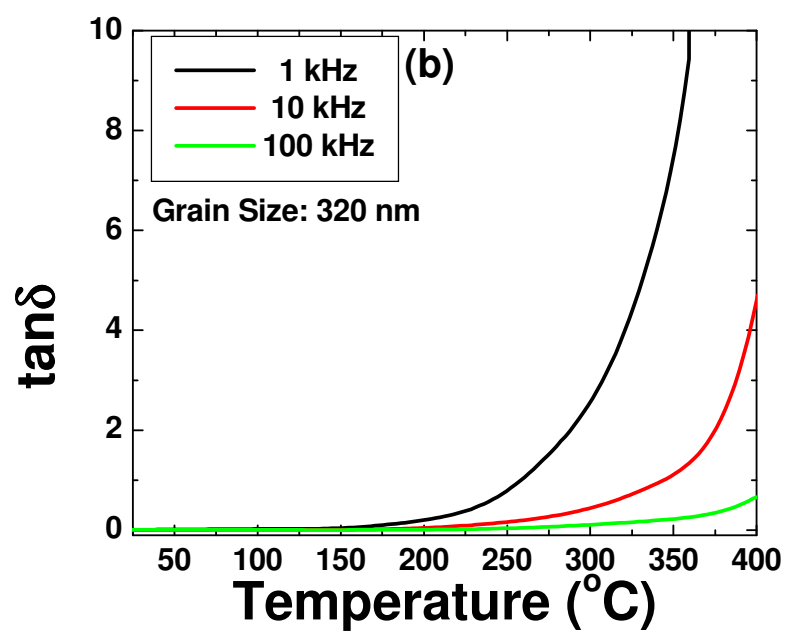
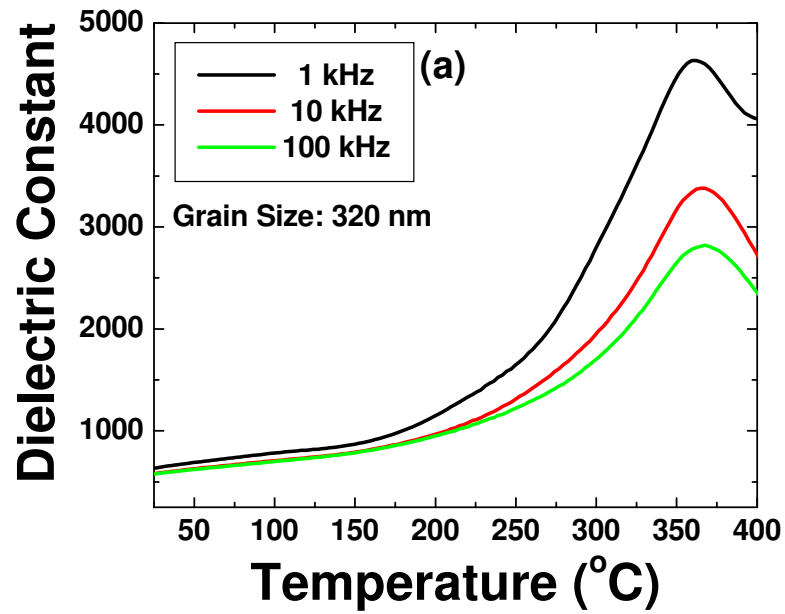


Figure 6.9: Dielectric properties as a function of temperature (a) dielectric constant for 320 nm, (b) loss factor for 320 nm.

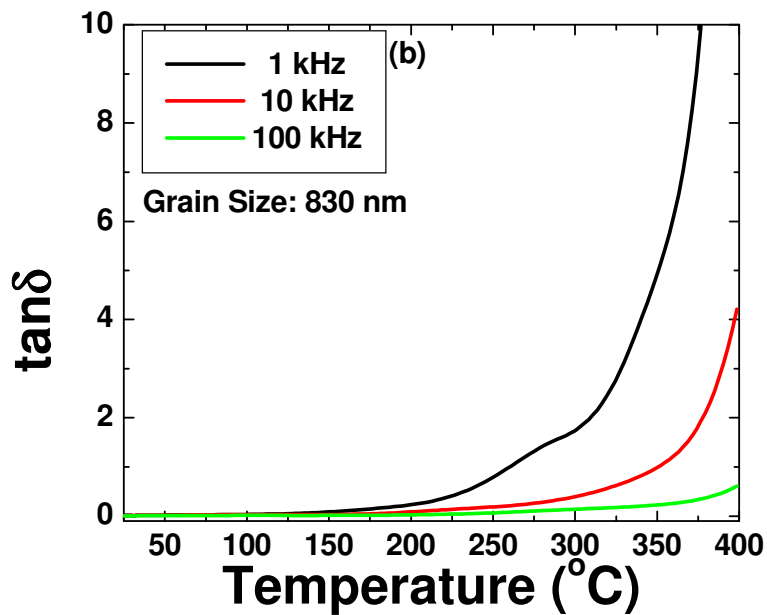
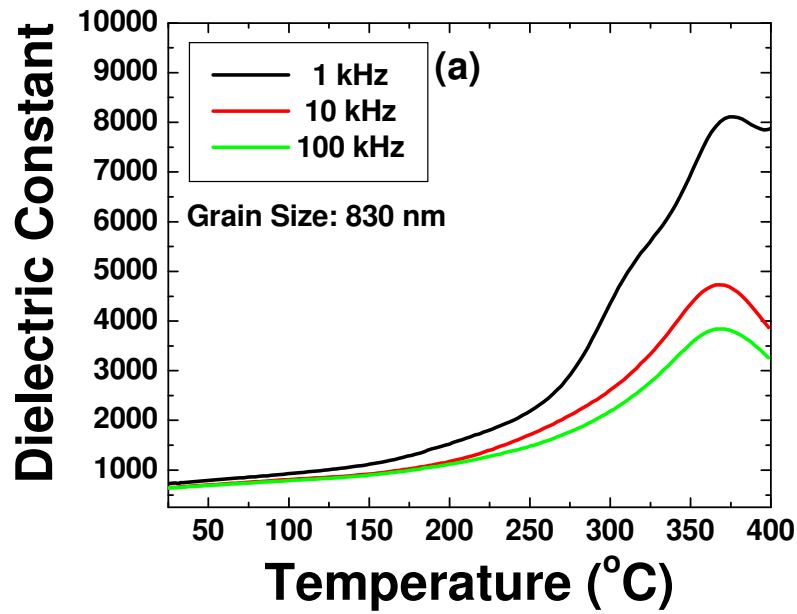


Figure 6.10: Dielectric properties as a function of temperature (a) dielectric constant for 830 nm, and (b) loss factor for 830 nm.

6.2.3 Variation of magnetization and coercivity for different grain size samples.

The magnetic properties of the composites with different grain sizes were found to be in the same range as shown in Table I. The saturation magnetization varied between 10.3 to 10.8emu/gm and the remnant magnetization varied between 0.71 to 0.88emu/gm. The coercive field for all the composites was between 62.2 to 75.1Oe. The data in Table 6.1 indicates that the variation in the magnetoelectric property of these composite will mostly depend upon the piezoelectric properties of the matrix.

6.2.4 Grainsize dependency of magnetoelectric properties of PZT – 20 NZF composite

Figure 6.11 (a) shows the variation of the ME voltage coefficient as a function DC bias field for different grain sizes. The magnetic field direction is perpendicular to the sample surface or parallel to the poling directions. For all the samples, as the bias field increases, ME coefficient increases and drops again. The optimum bias field is around 900 – 1000 Oe. As the grain size increases the optimum DC bias field slightly shifts towards higher field. Figure 6.11 (b) shows the grainsize dependency of ME coefficient. It was found that as the grain size decreases, ME voltage coefficient drops and shows similar trend as that of piezoelectric property. Above 200nm grain size, the ME voltage coefficient increases and it saturates at 600 nm grain size as shown in Fig. 6.9 (b). For the grain size of 97 and 830 nm the ME voltage coefficient was found to be as 54.4 and 157.5 mV/cm.Oe respectively. The results of this study demonstrate that grain size can be used to modulate the magnitude of piezoelectric and dielectric constant. Brown et. al. have shown from thermodynamic considerations that upper limit on the magnetoelectric susceptibility is given as: [123]

$$\alpha_{ij} < (\epsilon_{ij}\mu_{ij})^{1/2} \quad (6.1)$$

where α is magnetoelectric susceptibility, ϵ is dielectric permittivity, and μ is magnetic permeability. Equation (6.1) indicates that a high dielectric permittivity is required for larger

Table 6.1: Magnetic Properties of the composite as a function of average grain size.

| Grain size (nm) | Saturation Magnetization (emu/gm) | Remnant Magnetization (emu/gm) | Coercive field (Oe) |
|-----------------|-----------------------------------|--------------------------------|---------------------|
| 97 | 10.8 | 0.84 | 75.1 |
| 215 | 10.8 | 0.75 | 66.9 |
| 320 | 10.5 | 0.76 | 69.6 |
| 431 | 10.4 | 0.72 | 66.1 |
| 556 | 10.7 | 0.88 | 67.9 |
| 620 | 10.4 | 0.79 | 67.3 |
| 758 | 10.6 | 0.87 | 73.9 |
| 830 | 10.3 | 0.71 | 62.2 |

magnetolectric susceptibility. Zubkov has proposed the following expression for ME voltage coefficient (α_E): [124]

$$\begin{aligned}\alpha_E &= (dE/dH)_{\text{comp}} = (dS/dH)_{\text{comp}}(dE/dS)_{\text{comp}} \\ &= m_v (dS/dH)_{\text{ferrite}} (1-m_v) (dE/dS)_{\text{piezoelectric}}\end{aligned}\quad (6.2)$$

where m_v is the volume fraction of ferrite, (dE/dS) is the inverse of change in strain per unit electric field, and (dS/dH) is the change in strain per unit magnetic field. Since, $dE = g.dX$ and $dS = dX/C$, where X is the stress, S is strain, g is piezoelectric voltage constant, and C is the stiffness, Eq.(2) can be written as:

$$\alpha_E = m_v (dS/dH)_{\text{ferrite}} (1-m_v) (g_{ij}C_{ij})_{\text{piezoelectric}}\quad (6.3)$$

Assuming the deformation is occurring along the thickness direction and electric field is

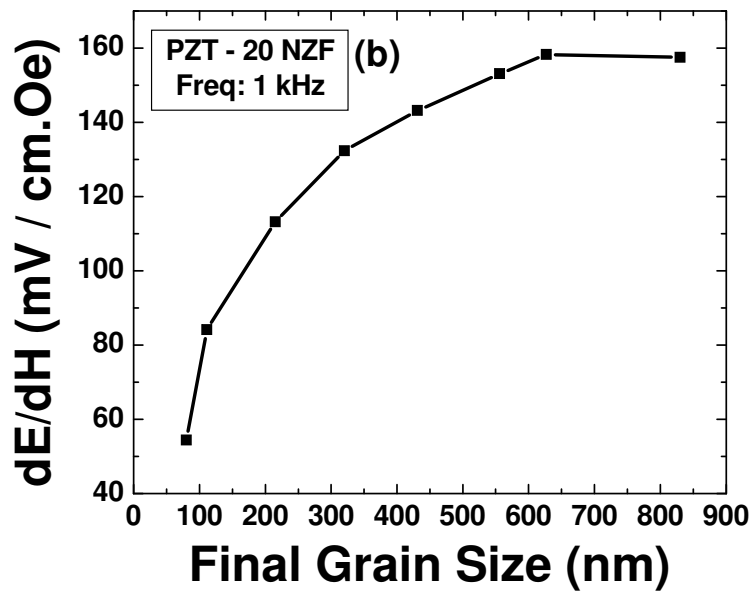
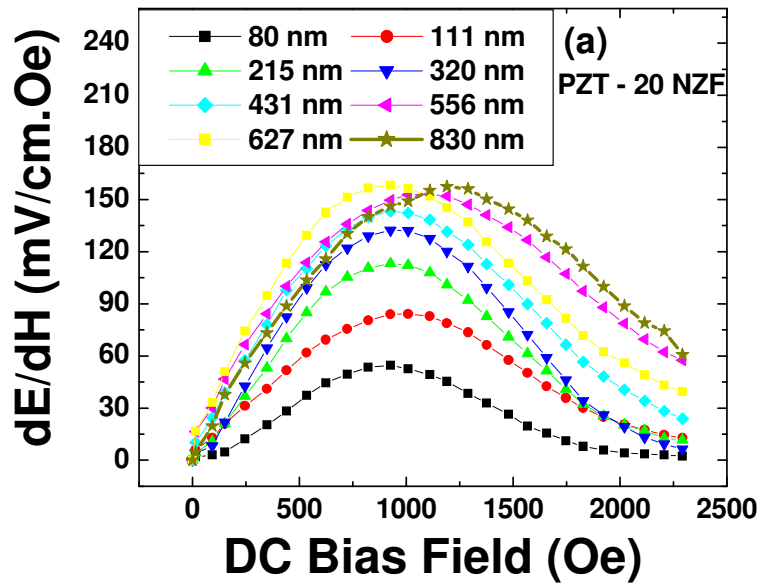


Figure 6.11: Magnetoelectric coefficient as a function of (a) DC bias field and (b) grain size.

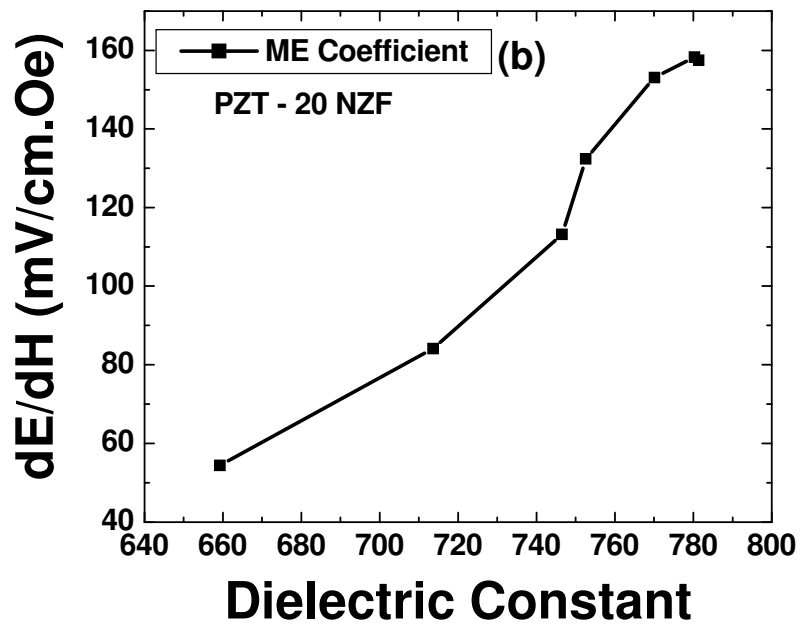
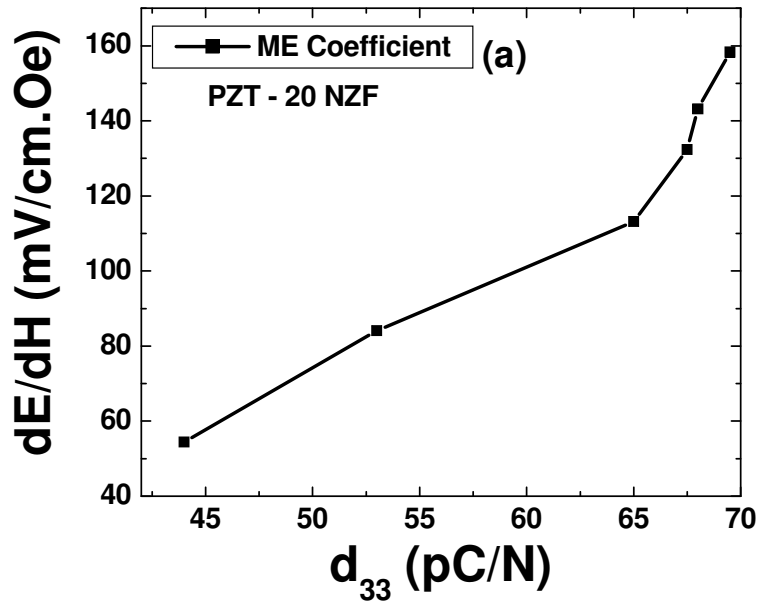


Figure 6.12: Magnetolectric coefficient as a function of (a) piezoelectric strain constant and (b) dielectric constant.

measured along the same direction, Eq. (6.3) can be approximated as:

$$\alpha_E = m_v (dS/dH)_{\text{ferrite}} (1-m_v) (g_{33}C_{33})_{\text{piezoelectric}} \quad (6.4)$$

Figure 6.12 (a) and (b) shows the variation of ME coefficient with piezoelectric constant and dielectric constant. It was found that as the piezoelectric and dielectric constant increases the ME coefficient increases. At larger grain size (above 600nm) where dielectric constant saturates to a value of 780, ME coefficient was also found to be saturated to a value of 155mV/cm.Oe. Using Eq.(4), the magnitude of magnetoelectric voltage coefficient can be approximated as following. The magnitude of (dS/dH) for common ferrite materials is of the order of 1×10^{-9} m/A (= 79.577×10^{-9} Oe⁻¹) [125], $m_v = 0.2$, and $C_{33} \sim 11 \times 10^{10}$ N/m². Substituting these values in Eq. (6.4), the magnetoelectric coefficient can be expressed in terms of piezoelectric voltage coefficient as [126]:

$$\alpha_E = 865.8 (g_{33})_{\text{piezoelectric}} \quad (6.5)$$

Figure 6.13 compares the plot of the ME voltage coefficient calculated using the data from Fig. 6.12 and Eq. (6.5) with that of experimental measurement. At lower grainsizes or lower magnitude of g_{33} , the magnitude of ME voltage coefficient shows similar trend as that predicted by Eq. (6.5). However, at higher grain sizes the magnitude of measured ME coefficient is higher than that predicted by Eq. (6.5). The derivation of expression (6.5) does not take into account any microstructure variable such domain size and grain boundary defect density. In general, the grain size is related to domain size through the expression: [127]

$$\text{Domain size} \propto (\text{Grain size})^m$$

where $m > \frac{1}{2}$ for grain size $< 1\mu\text{m}$. Thus, with increasing grain size the contribution from extrinsic effects, i.e., domain wall motion will increase which could provide some explanation for the enhancement of the ME coefficient. For the calculation of Fig. 6.13, the elastic stiffness was taken as a constant. However, it is known that elastic properties vary with the grain size and it should be accommodated in the model. In the derivation of Eq. (6.3) it was assumed that elastic properties of the PZT and ferrite phases are equal which needs to be revised.

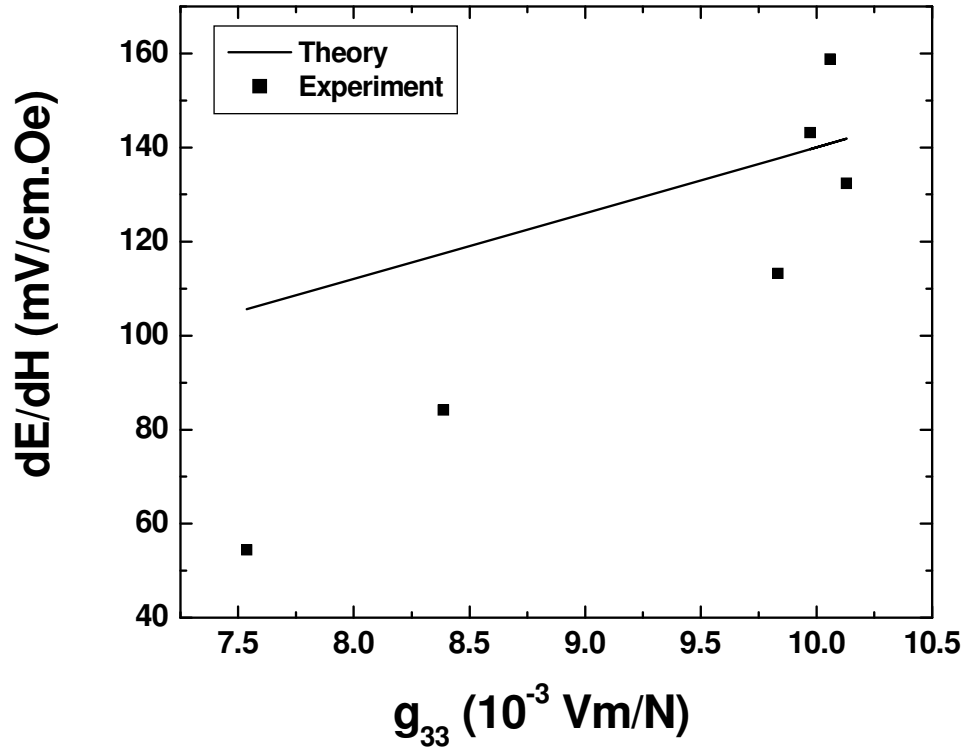


Figure 6.13: Comparison of the measured ME coefficient with that predicted from theory.

6.3 Chapter Summary

In this chapter the effect of grain size on magneto-electric coefficient of PZT – 20 NZF particulate composite was studied. A 3 D ball milling machine was used in order to synthesize the particles in size range of 100 – 300 nm. It was found that grain size has significant effect on the piezoelectric, ferroelectric and dielectric properties of the composite and hence influences the magneto-electric property. There is a critical grain size (150 – 200 nm) below which d_{33} , dielectric constant, g_{33} decreases rapidly, whereas these properties saturate at larger grain size above 600 nm. The ferroelectric Curie temperature was found to decrease from 377°C to 356°C as the average grain size decreases from 830nm to 111nm. There is no significant variation

observed in magnetic properties for these composites. Magnetoelectric coefficient is affected by the variation of piezoelectric and dielectric properties. Samples having grain size of around 100nm show small magnitude of ME coefficient (54.4 mV/cm.Oe) while those with grain size of 600nm exhibited magnitude of 155 mV/cm.Oe.

CHAPTER 7

EFFECT OF GEOMETRY ON MAGNETOELECTRIC COEFFICIENT

Recently, laminated magnetoelectric (ME) composites synthesized by using piezoelectric and magnetostrictive materials have gained attention because they exhibit superior ME response [36 – 53]. The laminates are generally fabricated by sandwiching and bonding piezoelectric plate/disk/fibers between two layers of magnetostrictive plates/disks/foils. In order to fabricate miniature sensors the approach based on co-firing is more attractive similar to that of multilayer ceramic capacitors. Srinivasan et al. have conducted several studies on multilayers of piezoelectric – ferrite system and shown promising results for ME response [40]. However, the ME response still remains weaker than that desired for practical applications. Further progress in tailoring the ME properties of the layered composites can be obtained by understanding the microstructural changes in the vicinity of the interface and by quantifying the effect of dopants.

7.1 Comparison Between Bulk (0 – 3) and Bilayer (2 – 2) Magnetoelectric Composites of $\text{Pb}(\text{Zr}_{0.56}\text{Ti}_{0.44})\text{O}_3$ - $\text{Ni}_{0.6}\text{Zn}_{0.2}\text{Cu}_{0.2}\text{Fe}_2\text{O}_4$ [PZT (H) – NCZF] System

The challenge in the synthesis of $\text{Pb}(\text{Zr},\text{Ti})\text{O}_3$ based cofired bilayer composites utilizing $(\text{Ni},\text{Zn})\text{Fe}_2\text{O}_4$ as ferromagnetic phase is the mismatch in sintering temperature and shrinkage rate which results in delamination. The addition of CuO to $(\text{Ni},\text{Zn})\text{Fe}_2\text{O}_4$ helps in reducing the sintering temperature by forming a liquid phase in early stages of sintering which dissolves in the matrix at the later stage [130]. Further, Cu-doped $(\text{Ni},\text{Zn})\text{Fe}_2\text{O}_4$ has been found to exhibit large grain size and higher density [131, 132]. Thus, 20 mole% CuO doped $(\text{Ni},\text{Zn})\text{Fe}_2\text{O}_4$ was selected as the ferromagnetic phase. For piezoelectric phase, hard PZT of the composition $0.98[0.9\text{Pb}(\text{Zr}_{0.56}\text{Ti}_{0.44})\text{O}_3 - 0.1\text{Pb}(\text{Zn}_{0.8/3}\text{Ni}_{0.2/3})\text{Nb}_{2/3}] + 0.02\text{MnO}_2$ [PZT (hard)] was selected since

this formulation has been shown to provide high piezoelectric voltage constant of 83×10^{-3} V-m/N [113].

7.1.1 Microstructural comparison of PZT(H) – NCZF bulk and bilayer composite

Figure 7.1 (a) shows the high magnification interface microstructure of cofired bilayer composite observed using Zeiss Leo Smart SEM on the polished and thermal etched samples. The PZT grain size in the vicinity of the interface was larger than the grains far away from the interface. Liquid phase sintering was found to occur in the PZT phase near the interface which may be associated to the diffusion of Cu at the interface and formation of low melting temperature phase. A low magnification microstructure of the interface showed the presence of porosity along the interface. Far from the interface, the microstructure was found to be dense on both sides. Fig 7.1 (b) shows the microstructure of bulk composite synthesized for comparison purposes under similar sintering conditions. PZT grain size observed in the bulk composite was in the range of 400 – 500 nm and the NCZF grains were in the range of 200 – 300 nm. The microstructure was dense with density higher than 98%.

Using SEM Inlens detector, it was found that there is columnar grain growth in PZT phase as shown in Fig. 7.2 (a) which indicates the presence of the liquid phase. EDX analysis of this region shows significant concentration of Cu atoms and by using SEM quadrant back scattering detector (QBSD) it was found that Cu atoms have diffused through the interface from NCZF side to the PZT side as shown in Fig. 7.2 (b). Near the interface there is a thin region where the presence of ferrite clusters is observed. As the distance from the interface increases towards PZT layer, the concentration of ferrite particles decreases which is expected. Careful observation revealed a contrast in ferrite layer near the interface which investigated by point EDX indicated that the light contrast is Cu-rich phase whereas the dark contrast is the NCZF.

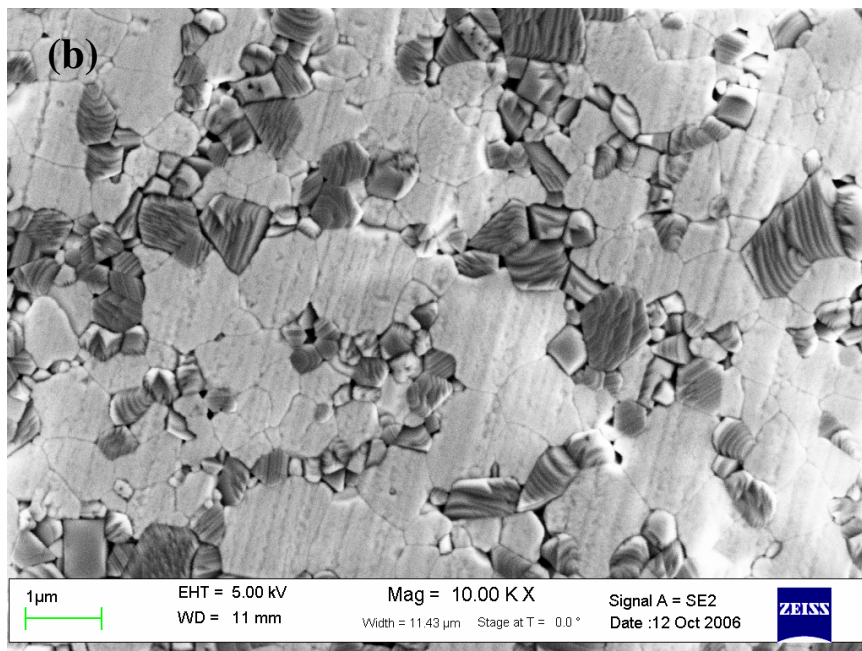
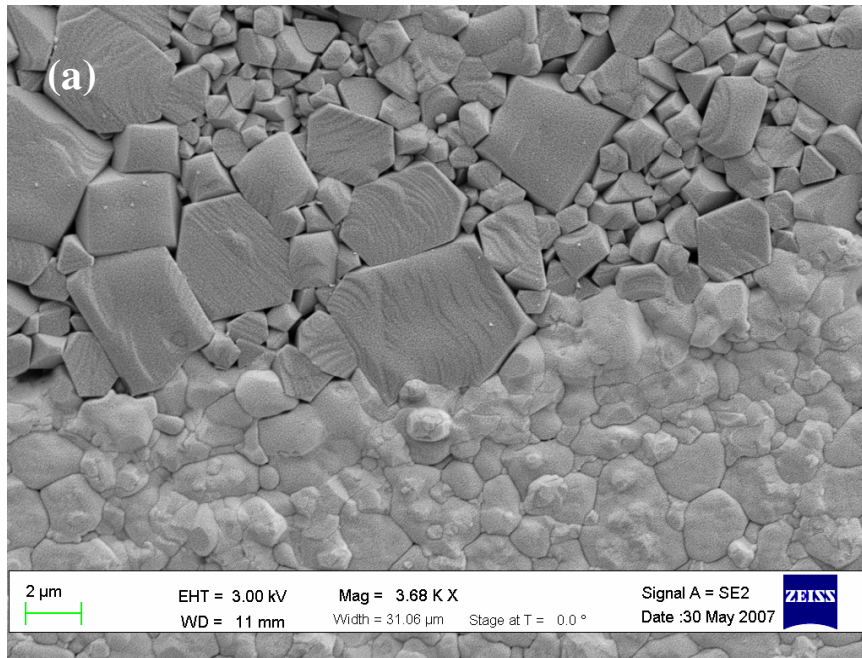


Figure 7.1: Microstructure of bilayer and bulk composites, (a) bilayer composite and (b) bulk composite.

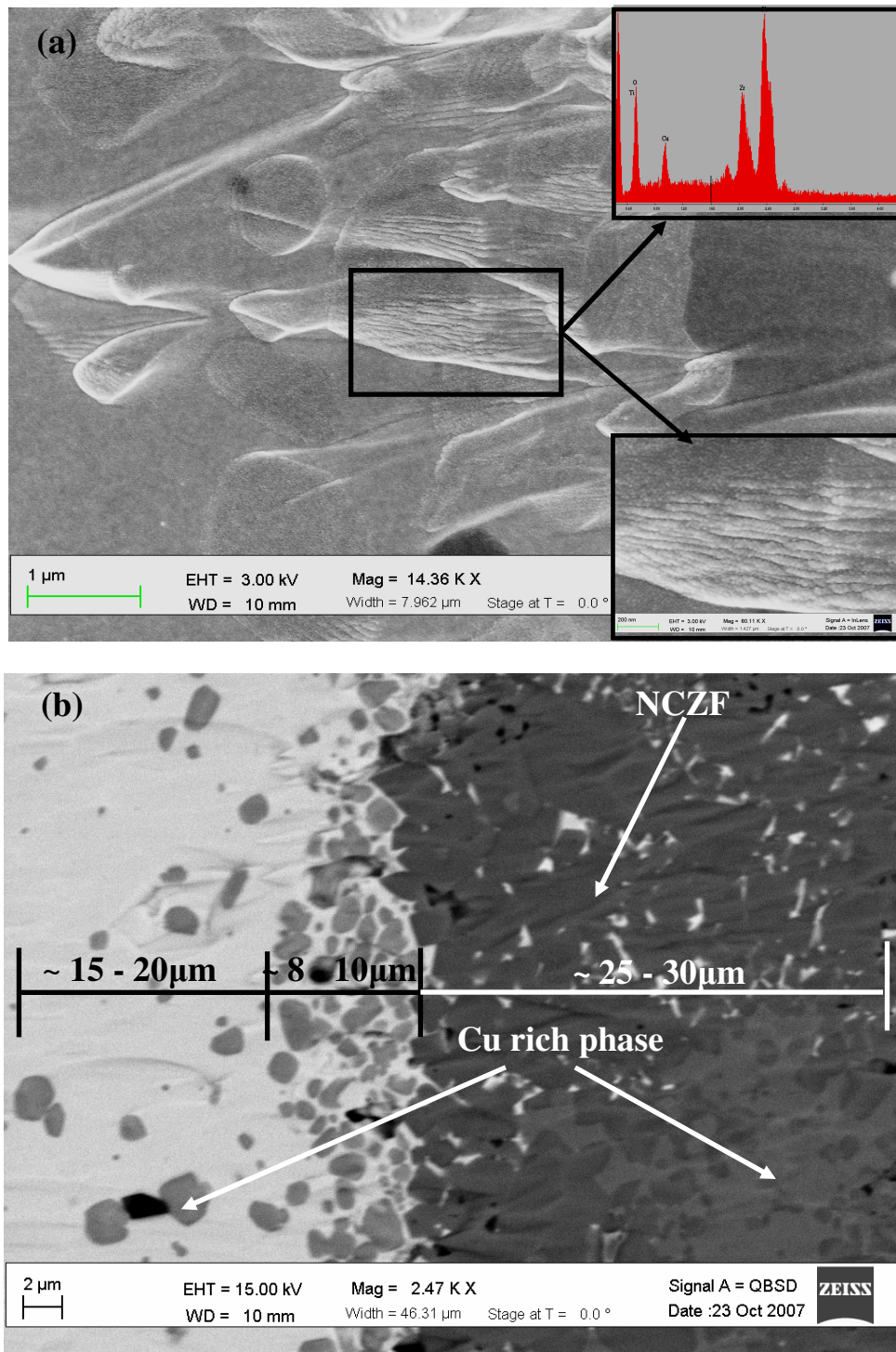


Figure 7.2: Microstructure of bilayer bulk composites using (a) Inlens detector, (inset: magnified view and EDS pattern) and (b) quadrant back scattering detector.

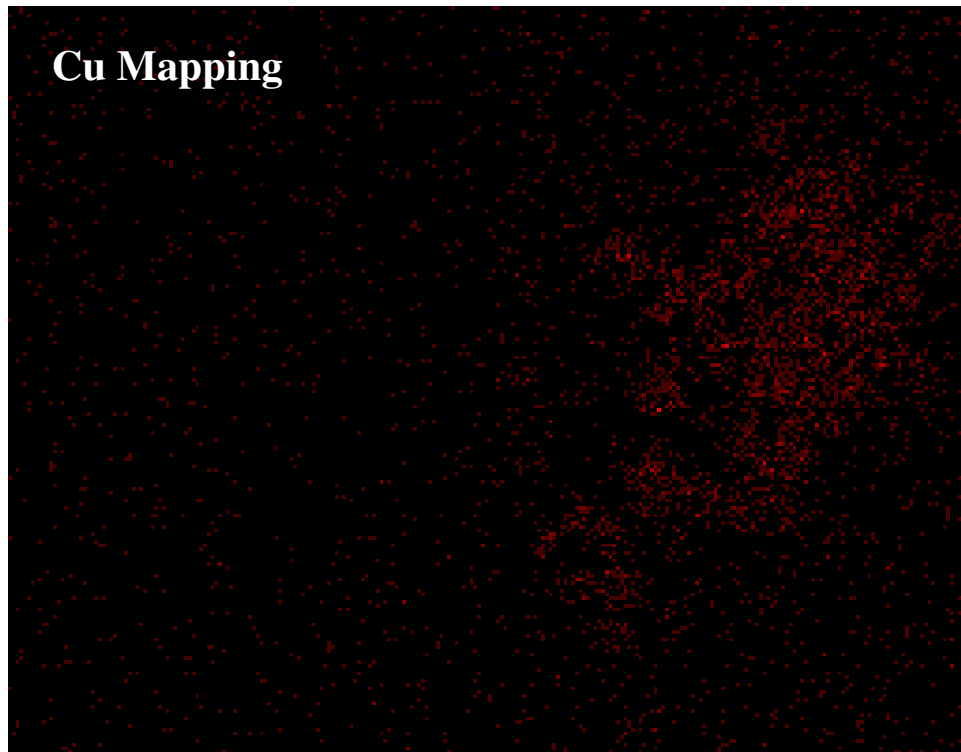
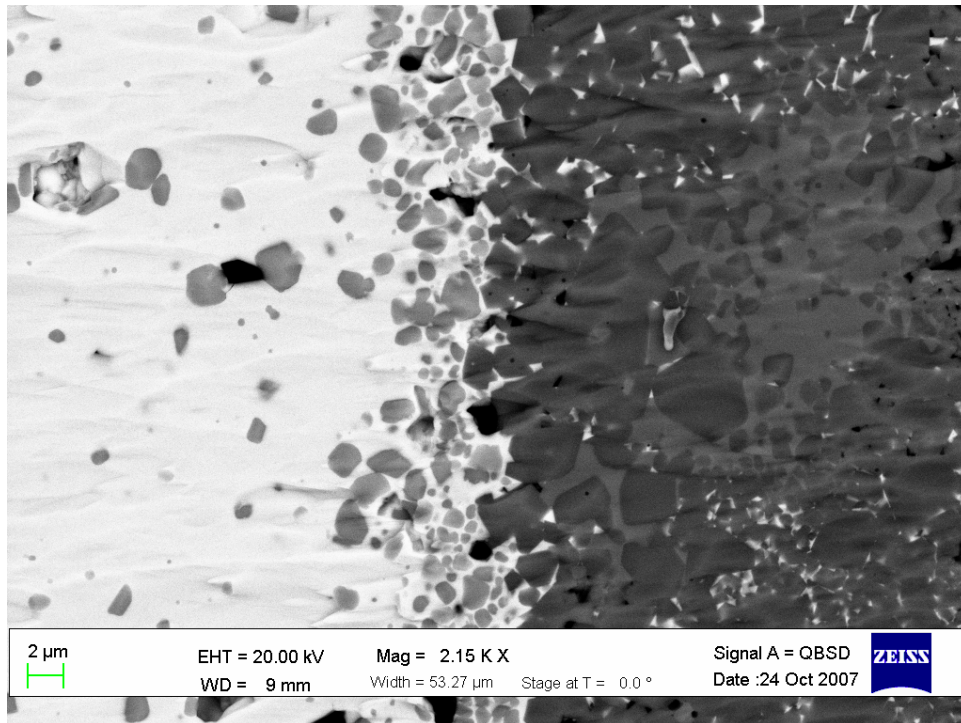


Figure 7.3: Cu elemental mapping in the vicinity of the interface.

Based on these results it is hypothesized that there is a finite concentration of Cu rich phase formed near the interface. An SEM elemental mapping of Pb, Zr, Ni, Fe and Cu was conducted near the bilayer interface as shown in Fig. 7.3. The interface was found to exhibit sharp concentration gradients with slight diffusion of Pb in NCZF phase and Ni in PZT phase. Increased concentration of Cu was found in the PZT phase close to interface which may be responsible for the liquid phase sintering. This Cu may be present as $\text{Cu}_2\text{O}/\text{CuO}$ or CuFe_2O_4 . X-ray elemental mapping of Cu atoms showed that the region with light contrast is rich in Cu as observed in Fig. 7.3. The phase diagram for $\text{Cu}_2\text{O}/\text{CuO}$ and PbO shows that there is a eutectic point around 1008K (735°C) [18-19]. Thus the presence of excess PbO and $\text{CuO}/\text{Cu}_2\text{O}$ can produce liquid phase. Figure 7.1 (a) shows the evidence for the liquid phase sintering. We can also hypothesize that $\text{CuO}/\text{Cu}_2\text{O}$ reacts with the Fe_2O_3 to form non-stoichiometric CuFe_2O_4 as it is possible that this reaction occurs in Fe_2O_3 rich environment [20]. Based on Fig. 7.2 and 7.3 we can propose that at the interface there is presence of $\text{PbO}-\text{CuO}/\text{Cu}_2\text{O}$ eutectic phase and non-stoichiometric CuFe_2O_4 which forms a gradient structure given by PZT-PZN/Cu-ferrite/NCZF. Careful investigation of Fig. 7.2 (b) shows that the migration of the ferrite into PZT – PZN occurs over a distance of 25 – 30 μm . The 8 - 10 μm thickness layer adjacent to the interface has high concentration of Cu rich phase. We estimate the overall thickness of the interface layer as $\sim 50 \mu\text{m}$. Next, we try to understand the effect of this gradient structure on the ferroelectric, ferromagnetic and magnetoelectric properties.

7.1.2 Ferroelectric and dielectric properties of PZT(H) – NCZF bulk and bilayer composite

Figure 7.4 (a) shows the ferroelectric properties of the cofired bilayer composite. High polarization of $60\mu\text{C}/\text{cm}^2$ and strain of 0.1% was recorded at an applied electric field of 4.5kV/mm. The longitudinal piezoelectric constant, d_{33} , was measured using Berlincourt meter and was found to be of the order 80 pC/N. The P – E loop for the bulk composite was significantly weak compared to the bilayer as shown in Figure 7.4 (b). The edges of the loop near the saturation voltage were rounded which signifies the drop in resistivity. This is expected

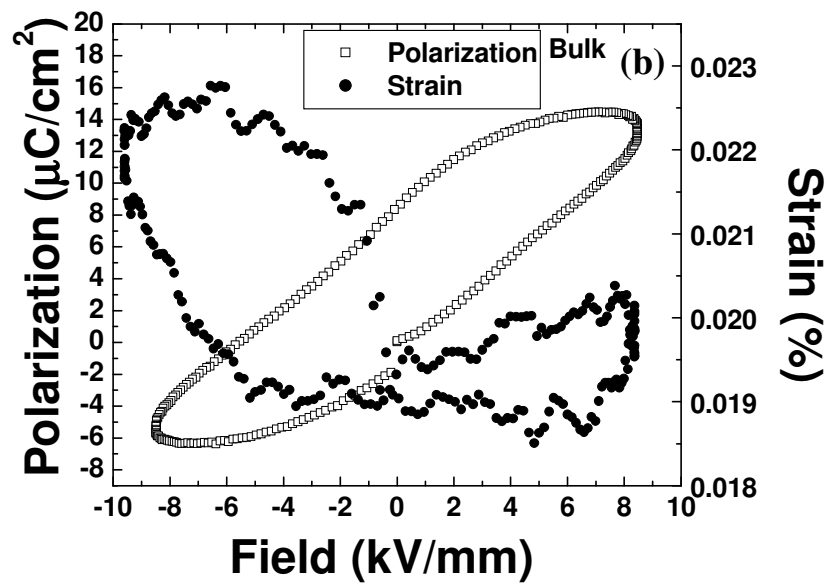
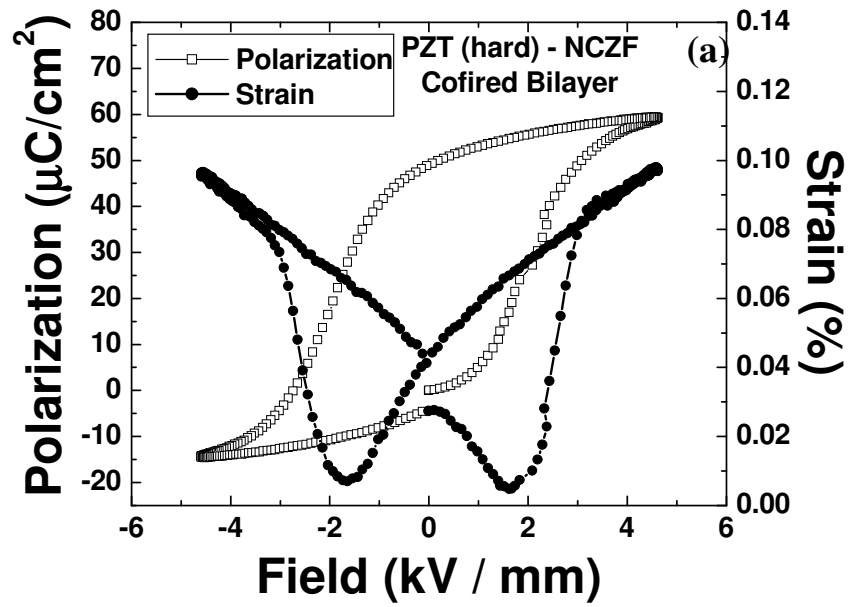


Figure 7.4: Ferroelectric loop of PZT – NCZF composite, (a) cofired bilayer composite and (b) bulk composite.

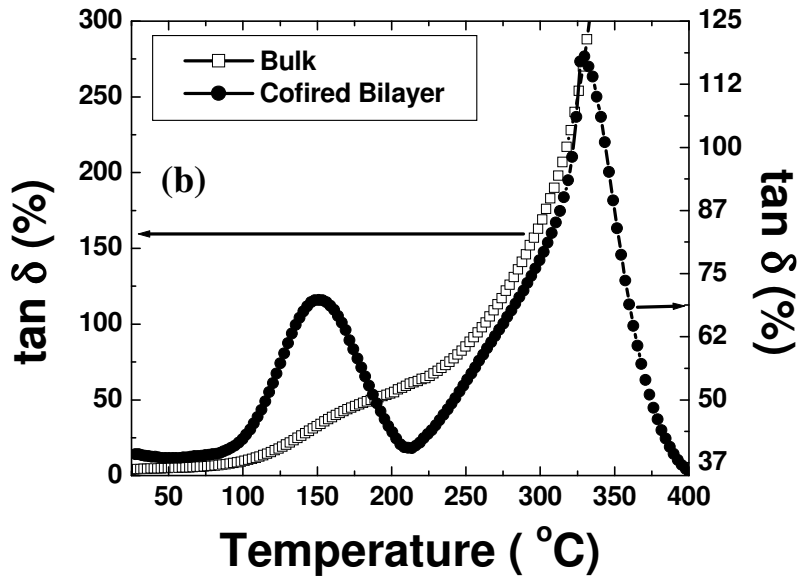
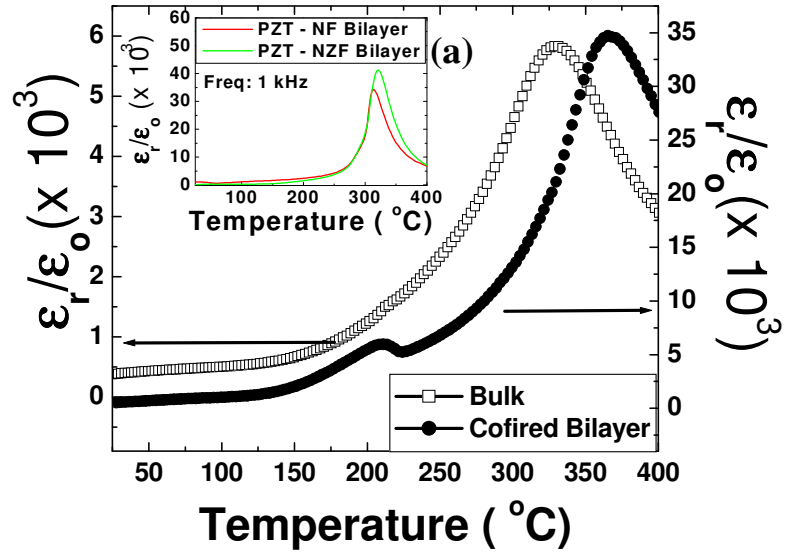


Figure 7.5: Dielectric properties of bulk and bilayer as a function of temperature, (a) dielectric constant (inset: dielectric constant vs. temperature of PZT – NF and PZT – NZF bilayer) and (b) dielectric loss.

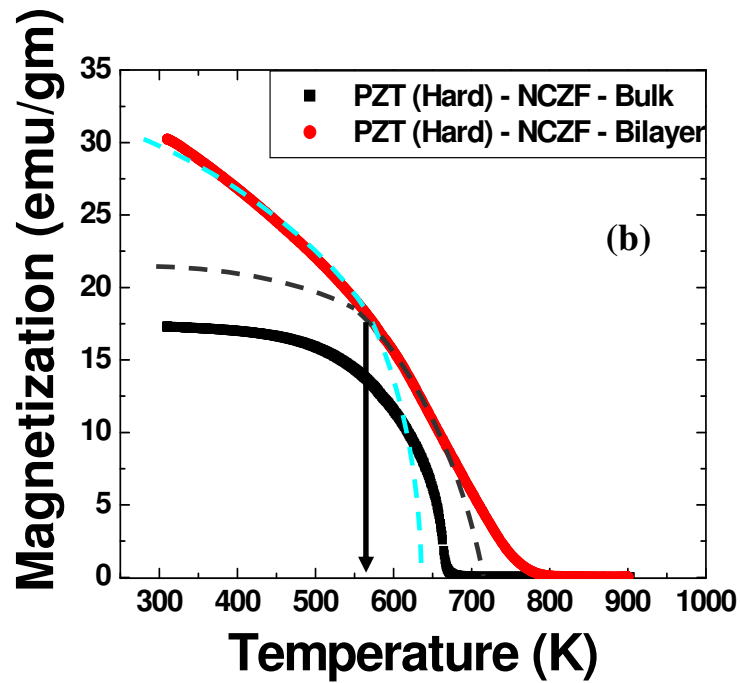
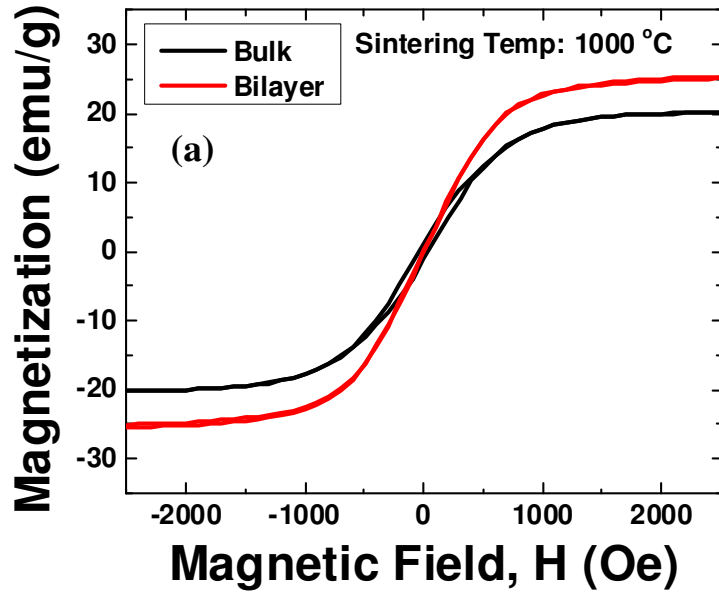


Figure 7.6: Ferromagnetic property of two types of composite. (a) Moment vs. Field (hysteresis loop) and (b) magnetization as a function of temperature.

due to the high concentration of Cu atoms. The saturation polarization of $16\mu\text{C}/\text{cm}^2$ and strain of 0.022% was recorded at high electric field of 8 kV/mm. The d_{33} magnitude was also found to be very low for the particulate sintered composite of the order of 25 - 27 pC/N. The results clearly show that the gradient structure in bilayer does results in improved ferroelectric and piezoelectric properties. In order to further elucidate the effect of the gradient structure we measured the dielectric and magnetic properties which could show if there is any change occurring in the phase symmetry or if there is any averaging of properties.

Figure 7.5 (a) and (b) compares the dielectric constant and dielectric loss of the bulk and bilayer composites over a wide range of temperature. The ferroelectric Curie temperature for the bilayer composite was found to be $\sim 355^\circ\text{C}$ which is higher than that for bulk composites $\sim 325^\circ\text{C}$. A notable distinction in the dielectric response can be seen in the temperature range of $200\text{-}225^\circ\text{C}$ where bilayer composite exhibits a secondary peak. To confirm this result, the test was repeated three times with three different samples and every time the peak was observed. Inset compares the dielectric response of Mn-modified PZT - NiFe_2O_4 and PZT - $\text{Ni}_{0.7}\text{Zn}_{0.3}\text{Fe}_2\text{O}_4$ bilayers with that of the PZT-PZN-NCZF. It can be noted that the PZT – ferrite bilayers with no CuO didn't show the secondary peak in dielectric spectra. The dielectric loss behavior of the bilayer composite also exhibited secondary peak at the temperature of $\sim 160^\circ\text{C}$. This data combined with that of SEM analysis does indicate the possibility of secondary phase formation at the interface or stabilization of a metastable phase.

7.1.3 Comparison of magnetic moment between bulk and bilayer composite

Figure 7.6 (a) compares the magnetization – magnetic field hysteresis curve of bilayer and bulk composites measured with an alternating gradient magnetometer (AGM) up to 1.4T. It was found that the saturation magnetization (M_s) is higher in bilayer composite than the bulk and the coercivity (H_c) drops from 43Oe to a very low magnitude of 2.8Oe. Figure 7.6 (b) shows the temperature dependence of magnetization for bilayer and bulk composites measured in a high-temperature oven installed with Quantum design physical property measurement system

(PPMS). The magnetic Curie temperature (T_c) was determined from the intersection of extrapolations of the greatest slope and flat region above T_c . It was found that T_c of the bilayer composite is higher than that of bulk composite. It can be noticed from Fig. 7.10(b) that the magnetization-temperature behavior of the bilayers shows a change in slope at 530K ($\sim 257^\circ\text{C}$). This temperature range is similar to where peak in the dielectric behavior was observed, as shown in Fig. 7.5(a). The results of Fig. 7.5 and 7.6 together indicate the presence of secondary phase in the bilayer composites which is reflected both in dielectric and magnetic properties. This transition could be related to the presence of $\text{Cu}_2\text{O}/\text{CuO}$ or a 2nd ferromagnetic phase evolving from CuFe_2O_4 which forms a gradient composite structure with the PZT. Shrotri et. al. have shown that doping above 20 mole% Cu in $(\text{Ni,Zn})\text{Fe}_2\text{O}_4$, makes it unstable and at first CuO starts to form followed by a secondary phase corresponding to the formulation CuFe_2O_4 [137, 138]. The free CuO if present on the piezoelectric side will react with the PZT-PZN to form low temperature melting composition which is commonly observed in the low temperature sintering of ceramics. CuO is a common liquid phase sintering agent in that case. The composite of this low temperature melting phase and CuFe_2O_4 phase may be associated with the transitions observed in the PZT – NCZF composites though more careful studies using high temperature X-ray diffraction are required to confirm this hypothesis. The magnetization vs. temperature behavior for bilayer composites can be resolved as summation of two curves, shown by different colored dashed line in Fig. 7.6 (b). CuFe_2O_4 has a Curie temperature of 743K [139] and the dashed line (dark blue) indicates the Curie temperature of around 720 – 730K. The 2nd line (light blue) corresponds to the $(\text{Ni,Zn})\text{Fe}_2\text{O}_4$, which has a Curie temperature of about $\sim 640\text{K}$. This value approximately corresponds to the curie temperature of $\text{Ni}_{0.65}\text{Zn}_{0.35}\text{Fe}_2\text{O}_4$ [109]. Thus, the overall magnetic response is average of the individual contributions from CuFe_2O_4 and $\text{Ni}_{0.65}\text{Zn}_{0.35}\text{Fe}_2\text{O}_4$ proportional to the volume fraction.

7.1.4 Effect of gradient composite microstructure on magnetoelectric properties

Figure 7.7 (a) compares the magnetoelectric (ME) coefficient of Mn-modified PZT – NCZF bilayer and bulk composite. The bilayer composite shows much higher ME coefficient of ~200 mV/cm.Oe whereas the ME coefficient of bulk composite is around 120 mV/cm.Oe. The DC bias field at which the composites show maximum ME coefficient is in the range of 900 – 1200 Oe. This value corresponds to the saturation magnetostriction value of the NCZF phase. The reason behind higher ME coefficient can be attributed to better piezoelectric (d_{33}), ferroelectric polarization, and magnetization of the bilayers. Further, bilayer composites have smaller coercivity as compared to bulk. We also think that the gradient structure obtained in this particular system (PZT-PZN/CuFe₂O₄/ Ni_{0.65}Zn_{0.35}Fe₂O₄) plays role in the higher ME response. The gradient structure reduces the mismatch in the mechanical impedance which facilitates the strain transfer. Further, it influences the magnitude of the magnetostrictive strain. One way to further enhance the magnitude of the ME coefficient will be to allow the formation of the higher volume fraction magnetostrictive phase at the interface. This could reduce the defects at the interface layer and further enhance the coupling. This may also increase the magnitude of dielectric constant at the room temperature which will result in higher ME coefficient. Figure 7.7 (b) shows the frequency dependence of ME coefficient under a 200Oe DC field. It was found that at resonance frequency in the range of 200 – 300 kHz, both the composites show a sharp peak in magnetoelectric coefficient. The bulk composite shows maximum response of 11 mV/cm.Oe whereas bilayer exhibits 43 V/cm.Oe.

7.2 Chapter Summary

This chapter introduced the cofiring technique for synthesizing bilayer ME composite. A detailed comparison between bulk (0 – 3) and bilayer (2 – 2) composite of PZT (H) – NCZF composite was conducted in order to see the effect of geometry in sintered composites. It was found that

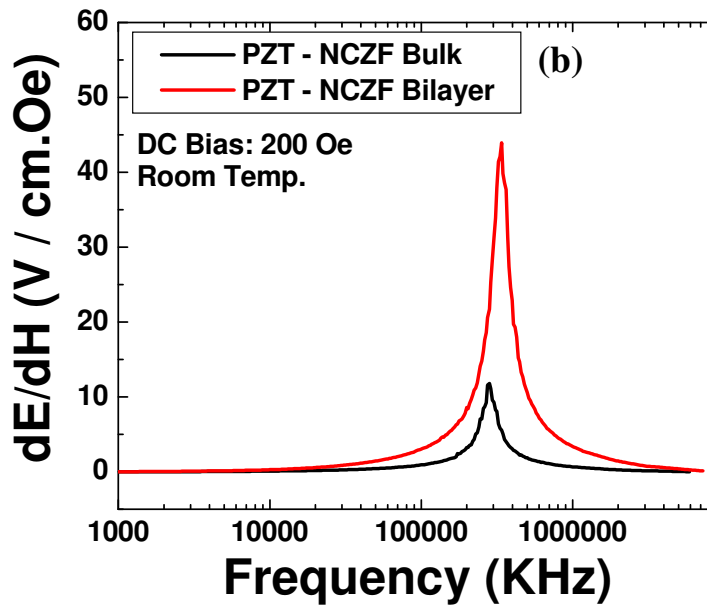
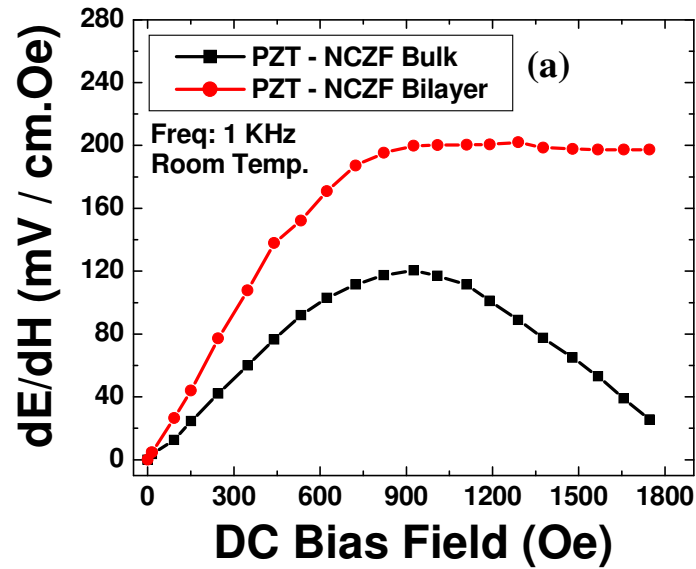


Figure 7.7: ME coefficient of PZT – NCZF bilayer and bulk composite. (a) ME coefficient as a function of DC bias in T – T mode, (b) ME coefficient as a function of frequency.

CuO results in the formation of the secondary CuFe_2O_4 phase at the interface. It was also noticeable that Cu rich phase migrates into the PZT phase through the interface, which results in gradient microstructure. The gradient structure induces changes in the dielectric and magnetic characteristics. The formation of secondary phase enhances the Curie temperature and saturation magnetization, which contributes to the enhanced magnetoelectric coefficient. The (2 – 2) composite were found to exhibit better ferroelectric, dielectric and magnetoelectric properties compared to that of (0 – 3) composite.

The interface characteristics between the piezoelectric and magnetostrictive phase are of fundamental interest as their elastic characteristics affects the ME coupling. The next chapter addresses the post-sinter heat treatment process which can provide a method for changing the properties of the interface.

CHAPTER 8

EFFECT OF POST SINTER HEAT TREATMENT ON MAGNETOELECTRIC COEFFICIENT OF SINTERED PARTICULATE COMPOSITE

Co-firing of piezoelectric and magnetostrictive phases at high temperature induces strain in the sintered composite due to lattice and thermal mismatch. Thus, a post sintering heat treatment is necessary to homogenize the matrix grain structure, reduce the strain and remove the chemical or stress gradients at the interface. It has been shown that piezoelectric and dielectric properties of sintered ceramics improve after annealing [reference]. Annealing also enhances the magnetostrictive properties of some common ferrites such as CoFe_2O_4 . The annealing and aging technique for this reason has been used in fabricating materials with strong permanent magnetism [141, 142]. In this case, precipitates with soft magnetic nature are dispersed in a hard magnetic matrix, resulting in one of the best hard magnets [reference]. This chapter investigates the annealing and aging technique for synthesizing ME composites with the objective of achieving a strong coupling between ferroelectric and magnetic order parameters.

8.1 Effect of annealing and aging

Figure 3.3 (a) shows the post sinter thermal treatment used in this study (henceforth, thermal treatment in this thesis will refer to the annealing, quenching and aging cycle). The unidirectional quenching was achieved by enclosing the samples in an alumina tube and rapidly moving the tube out of the hot zone in the furnace.

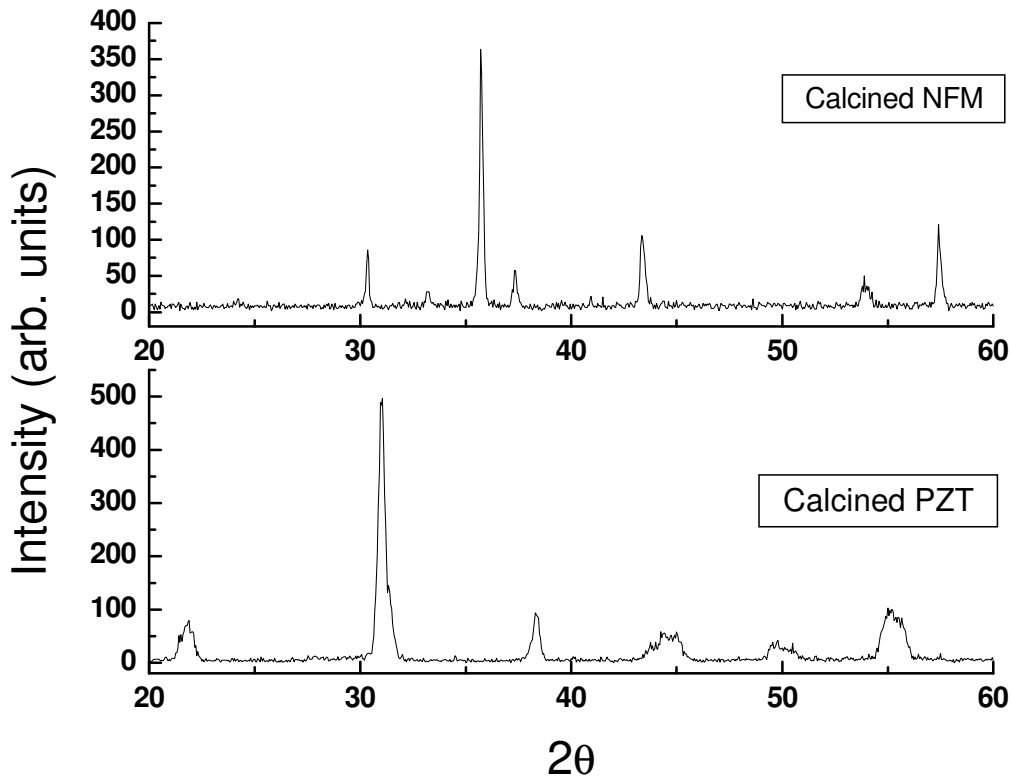


Figure 8.1: X-ray diffraction patterns of calcined PZT and NFM.

8.1.1 Phase Analysis of sintered, annealed and aged PZT – NFM composites

The phase equilibrium diagram for the system Pb-Ti-Zr-Ni-Fe-O is not documented in literature. Thus, initially a simple phase analysis using XRD was performed to find the phase distribution in binary system PZT - $\text{NiFe}_{1.9}\text{Mn}_{0.1}\text{O}_4$ (NFM). Figure 8.1 shows XRD patterns of calcined PZT (750°C for 2 hrs) and calcined NFM powder (1000°C for 5 hrs). The XRD patterns of these calcined powders had pure perovskite and spinel phase with no sign of incomplete reaction. The perovskite phase showed the tetragonal symmetry as evident by the minor splitting in 200/002 peaks. Figure 8.2 shows the XRD patterns of composite samples sintered at 1125°C for 2 hrs. A pure perovskite phase was obtained with small fraction of spinel phase.

Other than perovskite and spinel, no other phase was detected within the limits of the instrument. PZT composition corresponding to Zr:Ti = 52:48 was selected as it is closer to the morphotropic phase boundary (MPB) providing high piezoelectric property. Recently presence of monoclinic phases has been reported near the MPB, however for simplicity MPB will be considered as the separation between the rhombohedral and tetragonal phases [145]. On modification with NFM the perovskite phase was found to exhibit rhombohedral symmetry as shown by reduced splitting of 200/002 peaks. Figure 8.2 also shows the calculation of the area under the perovskite and spinel peak (by integrating the plot of

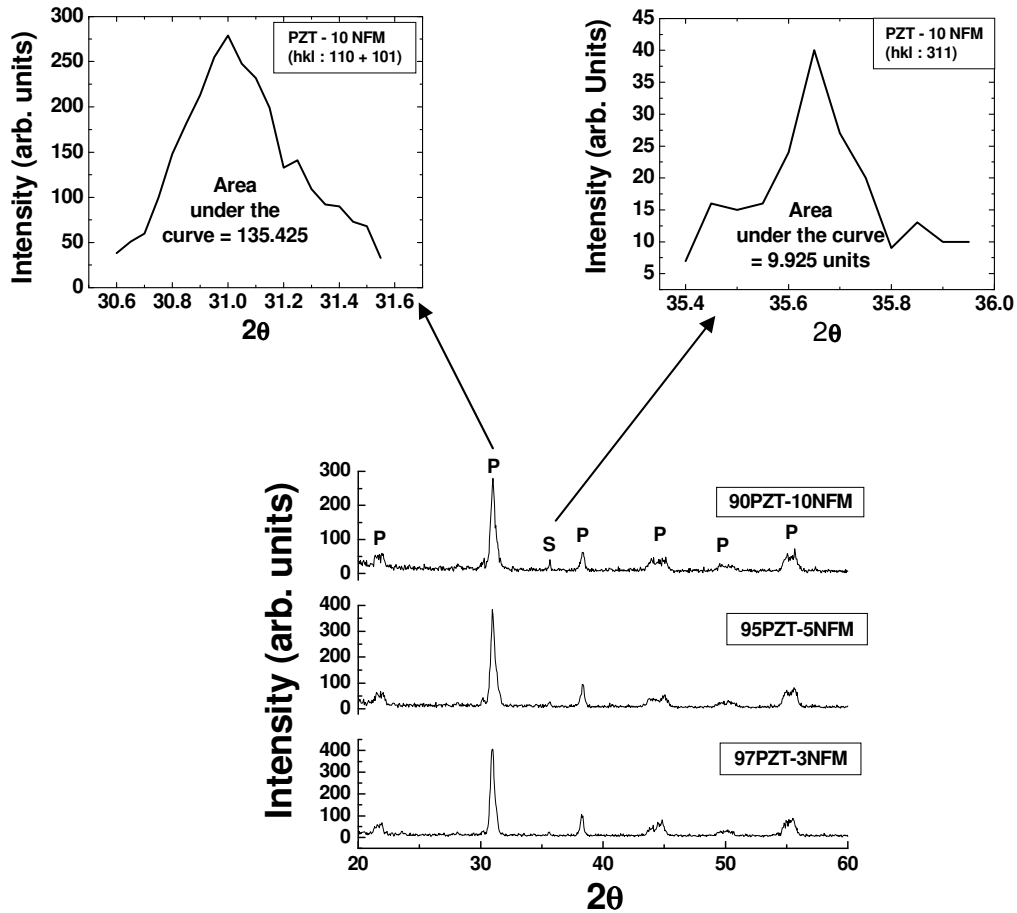


Figure 8.2: X-ray diffraction patterns of as-sintered (1-x) PZT-x NFM samples for 2 hrs at 1125°C

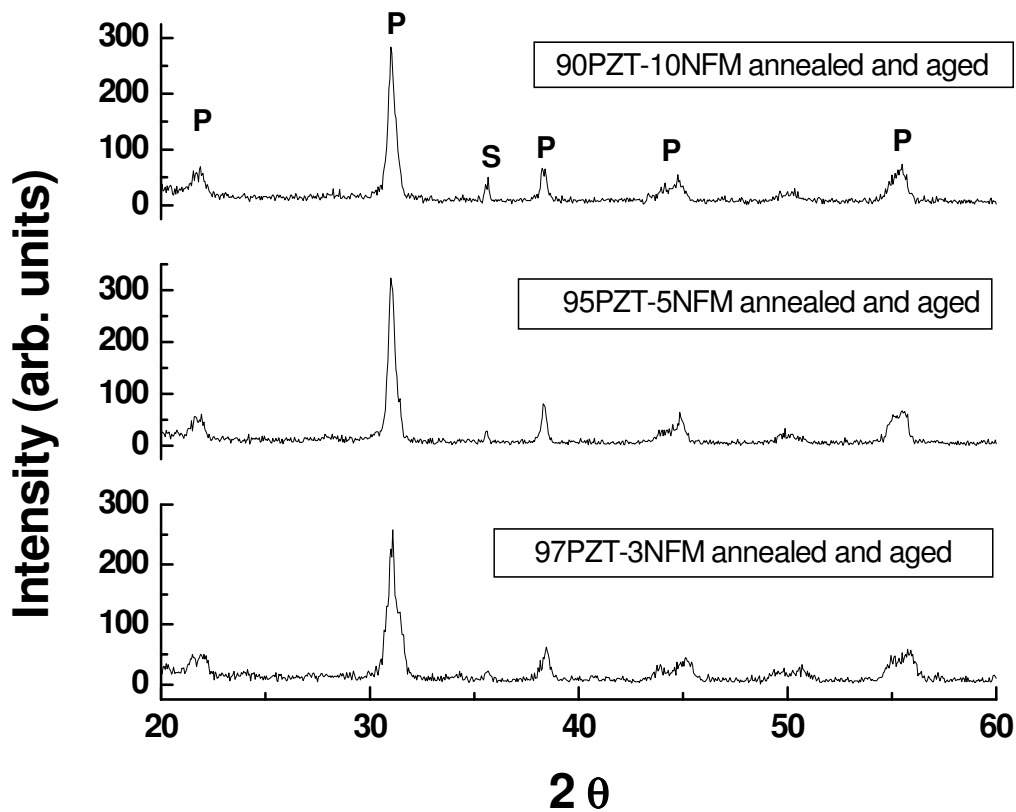


Figure 8.3: X-ray diffraction patterns of (1-x) PZT-x NFM composite - sintering followed by annealing at 800°C for 10 hrs and then aging at 400°C for 5 hrs.

selected range). As expected, a higher sintering temperature resulted in higher content of spinel phase. All the sintered samples exhibited high density (Table 8.1) and as the mole% NFM increases the density also increases due to better compaction and sinterability. Figure 8.3 shows the XRD pattern for same samples after annealing at 800°C for 10 hrs and then aging at 400°C for 5 hrs. It can be clearly seen in this figure that there is increase in the fraction of spinel phase. The fraction of the spinel phase present was computed using the expression:

$$\% \text{ spinel} = \frac{\text{Area under the spinel peak (311)}}{\text{Area under the perovskite peak } \{(110) + (101)\} + \text{Area under the spinel peak (311)}} \times 100$$

(8.1)

Table 8.1: Variation of density for two different sintering temperatures.

| NFM Mole% | Density(gm/cm ³) | |
|-----------|------------------------------|--------------------|
| | Sintered at 1100°C | Sintered at 1125°C |
| 3 | 7.26 | 7.38 |
| 5 | 7.63 | 7.7 |
| 10 | 7.75 | 7.81 |

For all three compositions studied in this thesis, a considerable increase of spinel phase was obtained after annealing followed by aging. PZT- 10 NFM sintered at 1125 °C showed an increment of spinel content of 1.03% (from 6.82% after sintering to 7.85% after annealing and aging). This is a considerable increase considering the difference in the lattices of two phases. As the sintering time was varied no other phases were detected. Comparing this result with the thermal treatment, it can be hypothesized that there is possibility of homogenization in the PZT – NFM system.

8.1.2 *Ferroelectric, piezoelectric and dielectric properties of thermally treated PZT – NFM composites*

Figures 8.4 – 8.6 shows the polarization – electric field (P-E) and strain – electric field (S-E) bipolar loops for all the samples sintered at 1100 °C before and after thermal treatment (post sintering). The P-E loop is slim in the negative field region and wide in the positive

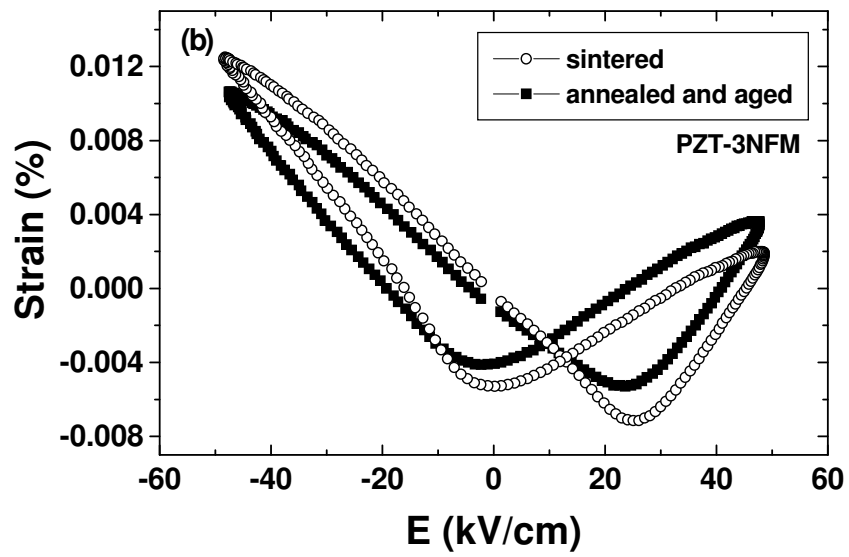
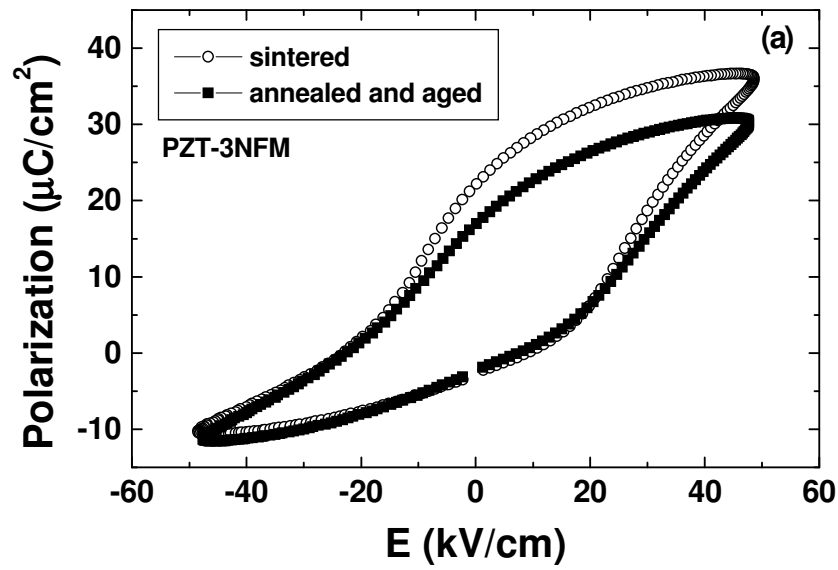


Figure 8.4: Polarization – electric field (P-E) and strain – electric field (S-E) bipolar loops for all the three composition before and after the thermal treatment for the samples sintered at 1100 oC. (a) and (b) PZT – 3 NFM,

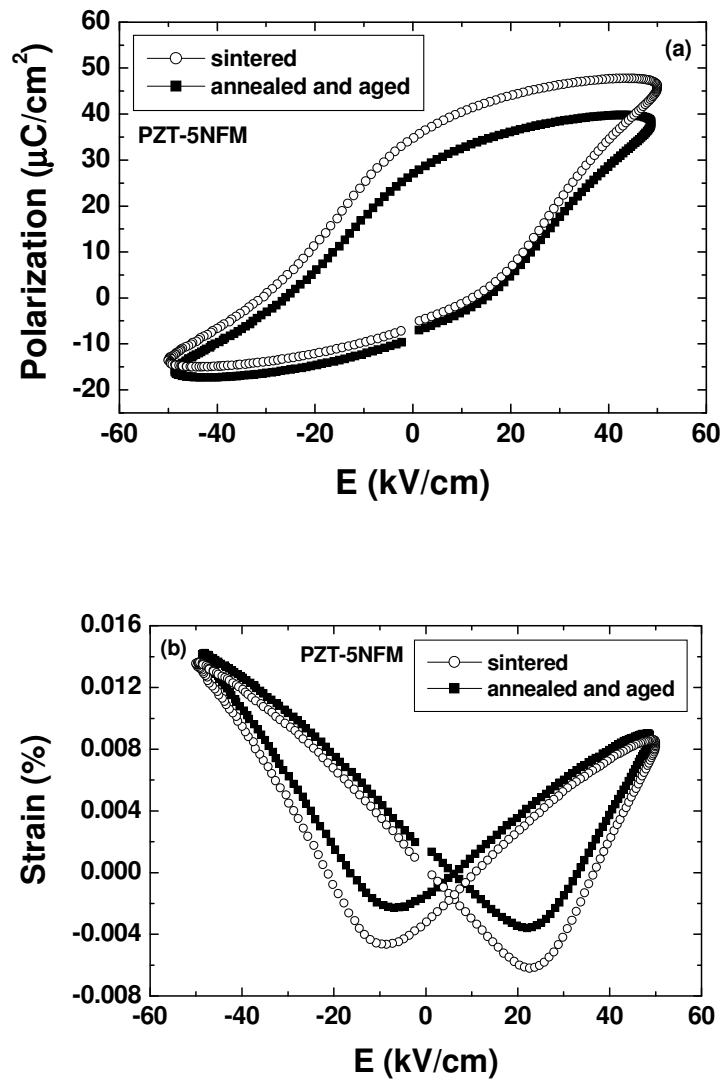


Figure 8.5: Polarization – electric field (P-E) and strain – electric field (S-E) bipolar loops for all the three composition before and after the thermal treatment for the samples sintered at 1100 oC. (a) and (b) PZT – 5 NFM,

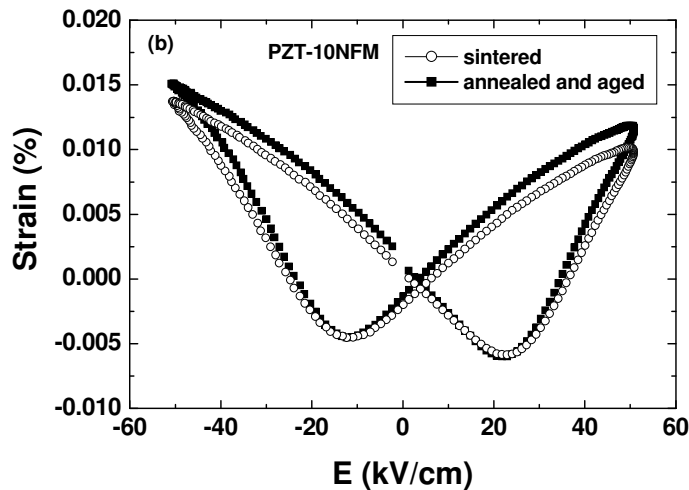
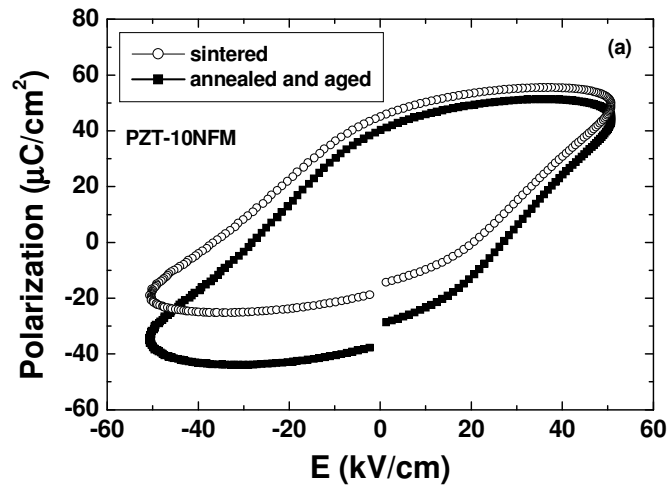


Figure 8.6: Polarization – electric field (P-E) and strain – electric field (S-E) bipolar loops for all the three composition before and after the thermal treatment for the samples sintered at 1100 oC. (a) and (b) PZT – 10NFM.

field region. The reason is associated with the presence of the oxygen vacancies [146 – 148]. In the case of PZT-10NFM, the P-E loop is wider in the negative region and broader at the tip, which is associated with lower resistivity of this composition. The polarization decreases after thermal treatment in the case of PZT-3NFM and PZT-5NFM while it remains of the same order in the case of PZT-10NFM. The total polarization under field is given as $P = P_s + \epsilon E$, where P_s

is the spontaneous polarization of the materials, ϵ is the dielectric constant and E is the electric field. The decrease in the magnitude of P is related to the decrease either in P_s or low field dielectric constant. The dielectric constant magnitude depends upon two factors (i) magnitude of the internal stress governed by the fraction of the spinel and perovskite phase present in composite, and (ii) domain structure. It is possible that during annealing the oxygen vacancies migrate to the surface where they are compensated resulting in domain growth. For the PZT-5NFM samples, the magnitude of the positive and negative remanent polarization (P_r) was $+27 \mu\text{C}/\text{cm}^2$ and $-7.5 \mu\text{C}/\text{cm}^2$ respectively. They are quite high for the composites.

The S-E plots for the both the cases, as sintered and thermally treated samples, showed similar behavior. The magnitude of strain under a electric field is given as $S = QP_s^2 + dE + Q(\epsilon E)^2$ (where piezoelectric constant, $d = 2QP_s\epsilon$). The electric field dependence of the strain can be explained by taking into account the reverse behavior of dielectric and piezoelectric constant, (piezoelectric constant increases while the dielectric constant decreases after thermal treatment). Figure 8.7 (a) shows the variation of the piezoelectric constant with NFM mole%. With increasing NFM concentration, d_{33} decreases due to the decrease in the perovskite phase [149]. The piezoelectric constant increased after the thermal treatment for two different sintering conditions. For the PZT – 5NFM samples, the increase was 14% in the case of samples sintered at 1100°C and 6% in the case of samples sintered at 1125°C . The difference in the magnitude of d_{33} before and after thermal treatment for the PZT – 3 NFM and PZT – 10 NFM samples sintered at 1125°C was small. Again this can be associated to simultaneous increase

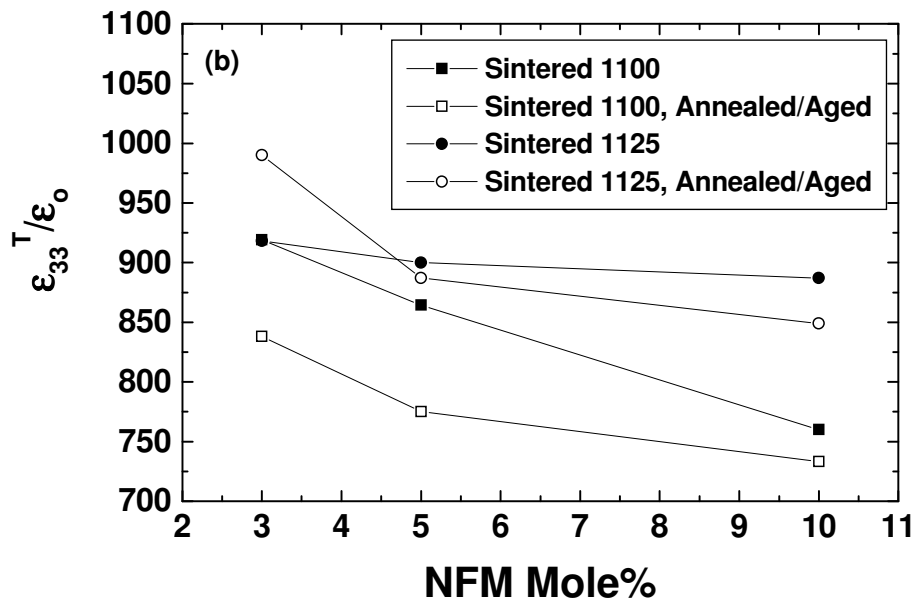
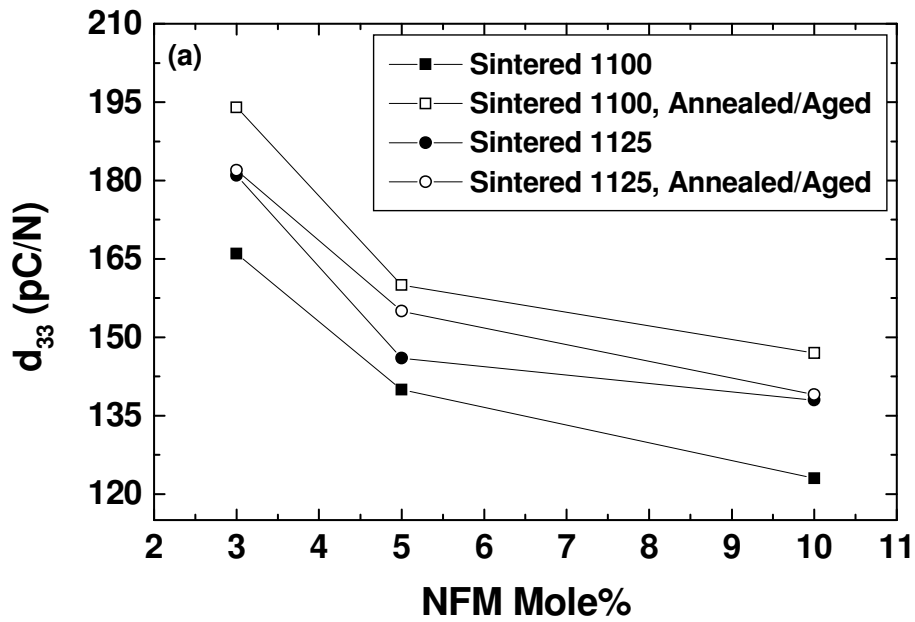


Figure 8.7: Variation of piezoelectric and dielectric constant with NFM mol% before and after thermal treatment for the samples sintered at 1100 and 1125 °C. (a) piezoelectric constant (b) dielectric constant,

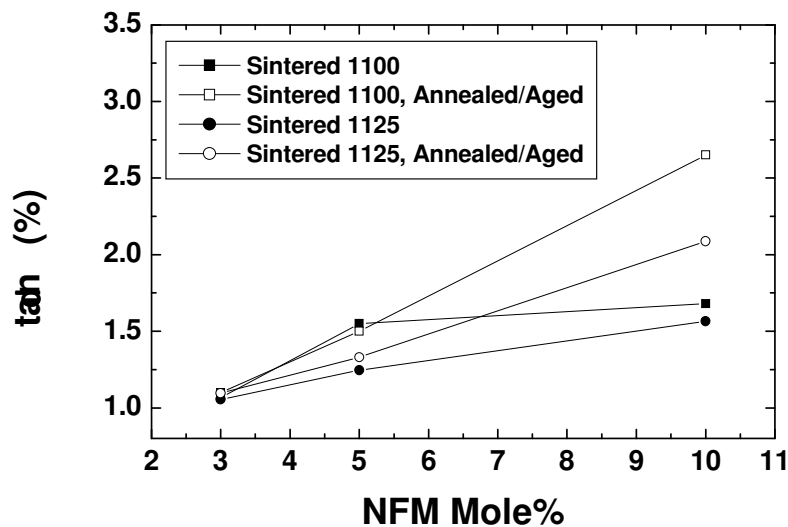


Figure 8.8: Variation of dielectric loss factor with NFM mol% before and after thermal treatment for the samples sintered at 1100 and 1125 °C.

in the internal stress due to structural difference and domain size. Increase in stress decreases d_{33} while increase in domain size increases d_{33} . Figure 8.7 (b) shows the variation of the dielectric constant with NFM concentration. The dielectric constant magnitude for the samples sintered at 1100 °C showed a decrease of about 10% after thermal treatment. Based on the behavior of the piezoelectric and dielectric constant, it can be seen that the total strain magnitude remains of the same order for the samples before and after the thermal treatment. Figure 8.8 shows the plot of the dielectric loss factor. The loss factor was of the order of 1.2% for PZT-3NFM before and after the thermal treatment but the other compositions showed higher losses. Figure 8.9 (a) and (b) shows the dielectric constant and loss factor as a function of temperature measured at frequency of 1 kHz under 1V excitation. The Curie temperature (T_{max}) was quite high for all the compositions, in the vicinity of 375 °C. There was slight decrease in

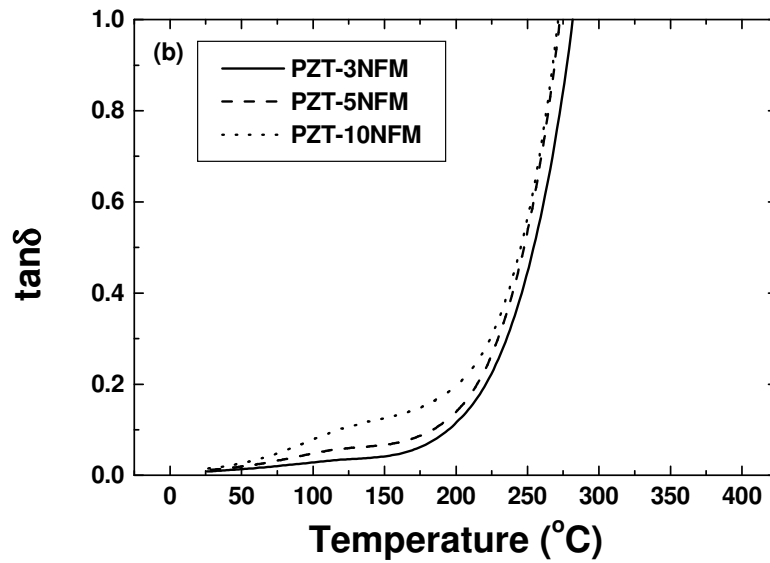
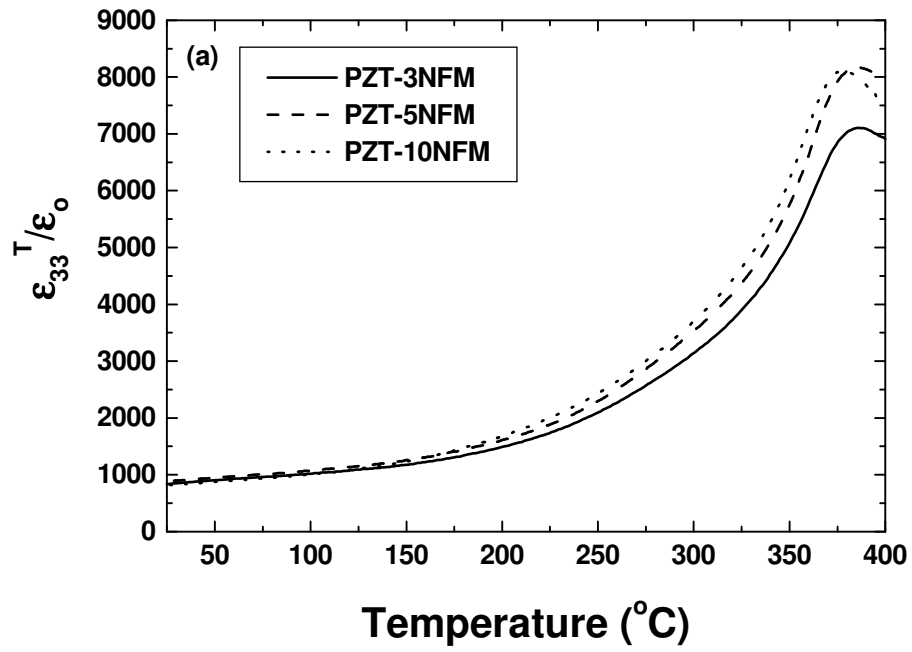


Figure 8.9: Variation of the ferromagnetic properties for three compositions before and after thermal treatment (a) PZT – 3NFM, (b) PZT – 5NFM, and (c) PZT – 10NFM.

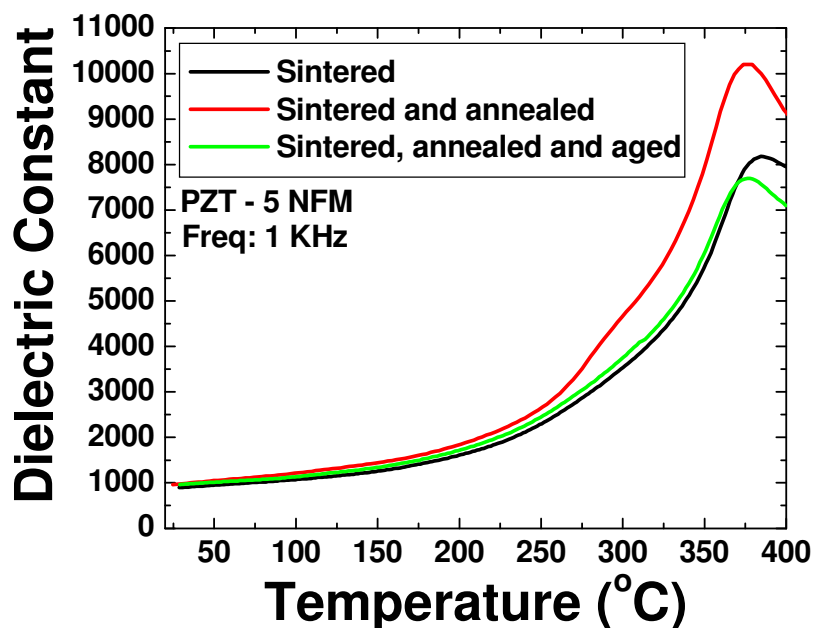


Figure 8.10: Dielectric constant as a function of the temperature at 1 kHz for PZT – 5 NFM at three different conditions.

T_{max} with increasing NFM content. The magnitude of loss factor was around 2% below 80 °C upon which it increased sharply. This increase is associated with the space charge effect and low resistivity of the samples at high temperature. The T_{max} for the thermal treated samples had the same order as that for the samples without thermal treatment. Figure 8.10 shows the dielectric constant as a function of temperature for PZT – 5 at% NFM composite. Data is shown in the figure for three different thermal conditions. The ferroelectric Curie temperature, as identified by the temperature of the maximum in the dielectric constant, was only decreased slightly (~8°C) by annealing and aging. This drop in Curie temperature may be associated with the stress relaxation which can be more accurately determined by diffraction studies. This increase in dielectric constant after annealing can be explained by grain growth as the samples were soaked at 800°C for 10 hours. The dielectric loss also shows similar trend with reduced dielectric loss factor in annealed and aged samples.

8.1.3 Magnetic moment as a function of magnetic field and temperature for thermally treated PZT–NFM composite

Figure 8.11 – 8.12 shows the variation of magnetic properties with thermal treatment. A significant enhancement in the value of the remanent (M_r) and saturation (M_s) magnetization was obtained after the annealing and aging treatment. Table 8.2 compares the magnetic data for the calcined powder, sintered samples and thermally treated samples. Magnetization values increased sharply after thermal treatment. The magnitude of the coercive fields had the same order for the sintered and thermally treated samples while a notable difference was seen in the magnitude of the magnetic resonance which decreased significantly after thermal treatment. These results can be explained if it is assumed that the size of magnetic phase (spinel) increases with the thermal treatment. This is probable since the intrinsic similarity in the oxygen coordination chemistry between the perovskite and spinel structure leads to the lattice dimensions that are compatible with the spinel building blocks (considering growth is along the c-axis).

Figure 8.13 shows temperature dependent magnetization from room temperature to 900 K. It was found that the ferromagnetic Curie temperature decreases from 828K in the as-sintered condition to 788K after annealing. In addition, it was found that saturation magnetization at room temperature increases from 0.58 emu/gm to 0.64 emu/gm after annealing. This modest change in magnetization after annealing at 800°C may be related to Mn valence change in the ferrite phase. Previously, it has been shown that $Mn^{+3} \rightarrow Mn^{+2}$ begins to occur for temperatures above 700°C [150], resulting in an adjustment in the stoichiometry of the ferrite phase to $[Ni(Mn)_y]Fe_{1.9}Mn_{(0.1-y)}O_4$ where y is the concentration of Mn^{+2} . On quenching, this adjusted stoichiometry will be metastably frozen-in to room temperature. Since, Mn^{+2} has a higher magnetic moment than Mn^{+3} , it reasonable to expect a slight increase in saturation magnetization after annealing [151].

Table 8.2: Magnetic Properties of PZT-NFM powders

| | PZT - 3NFM | | PZT - 5NFM | | PZT - 10NFM | |
|------------------------------------|--------------------|-----------------------|--------------------|-----------------------|--------------------|-----------------------|
| | Sintered at 1100°C | Sintered and annealed | Sintered at 1100°C | Sintered and annealed | Sintered at 1100°C | Sintered and annealed |
| H_c (Oe) | 86.94 | 89.91 | 75.62 | 78.76 | 69.78 | 70.24 |
| M_r (μemu) | 1010 | 1480 | 904.1 | 2538 | 5305 | 5575 |
| M_s (memu) | 5.766 | 8.653 | 6.472 | 19.25 | 48.64 | 57.13 |
| M_r/M_s | 0.1751 | 0.1711 | 0.1397 | 0.1318 | 0.1091 | .0976 |
| S* | 0.005 | 0.0043 | 0.0048 | 0.0036 | 0.0034 | 0.0029 |
| Resonance (Hz) | 509.4 | 465.2 | 543 | 463 | 453.9 | 439.8 |

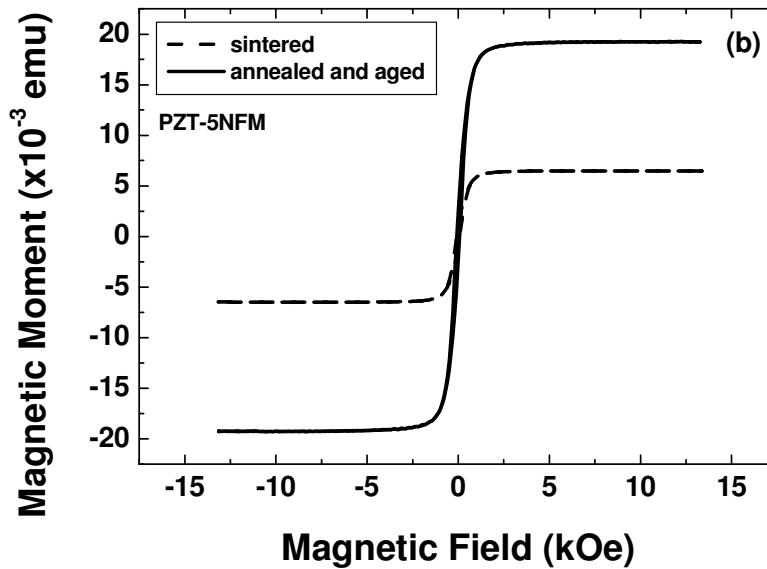
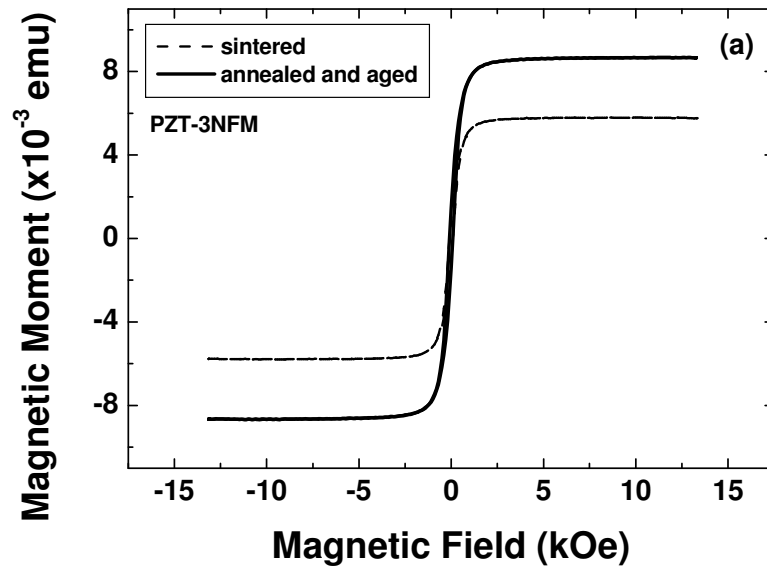


Figure 8.11: Variation of the ferromagnetic properties for three compositions before and after thermal treatment (a) PZT – 3NFM, (b) PZT – 5NFM.

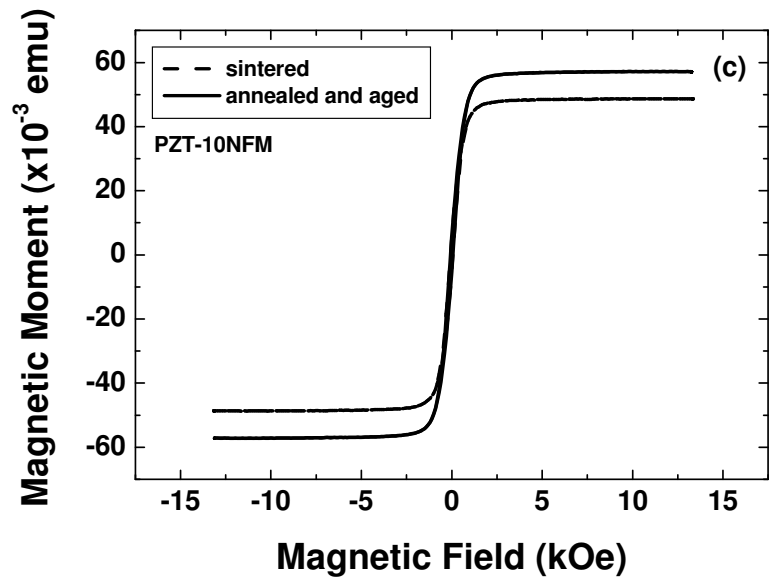


Figure 8.12: Variation of the ferromagnetic properties for three compositions before and after thermal treatment PZT – 10NFM.

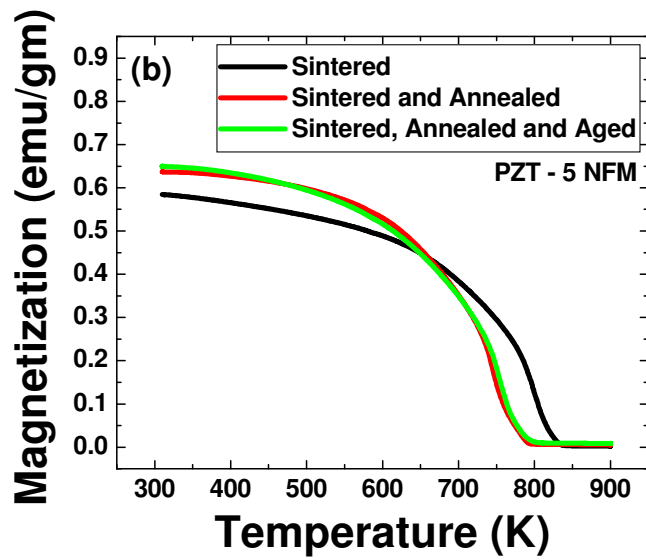


Figure 8.13: Temperature dependent ferromagnetic property (saturation magnetization) of PZT – 5 NFM composite.

8.1.4 Effect of annealing and aging on Magnetolectric properties of PZT – NFM composites

Figures 8.14 – 8.15 shows the ME voltage coefficient for $x = 3, 5$ and $10\text{at}\%$. Data are given in each figure for the three different thermal histories. For $x = 10 \text{ at}\%$, the ME coefficient increased from 60mV/cm-Oe to 88mV/cm-Oe which is nearly 50% increase. We attribute this increase is due to the expansion of lattice constant in PZT phase, reduction of defects at that interphase interfaces after annealing. Presence of defects at the interfaces would decrease the ability of piezoelectric phase regions to elastically respond to strictions imposed on it by neighboring magnetostrictive ones, or vice versa. To achieve high ME properties, the boundary conditions between phases needs to be as mechanically free as possible. Contributions to the enhancements in the ME coefficient may also result from increased magnetization from $\text{Mn}^{+3} \rightarrow \text{Mn}^{+2}$, as an enhanced magnetic permeability has been reported to increase the effective piezomagnetic coefficient ($d\lambda/dH$) [50].

8.1.5 Structural characterization for high ME coefficient of PZT – NFM composites.

Figure 8.16(a) shows a bright-field TEM image of as-sintered sample. This image consists of facet phases/particles (bright contrast) embedded in the matrix. The former ones (facet phases) correspond to the NFM phase, while the latter one (matrix) corresponds to the PZT phase, as identified by the EDS and SAED patterns. The NFM particles vary from 300 nm to 1500 nm. Figure 8.16 (c) and (d) are SAED patterns obtained from the PZT matrix, which can be identified as the [101] and [001] zone axes of the tetragonal PZT structure, respectively. The lattice parameter of this PZT structure in the sintered sample can be determined to be $a_{\text{PZT}}^{\text{s}}=3.87\text{\AA}$ and $c_{\text{PZT}}^{\text{s}}=4.07\text{\AA}$, with $c/a=1.052$. Figs. 8.16 (e) and (f) are SAED patterns taken from NFM phase in Figure 8.16(a) which can be identified as the [211] and [110] zone axes of the pseudo-cubic structure of NFM, respectively. This pseudo-cubic structure has a lattice parameter of $a_{\text{NFM}}=8.42\text{\AA}$, as measured from the electron diffraction pattern. 8.16(b) shows a bright field TEM image of the sample annealed at 800°C for 10hrs.

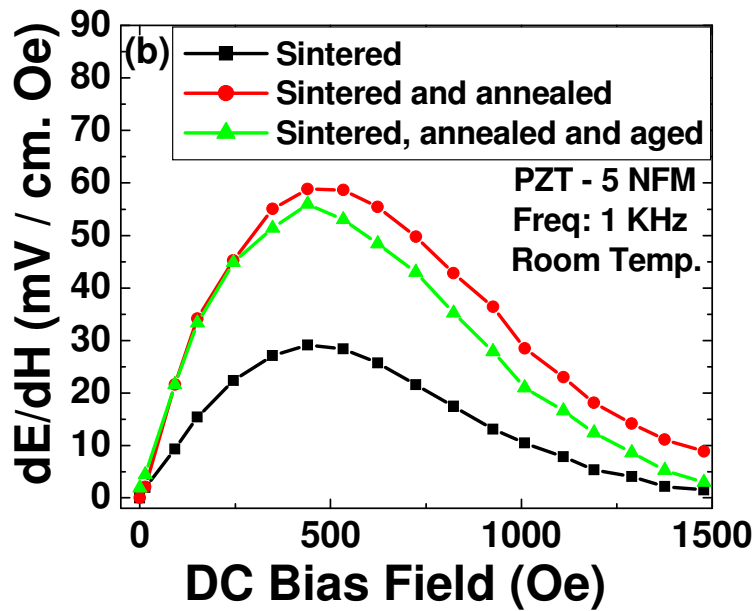
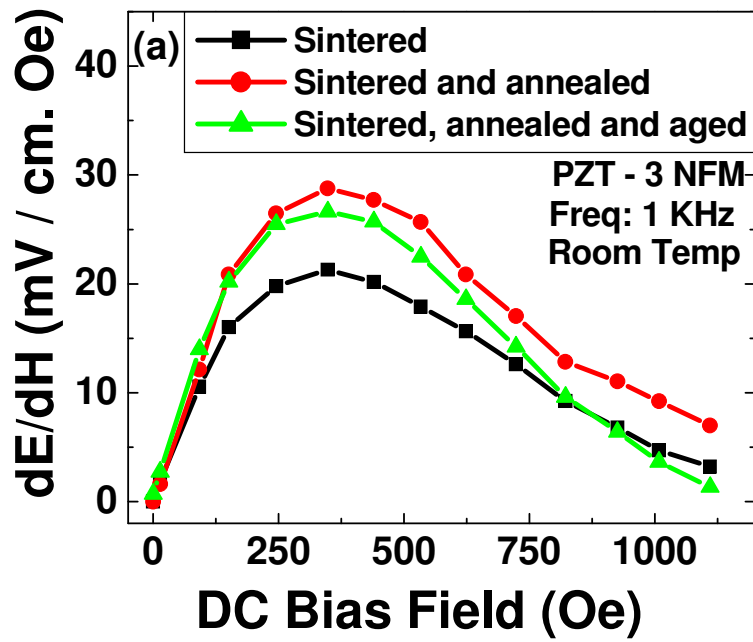


Figure 8.14: Magnetolectric coefficient for different composites at three different conditions, (a) PZT – 3 NFM, (b) PZT – 5 NFM

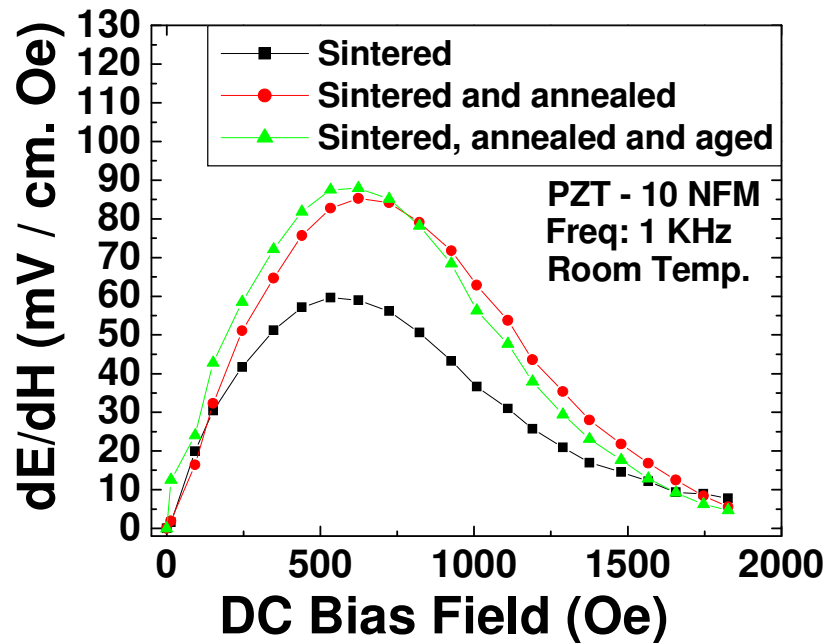


Figure 8.15: Magnetolectric coefficient for different composites at three different conditions PZT – 10 NFM.

Figure 8.16(b) shows another variation of microstructural characteristics from those shown in Figure 8.16 (a). The density of the NFM particles in this annealed sample is much less than that in the sintered sample. In addition, the NFM particles in the annealed sample have a typical size of 500 nm, much smaller than that in the sintered sample. The PZT phase in the annealed sample has a tetragonal structure with a lattice constant of $a_{PZT}^a = 4.07\text{\AA}$ and $c_{PZT}^a = 4.09\text{\AA}$, with $c/a = 1.005$. The samples treated by annealing at 800°C for 10hrs, followed by quenching in air and subsequent aging at 300°C shows similar microstructure as that of the annealed sample shown in Figure 8.16 (b), but the density of the NFM phase was further reduced. Another noticeable feature observed in the sintered sample was diffused grain boundaries which may be due to the presence of large amount of defects. During annealing as the structure finds more time to reduce the defects from its structure, sharp grain boundaries are observed. The above

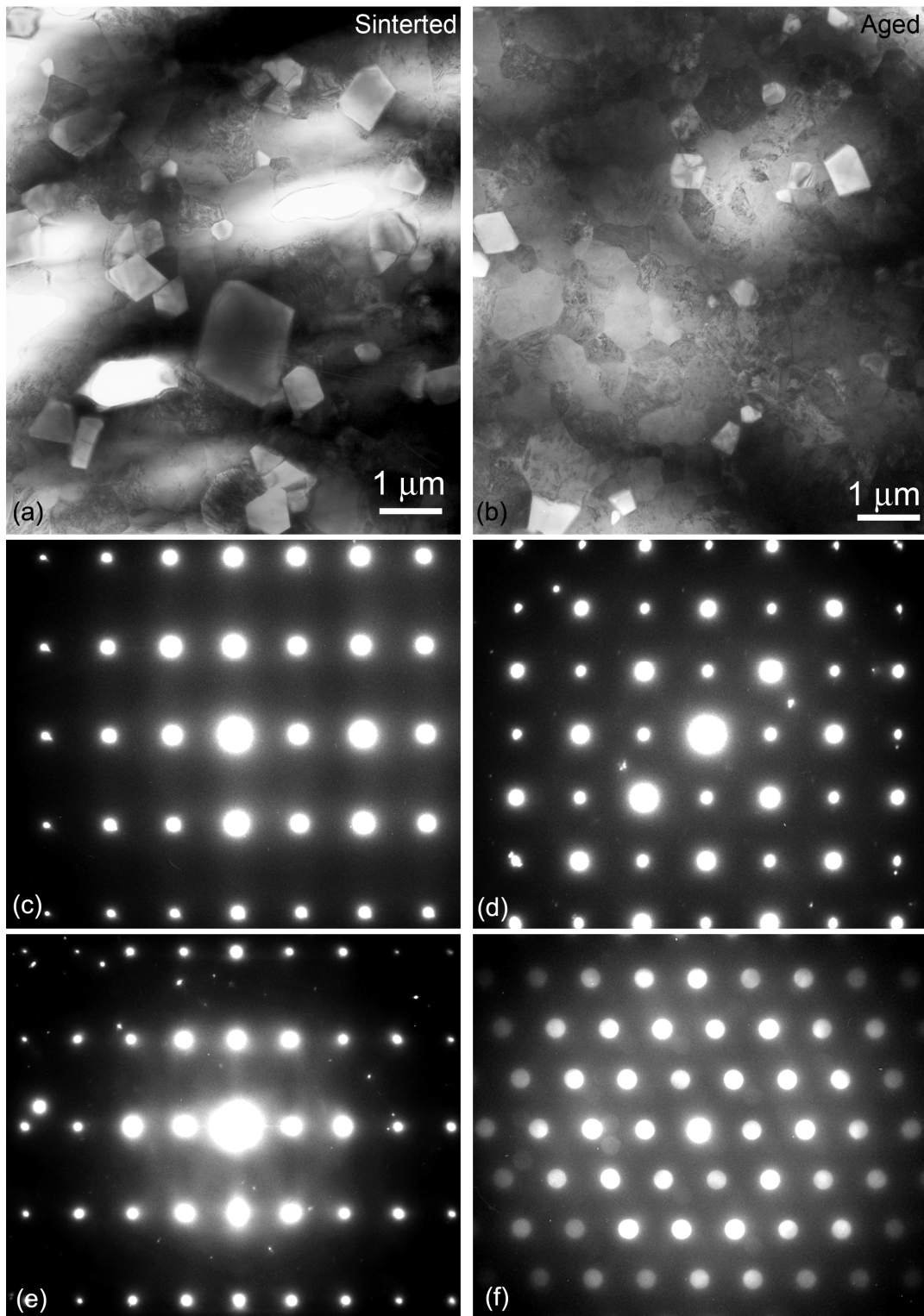


Figure 8.16: Bright field TEM images PZT – 5 NFM composites after (a) sintering, and (b) annealing. Selected area electron diffraction (SAED) pattern of PZT phase after sintering for (c) [101], (d) [001] zone axis and NFM phase after sintering (e) [211], (f) [110] zone axis.

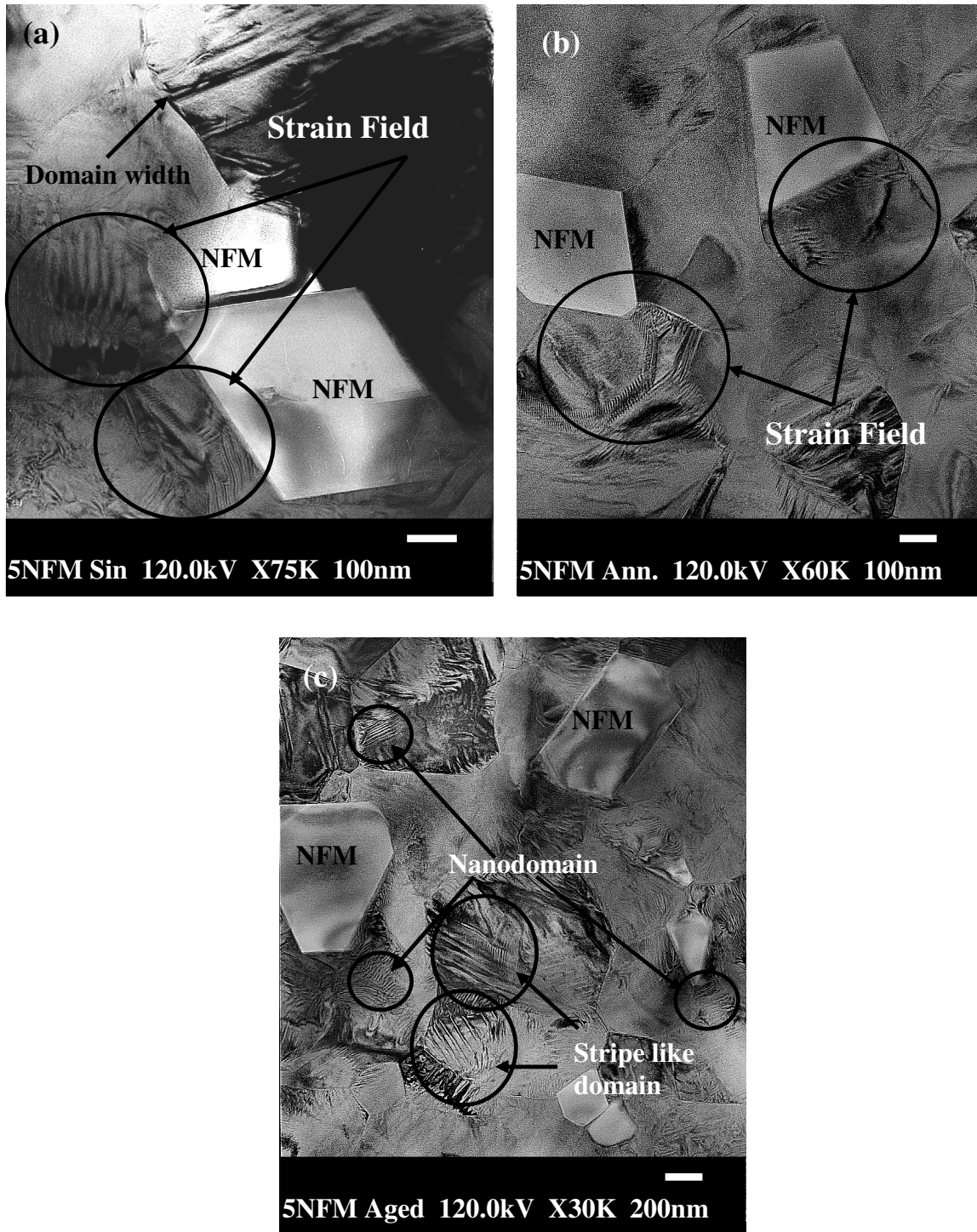


Figure 8.17: Bright field TEM images PZT – 5 NFM composites after (a) sintering, (b) annealing and (c) aging.

results demonstrate that the post-sinter thermal treatments at 800°C for 10 hrs results in reduction of NFM phase by diffusing into the PZT structure. Meanwhile, PZT phase transfer from the tetragonal structure to a pseudo cubic structure with a larger lattice constant. Figure 8.23 (a) – (c) show the high magnification bright field TEM images of the sintered, annealed and aged samples. The sintered samples were found to consist of high misfit strain fields near the PZT/NFM interface which develops in order to accommodate the mismatch in the PZT and NFM lattice. The domain patterns had larger width characteristic of 90° domains and there is intergranular heterogeneity in domain width [152]. The image after annealing shows less misfit strain near the interface. The residual strain fields in this case consist of additional component due to the rapid cooling and quenching process after annealing. After annealing diffused grain boundary was observed in low magnification images. The image after the aging process shows significantly reduced strains. The domain structure has stripe like morphology and extend from grain boundary to grain boundary. A finer scale domain structure is also observed to exist within larger domain patterns. This finer domain pattern has striation like morphology and is periodically spaced [153, 154].

8.2 Effect of aging time and temperature

8.2.1 Phase analysis for variation in aging time and temperature

A simple phase analysis using XRD was performed to find the fraction of the phases in the binary system PZT - $\text{NiFe}_{1.9}\text{Mn}_{0.1}\text{O}_4$ (NFM) after aging at different temperature and time. Figure 8.18(a) shows XRD patterns of PZT – 10 NFM composite after aging at temperature between 300 – 400°C for 5 h. The XRD patterns of the thermally treated composite showed no phase other than perovskite (PZT) and spinel (ferrite). Figure 8.18 (b) shows the XRD patterns of the PZT – 10 NFM composite samples sintered at 1125°C for 2 h followed by annealing at 800°C for 10 h and aging at 400°C for various time intervals (3 to 15 h). It can be clearly seen

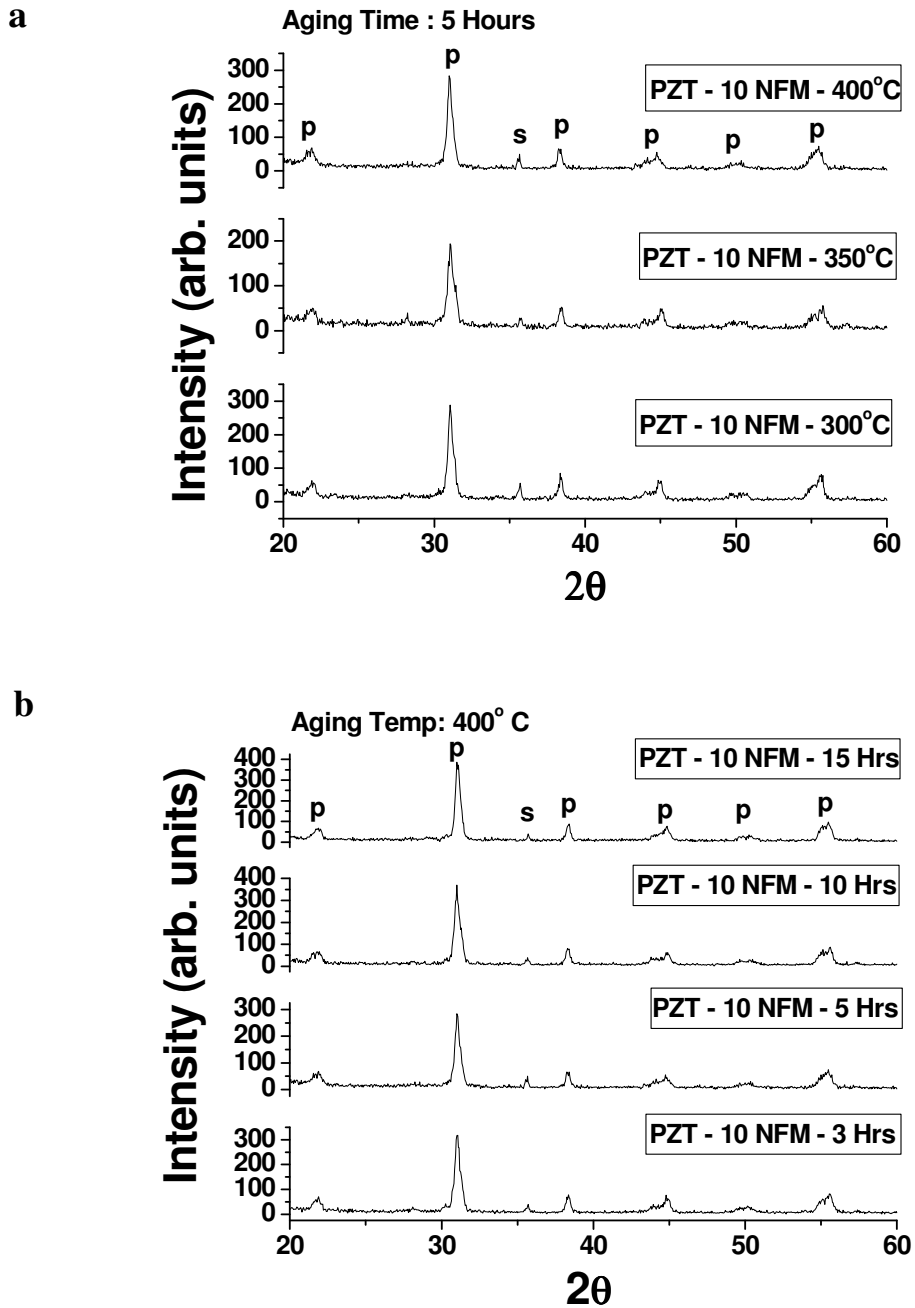


Figure 8.18: XRD patterns of PZT -10 NFM at different aging condition showing variation of spinel peaks. (a) function of aging temperature, and (b) function of aging time.

from these figures that there is some variation in the fraction of the spinel phase. The fraction of the spinel phase present was computed using equation 8.1. It was found that when the aging temperature was decreased from 400°C to 300°C the spinel content for PZT – 10 NFM increased from 1.03% to 2.36%. This is a considerable increase considering the difference in the lattices of two phases.

8.2.2 Effect of aging time and temperature on piezoelectric and dielectric properties of PZT – NFM composite

Figure 8.19 (a) and (b) shows the variation of the piezoelectric constant (d_{33}) with aging temperature and time respectively. As the aging temperature increases from 300°C to 400°C, d_{33} increases from 127 pC/N to 155 pC/N for PZT – 5NFM. This may be explained by invoking the results of XRD data. At 300°C after 5 h aging, a high spinel fraction (9.18%) was found and with increasing temperature, spinel fraction decreases. The variation of d_{33} with aging time shows maxima (155 pC/N for PZT – 5NFM) at 400°C for 5 h and decrease if the aging time is lower or higher than 5 h. This can be associated to simultaneous increase in the internal stress due to structural difference and domain size. Figure 8.20 (a) and (b) show the variation of the dielectric constant as a function of aging temperature and time respectively. For PZT – 5 NFM the dielectric constant was found to increase from 840 to 885 when aging temperature increased from 300 to 400°C. The dielectric constant as a function of aging time showed minima at 5 h for all the compositions. The samples aged for 3 h show higher dielectric constant (more than 1000) for all three compositions. Enhancement of piezoelectric and dielectric properties with aging temperature indicates that the fraction of piezoelectric phase is higher at higher temperature. The piezoelectric voltage constant (g_{ij}) is the most important factor to obtain a superior magnetoelectric voltage constant. In the case of the laminate composites, the output voltage (V_{out}) obtained is proportional to the piezoelectric voltage constant g_{ij} , and is given as:

$V_{out} = 2 \times g_{ij} \times t_p \times \sigma_{ij_p}^E$, where t is the thickness, subscript p denotes piezoelectric and σ is the stress applied on the piezoelectric phase. The magnetoelectric coefficient is simply obtained

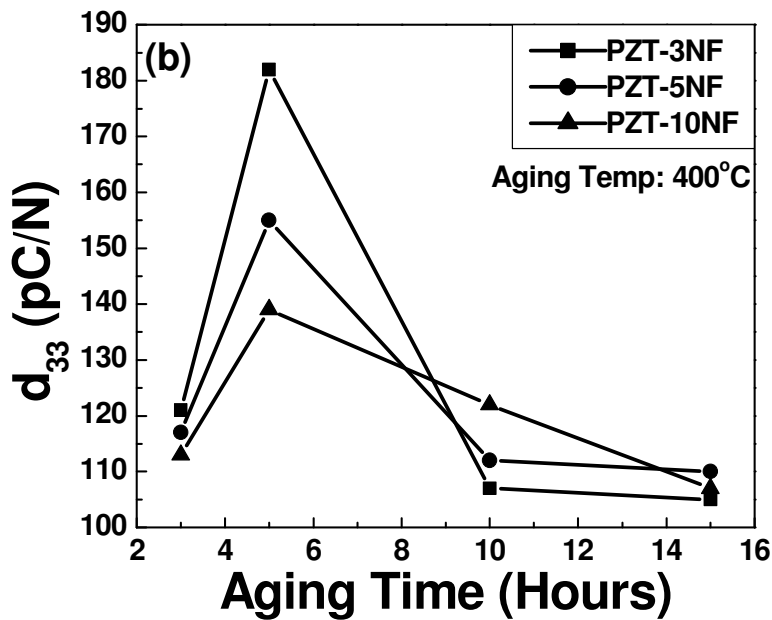
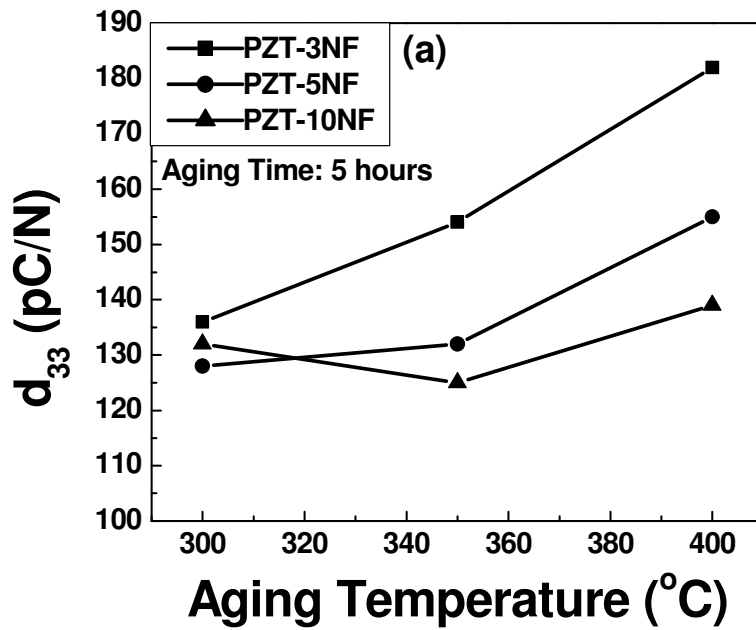


Figure 8.19: Variation of piezoelectric constant with aging time and temperature. (a) Piezoelectric constant as a function of aging temperature, (b) Piezoelectric constant as a function of aging time.

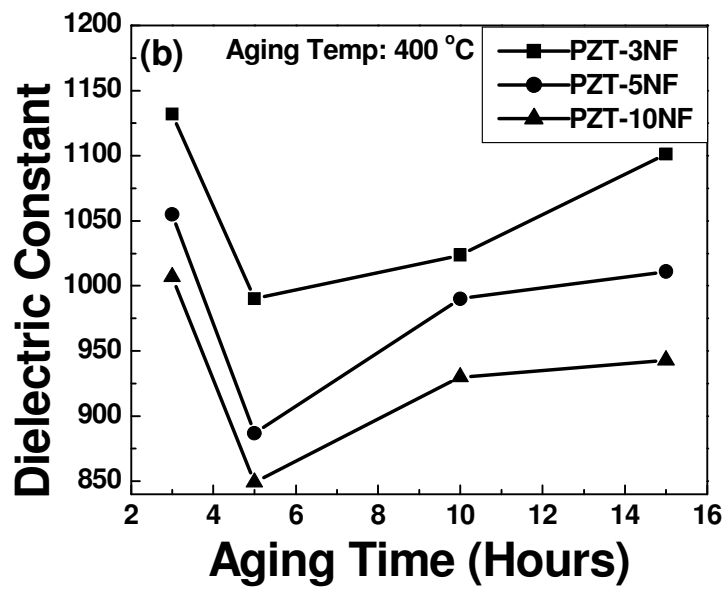
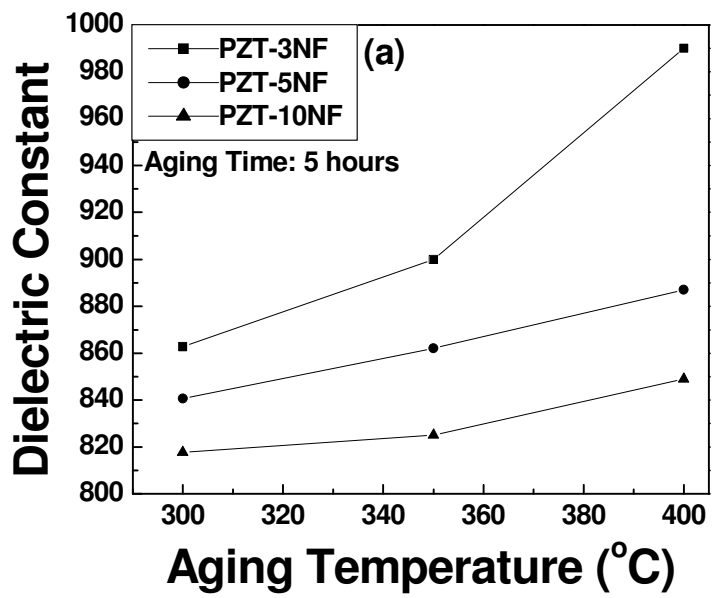


Figure 8.20: Variation of dielectric constant with aging time and temperature (a) Dielectric constant as a function of aging temperature and (b) dielectric constant as a function of aging time.

by the following relation:

$$\frac{\delta E}{\delta H} = \frac{V_{out}}{H_{ac} \times t_p} = \frac{2 \times g_{31} \times \sigma_{31p}^E}{H_{ac}} (V/cm \cdot Oe) \quad (8.4)$$

where, H_{ac} is the applied ac magnetic field. The above relation will be significantly different with the case of the particulate composites, as the stress term has to be expressed in terms of microstructural parameters such as grain size, shape, particle distribution and lattice strain. However, it can be used for the qualitative analysis of the results. Figure 8.21 (a) and (b) shows the variation of the g_{33} as a function of aging temperature and time respectively. The magnitude of g_{33} increases from 17.23 V-m/N at 300°C for 5 h aging to 19.8×10^{-3} V-m/N when the samples are aged at 400°C for 5 h. For PZT –10 NFM, almost equal amount of magnitude in g_{33} was found at aging condition of 300° and 400°C but there is a drop in magnitude at aging condition of 350°C. The variation of g_{33} with aging time shows maxima at 5 h aging, which indicates that this is the optimum aging time. This enhancement in g_{33} constant will contribute to the magnitude of ME coefficient.

8.2.3 Aging time and temperature dependent magnetic properties

Figure 8.22 (a) and (b) shows the variation of magnetic properties, saturation magnetization (M_s) and remnant magnetization (M_r) respectively with thermal treatment. A significant enhancement in the value of the saturation (M_s) and remnant (M_r) magnetization was obtained after the annealing and aging treatment. For PZT – 5NFM the M_s value increased from 19.25 memu at 400°C for 5 h to 37.17 memu at 300°C for 5 h aging, which is almost two times higher. Almost similar variation was observed for PZT – 10 NFM in which case M_s value increases from 57.13 memu to 94.78 memu. Significant increase in M_r was recorded for all the compositions. For PZT -10 NFM almost twice the value of M_r was recorded for samples aged at 300°C (9.65 memu) than that at 400°C (5.575 memu). This can be associated to the increase in the fraction of spinel phase after annealing and aging.

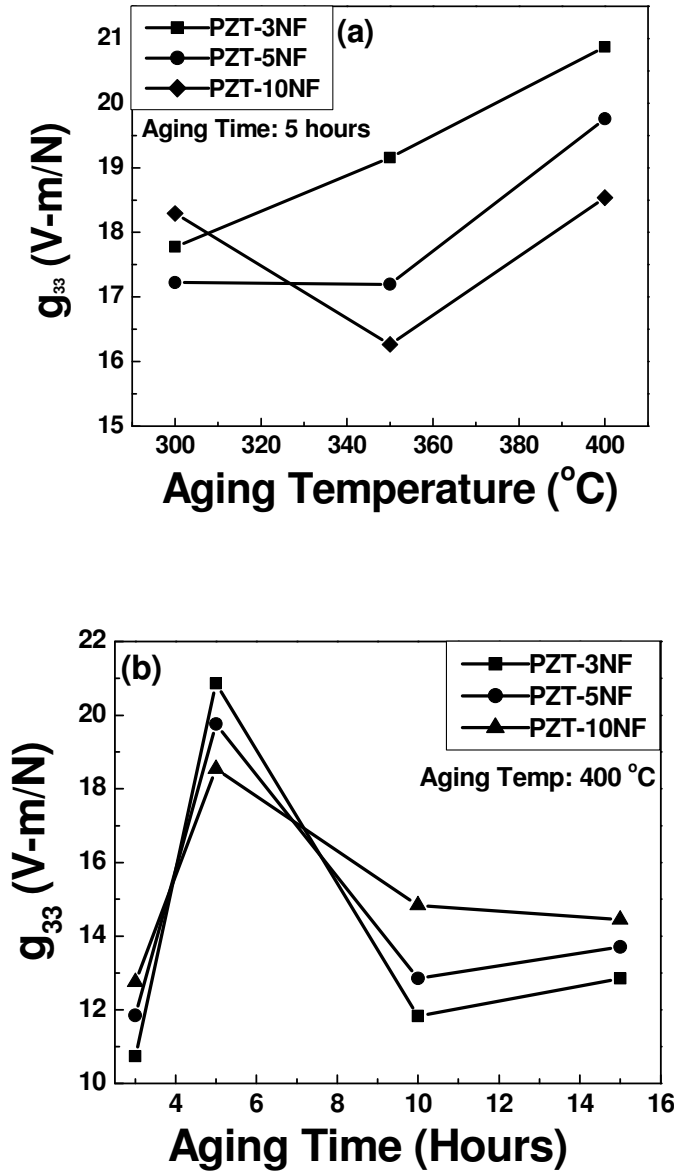


Figure 8.21: Variation of piezoelectric voltage constant (g_{33}) as a function of aging temperature and time. (a) aging temperature dependence of g_{33} and (b) aging time dependence of g_{33} .

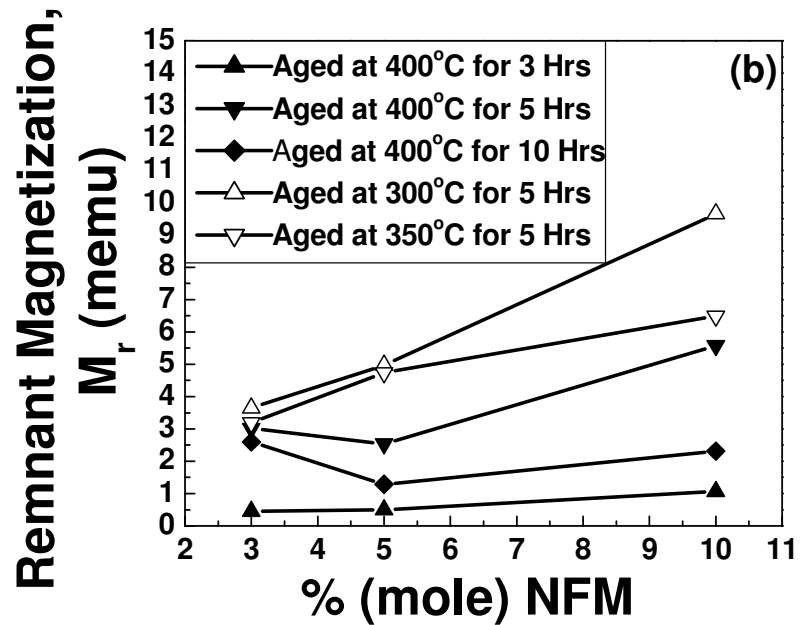
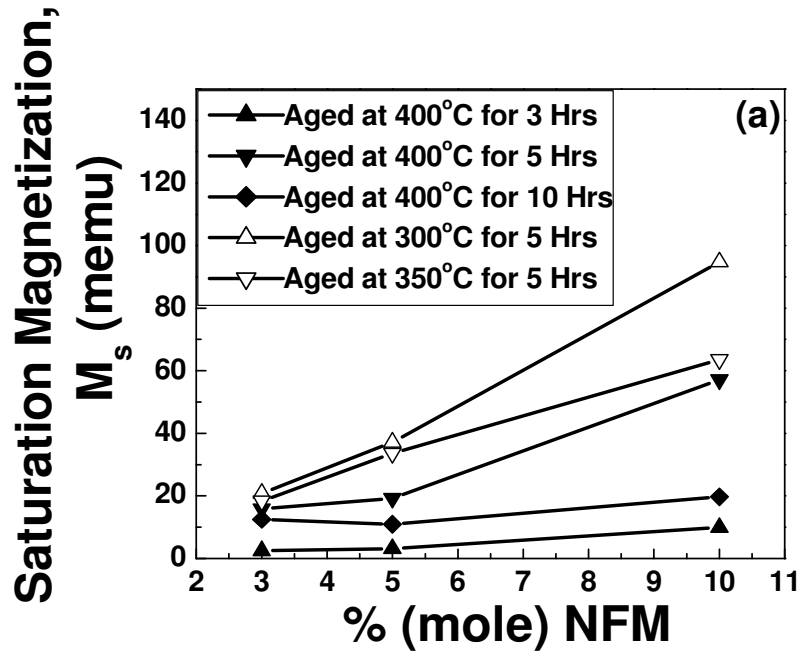


Figure 8.22: Variation of ferromagnetic property as a function % (mole) NFM at different aging temperature and time. (a) Saturation magnetization M_s and (b) Remnant magnetization M_r .

8.2.4 Effect of aging time and temperature on magnetoelectric properties of PZT – NFM composite

Figure 8.23 shows the peak amplitude of the magnetoelectric effect measured for the three different samples after aging at different conditions. The optimum magnetoelectric coefficient was found for the aging condition of 300°C and 5 h. For PZT – 10NFM the sintered sample showed a magnetoelectric coefficient of 78 mV/cm Oe. After aging at 400°C for 5 h it increases to 114 mV/cm Oe. This aging temperature is above the Curie temperature, which was found to be around 365°C. On decreasing the aging temperature below Curie temperature to

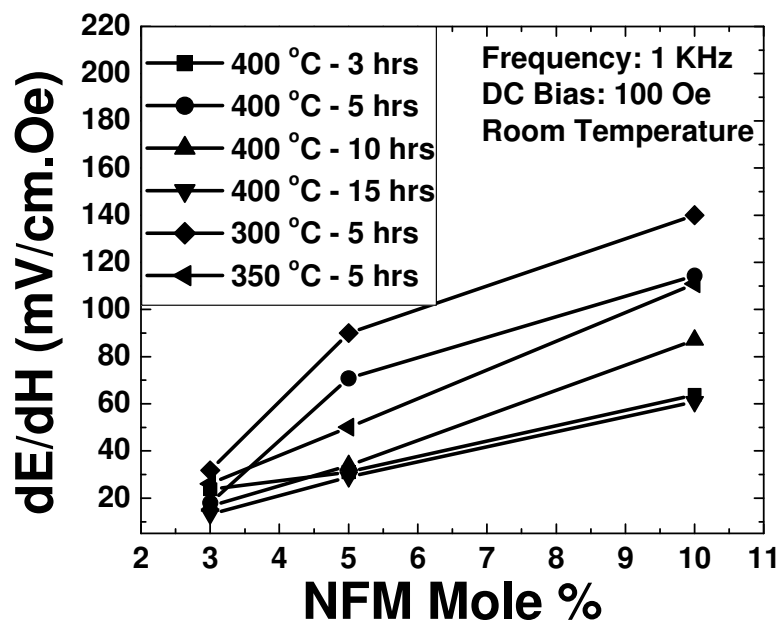


Figure 8.23: Magnetoelectric Coefficient (dE/dH) as a function of mole% NFM at different aging condition.

300°C the magnetoelectric coefficient was found to increase to 140 mV/cm Oe, which is almost twice the magnetoelectric coefficient of sintered sample. This enhancement is consistent with the XRD phase analysis, piezoelectric and ferromagnetic data.

8.2.5 Microstructural analysis for time – temperature variation of PZT – NFM composite

8.24 (a) and (b) shows the microstructure of the samples sintered at 1125 °C for compositions PZT-5NFM at 5kX and 20kX magnification respectively. A dense microstructure for all compositions was obtained. Elemental analysis using the EDX showed that NFM grains are randomly distributed in the piezoelectric matrix. Figure 8.24 (a) and (b) shows the microstructure of the PZT-5NFM after annealing and aging at 400°C for 5 h. An immediate observation of the low magnification images of sintered and aged sample provides noticeable difference in the distribution of the NFM particles. An even distribution of NFM particles can be observed after the aging treatment. Elemental X-ray mapping showed that nickel and iron are distributed in the whole matrix but in certain areas (black regions) their concentration is higher than the surrounding. This observation is consistent with the XRD analysis that after aging treatment, spinel phase grows in the PZT matrix. The growth of the nickel ferrite region inside the PZT grains will lead to effective transfer of the interfacial stress, which will result in higher ME coefficient. The high magnification images of the sintered (Figure 8.24 b) and aged (Figure 8.25 b) sample give us an indication about the orientation relationship. A thicker grain boundary was observed in the sintered sample whereas a very thin grain boundary was observed in the annealed and aged samples. There is a considerable reduction in piezoelectric grain size and NFM particle size after annealing and aging, as can be seen from the SEM micrographs. Figure 8.26 (a) and (b) compares the PFM images of the sintered and aged PZT–5NFM samples. It was found that in the sintered condition NFM phases are not homogenized as they are concentrated in one part. On the other hand in the aged condition, they are homogenized all over the structure. Assuming that spinel phase is single domain it can be hypothesized that the annealing and aging treatment results in redistribution of the magnetic phase.

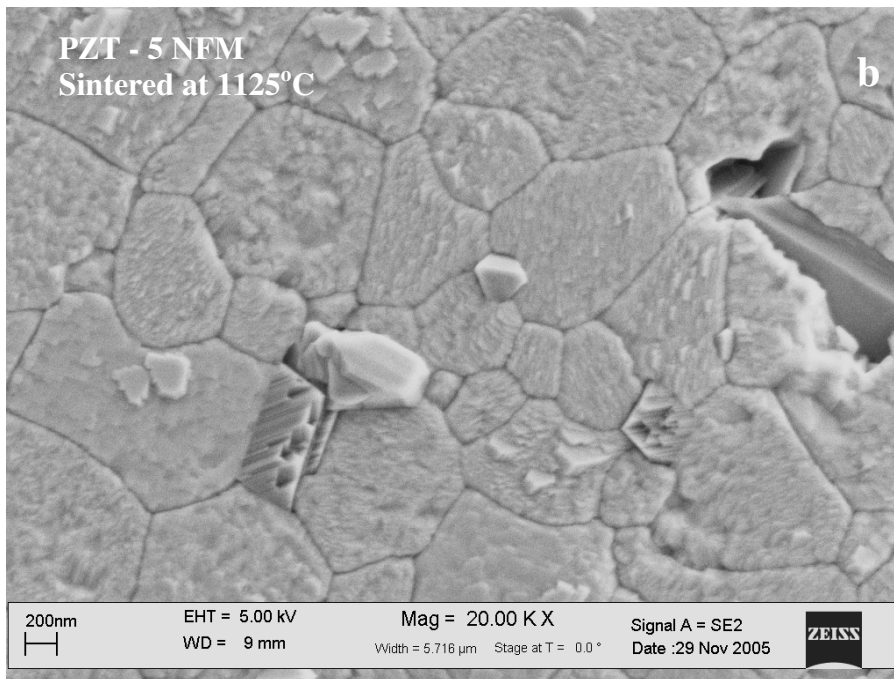
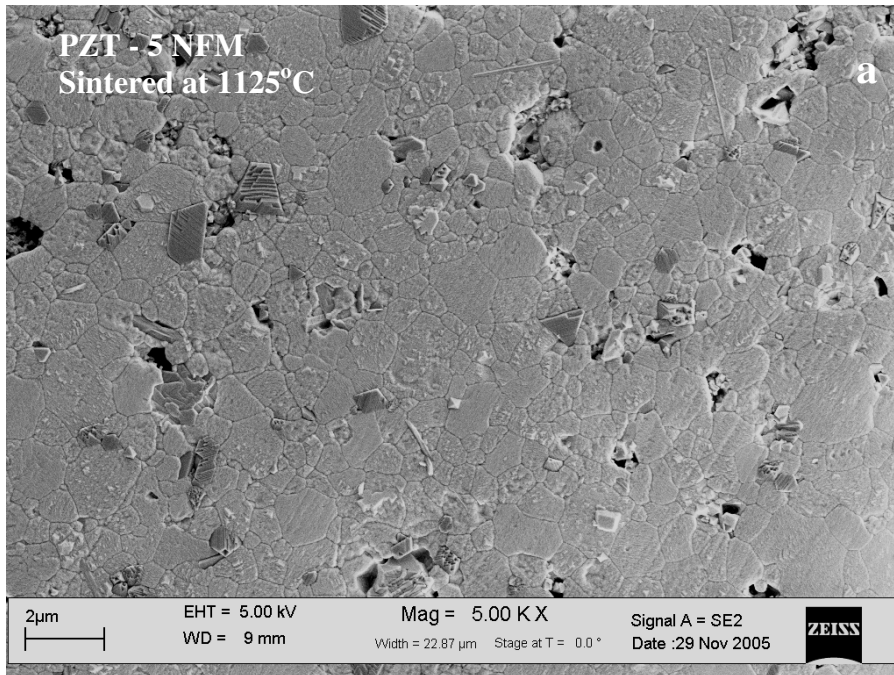


Figure 8.24: SEM microstructure of PZT – 5 NFM at different conditions and different magnifications. (a) Sintered sample at 5kX magnification, (b) sintered sample at 20kX magnification.

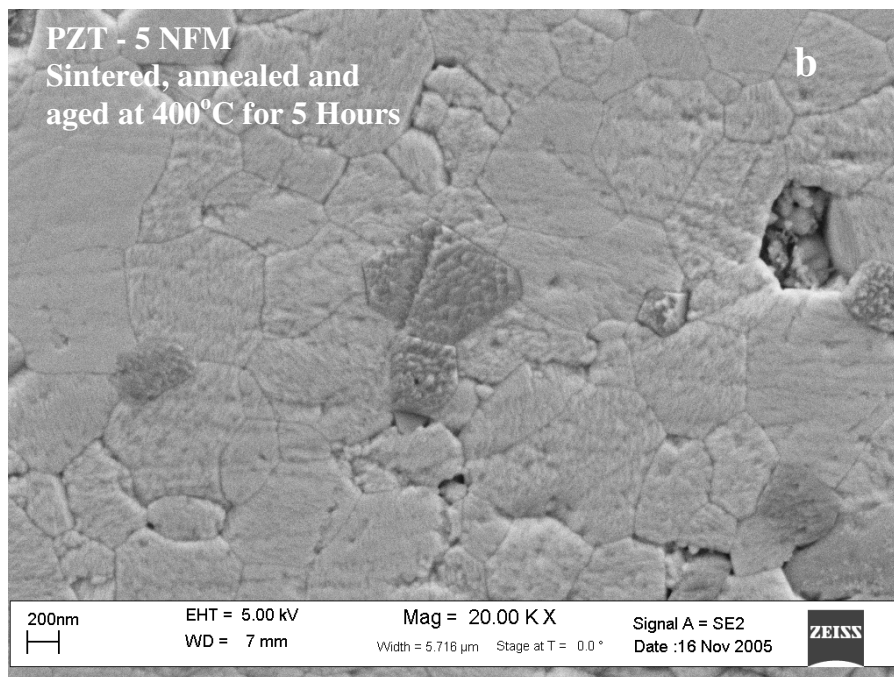
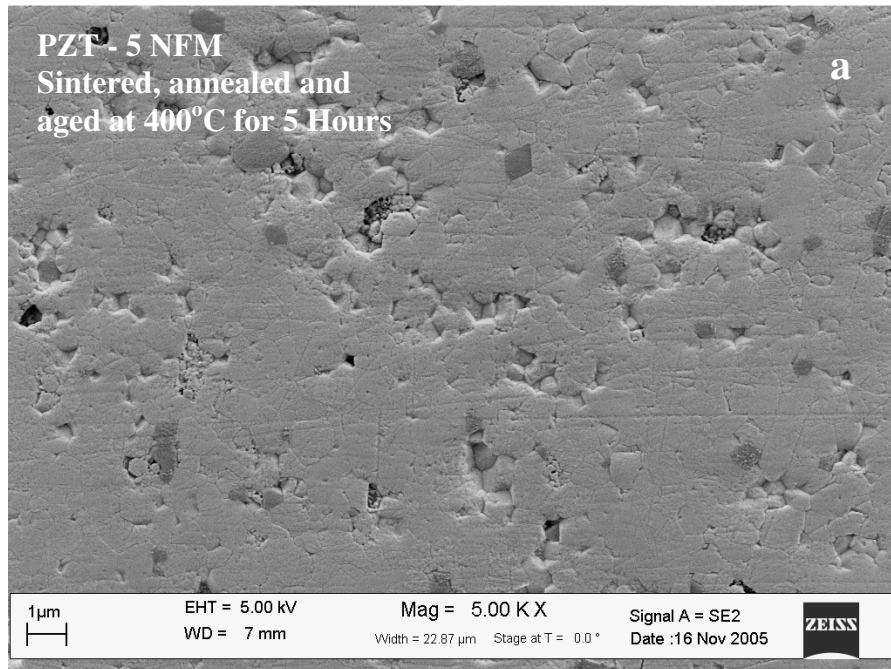


Figure 8.25: SEM microstructure of PZT – 5 NFM at different conditions and different magnifications. (a) sintered, annealed and aged sample at 5kX magnification and (b) sintered, annealed and aged sample at 20kX magnification.

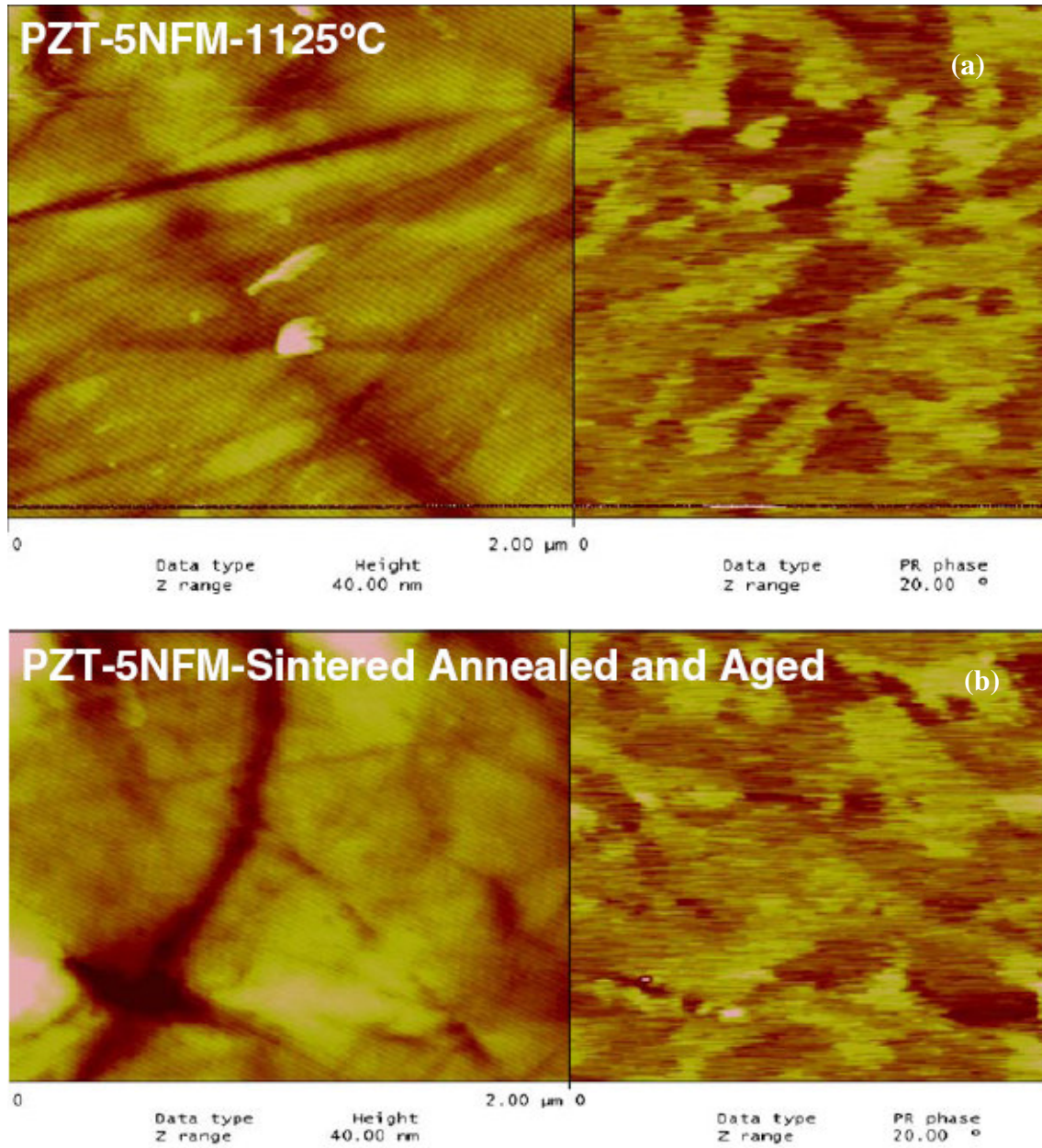


Figure 8:26: PFM images of PZT – 5 NFM after (a)sintering and (b)annealing/aging

8.3 Chapter Summary

A thermally treated composite sample of 10 mole% manganese modified nickel ferrite - PZT was able to provide ME coefficient of 88 mV/cm.Oe. The effects of aging time and temperature on piezoelectric, dielectric and magnetoelectric properties were also studied. It was found that 300°C and 5 hours are the best aging condition for PZT – NFM composite where at least 50% enhancement of ME coefficient was observed. This condition also shows better magnetic properties. A correlation between structural deformation in PZT matrix, presence of defects between component phases in piezoelectric-magnetostrictive composites and the change in magnetization with changes in the ME coefficient was observed. It can be concluded from phase analysis, magnetic properties measurement, SEM and TEM investigations that by annealing and aging treatment, stress relaxation of PZT grains and homogeneous dispersion of magnetization can be achieved, which enhances the magnetoelectric property. Based on this result it can be hypothesized that annealing temperature, annealing time, quenching rate, aging temperature and aging time are important parameters controlling the magnitude of ME coefficient.

CHAPTER 9

TRILAYER (2 – 2) COMPOSITE SYNTHESIS

Previous chapters have shown that cofiring multiple layers can provide higher ME coefficients. However, the drawback is that tape-casting process for synthesizing multilayers of heterogeneous materials is complex. Thus, in order to improve the property of sintered ME composites, other variables such as composition, microstructure, geometry, texture, and post sinter heat treatment needs to be optimized. In the previous chapters, it has been shown that soft piezoelectric phase (high dielectric and piezoelectric constant), soft magnetic phase (high permeability and low coercivity) [155], large piezoelectric grainsize ($> 1 \mu\text{m}$) [156], layered structure (bilayer / trilayer) [157] and post sintering thermal treatment (annealing and aging) [158] improves the magnetoelectric property. In order to combine all the parameters together, the challenge is to develop a unique fabrication process, in which layers of piezoelectric and magnetostrictive can be cofired together. Moreover the poling process of the piezoelectric phase requires high resistivity and thus electrodes have to be preserved during sintering.

9.1 Trilayer synthesis

It was found that pressure assisted sintering can produce trilayer composites with any desired dimensions. Further, the compositions were designed such that sintering can be done at low temperatures of 900°C which results in stable electrodes. The objective of this chapter is to analyze the microstructural, piezoelectric, dielectric and magnetoelectric properties of this trilayer sintered ME composite. Powders of $0.9 \text{ Pb (Zr}_{0.52}\text{Ti}_{0.48}\text{)O}_3 - 0.1 \text{ Pb (Zn}_{1/3}\text{Nb}_{2/3}\text{)O}_3$ [0.9 PZT – 0.1 PZN] and $\text{Ni}_{0.6}\text{Cu}_{0.2}\text{Zn}_{0.2}\text{Fe}_2\text{O}_4$ [NCZF] were synthesized using conventional mixed

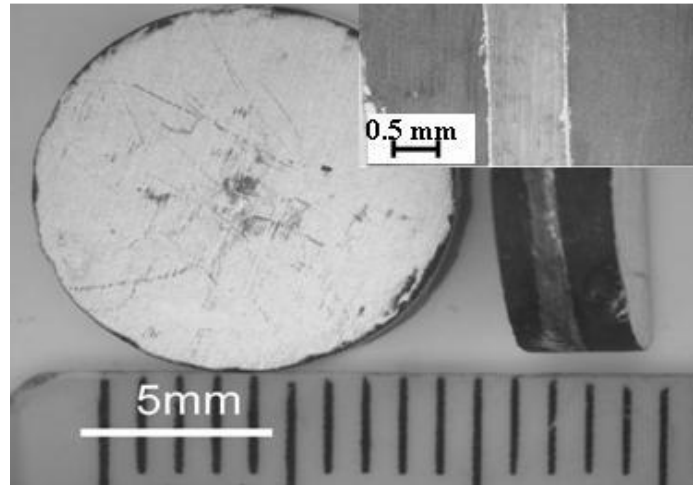


Figure 9.1: Optical image of sintered sample (inset – cross section).

oxide method. Trilayer synthesis has been discussed in chapter 3. Figure 9.1 shows the sintered trilayer sample with dimensions of 3.25 mm in thickness and 11 mm in diameter. Annealing was done after sintering at 800°C for 10 hours under load. In order to polarize the samples, Ag – Pd electrode (DuPont 7174 conductor paste) was applied on top and bottom of the sample. The top electrode layer of the composite was then connected to the top of the [0.9 PZT – 0.1 PZN]. Similarly, bottom electrode of the composite was connected to the bottom electrode of the [0.9 PZT – 0.1 PZN].

9.1.1 Microstructural characterization of trilayer cross section

Figure 9.2(a) shows the low magnification SEM image of the sintered sample with all the layers visible. The interface electrode layers are 10µm thick, center layer is 0.9PZT – 0.1 PZN, whereas outside layers are NCZF. There were some micro and macrocracks formed during the sintering which could be related to the thermal mismatch between these three layers and insufficient homogenization. Figure 9.2(b) shows the magnified view of an interface. The microstructure is dense in both the phases with excellent adherence with the Ag-Pd electrode.

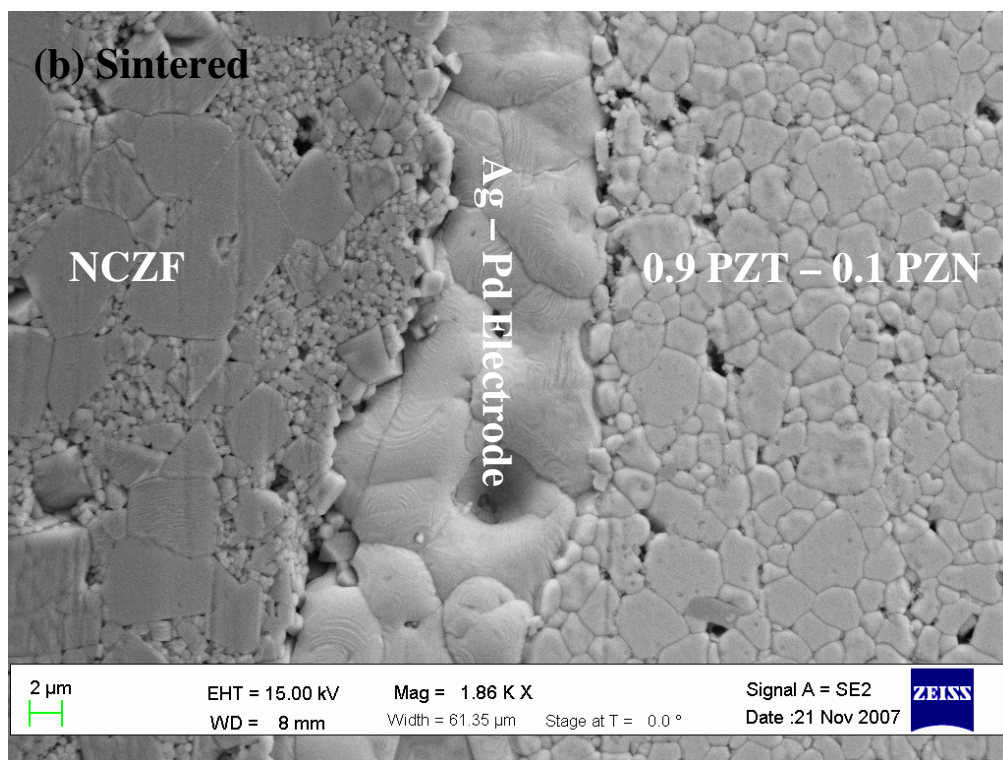
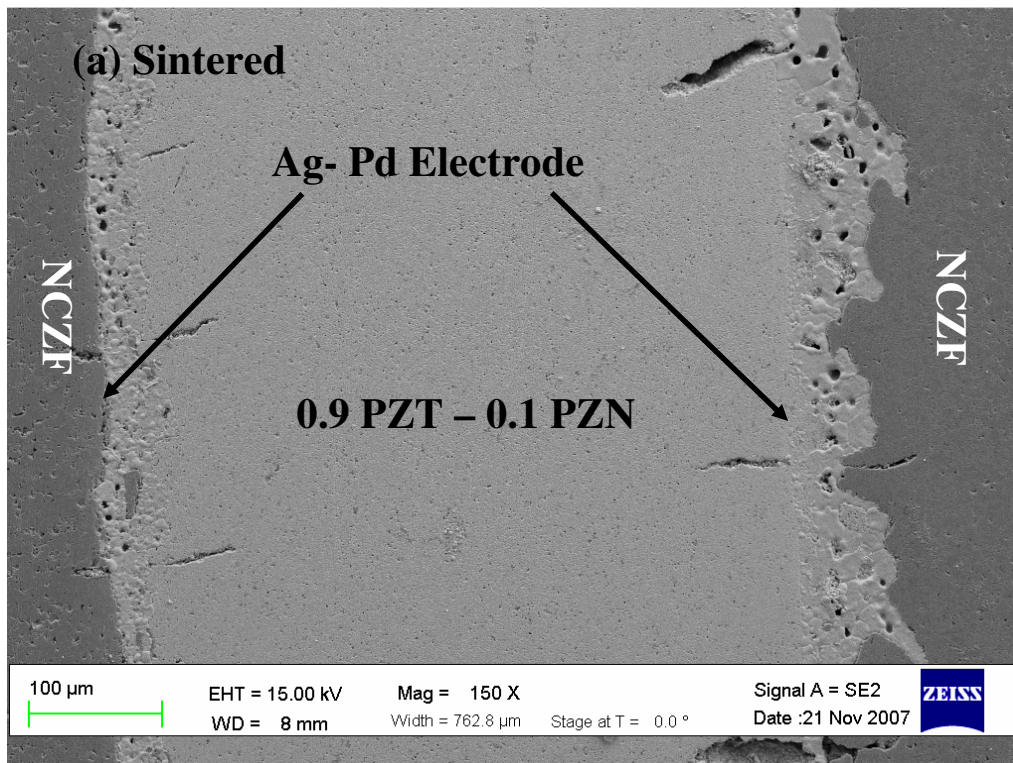


Figure 9.2: SEM micrographs. (a) low magnification image of sintered trilayer sample, (b) interface microstructure.

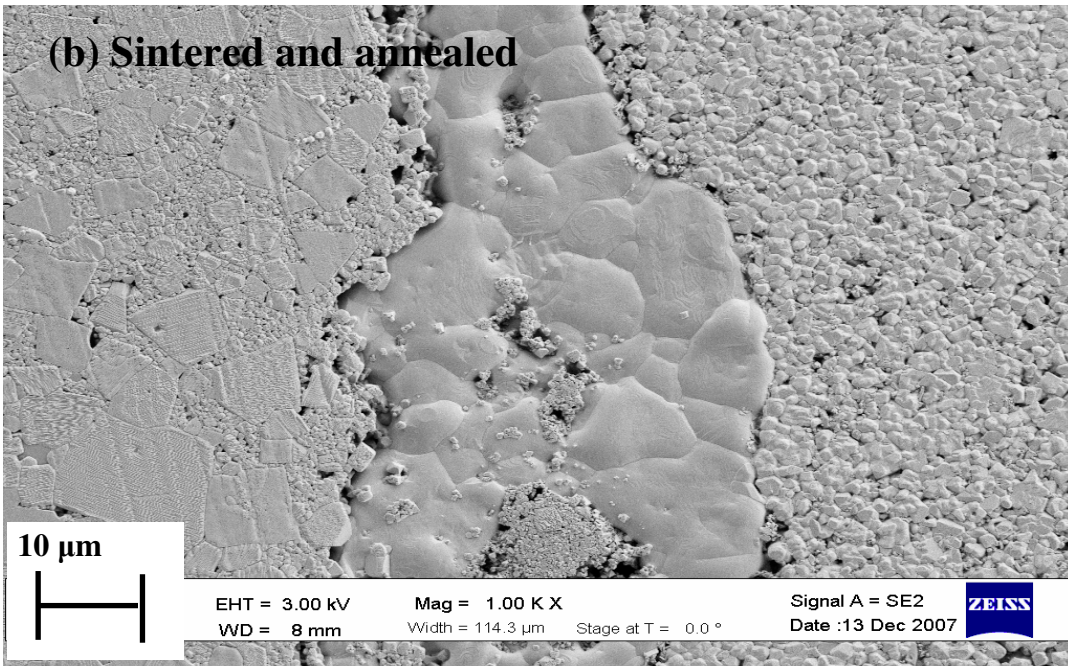
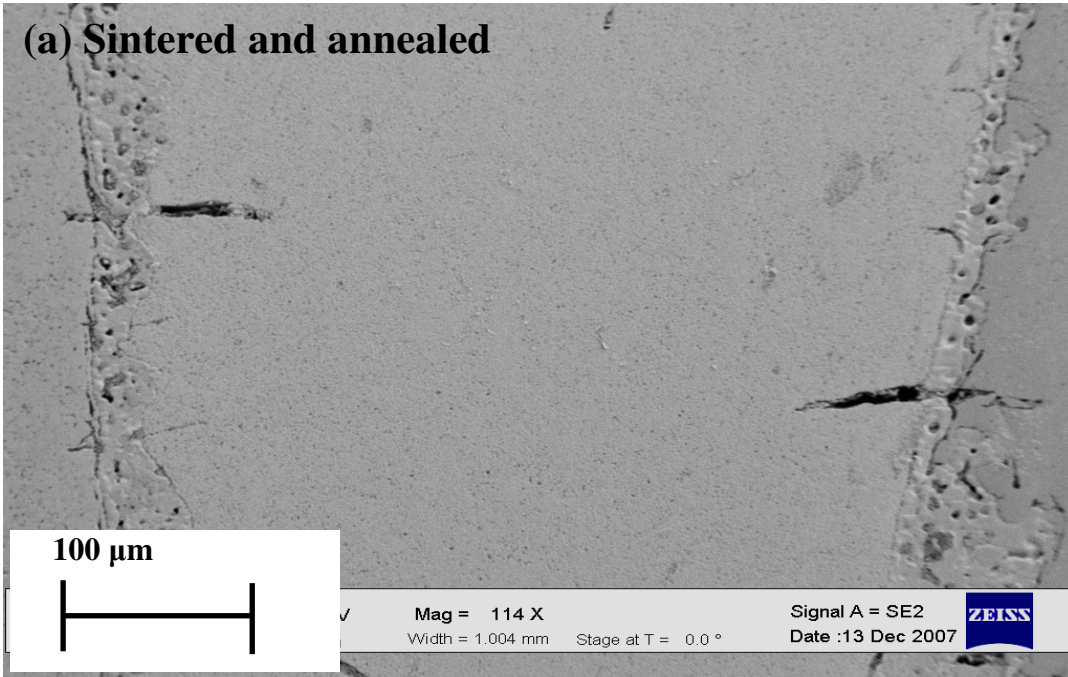


Figure 9.3: SEM micrographs of (a) low magnification image of sintered and annealed sample, (b) interface microstructure of sintered and annealed trilayer sample,

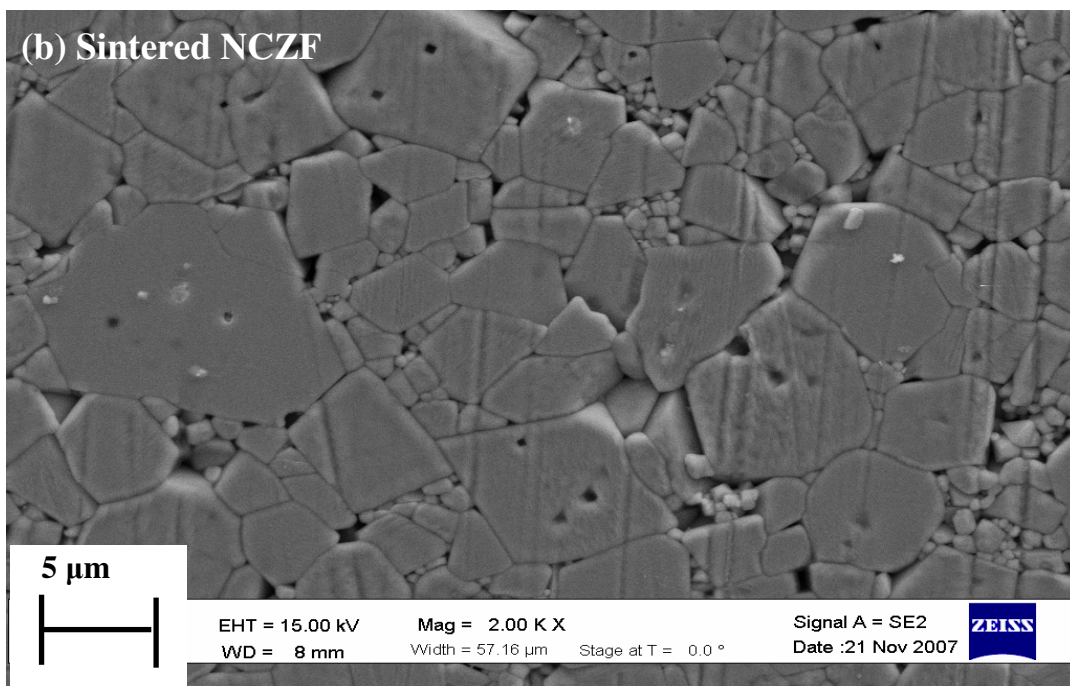
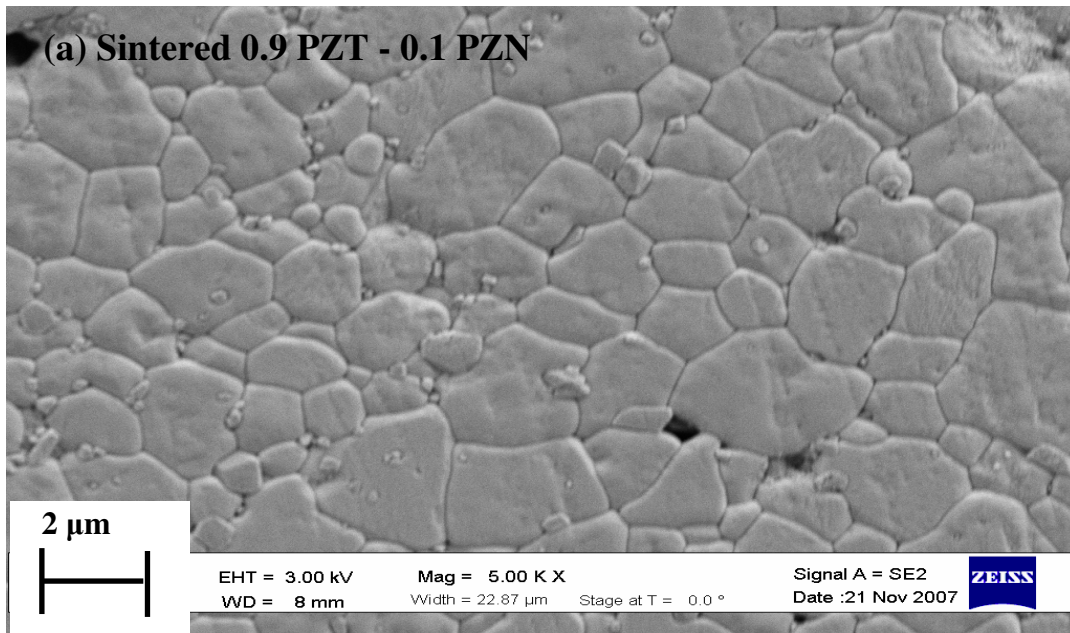


Figure 9.4: SEM micrographs. (a) grain structure of [0.9 PZT – 0.1 PZN] side and (b) grain structure of ferrite side.

Figure 9.3 (a) and (b) shows the low magnification image and interface microstructure of the annealed samples. The annealed samples resulted in the homogenization at the interface reducing the porosity and micro-crack density. Figure 9.4 (a) and (b) shows the high magnification grain structure of the sintered 0.9 PZT - 0.1 PZN and NCZF. The grainsize observed in 0.9 PZT – 0.1 PZN was more than 1µm and that in NCZF in the range of 3–5 µm.

9.1.2 Piezoelectric and dielectric properties of NCZF – [PZT – 0.1 PZN] – NCZF trilayer

Table 9.1 compares the piezoelectric and dielectric properties between sintered and annealed samples. A significant increase in piezoelectric and dielectric properties was observed after annealing which is consistent with our previous results. The magnitude of the electromechanical coefficients d_{33} , g_{33} , ϵ_r/ϵ_0 increased from 204 pC/N, 20.4×10^{-3} V-m/N, and 1132 to 250 pC/N, 22.4×10^{-3} V-m/N, and 1257. The magnitude of the loss factor ($\tan\delta$) decreased from 5.08% to 3.45% at room temperature. The loss factor increased sharply at high temperature which could be related to space charge polarization. At 100 kHz, the Curie temperature observed was around 330°C. Figure 9.5 shows the resonance spectrum of the

Table 9.1: Piezoelectric properties of NCZF – (0.9PZT – 0.1 PZN) – NCZF trilayer after different thermal treatment

| | Sintered | Sintered and Annealed |
|---------------------------------------|---|--|
| d_{33} | 204 pC/N | 250 pC/N |
| Dielectric Constant (at 1 kHz) | 1132 | 1257 |
| Dielectric Loss (at 1 kHz) | 5.08 % | 3.45% |
| g_{33} | 20.4×10^{-3} V-m/N | 22.46×10^{-3} V-m/N |
| k_p | 14% | 16.38% |
| f_s | 258 kHz | 255 kHz |
| f_a | 261 kHz | 258 kHz |

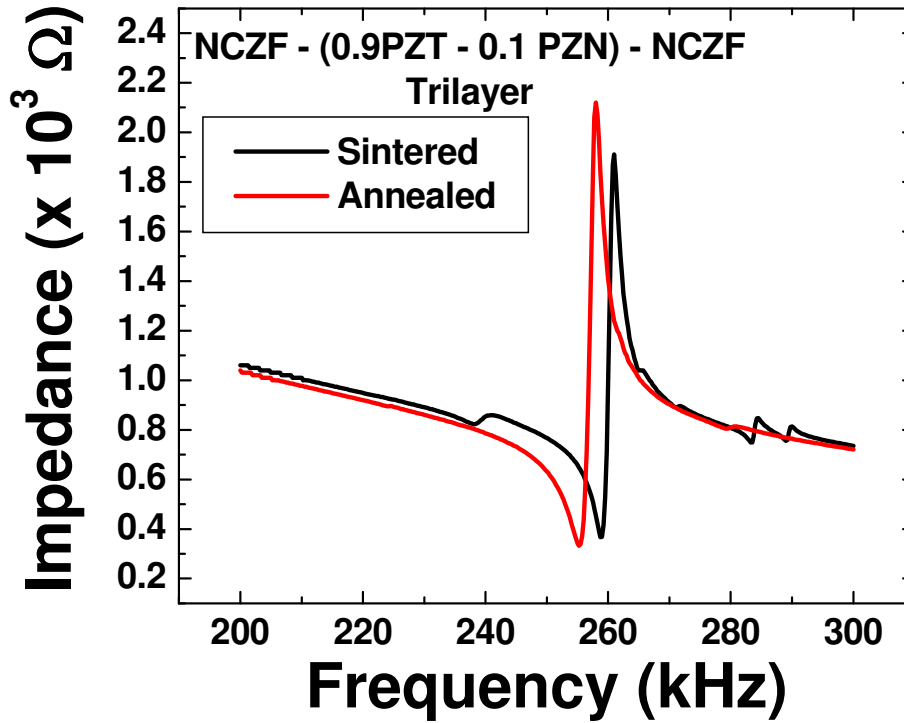


Figure 9.5: Impedance spectrum of the trilayer composite

sintered and annealed samples. Interestingly, the spectrum for annealed sample has less spurious and lower impedance at the resonance indicating higher mechanical quality factor. Figure 9.6 (a) and (b) shows the temperature dependent dielectric properties of the trilayer samples after sintering and annealing respectively. Curie temperature observed was 340°C for sintered sample and 344°C for annealed sample. Room temperature dielectric loss ($\tan \delta$) was found to decrease from r 5% in sintered condition to 3.5% in annealed condition.

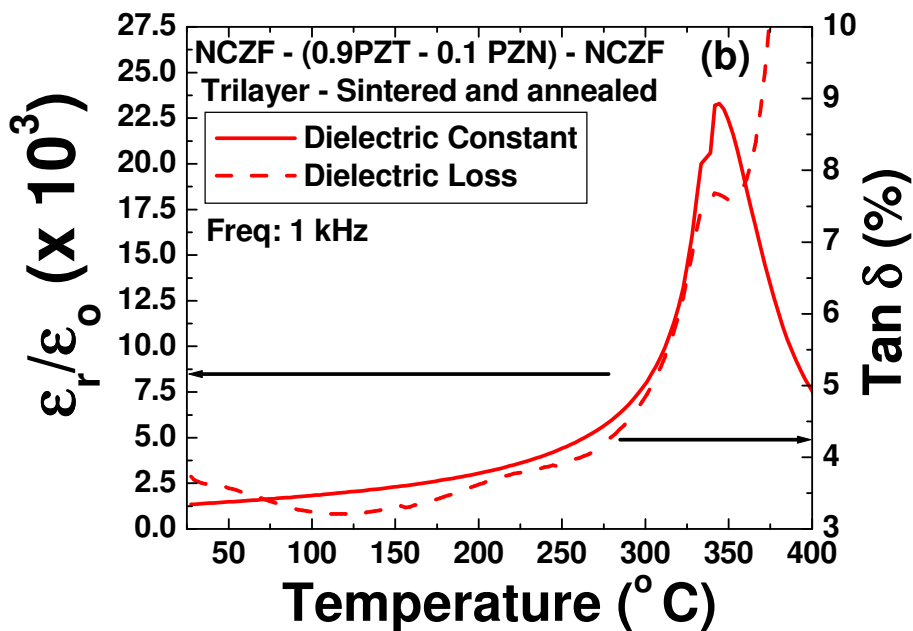
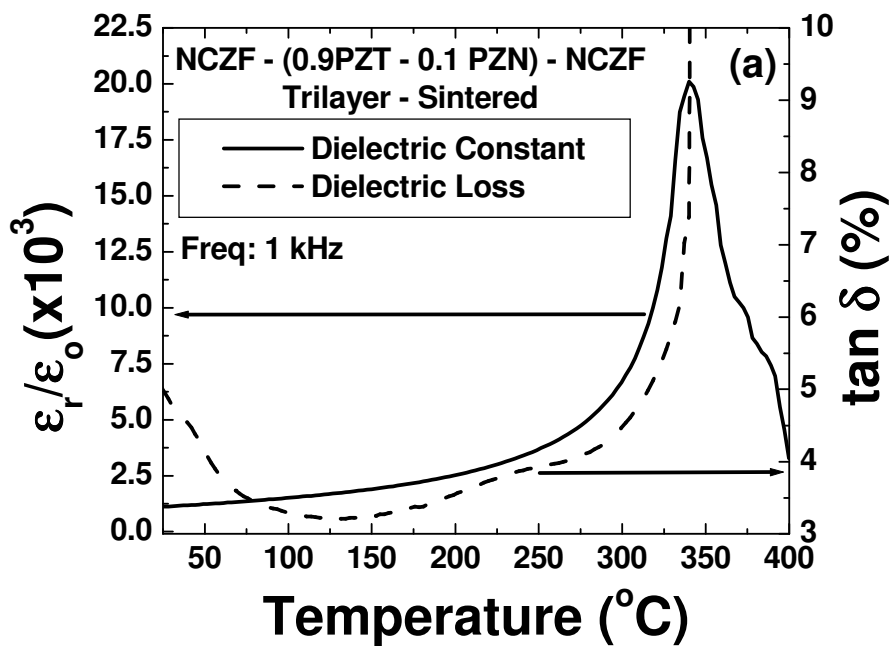


Figure 9.6: Dielectric properties as function of temperature of (a) sintered sample and (b) sintered and annealed sample.

9.1.3 Analysis of NCZF – [PZT – 0.1 PZN] – NCZF trilayer magnetolectric response

Figure 9.7 shows the magnetolectric behavior of trilayer composite. The magnitude of ME coefficient for sintered sample was of the order of 412 mV/cm.Oe with saturation field near 400Oe. Annealed samples showed improved ME coefficient of 494 mV/cm.Oe which is about 20% higher than sintered ones. Srinivasan et. al. have shown that the transverse ME coefficient can be obtained using the following equation [39]:

$$\frac{\delta E_3}{\delta H_1} = \frac{-2d_{31}^p q_{11}^m v^m}{(s_{11}^m + s_{12}^m) \epsilon_{33}^{T,P} v^p + (s_{11}^p + s_{12}^p) \epsilon_{33}^{T,P} v^m - 2(d_{31}^p)^2 v_m} \quad (9.1)$$

$$\frac{\delta E_3}{\delta H_1} = \frac{-2d_{31}^p q_{11}^m \frac{v_m}{v_m + v_p}}{(s_{11}^m + s_{12}^m) \epsilon_{33}^{T,P} \frac{v_p}{v_m + v_p} + (s_{11}^p + s_{12}^p) \epsilon_{33}^{T,P} \frac{v_m}{v_m + v_p} - 2(d_{31}^p)^2 \frac{v_m}{v_m + v_p}} \quad (9.2)$$

As the piezoelectric and magnetostrictive layers area are same, volume fraction can be written in terms of thickness ratio as shown in Eq. (9.3)

$$\frac{\delta E_3}{\delta H_1} = \frac{-2d_{31}^p q_{11}^m \frac{t_m}{t_m + t_p}}{(s_{11}^m + s_{12}^m) \epsilon_{33}^{T,P} \frac{t_p}{t_m + t_p} + (s_{11}^p + s_{12}^p) \epsilon_{33}^{T,P} \frac{t_m}{t_m + t_p} - 2(d_{31}^p)^2 \frac{t_m}{t_m + t_p}} \quad (9.3)$$

where d_{31}^p is the piezoelectric coefficient, v^m and v^p are the volume of magnetic and piezoelectric phase, t^m and t^p are the thickness of magnetic and piezoelectric phase, s_{11}^p, s_{12}^p are the elastic compliances for piezoelectric phase, s_{11}^m, s_{12}^m are the elastic compliances for magnetostrictive phase, q_{11} is the piezomagnetic coefficient of the magnetic phase and $\epsilon_{33}^{T,P}$ is the permittivity of the piezoelectric phase. For a radial mode disk, s_{11}^p can be expressed as:

$$s_{11}^p = \frac{\eta_1^2}{\rho(2\pi f_s a)^2 [1 - (\sigma^p)^2]} \quad (9.4)$$

where η_1 is frequency constant, σ^p is the planar poisons ratio, f_s is the resonance frequency, a is the radius and ρ is the density (~ 7.52 gm/cc). The values for η_1 and σ^p can be found from the IEEE Standard on Piezoelectricity (Table 12)²⁶, where η_1 and σ^p values are listed as a function of the ratio of 1st overtone (~ 648 kHz for sintered samples) to fundamental resonance frequency (255 kHz). For the ratio of 2.512 (for sintered sample), η_1 and σ^p values are 2.065 and 0.341 respectively. Using these values s_{11}^p can be calculated as 8.588×10^{-12} m²/N for the sintered sample. The magnitude of transversal coupling factor, k_{31} , can be calculated from Eq.(9.5) as: [86]

$$k_{31}^2 = k_p^2 \frac{(1 - \sigma^p)}{2} \quad (9.5)$$

The values of k_p are listed in Table 1. Using these values k_{31} can be calculated to be as 0.085.

If we know k_{31} and s_{11}^E , then d_{31} can be calculated to be as 23.56×10^{-12} V/m using the following equation:

$$k_{31}^2 = \frac{d_{31}^2}{(s_{11}^E \epsilon_{33}^T)} \quad (9.6)$$

The magnitude of s_{12}^E was found to be -2.935×10^{-12} m²/N by using Eq. (9.7) [159].

$$k_p^2 = \frac{2d_{31}^2}{[(s_{11}^E + s_{12}^E)\epsilon_{33}^T]} \quad (9.7)$$

Using the values of s_{11}^m, s_{12}^m as 6.5×10^{-12} m²/N and -2.4×10^{-12} m²/N²⁵ and q_{11} as -65×10^{-9} /Oe (at 400 Oe field), the theoretical ME coefficient can be calculated to be 437.1 mV/cm.Oe ~ which is close to the experimental value of 412 mV/cm.Oe. Theoretical calculation shows slightly lower values (468 mV/cm.Oe) than the experimental one (494 mV/cm.Oe) for annealed samples.

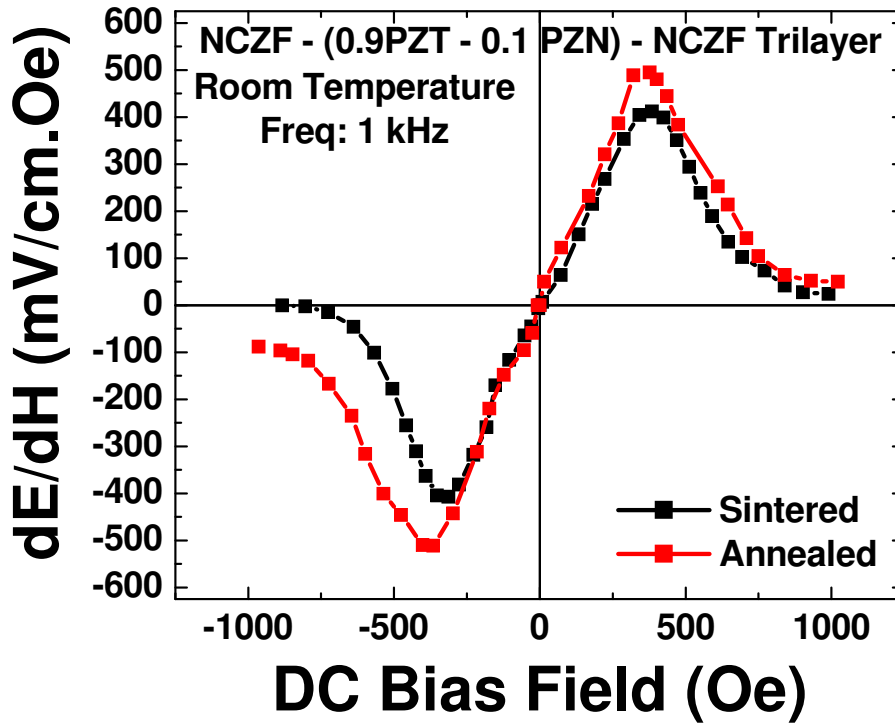


Figure 9.7: Magnetolectric coefficient as a function of dc bias field.

9.2 Effect of Thickness

The thickness ratio plays an important role in the trilayer geometry. From the expression for magnetolectric coefficient for layered structure, it can be found that the magnetolectric coefficient depends on piezoelectric coefficient (d_{31}), permittivity (ϵ_{33}), elastic compliance (s_{11} and s_{12}), thickness (t_p) of the piezoelectric phase, piezomagnetic coefficient (q_{11}), elastic compliance (s_{11} and s_{12}) and thickness (t_m) of the magnetic phase. Equation 9.3 can be rewritten as:

$$\frac{\delta E_3}{\delta H_1} = \frac{-2d_{31}^p q_{11}^m \frac{t_m}{t_p}}{(s_{11}^m + s_{12}^m)\epsilon_{33}^{T,P} + (s_{11}^p + s_{12}^p)\epsilon_{33}^{T,P} \frac{t_m}{t_p} - 2(d_{31}^p)^2 \frac{t_m}{t_p}} \quad (9.9)$$

In order to experimentally investigate the effect of thickness ratio and achieve a higher magnetoelectric coefficient, composites of different [0.9 PZT – 0.1 PZN] thicknesses were synthesized.

9.2.1 Microstructural Investigations of different thickness ratio

NCZF composition was used as the magnetostrictive layer and 0.9 PZT – 0.1 PZN composition was used as piezoelectric layer. The amount of NCZF was fixed at 0.7 gm for top and bottom layer whereas the weight of 0.9PZT – 0.1 PZN was varied from 0.8 to 0.3 gm. The interface electrode used was Dupont 6160 Ag – Pd conductor paste. The sintering was done at 900°C for 3 hrs using a load of 450 gm which is equivalent to 50 kPa. After sintering each composite were cross sectioned and polished for scanning electron microscopy. Figure 9.8 to 9.10 shows the cross sections of each composite. The thickness of interface electrode observed in these composites was in the range of 5 – 10 µm. The adherence of the interface electrode with [0.9 PZT – 0.1 PZN] and NCZF was found to be good. The [0.9 PZT – 0.1 PZN] grainsize observed in all the composites was above 1µm as can be seen from Fig. 9.11. All the composites show piezoelectric charge constant above 225 pC/N, dielectric constant above 1150 and dielectric loss of 3 – 5%. X-ray elemental analysis was performed using the

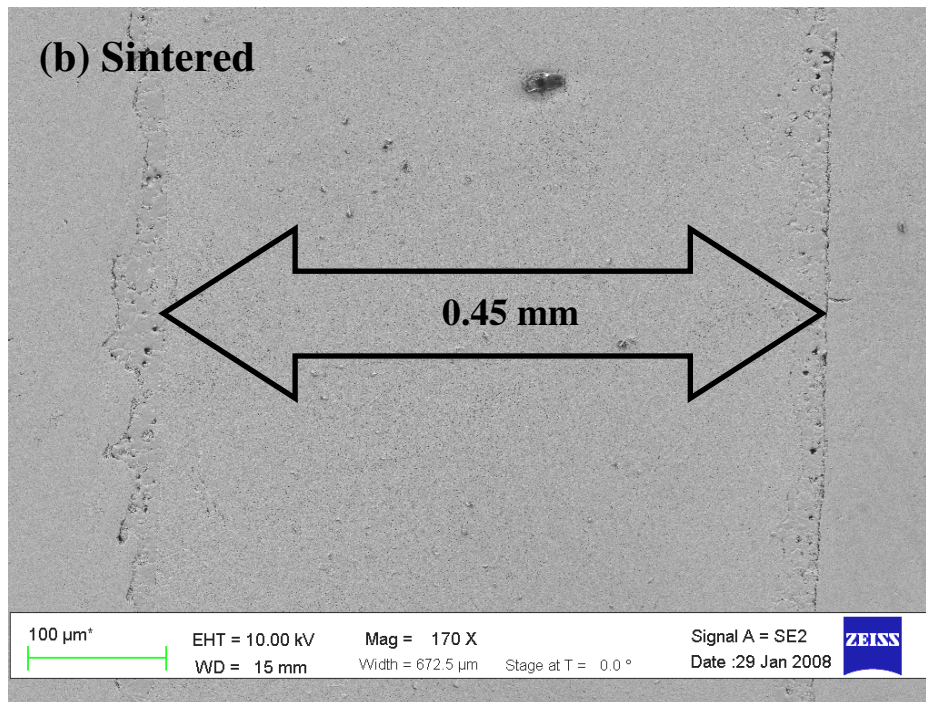
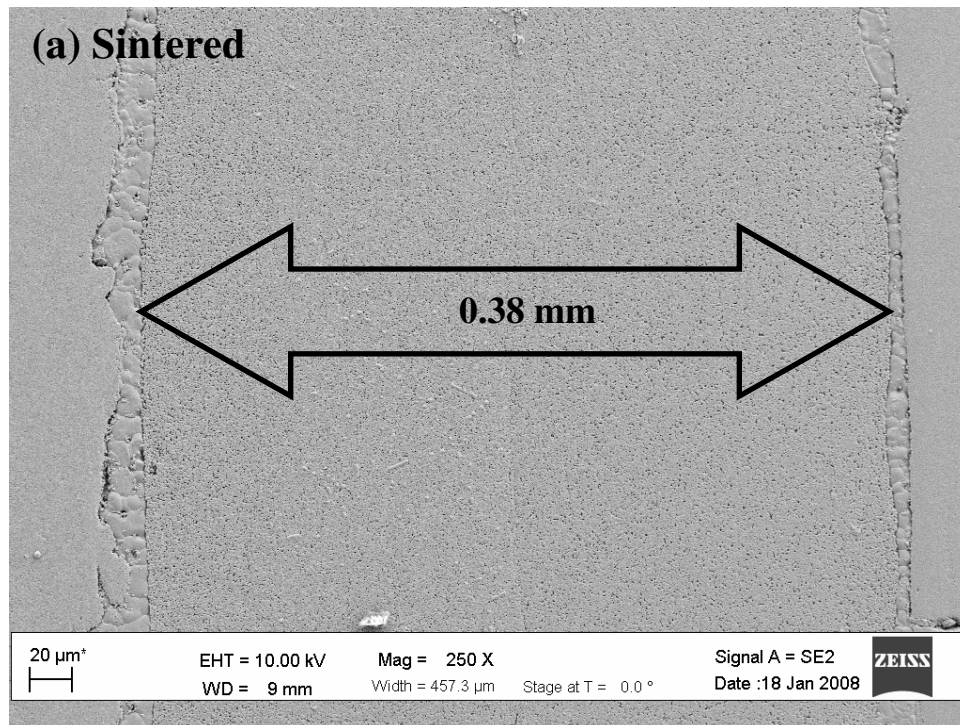


Figure 9.8: Composite of Different thicknesses, (a) 0.38 mm, (b) 0.45 mm.

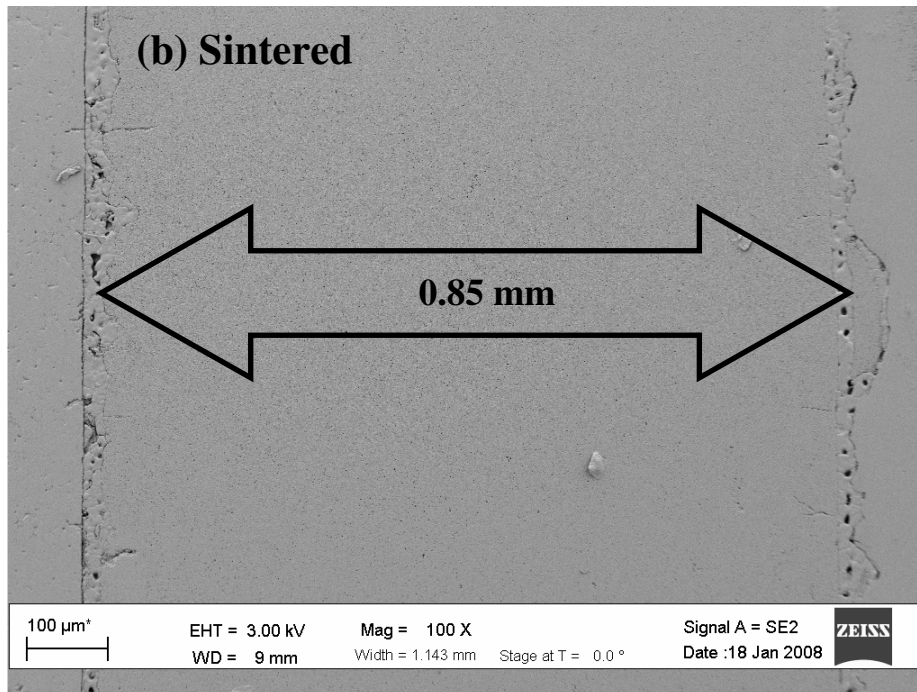
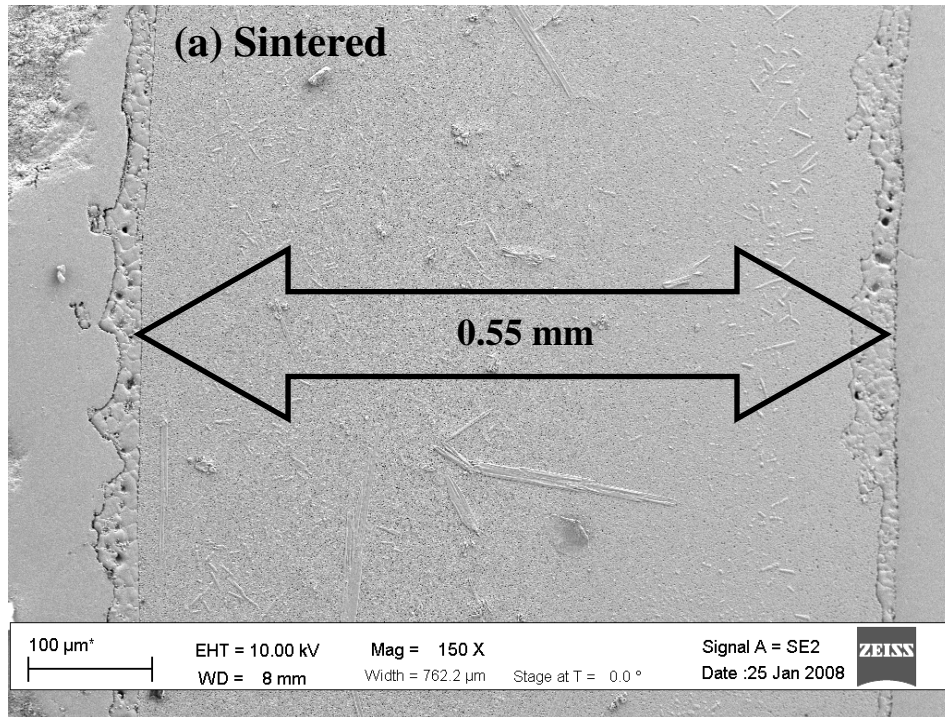


Figure 9.9: Composite of Different thicknesses, (a) 0.55 mm, (b) 0.85 mm.

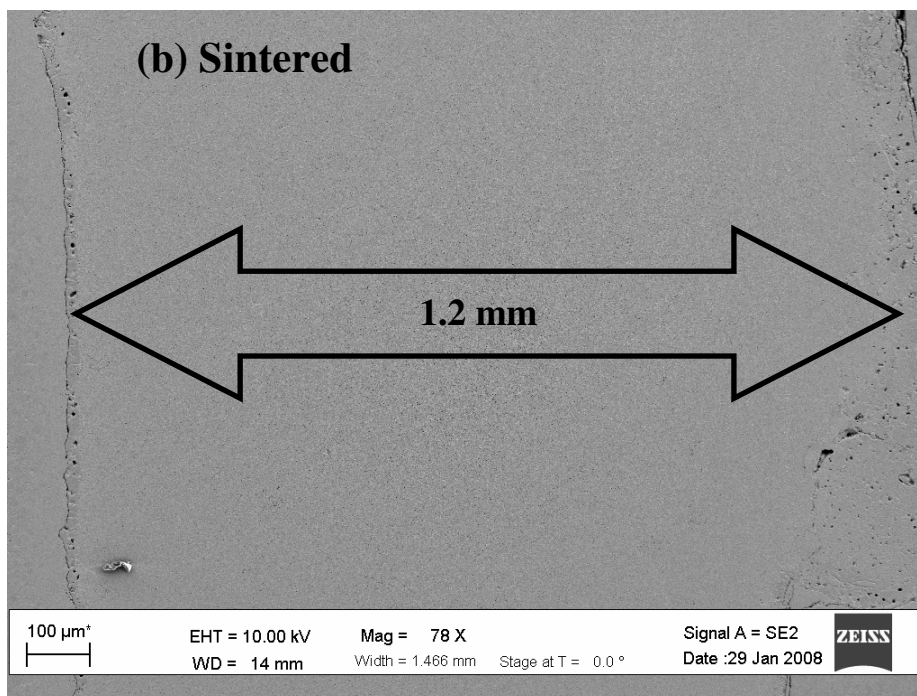
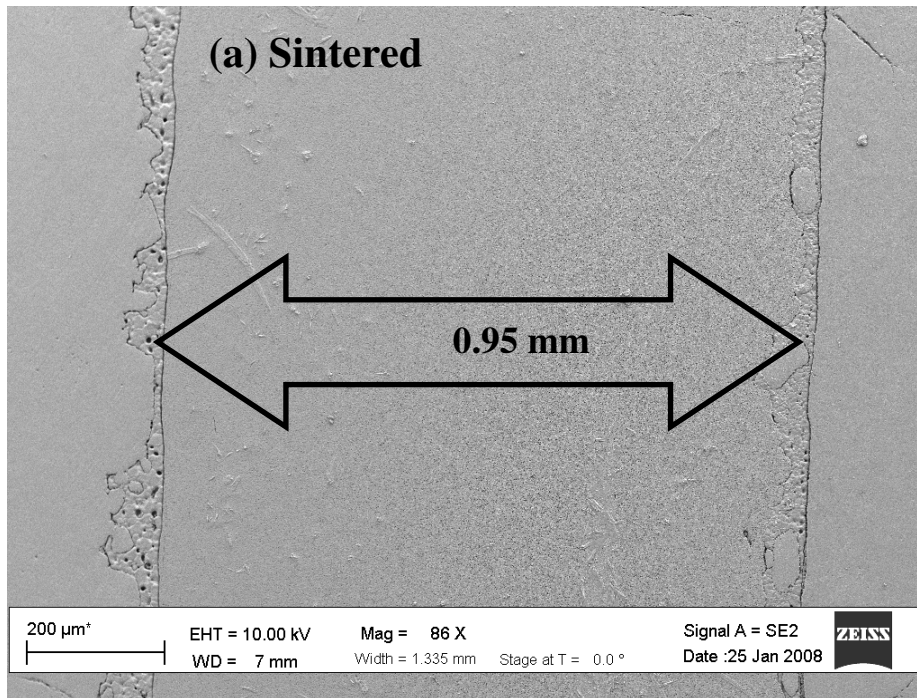


Figure 9.10: Composite of Different thicknesses, (a) 0.95 mm and (b) 1.2 mm.

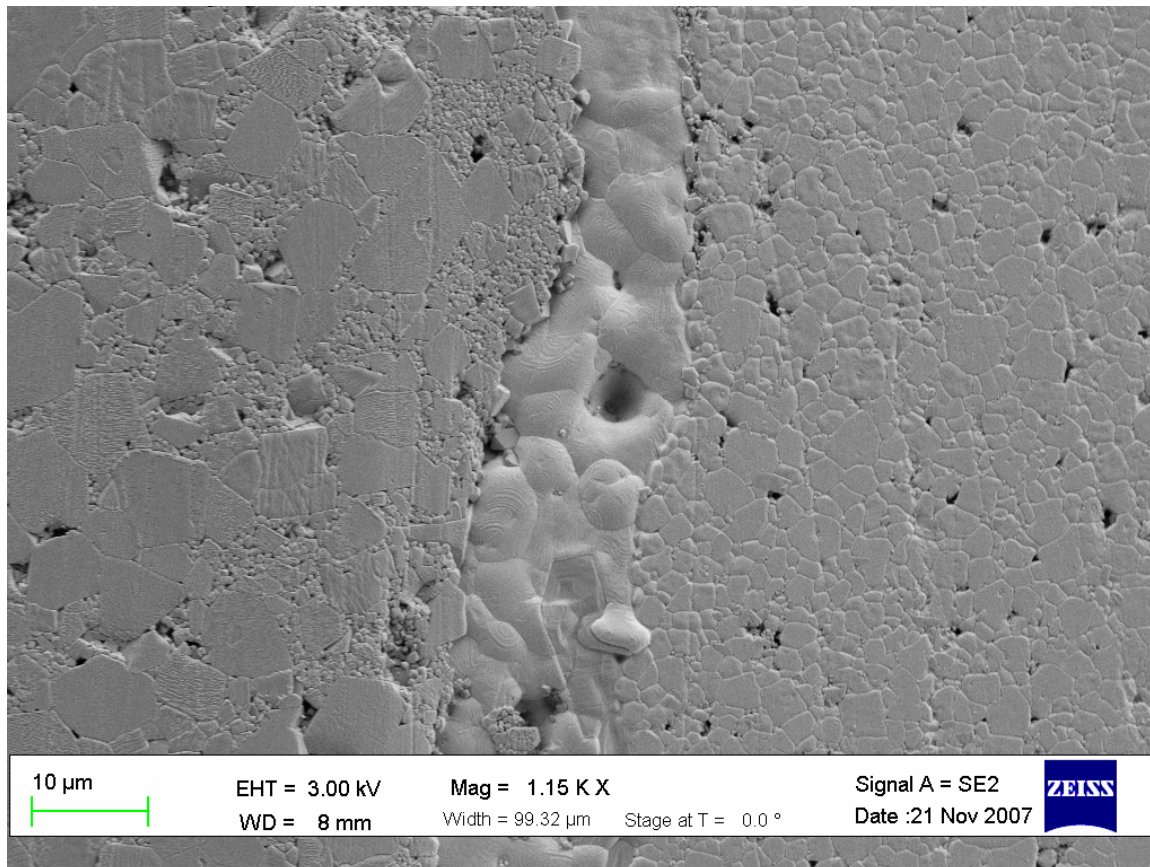


Figure 9.11: Interface microstructure of trilayer sample showing NCZF, electrode and [0.9 PZT – 0.1 PZN] layer.

scanning electron microscope in order to identify any elemental diffusion through the electroded interface. Figure 9.12 shows the elemental analysis of Pb, Fe and Ag. A strong concentration of Pb was found on the [0.9 PZT – 0.1 PZN] side and Fe on the NCZF side. Ag was found to be concentrated in the electroded area. By adding this interface electrode the piezoelectric property was improved from 80 pC/N for cofired bilayer to 225 pC/N for trilayer composite. An improved dielectric constant and remarkable decrease in dielectric loss (from 29% to 5%) was recorded.

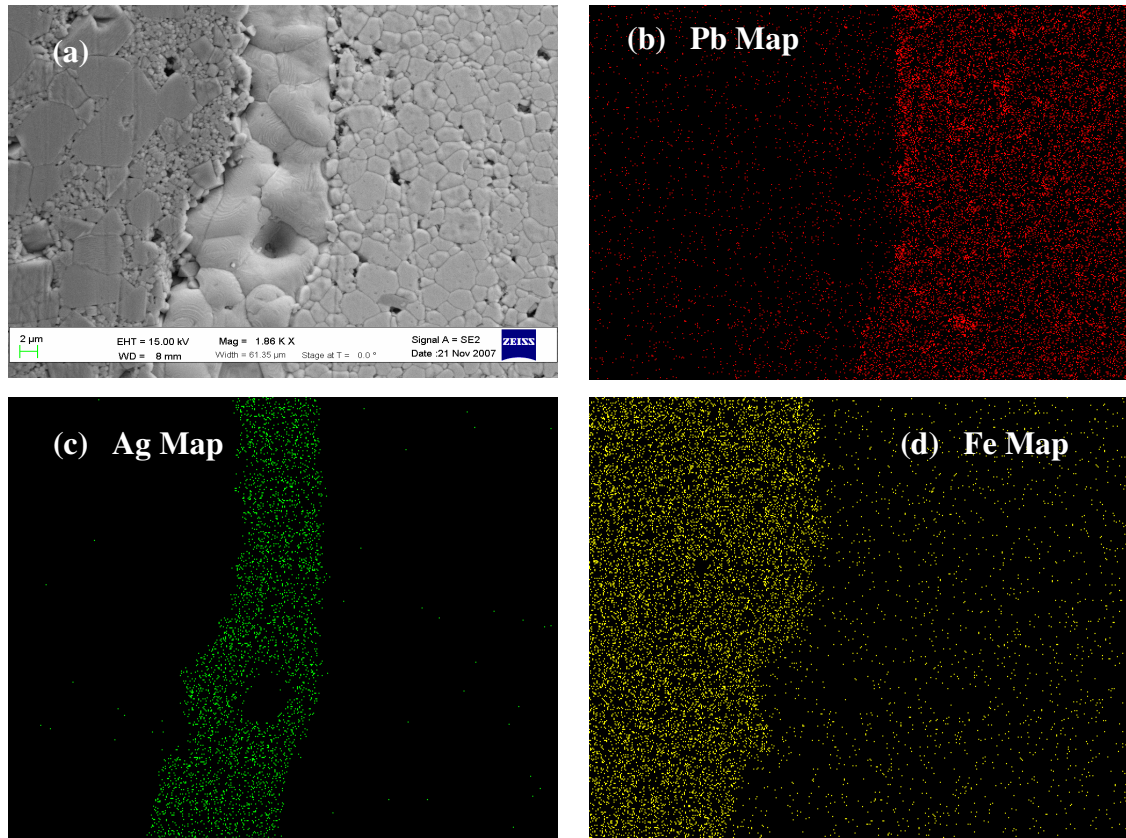


Figure 9.12: X-ray elemental mapping of trilayer sample, (a) image of trilayer sample, (b) Pb map, (c) Ag map and (d) Fe map.

9.2.2 Effect of [0.9 PZT – 0.1 PZN] thickness and orientation on ME coefficient

Equation (9.9) shows the theoretical dependency of magnetolectric coefficient on the magnetostrictive to piezoelectric layer thickness ratio. Figure 9.13 shows the magnetolectric coefficient as a function of DC bias field for different thickness of [0.9 PZT – 0.1 PZN]. It was found that as the thickness ratio of magnetic layer to piezoelectric layer increases (thickness of [0.9 PZT – 0.1 PZN] decreases as the magnetic layer thickness was fixed) magnetolectric coefficient increases from 354 to 526 mV/cm.Oe. The maximum magnetolectric coefficient of 526 mV/cm.Oe was found when the thickness ratio was 5.3 ([0.9 PZT – 0.1 PZN] thickness was 0.45 mm). The theoretical value of magnetolectric coefficient calculated using Eq. (9.9) and plotted in Fig. 9.14 with the experimental values. The theoretical values fit with the experimental values. The experimental values show low coefficient of 350 mV/cm.Oe for [0.9 PZT – 0.1 PZN]

thickness of 1.2 mm (ratio: 2) and it increases as the ratio increases. The increase in ME coefficient with decrease in [0.9 PZT – 0.1 PZN] thickness layer can be explained in terms of increased compressive stress on [0.9 PZT – 0.1 PZN] layer. Ryu et al. have shown that the compressive and tensile stress in [0.9 PZT – 0.1 PZN] and ferrite layer can be calculated using beam theory given as:

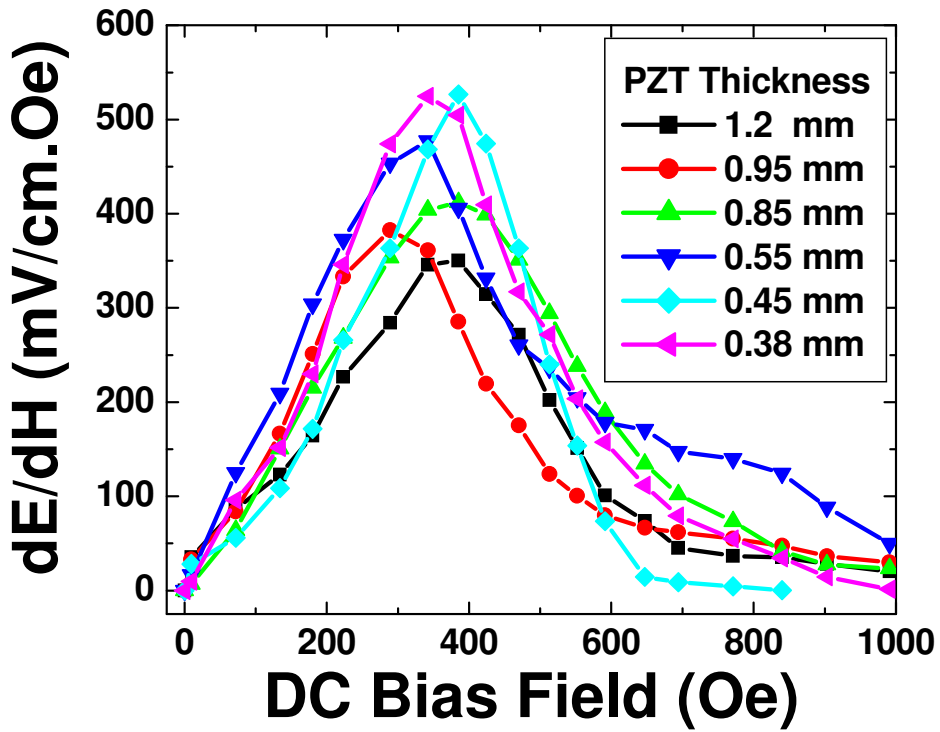


Figure 9.13: Magnetolectric Coefficient as a function of DC bias field for different thickness of [0.9 PZT – 0.1 PZN].

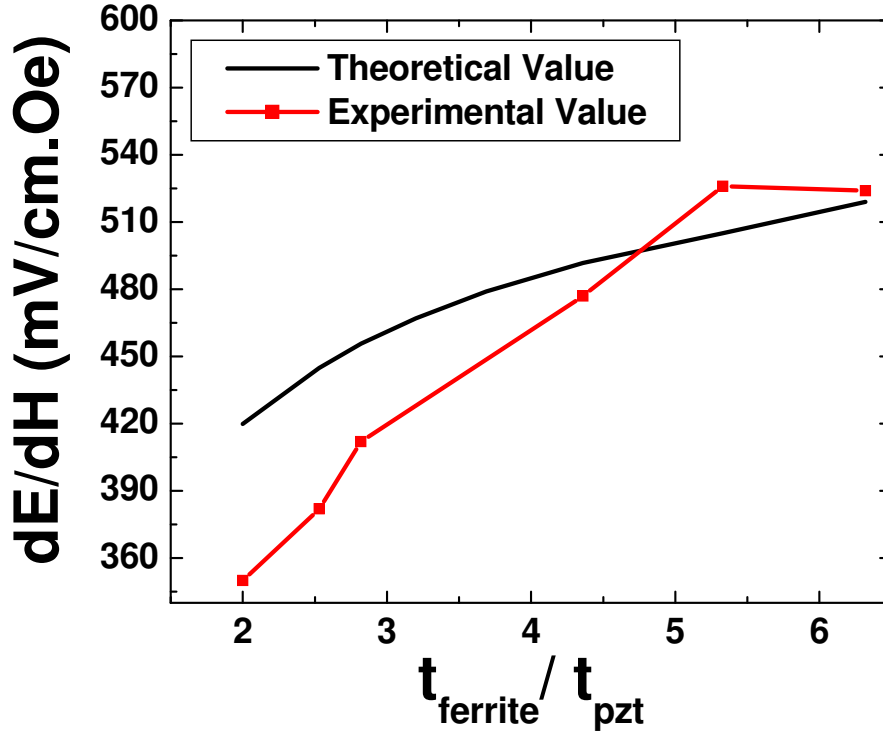


Figure 9.14: Comparison between theoretical and experimental magnetoelectric coefficient for different thickness ratio of magnetic to piezoelectric layer.

$$\sigma_{31f}^E = \frac{E_f E_p t_p \Delta \epsilon_o}{(1 - \gamma)(2E_f t_f + E_p t_p)} \quad (9.9)$$

$$\sigma_{31p}^E = -\frac{2E_f E_p t_p \Delta \epsilon_o}{(1 - \gamma)(2E_f t_f + E_p t_p)} \quad (9.10)$$

As the thickness of the ferrite layer remains same (1.2 mm on top and bottom) the compressive stress on [0.9 PZT – 0.1 PZN] layer can be increased if the thickness of the [0.9 PZT – 0.1 PZN] layer is decreased. The compressive stress is related to magnetoelectric coefficient as:

$$\frac{dE}{dH} = \frac{2 \cdot g_{31} \cdot \sigma_{31P}^E}{H_{ac}} \quad (9.11)$$

As the compressive stress in [0.9 PZT – 0.1 PZN] is increased, magnetoelectric coefficient increases.

Figure 9.15 shows the magnetic field (AC and DC) orientation dependence of ME coefficient for trilayer composite ([0.9 PZT – 0.1 PZN] thickness = 0.45 and 0.85 mm). It was found that composite shows an increase in ME coefficient from zero degree (when magnetic field direction is parallel to the sample surface) to 45°. Maximum magnetoelectric coefficient of 589 and 463 mV/cm.Oe was measured at 45°. As the angle is increased beyond 45°, the ME coefficients starts to drop rapidly and when the sample surface is perpendicular to the magnetic field direction (T – T mode), a low value of 274 and 134 mV/cm.Oe was observed. It has been shown that with areal angle change, strain of the magnetic phase changes and is maximum around 51°. As the strain increases compressive stress on [0.9 PZT – 0.1 PZN] also increases which contributes to the high magnetoelectric coefficient as expressed by Eq. (12). At 90° angle the maximum magnetoelectric coefficient was found to have low magnitude.

9.3 Effect of [0.9 PZT – 0.1 PZN] Multilayering

In our trilayer magnetoelectric composite based on NCZF – [PZT – PZN] – NCZF composition optimum d_{33} and dielectric constant was found to be 225 pC/N and 1150. In order to achieve higher piezoelectric and dielectric constant it is necessary to change the electrode pattern of the [0.9 PZT – 0.1 PZN] layer. In this section, the introduction of stacked [0.9 PZT – 0.1 PZN] configuration in trilayer geometry will be discussed. [0.9 PZT – 0.1 PZN] stacking is most common design in actuator application. This type of stack actuator design provides large coupling, fast response time and strong force. In our trilayer ME composite we incorporated the stacked PZT-PZN as intermediate layer between two NCZF layers.

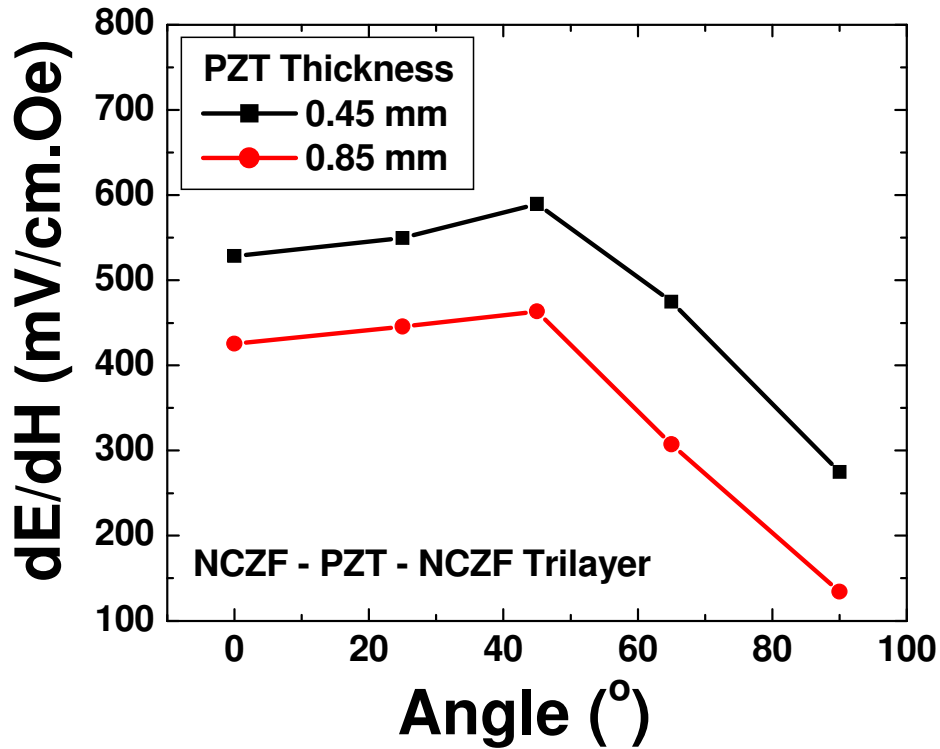


Figure 9.15: Effect of orientation on ME coefficient of NCZF – [PZT – 0.1 PZN] – NCZF trilayer composite with two different [0.9 PZT – 0.1 PZN] thickness

9.3.1 Design and synthesis of NCZF – [0.9 PZT – 0.1 PZN] (Stack) – NCZF trilayer

Figure 9.16 shows the schematic of new trilayer design with stacked PZT – PZN. Same fabrication process was used for the synthesis of new design. But instead of single PZT - PZN layer there were three PZT – PZN layer and interdigital electrode layer along thickness direction. The yellow layer and the black lines are identified as PZT – PZN and electrodes respectively. To improve the sinterability of PZT – PZN, 0.5 wt% of CuO was doped. The sintering temperature and time was 900° C for 3 hours with very slow heating and cooling rate (~ 1°C/min). Pressure applied during sintering was 50 KPa to avoid any delamination. After sintering the trilayer was cross sectioned and the optical images were taken in order measure

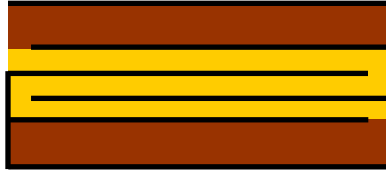


Figure 9.16: Schematic diagram for NCZF – Stack [0.9 PZT – 0.1 PZN] – NCZF trilayer ME composite.

the apparent thickness of the [0.9 PZT – 0.1 PZN]. It was found that each layer of the [0.9 PZT – 0.1 PZN] is around 300 μm with a combined thickness of 0.9 mm. NCZF layers were found to have thickness of 1.2 mm. Figure 9.17 shows the optical image of the cross section of NCZF – stack PZT - PZN – NCZF trilayer.

9.3.2 Piezoelectric and dielectric properties of NCZF – Stack (0.9 PZT- 01. PZN) – NCZF trilayer

Table 9.2 shows the piezoelectric and dielectric properties of these newly designed composites. The piezoelectric constant (d_{33}) increased from 204 to 535 pC/N and dielectric constant from 1132 to 5500. However, the dielectric loss of stack [0.9 PZT – 0.1 PZN] increased from 5 to 13.4%, which may be due to the diffusion across the Ag – Pd electrode, which is a conductive layer. The increase in electromechanical coupling constant from 0.14 to 0.21 was observed. Figure 9.18 shows the impedance spectrum of the trilayer ME composite. The resonance frequency was measured to be 523 kHz which is higher than that of single layer [0.9 PZT – 0.1 PZN] which shows resonance at 258 kHz for same dimensions. Also the bandwidth (difference between resonance and anti resonance) was found to be higher (17 kHz) in case of trilayer composite with stack actuator configuration.

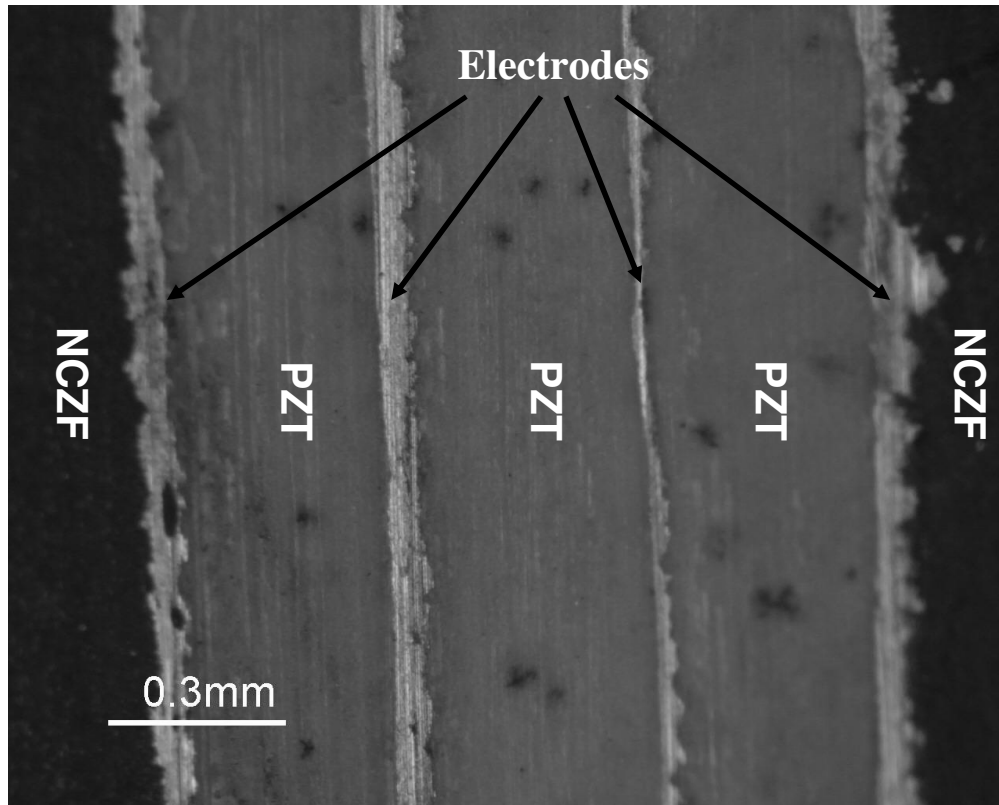


Figure 9.17: Cross sectional optical image of NCZF – Stack [0.9 PZT – 0.1 PZN] – NCZF trilayer.

Table 9.2: Piezoelectric and dielectric properties of NCZF – Stack [0.9 PZT – 0.1 PZN] – NCZF.

| | |
|---------------------------------------|-----------------|
| | Sintered |
| d_{33} | 535 pC/N |
| Dielectric Constant (at 1 kHz) | 5500 |
| Dielectric Loss (at 1 kHz) | 13.4 % |
| k_p | 21% |
| f_s | 523 kHz |
| f_a | 540 kHz |

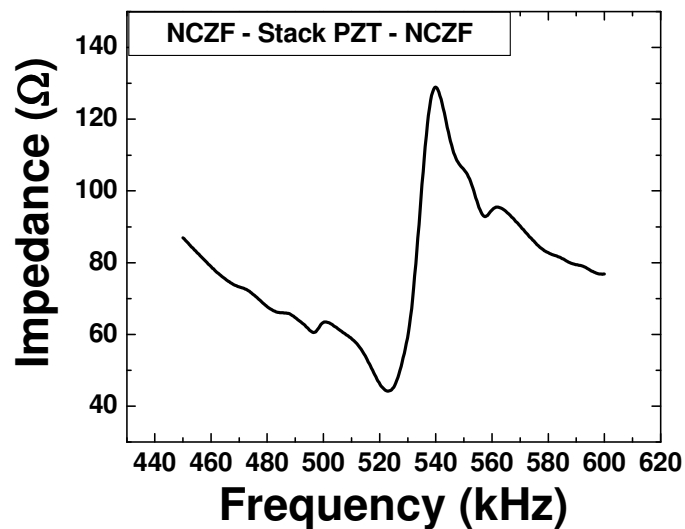


Figure 9.18: Impedance spectrum for NCZF – Stack [0.9 PZT – 0.1 PZN] – NCZF trilayer.

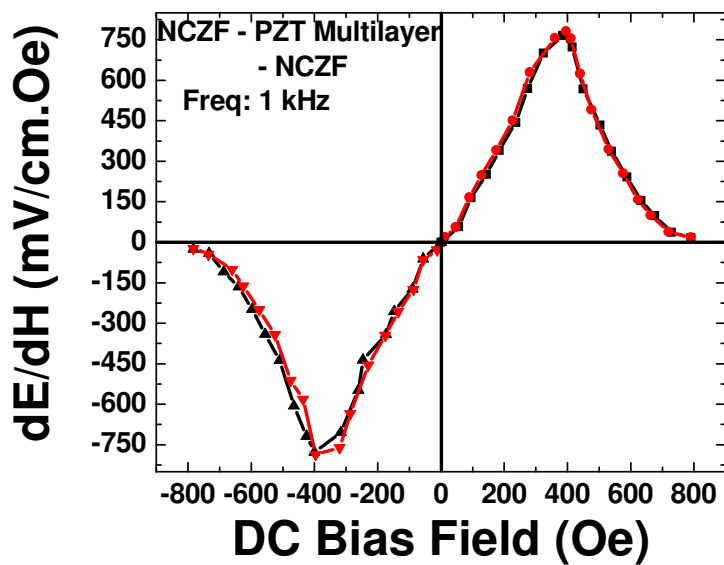


Figure 9.19: Magnetoelectric coefficient of multilayer [0.9 PZT – 0.1 PZN] based trilayer composite.




9.3.3 Magnetolectric coefficient of stack [0.9 PZT – 0.1 PZN] based trilayer

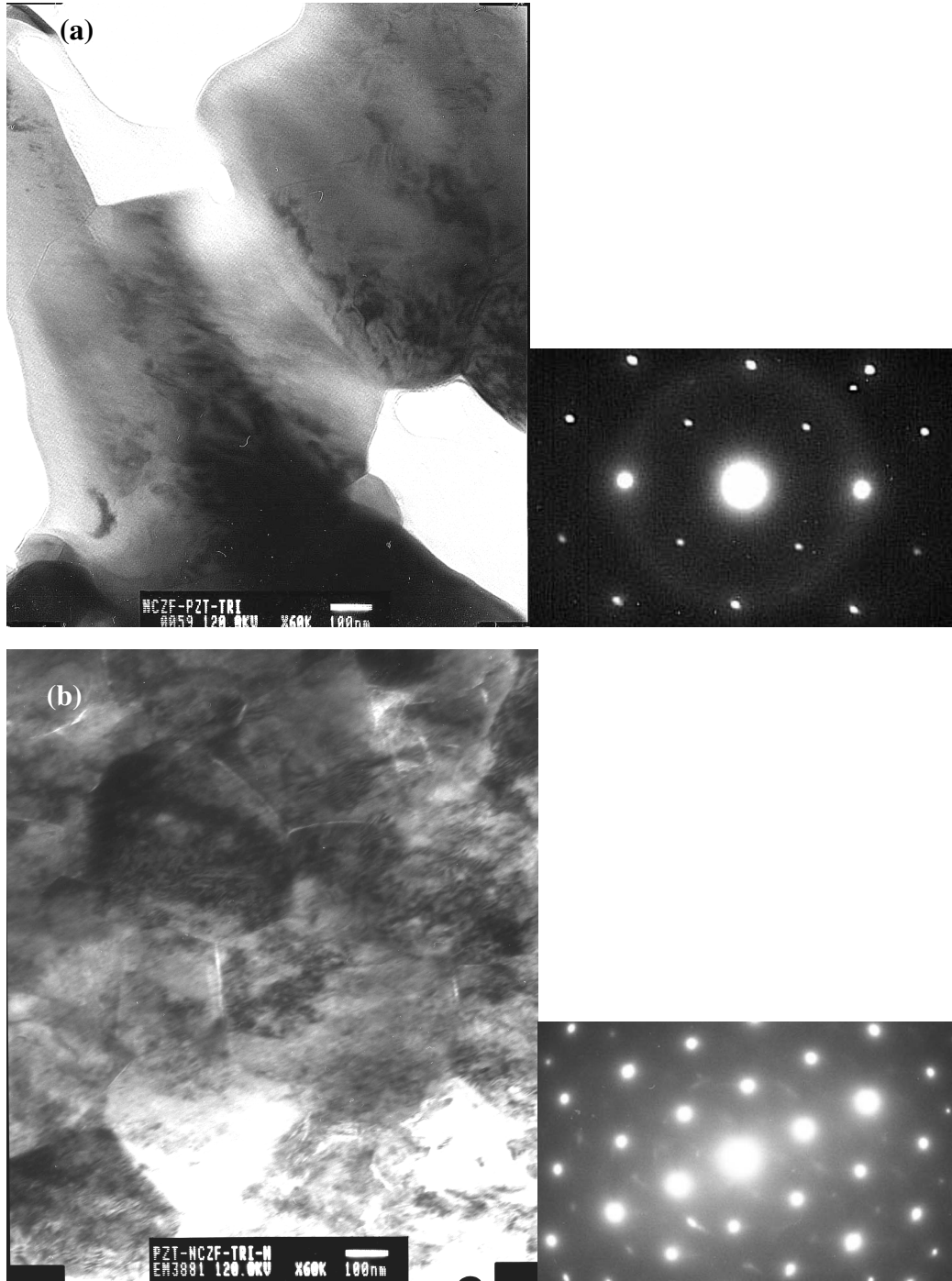
Figure 9.19 shows the magnetolectric coefficient of stack PZT based trilayer composite. It shows a peak coefficient of 782 mV/cm.Oe at 400Oe magnetic DC bias. In order to check whether there is any hysteresis behavior shown by this sample, the ME coefficient was measured from negative to positive high field and vice-versa. It was found that there is very small hysteresis in the response. Compared to the single layer PZT-PZN in trilayer configuration (412 mV/cm.Oe), stack PZT-PZN shows much higher ME coefficient.

9.3.4 Microstructure of individual phases near interface

Figure 9.20 (a) and (b) show the TEM micrographs of PZT – PZN and NCZF phases close to the interface. Inset of each image shows the SAED pattern. From the diffraction pattern, pure piezoelectric and magnetic phases can be identified as there is no super lattice structure. The grainsize observed was around 1 μm for piezoelectric phase and ~ 500 nm for NCZF phases. The lattice parameter was calculated to be: $a = 4.04$ and $c = 4.11$ \AA with tetragonality (c/a ratio) of 1.017. Lattice constant for NCZF was calculated as 8.41 \AA . The micrographs were taken within 10 μm from the interface on both sides. Table 9.3 compares the geometry, lattice constant, ME coefficient and DC bias field of bulk, bilayer and trilayer

Table: 9.3: Comparison between bulk, bilayer and trilayer ME composite

| Composite | Geometry | Lattice Constant | ME coefficient | DC Bias |
|-----------|---|---|---|---------------------------|
| Bulk |  | PZT (3.87 \AA , $c = 4.07$ \AA) and NFM = 8.42 \AA | 110 mV/cm.Oe for PZT – 20 NZF | 900 Oe (T – T) mode |
| Bilayer |  | | 200 mV/cm.Oe | 800 - 900 Oe (T – T) Mode |
| Trilayer |  | PZT (4.04 \AA , $c = 4.11$ \AA) and NCZF = 8.41 \AA | 526 mV/cm.Oe (single layer PZT) And 787 mV/cm.Oe (multilayer PZT) | 400 Oe (L – T Mode) |



9.20: TEM micrograph and SAED pattern for (a) PZT – PZN and (b) NCZF near the interface.

composite. For bulk composite PZT lattice constant is analyzed as strained by NFM lattice where as for trilayer the lattice constant is close to the pure phase. This clearly signifies that the interface diffusion didn't take place in the trilayer which was evident in bulk and bilayer composites. The interface diffusion observed in that bilayer composite was around 30 μm . Trilayer geometry with interface electrode was able to reduce the interface diffusion.

9.4 Chapter Summary

NCZF – (0.9 PZT - 0.1 PZN) – NCZF trilayer was fabricated using pressure assisted sintering. Soft piezoelectric phase with grain size of more than 1 μm and soft magnetostrictive phase (NCZF) were fabricated in a (2 – 2) trilayer geometry. Sintered and annealed samples showed ME coefficient of ~ 494 mV/cm.Oe, which is quite large compared to the previously reported values for particulate sintered composites. Optimization of ferrite to [0.9 PZT – 0.1 PZN] thickness was done in order to find out the most favorable [0.9 PZT – 0.1 PZN] thickness. It was found that with [0.9 PZT – 0.1 PZN] thickness of 0.45 mm (ferrite to [0.9 PZT – 0.1 PZN] thickness ratio of 5.33) the ME coefficient increases from 412 (for [0.9 PZT – 0.1 PZN] thickness 0.85) to 526 mV/cm.Oe. Optimization of magnetic field orientation measurement shows that if the angle between the magnetic field direction and the sample surface is 45° , then the ME coefficient reaches around 589 mV/cm.Oe (for 0.45 mm [0.9 PZT – 0.1 PZN] thickness). This is correlated with areal angular strain of magnetic phase which shows maximum around 51° . Instead of single [0.9 PZT – 0.1 PZN] layer a significant improvement in ME coefficient was obtained by using stacked [0.9 PZT – 0.1 PZN].

CHAPTER 10

IMPROVED PROPERTIES OF TRILAYERS COMPOSITES THROUGH GRAIN TEXTURING AND NANO PARTICULATES ASSEMBLY

10.1 Texturing

Crystallographic texturing of piezoelectric layer can improve the piezoelectric and ferroelectric response by exploiting the anisotropy of electrical properties. Results have been reported in literature on the effect of texturing in both lead-based and lead-free materials including BTO, PMN-PT, NBT-BT, and KNN [165 – 168]. Building upon this prior research, the goal of this study was to discover the texturing process in heterogeneous system consisting of varying crystal structure. This will allow developing novel hybrid materials that exhibit maximum response. As a simple rule, the rhombohedral phase oriented along the (100) direction provides higher piezoelectric response. Texturing can be accomplished through various processes including, hot pressing (HP), templated grain growth (TGG) [169] and reactive template grain growth (RTGG) [165]. The advantage of TGG over HP is that the process is conducted using steps similar to that of conventional ceramic processing except with added seed material. In HP, there is a chance of abnormal grain growth with columnar grain formation along preferred orientation. Hence in this study, the TGG technique was adopted to synthesize the textured ME coefficient. The texturing process consists of two important steps: (i) seed fabrication, and (ii) seed alignment in the matrix [170].

10.1.1 Seed Fabrication

To fabricate the seed (template), molten salt synthesis technique was followed [reference]. It is desirable to have the seed crystal of same crystal structure as that of matrix. In this respect, BaTiO₃ was chosen as the seed material since it can be grown in large size using Remeika process [171]. Other researchers have shown the formation of templates using mixed

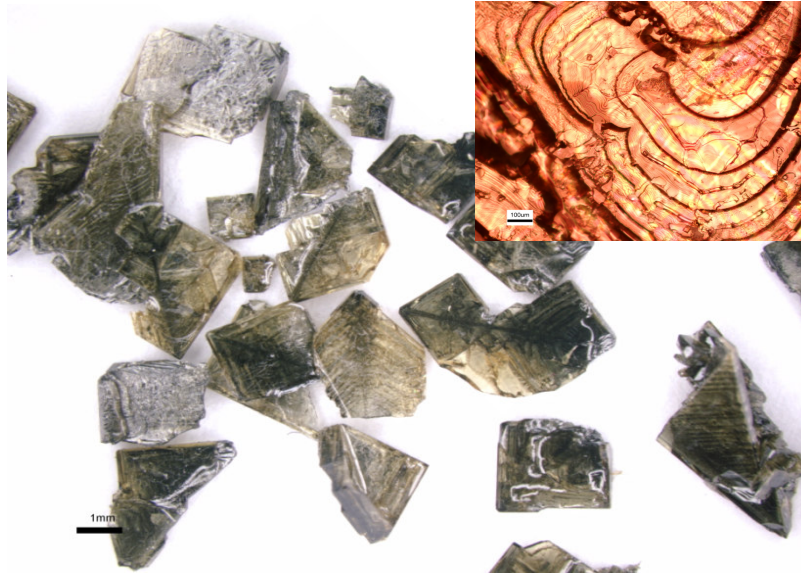


Figure 10.1: Optical images of large size BTO seed crystal, (inset: facets or growth marks)

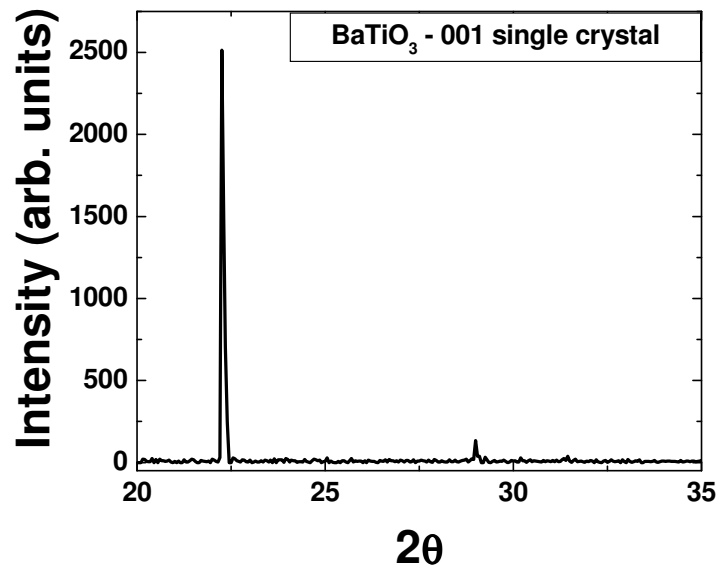


Figure 10.2: X-ray diffraction pattern of BTO seed showing (001) orientation.

salt (NaCl – KCl) [166, 167] method. Molten salt synthesis is comparatively easy because the crystals can be separated more conveniently. This synthesis process consists of heating the raw materials at 1150 to 1225°C (BTO covered with KF salt in Pt crucible) for 8-12 hours and then slowly cooling down to the room temperature.

10.1.1.1 Seed Characterization

The size of synthesized BaTiO₃ seed was found to be in the range of 75 – 100 μm. Some seeds were found to be as large as 2 – 3 mm plates. Figure 10.1 shows the optical image of the BTO seed fabricated using Remeika method. There were facets observed at the surface of the seed which could be related to the twins. A high magnification optical image (inset) shows these facets of single crystal cover the whole surface. X –ray diffraction pattern of the seeds shows strong intensity peak near 22.2°, which is the (001) peak of the perovskite BTO. Figure 10.2 shows the XRD pattern of BTO single crystal.

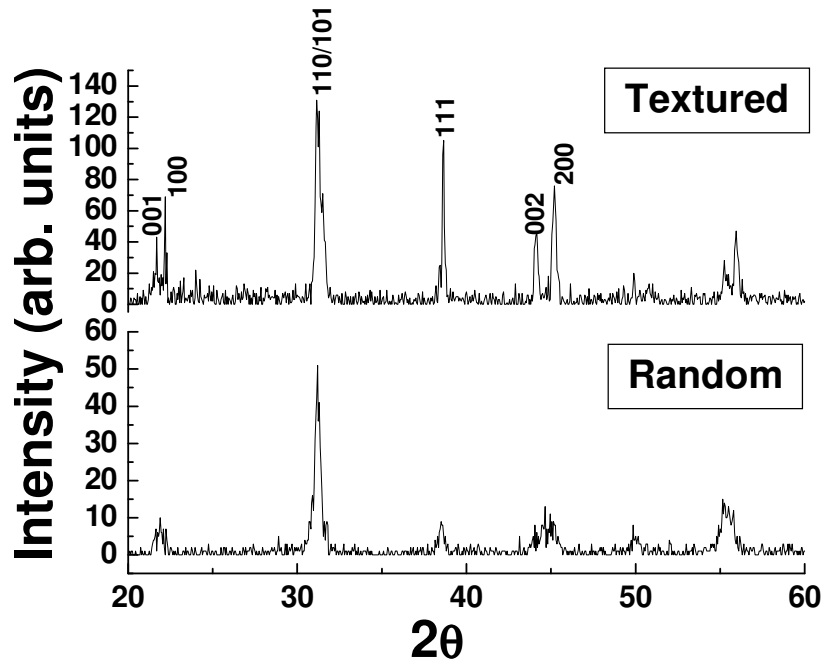


Figure 10.3: X – ray diffraction pattern of textured PZT – PZN compared to randomly oriented PZT - PZN

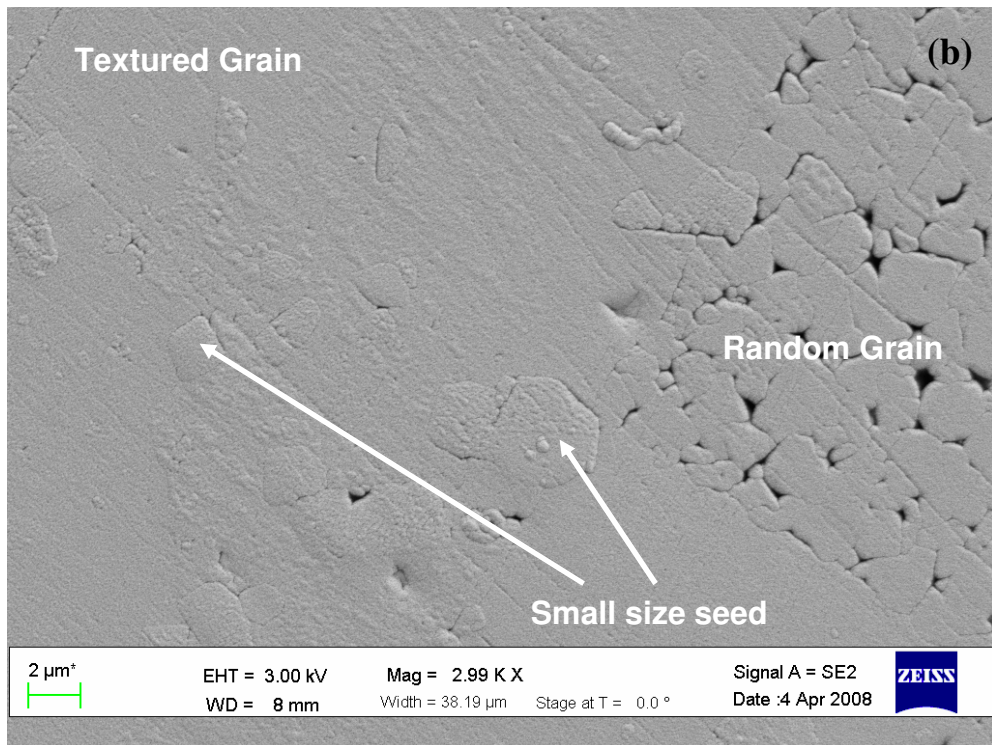
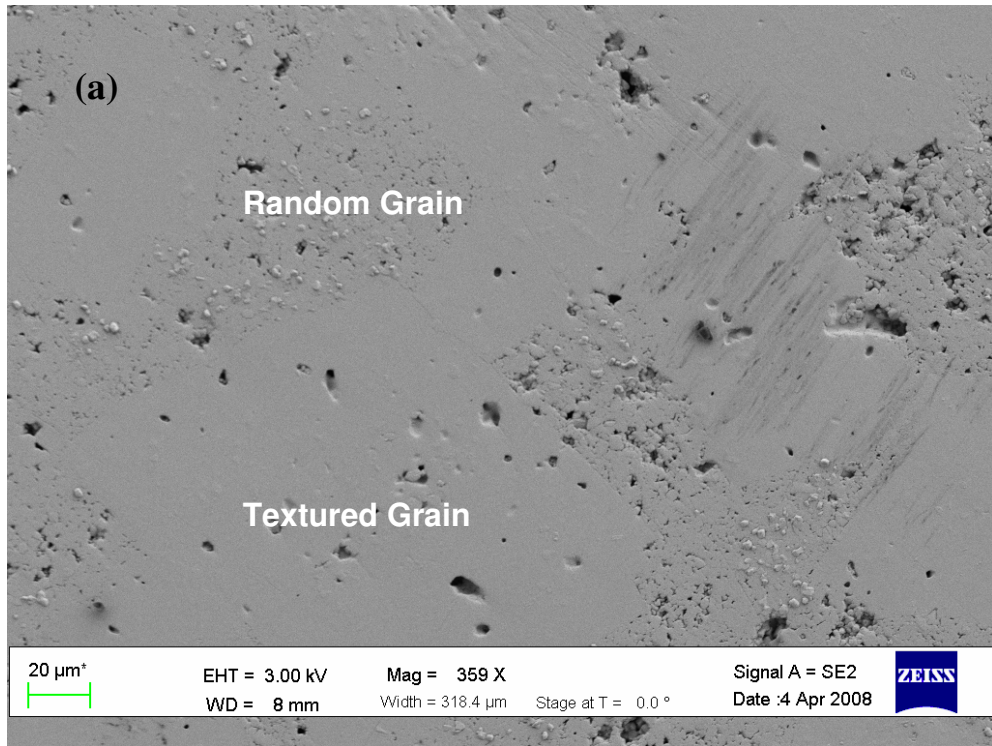


Figure 10.4: SEM micrographs of PZT – PZN with textured grains, (a) low magnification and (b) high magnification.

10.1.2 Synthesis of trilayer composite with textured PZT

The seed crystals were used as templates for texturing piezoelectric phase in the trilayer ME composite. For this purpose, small amount (1 – 5 wt. %) of seed (~ 75 - 300 µm dia.) was mixed with the magnetoelectric powder (e.g. PZT – 20 NZF). The seeded powder was mixed thoroughly and dried. Trilayer was pressed using NCZF top and bottom layer with seeded PZT – 15% PZN in between. The sample was kept for sintering in an air atmosphere for 50 hour soaking time so that the grains can grow along the preferred orientation of the seed crystal. A bilayer sample was also synthesized in order to study the structural characteristics of PZT layer. Figure 10.3 shows the X-ray diffraction pattern of the sample synthesized according to the above mentioned procedure. The pattern shows considerable increase in (001)/(100), (111), (002)/(200) peak intensities compared to the (110)/(101) peak. Also the peak splitting is clearly observed in (001)/(100) and (002)/(220) peaks, which indicates the increase in tetragonality. From this pattern, the lattice parameter can be calculated to be: $a = 4.008 \text{ \AA}$ and $c = 4.098 \text{ \AA}$ and the c/a ratio can be calculated as 1.022. Figure 10.3 also compares the XRD pattern of textured PZT – PZN with randomly oriented PZT – PZN. From X-ray diffraction patterns the degree of texturing was calculated by following Lotgering method. Lotgering factor is defined as the ratio of area textured along the crystallographic plane of interest [170]. The formula for calculating the degree of texturing is given as:

$$f_{00l} = \frac{P_{00l} - P_0}{1 - P_0}, \text{ where } P_{00l} = \frac{\sum I_{00l}}{\sum I_{hkl}} \text{ and } P_0 = \frac{\sum I_{00l}^0}{\sum I_{hkl}^0}$$

where I_{hkl} and I_{hkl}^0 are the intensities of hkl plane for the textured and random sample and $\sum I_{00l}$ is the summation of the intensities of all 001 planes (001, 002 etc.). Using this formula the Lotgering factor was calculated to be $f = 0.35$ for samples textured along 001 direction. It was also found that there is considerable amount ($f = 0.22$) of texturing occurring along (111) orientation. Figure 10.4 shows the SEM micrographs of textured sample. Very large grains are

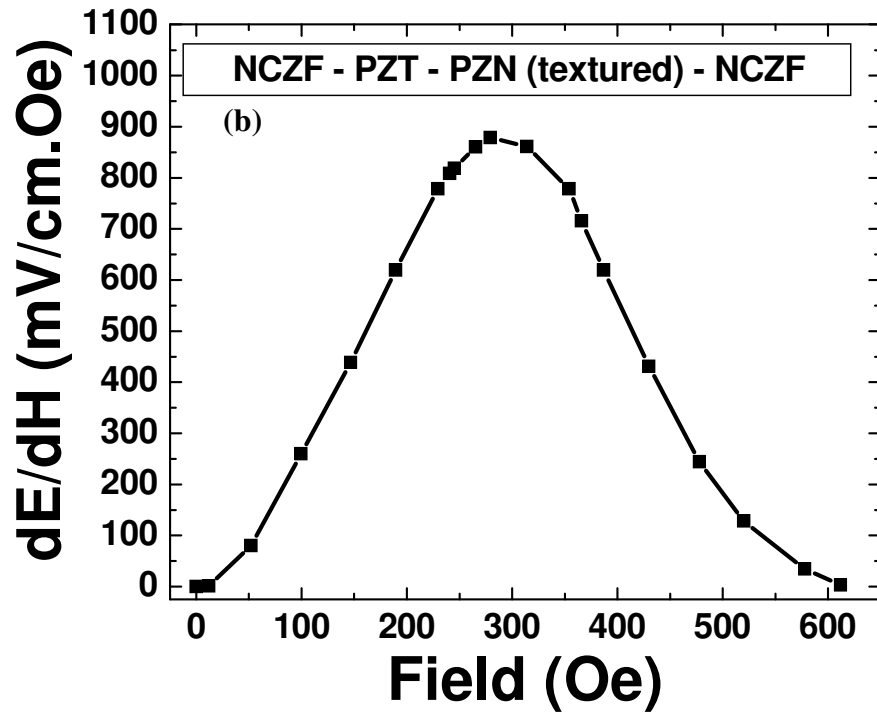
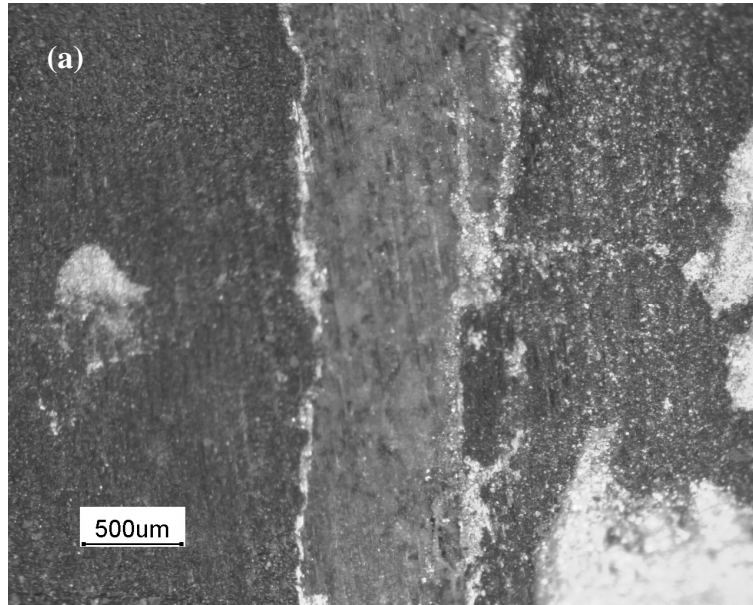


Figure 10.5: (a) Optical images of NCZF – (Textured PZT – PZN) – NCZF trilayer and (b) ME coefficient of this trilayer composite.

observed along with small size grains which are expected to be randomly oriented grains. The textured grain size observed here is in the range of 200 – 350 μm compared to 1 – 2 μm size for randomly oriented grains. The grain size observed is very high due to large soaking period of 50 hrs, which also helps to orient the grains. Small size seeds were observed near the textured grains. Figure 10.5 (a) shows the optical images of cross – section of the trilayer which was poled for piezoelectric and magnetoelectric characterizations. The cross section shows crack free interfaces with intact electrode layer. PZT-PZN layer was found to be 0.5mm in thickness and NCZF thickness was of the order of 1.2mm. The samples were poled at 120°C for 20 minutes under a field of 2.5 kV/mm in a silicone oil bath. The longitudinal piezoelectric constant (d_{33}) was measured to be 325 pC/N, with dielectric constant of 1865 and loss of 7% at room temperature at 1 kHz. Compared to the random PZT – PZN intermediate layer, d_{33} increases by 44% and dielectric constant increases by 50% for the moderate degree of texturing. Figure 10.5(b) shows the ME coefficient of trilayer with textured PZT – PZN as function of DC bias. The peak ME coefficient observed was around 878 mV/cm.Oe at 300Oe DC bias field. For the same thickness of randomly oriented grains, ME coefficient observed was around 526 mV/cm.Oe. This increase in piezoelectric and magnetoelectric coefficient in the textured trilayer can be explained as the increased spontaneous polarizations due to increased grain orientation along $\langle 001 \rangle$ direction. During poling as the field is increased, the domain rotation takes place along $\langle 001 \rangle$ from any of the four equivalent $\langle 111 \rangle$ directions, which increases the strains. These provide low hysteresis and high strains. Because of these reasons the piezoelectric and electromechanical coefficient are found to be higher in textured ceramics. And as the ME coefficient is directly related to the piezoelectric coefficient, an increased ME coefficient is also observed.

10.2 Magnetoelectric core-shell composite structures

Magnetoelectric sensitivity depends upon how efficiently the stress transfers from the magnetostrictive phase to piezoelectric phase through the interface. In the layered composite geometry stress developed in the magnetostrictive phase is larger than that in the particulate composite. For high sensitive magnetoelectric materials, a strong magnetoelectric coupling requires a strong interphase elastic interaction. The core-shell structure of piezoelectric and magnetostrictive phase will provide the most effective inter-phase exchange coupling, originating from the maximized inter-phase contact. The approach will be a bottom up approach, where single PZT particles will be coated first and stacking each core – shell particle into a three dimensional network. Flores et. al. demonstrated the core shell particulate composite of BTO and CFO which shows a piezoelectric constant of 44.6 pC/N and ME coefficient of 1.48 mV/cm.Oe.[2] In another approach Koo et. al showed the interesting coupling between dielectric core and ferromagnetic shell structure of BTO and Fe oxide[172]. It was found that the dielectric constant increases with magnetic field of this core shell structure. In order to use these core shell structure of piezoelectric and magnetostrictive phase, the core shell particles need to be arranged in some three dimensional network (e.g. layer). In this chapter, the goal is to synthesize a core-shell pattern of $\text{Pb}(\text{Zr,Ti})\text{O}_3$ (PZT) and NiFe_2O_4 (NF), where PZT will be the core and nanosize NF will be the shell and arrange it in a layered geometry..

10.2.1 Synthesis of PZT core – NFO shell composite powder

It is expected that ME properties will be increased if the interface can be made elastically rigid and thin. In order to further explore this concept, a nanoparticles-based approach was adopted which consisted of assembling core shell particles of PZT and NFO in a layered configuration. PZT particles corresponding to formulation $\text{Pb}(\text{Zr}_{0.52}\text{Ti}_{0.48})\text{O}_3$ were synthesized using conventional ceramic processing route. NFO particles were synthesized by chemical synthesis technique and provided by Dr. Ping Liu's research group. The processing steps were as following: A mixture of 256 mg of $\text{Ni}(\text{acac})_2$ and 500 mg of 1,2- hexadecanediol

was added to a 125 mL European flask containing a magnetic stir bar. Benzyl ether 20 mL was then transferred into the flask and the contents were stirred while purging with N₂ for 20 min at room temperature. The flask was then heated to 120°C and the temperature was held for 20 min. During this time, 0.2 mmol of Fe(CO)₅ was injected into the flask while the N₂ purging continued. After 1 minute, 1 mL of oleic acid and 1 mL of oleylamine were injected and the mixture was maintained under N₂ blanket and heated to 160°C at rate of 5°C per minute. The holding time for the solution was 10 minutes. The flask was then heated to the refluxing temperature of 295 °C for 30 min before cooling down to room temperature under the N₂ blanket. Size of NiFe₂O₄ was controlled by varying the amount of surfactants and heating rates. When faster heating rate and more surfactants were used bigger NiFe₂O₄ nanoparticles were obtained. Coating of NiFe₂O₄ nanoparticles on PZT was done using similar recipe as that for synthesizing the NiFe₂O₄ nanoparticles. PZT particles were added in the beginning of synthesis keeping the other parameters constant. Amount of PZT particles was varied from 500mg to 2 gm in order to vary the coating thickness and obtain different ratio of NiFe₂O₄ to PZT in the final product.

10.2.2 Nanosize NiFe₂O₄ Characterization

Figure 10.6 shows the TEM image of nanosize NiFe₂O₄ particles. The size of particles was between 20 – 30 nm. The particles were mostly of hexagonal shape. Figure 10.7 (a) shows the X-ray diffraction pattern of NFO nano particles (red) compared with large size particles (black) exhibiting spinel structure. The peak broadening was observed as the particle size becomes smaller. Intensity of XRD peaks was found to decrease for the nano size NFO particles. Figure 10.7 (b) shows the magnetic hysteresis loop of NFO nano particles. Coercive field and magnetization was found to be lower in comparison with the large size particles. From figure 10.7 (a) and (b), it can be seen that excellent structural and magnetic properties of NFO nano particles can be achieved using chemical synthesis method.

10.2.3 Characterization of PZT – NFO core shell structure

Figure 10.8 (a) shows the SEM images of PZT – NFO core shell structure. Fine particles (20 – 30 nm) can be observed in this SEM micrograph. These particles surround the PZT particles of 400 – 600 nm size. EDS spot analysis on these particles shows presence of both PZT and NFO. TEM analysis was conducted in order to understand the distribution of nanoparticles. Figure 10.8 (b) shows the TEM images of PZT particle coated with NFO nano particles. The difference in contrast was clearly observed in two different sizes of particles. TEM investigations showed that the NFO nano particles coating on top of PZT particles was about 2-3 layers in thickness.

10.2.4 Sintered PZT core – NFO shell structure

PZT – NFO core shell structure were sintered at low temperature of 950°C and long holding time of 5 hrs. In order to increase the resistivity, thin layers of pure PZT was pressed as top layer using 0.25 inch die under hydraulic pressure of 2 ksi followed by cold isostatic pressure of 30 ksi. After sintering, samples were characterized by transmission electron microscope, alternating field magnetometer and magnetolectric measurement system. Figure 10.9(a)

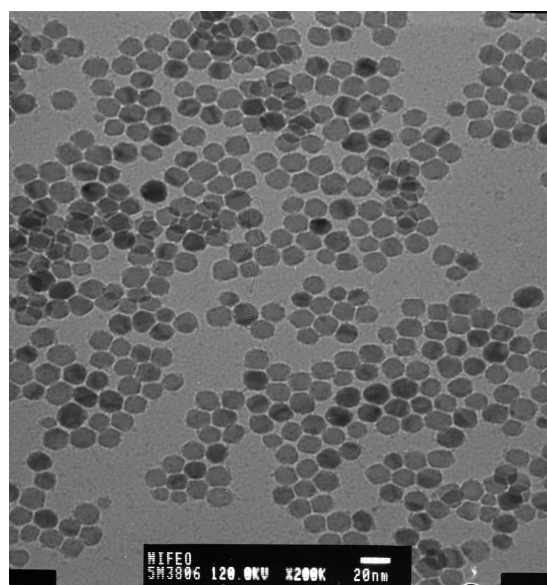


Figure 10.6: TEM image of NFO Nanoparticles

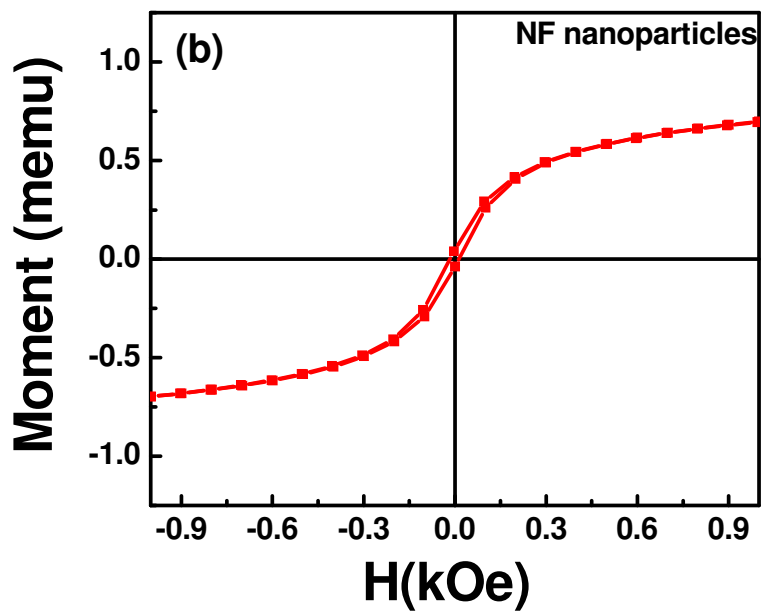
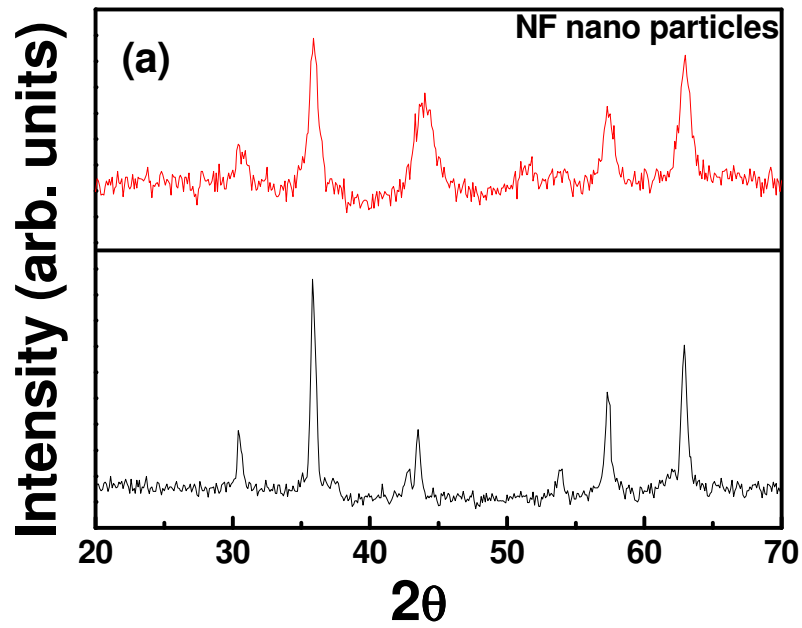


Figure 10.7: (a) X-ray diffraction pattern and (b) magnetic properties of NFO nano particles.

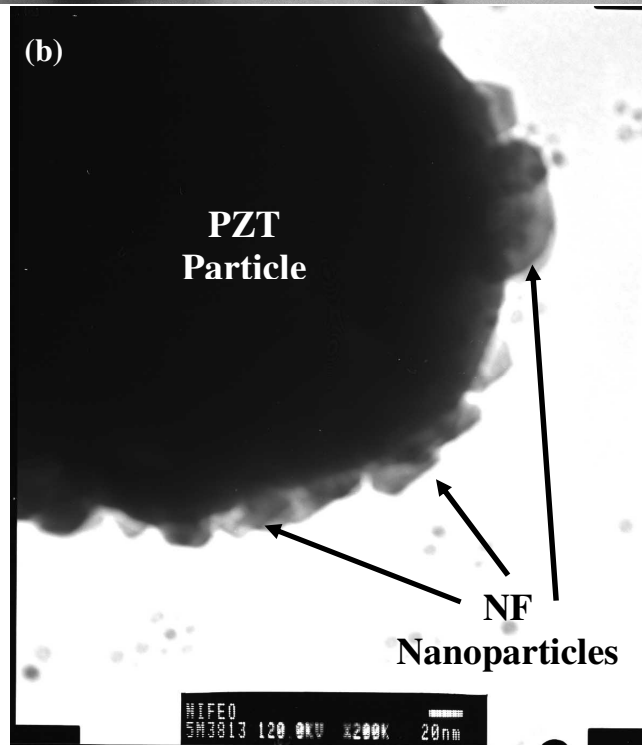
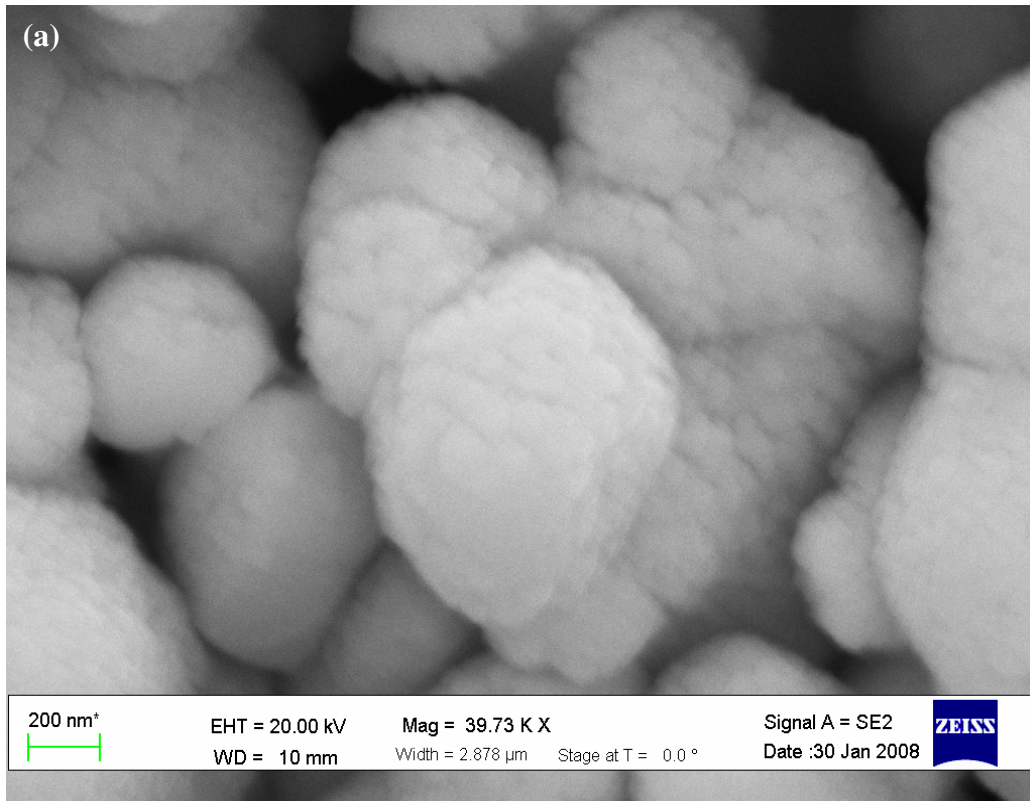


Figure 10.8: Micrographs for PZT – NFO core shell structure, (a) SEM and (b) TEM.

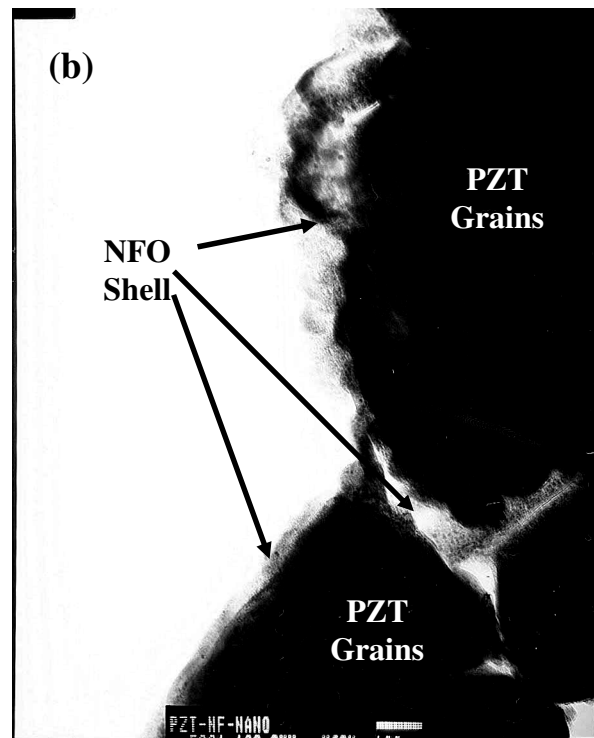
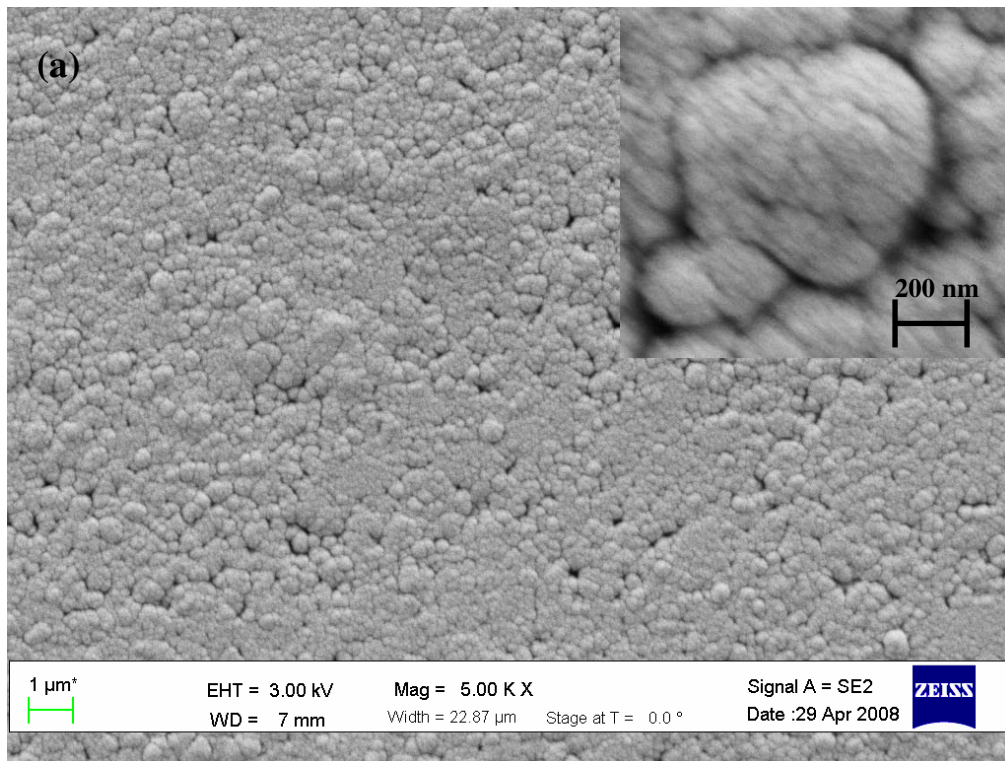


Figure 10.9: Microstructure of sintered PZT – NFO core shell structure (a) SEM and (b) TEM.

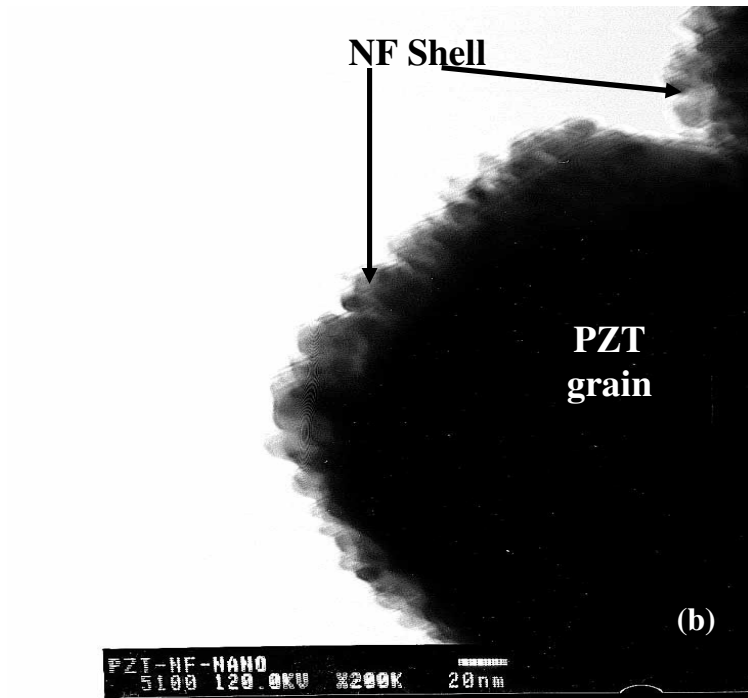
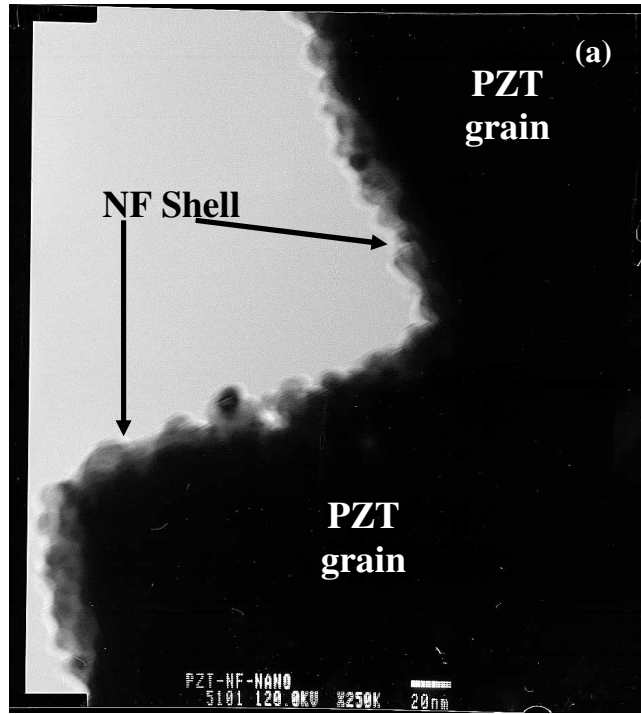


Figure 10:10: TEM images of sintered core shell structure.

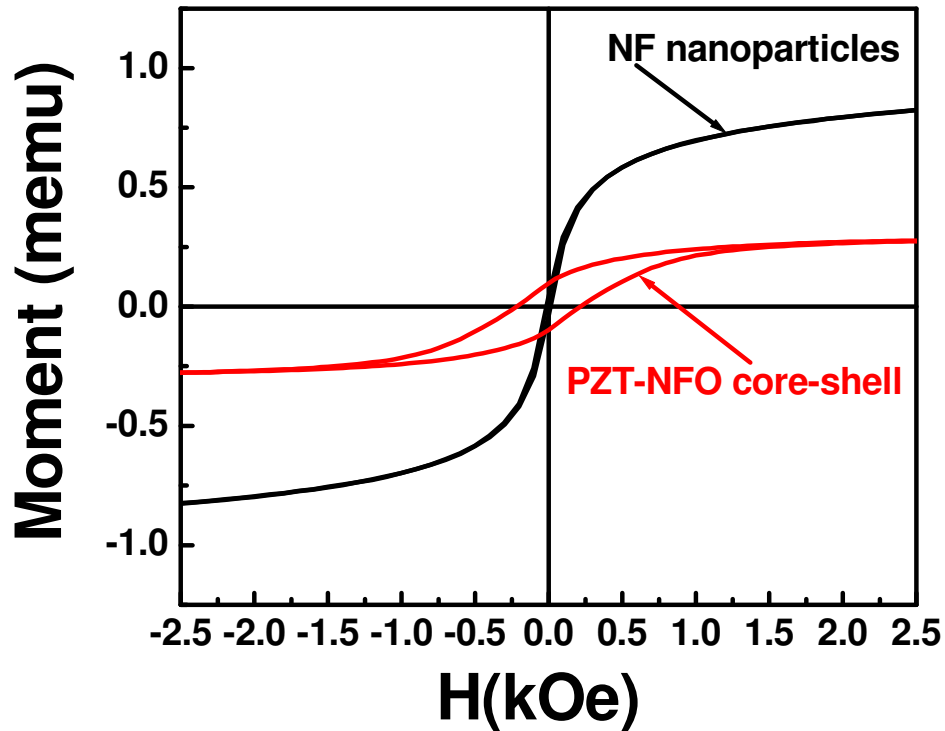


Figure 10.11: Comparison of magnetic hysteresis property of NF nano particles and PZT – NFO core – shell structure.

shows the low magnification SEM image of PZT – NFO core shell structure in order to observe the sintering characteristics. The microstructure is dense with small fraction of porosity. Inset shows a magnified view of a core shell grain. The size of the core particle was in the range of 600 – 650 nm with shell in the range of 40 – 90 nm. Figure 10.9 (b) shows the grain structure using TEM bright field imaging. It is very interesting to observe that the shell is present at the grain boundary of large fractions of grain. This indicates that the piezoelectric core and magnetostrictive shell can sustain high temperature. Figure 10.10 shows the high magnification transmission electron microscopy images of sintered composite. The micrographs show the presence of NFO shell on top of PZT grains. The coating thickness was equivalent to 2 – 3 layers, which varies from 40 - 50 nm. PZT grains were observed to vary from 500 – 600 nm. The size of nano particles in the shell was observed to be larger than as-synthesized nano

particles shown in Figure 10.6. Figure 10.11 shows the magnetic properties of as synthesized NFO nanoparticles and PZT – NFO core shell structure. One major difference is the increase in coercive field as compared to the nano particles. For PZT – NFO core shell the coercive field was around 216 Oe whereas for as synthesized nanoparticles very low magnitude of coercivity was recorded. This can be explained in terms of the increase in size during core shell synthesis. The shell thickness was 2 – 3 times larger than the size of the single nano particles. It is well known that the coercivity depends on the magnetic particle size. As the particles size decreases, coercivity decreases and for very low value of particles sizes it becomes super paramagnetic [173 – 174]. In the core – shell structure shown in Figure 10.8 to 10.10, it can be seen that the thickness is larger than single particles size. It has been shown that with increase in particle size coercivity increases and reaches maxima. The particle size where it shows maximum coercivity corresponds to single domain particle. The size of the shell may be close to the single domain particle size and hence the coercive field observed was high.

The bilayer was electroded top and bottom and polarized at 2.5 kV/mm for 30 minutes in silicone oil bath. The temperature was fixed at 120°C. The piezoelectric (d_{33}) constant of 60 pC/N, dielectric constant of 865 and dielectric loss of 5.45% was recorded. Figure 10.12 shows the magnetoelectric coefficient as a function of DC bias for bilayer of thin pure PZT and core shell of PZT – NFO. The peak ME coefficient of 195 mV/cm.Oe was observed at 454Oe DC bias. A notable feature in this figure is the range of DC bias field at which high ME coefficient was observed. It was found that in DC bias field range of 265 to 617Oe, the ME coefficient was above 175 mV/cm.Oe, which is almost 90% of the peak value. Compared to the particulate composite this wide range of high ME coefficient is advantageous for sensing purposes. This feature may be attributed to the hard nature (larger coercive field) of magnetic phase.

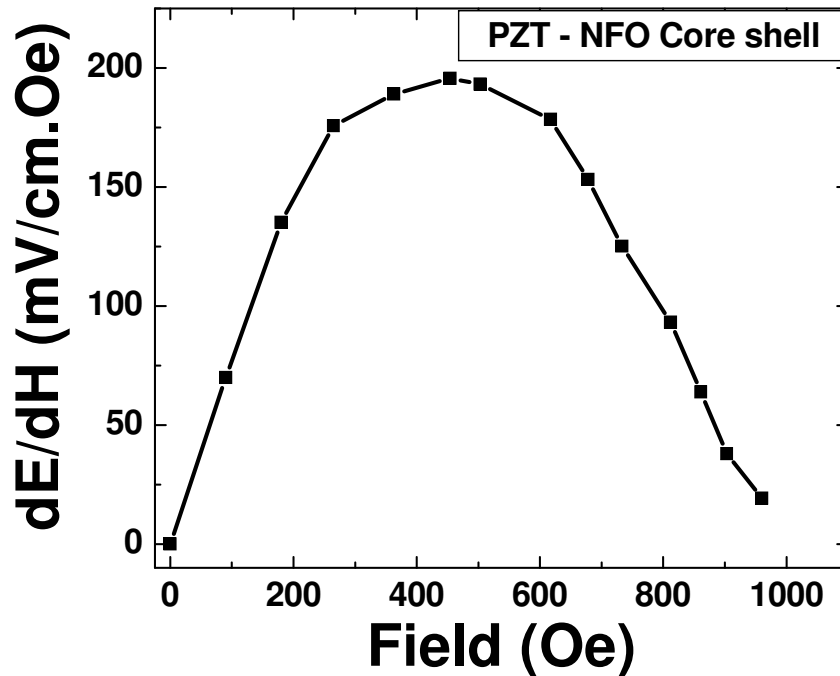


Figure 10.12: Magnetolectric coefficient as a function of DC bias field.

10.3 Chapter Summary

The contribution of moderate texturing on piezoelectric and magnetolectric properties was observed and it was found that piezoelectric constant improved by 44% leading to increase of ME coefficient by 67%. A high ME coefficient of 878 mV/cm.Oe was observed in the trilayer assembly with NCZF as top and bottom layer and textured PZT – PZN in the center.

In another approach the core - shell assembly of PZT and NFO was fabricated using chemical synthesis method. NFO particles in the size range of 20 – 30 nm were used to fabricate shell for piezoelectric core. The sintered composite exhibited d_{33} of 60 pC/N, dielectric constant of 865, and ME coefficient of 195 mV/cm.Oe. High ME coefficient was observed for wide range of DC bias magnetic field. This approach of fabricating layered composite has a promise to provide large ME coefficients in particulate sintered structures.

CHAPTER 11

MAGNETOELECTRIC DEVICES

Recent progresses in the understanding and fabrication of the magnetoelectric composites has prompted emergence of novel devices. Several devices based on the ME effect have been reported including high frequency electrical components, transformer, gyrator, and flow meter. In this chapter the design and working principle of some unique magnetoelectric sensors is presented.

11.1 Magnetoelectric Sensor

11.1.1 Structure and working principle

Figure 11.1 shows the schematic diagram of the unipoled piezoelectric transformer in the step-up mode [160]. On applying the electrical excitation to the external ring (input), the radial extensional vibration is generated through converse piezoelectric effect which is propagated to the center dot output. The ring and dot are separated from each other by an insulation gap. At the output, the mechanical vibrations are converted into electrical voltage through direct piezoelectric effect.

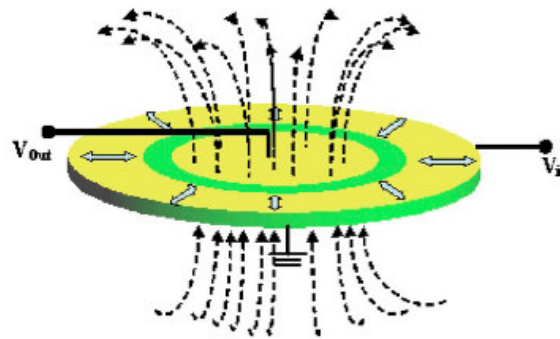


Figure 11.1: Structure of the piezoelectric transformer based magnetic field sensor.

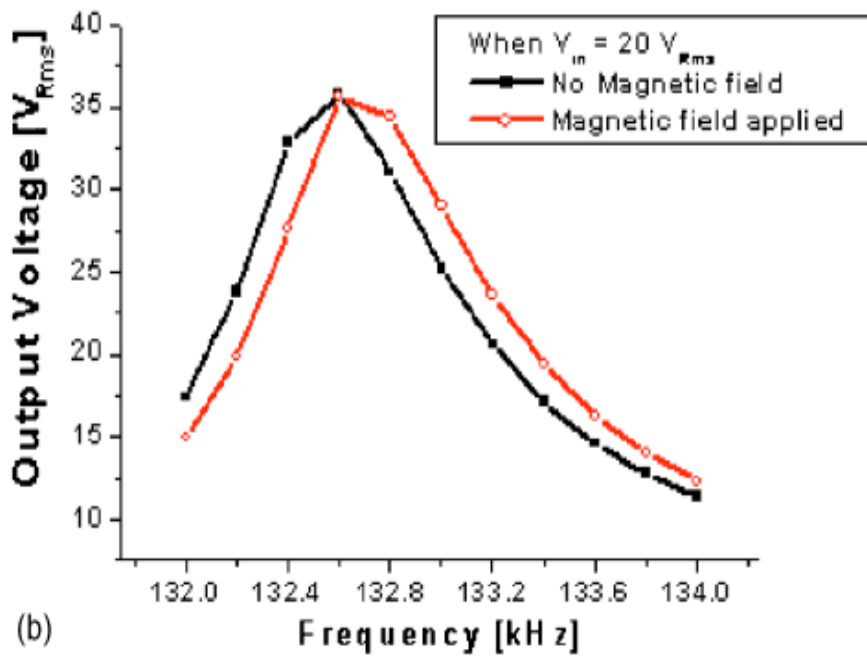
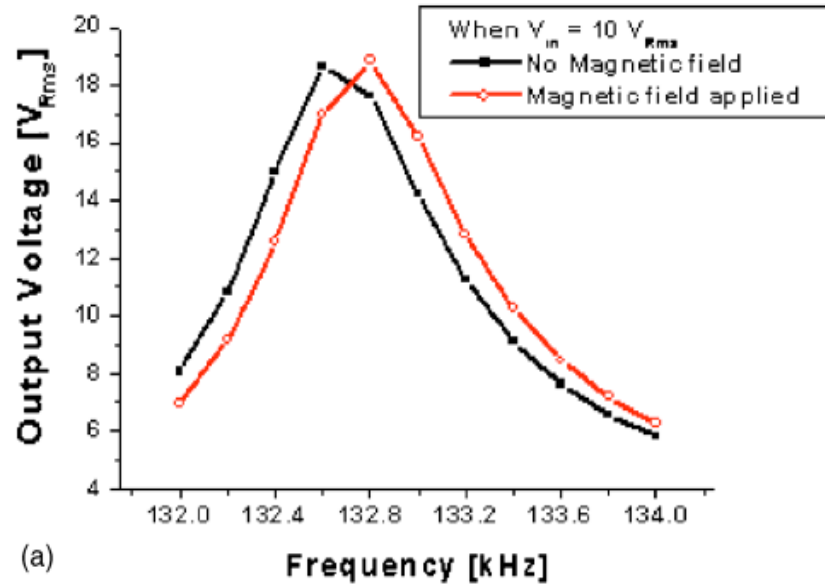


Figure 11.2: Sensor characterization showing the variation of the output voltage as a function of frequency with and without applied magnetic field: (a) input voltage = $10 V_{rms}$, (b) input voltage = $20 V_{rms}$.

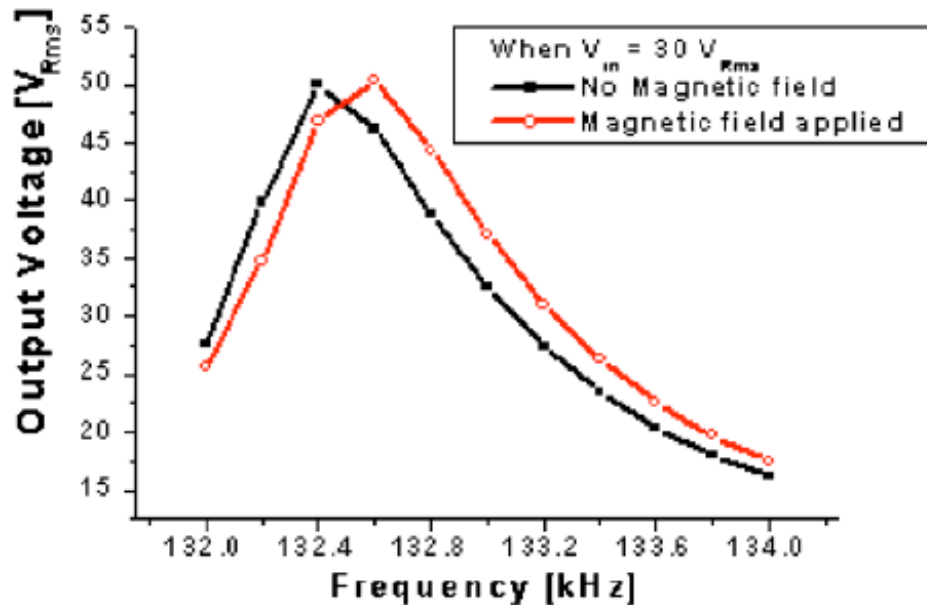


Figure 11.3: Sensor characterization showing the variation of the output voltage as a function of frequency with and without applied magnetic field: input voltage = 30 V_{rms}.

Since this transformer design utilizes radial mode for both input and output parts which are built-in on the same ceramic disk, it has much higher bandwidth as compared to other designs (since $k_{33} > k_p > k_{31}$).

11.1.2 Magnetic sensitivity

Figures 11.2 – 11.3 shows the results on the magnetic field sensor corresponding to the input voltages of 10, 20 and 30 V_{rms}. The current was kept constant in the measurement which is critical to avoid the influence onto the generated magnetic field pattern. Two points can be immediately noticed in this figure: (i) significant change in the magnitude of the output voltage over a wide frequency range and (ii) significant shift in the magnitude of frequency at which output voltage reaches maximum corresponding to the resonance of the sample. In Figure 11.2 (a), the magnitude of the maximum output voltage at the frequency of 132.6 kHz is 18.64 V_{rms} (input voltage=10 V_{rms}). When an external magnetic field of 360 G is applied onto the output section, the maximum output voltage magnitude changes to 18.83 V_{rms} ($\delta V = 0.19$

V_{rms}) at the frequency of 132.8 kHz. Similarly in Figure 11.3, there is a voltage change of $V = 0.411 V_{rms}$ at an input voltage of $30 V_{rms}$.

This result clearly illustrates that the proposed design has extremely high range of magnetic field sensitivity and it can be tailored by changing the applied input voltage. There are numerous advantages of the magnetic field sensor presented in this chapter including (i) simple fabrication technique as the whole structure is designed onto one piece of sintered ceramic, (ii) easy driving and sensing mechanism frequency shift and voltage gain, (iii) direct control over the sensitivity by changing the input driving voltage, ring-dot diameter, and number of layers, (iv) cost effectiveness, and (v) possible implementation onto the silicon. It is expected that this sensor design will bring the radical change in the application of the magnetoelectric materials.

11.2 Sensing mechanism

Figure 11.4 (a) shows the configuration of the ME sample for measuring the generated magnetic field in response to the applied electric field. In this case, the electrodes were applied over the whole top and bottom surfaces (fully electroded) and the electric field was applied using the high voltage high power amplifier. Figure 11.4 (b) shows the measured electrical impedance spectrum from the sample. The minimum in the impedance corresponds to the resonance frequency of 131 kHz while the maximum corresponds to the antiresonance frequency of 132.2 kHz. Figure 11.5 (a) shows the constant voltage input condition used to drive the sample. The input voltage of $30 V_{rms}$ was applied and the generated magnetic field was measured at various points on the electroded surface. The generated magnetic field was measured using a gauss meter (AlphaLab, Inc., Salt Lake City, UT) attached to the sample surface using epoxy. The measured field was of the order of $11 G_{rms}$ which originates from the strain occurring through converse piezoelectric effect and is converted into magnetic field by

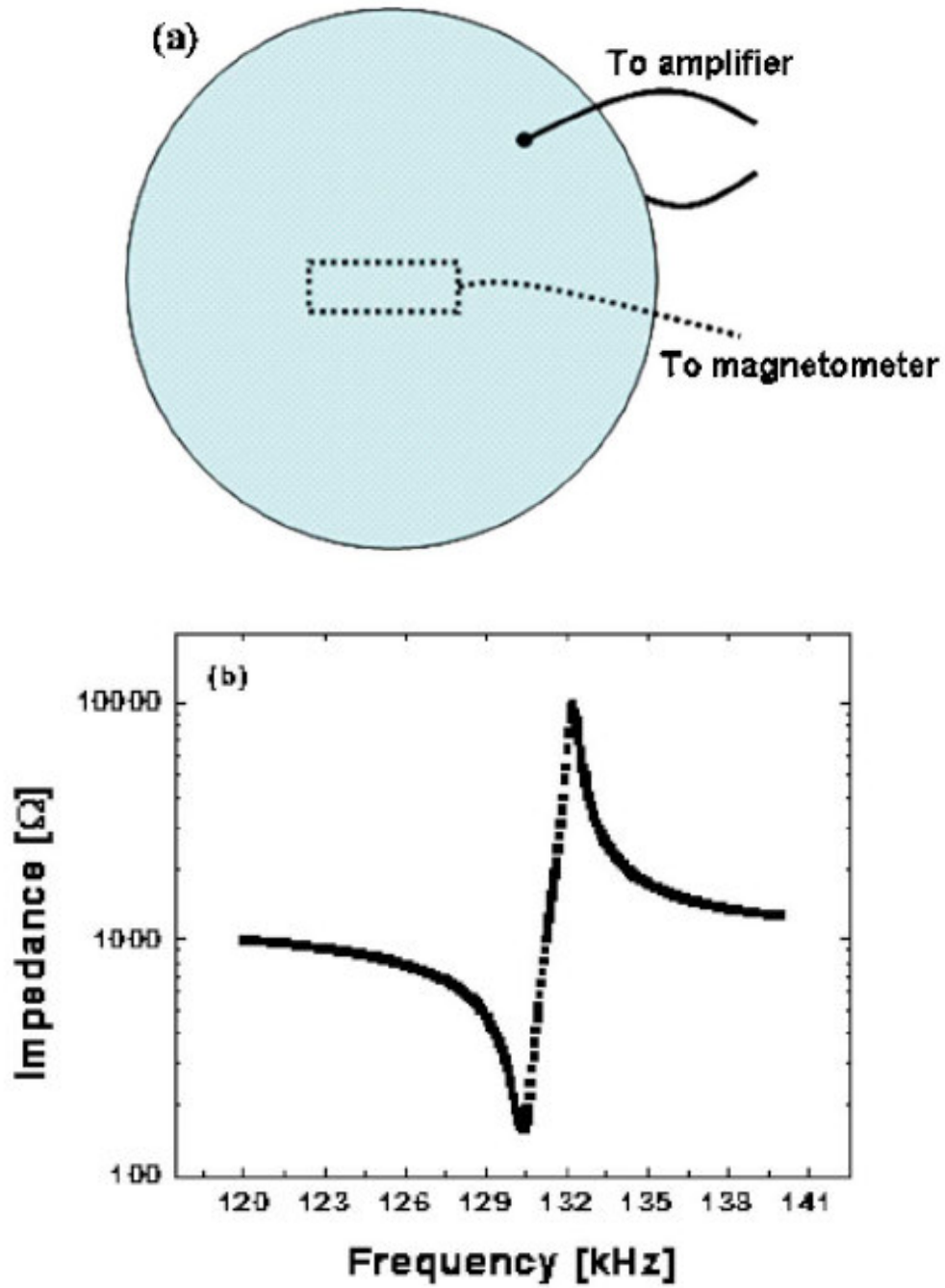


Figure 11.4: Electrical and magnetic data from the fully electroded sample. (a) Schematic description of the sample shape and magnetic field measurement technique, (b) impedance spectrum of the fully electroded sample,

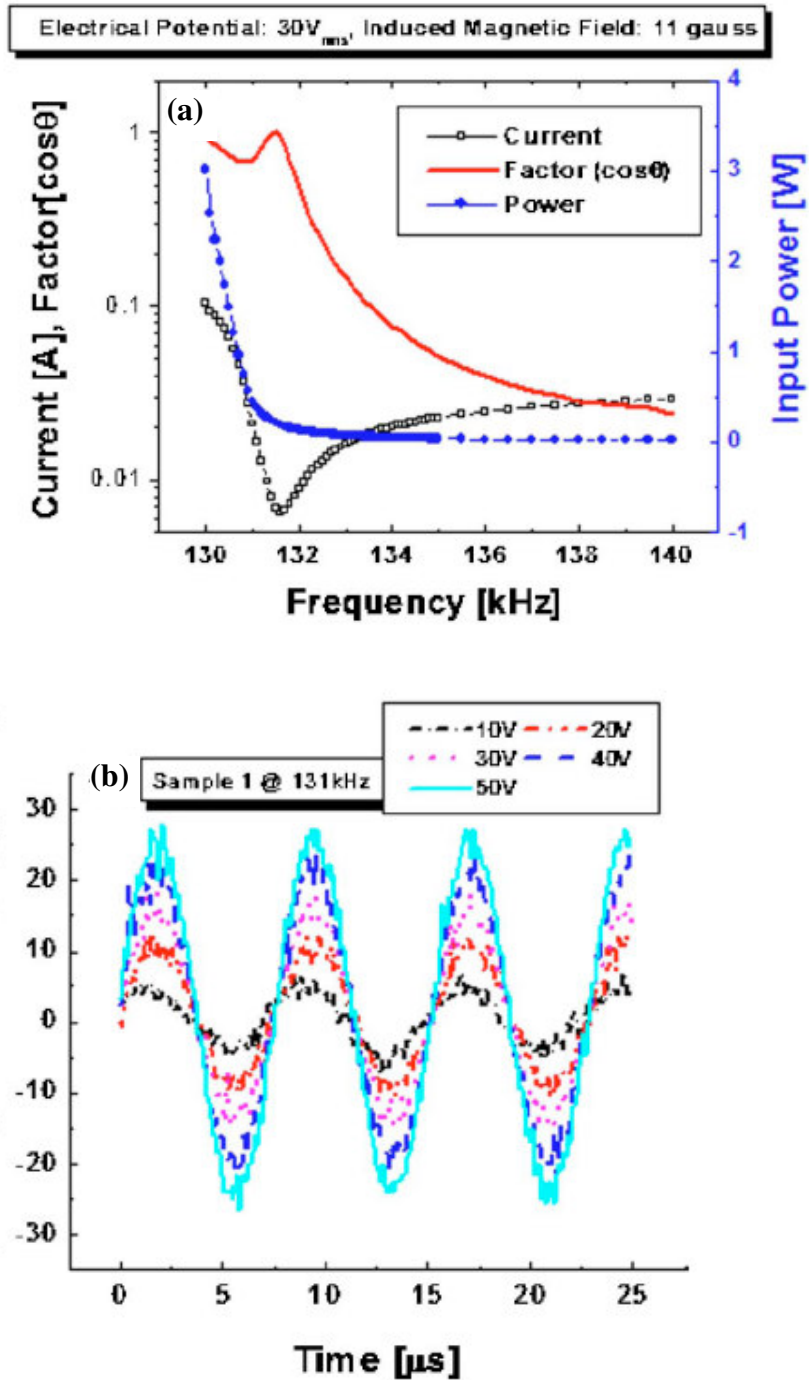


Figure 11.5: Electrical and magnetic data from the fully electroded sample, (a) input driving condition variation as a function of the frequency at constant voltage of $30V_{\text{rms}}$, and (b) magnetic field wave form from the sample as a function of driving voltage at the resonance frequency.

magnetostriction. It was observed that the amplitude of the magnetic field remained constant at all the frequencies over the whole electroded surface. However, the input current exhibited minimum at the resonance frequency (due to lower impedance) so the total power consumption decreased as shown in Fig. 11.5 (a). Thus, driving at the resonance frequency results in the highest efficiency and the lowest power consumption for the piezoelectric devices. Figure 11.5 (b) shows the magnetic field from the fully electroded sample as the function of input voltage at the resonance frequency. The magnitude of magnetic field was found to increase in proportion to the applied voltage and was constant over the whole electroded surface. Figure 11.6 (a) subset shows the modified structure of the ME composite samples with split electrodes having ring-dot pattern. In this design the ring section acts as the input and dot section as the output. The fabricated sample had the dimensions of $20 \times 1.5 \text{ mm}^2$ with dot section having the diameter of 11.5 mm. The ring and dot sections are separated by a gap of 2 mm. On applying the electrical field to the ring section close to the resonance frequency, radial mode vibration is generated in the ring section through converse piezoelectric effect. The radial strain is transferred to the dot section through the gap where it is converted into voltage through direct piezoelectric effect. At the same time, the dot section generates magnetic field in response to the radial strain through magnetostriction. This magnetic field affects the voltage measured at the dot section through direct magnetoelectric effect. Thus, the output voltage at the dot section is dependent upon the magnitude of the magnetic field. It is expected that the magnitude of the voltage at the dot section will be maximum at the resonance frequency, since the strain is amplified by the mechanical quality factor Q_m .

11.2.1 Voltage gain and magnetic field generation

Figure 11.6 (a) shows the measured voltage gain (ratio of the voltage applied to the ring section to the voltage measured at the dot section) of the ME composite sample in the frequency range from 132 to 134 kHz for various input voltages. The voltage gain was maximum at the resonance frequency of 133.6 kHz and was of the order of 1.8 at 10 V input

voltage. Figure 11.6 (b) shows the magnitude of magnetic field generated at the dot section as a function of the frequency for various input voltages. The generated magnetic field shows the maximum at the resonance frequency which corresponds with the voltage gain. These data confirm the hypothesis that the magnitude of the magnetic field has direct correlation with the strain and hence voltage gain of the dot section. Figure 11.7 (a) shows the variation of the generated magnetic field as a function of the input voltage at the resonance frequency. The magnitude of the generated magnetic field increased in proportion to the applied input voltage at the ring section. These data indicate that the ring-dot structure can be effectively tailored to provide a voltage controlled magnetic field. The generation of the magnetic field in the dot section allows us to design an effective magnetic field sensor. The sensing mechanism is as follows. A voltage is applied to the ring section at the resonance frequency which induces magnetic field in the dot section. If an external magnetic object is brought in the vicinity of the dot section, then the resulting differential magnetic field will induce change in the voltage gain due to magnetoelectric effect. Figure 11.7 (b) shows the plot of the voltage gain with and without an external magnetic field in the frequency range of 132 – 134 kHz. A permanent magnet of magnitude 365 Oe was used to apply the external magnetic field and was held ~ 3 mm away from the dot section. It can be seen in this figure that there is a significant change in the magnitude of the voltage gain with the applied external magnetic field which increases as the frequency approaches the resonance point. Further, for the same magnitude of the voltage gain, there is a large frequency shift with the application of external magnetic field. Thus, the detection circuit can be programmed to capture either the voltage shift or the frequency shift. The results of Figure 11.6 and 11.7 clearly demonstrate an effective magnetic field sensor. Preliminary experiments were conducted to characterize the effect of the source distance and magnetic field strength on the voltage gain. It was found that the change in voltage gain is small as the magnet

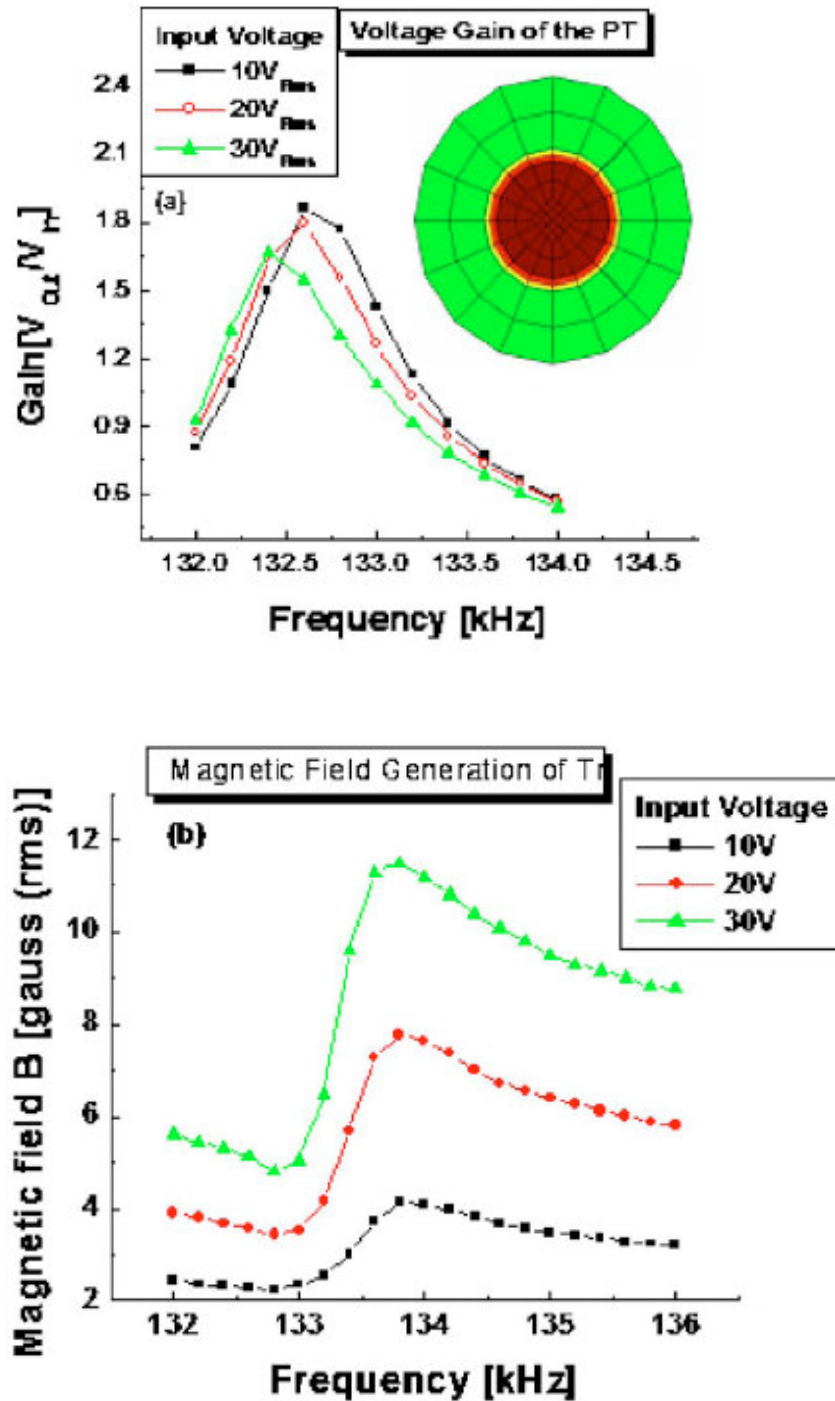


Figure. 11.6: Electrical and magnetic data from the sample with ring-dot electrode pattern. (a) Schematic representation of the sample and the voltage gain as a function of frequency. The maximum in the voltage gain corresponds to the resonance frequency of the dot section, (b) variation of the output magnetic field from the dot section as a function of the frequency.

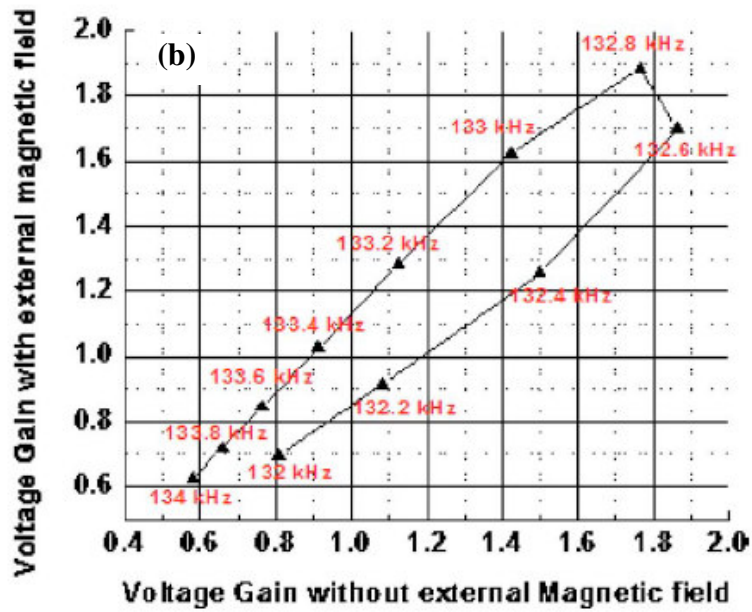
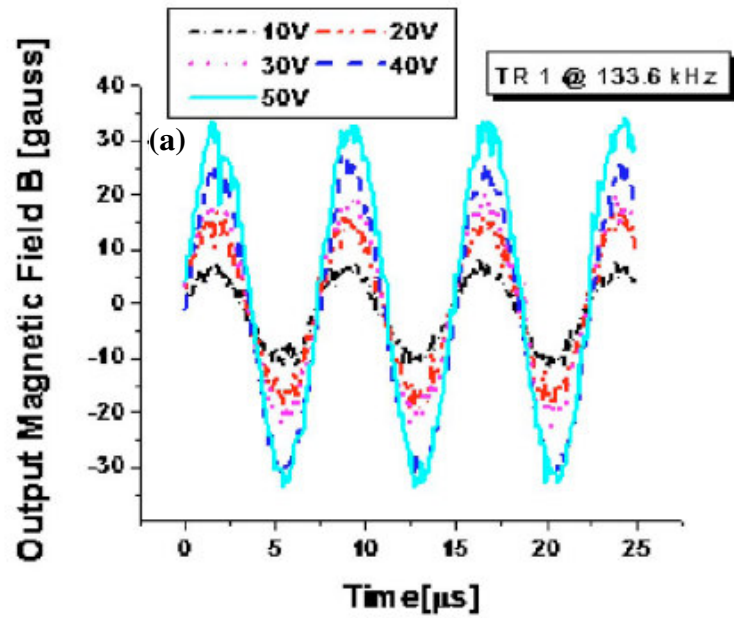


Figure. 11.7: Electrical and magnetic data from the sample with ring-dot electrode pattern. (a) output magnetic field wave form as a function of the input voltage in the ring section at the resonance frequency, and (b) change in voltage gain of the dot section in the frequency range of 132–134 kHz with and without the external dc magnetic field.

was moved away from the dot section. The reason for this observation may be related to the fact that generated magnetic field is quite small. Imposing an external dc magnetic bias in the dot section and a buffer layer with high permeability will increase the flux concentration and thus response of the sensor. The variation in the voltage gain as a function of the magnetic field strength (60, 150, 250, and 360 G) showed that before the resonance frequency the voltage gain increased at low magnetic fields and then decreased (after 150 G) with increase in the magnetic field. After the resonance frequency an opposite trend was observed.

11.3 Chapter Summary

In this chapter, magnetic sensor design, construction, working principle and experimental data were reported. The sensor was found to provide large changes in the magnitude of the output voltage and resonance frequency on application of magnetic field.

CHAPTER 12

CONCLUSION

The objective of this study was to develop a magnetoelectric sintered composite system which has high magnetoelectric coefficient. The desired range of magnetoelectric coefficient is between 1.0 to 1.5 mV/cm.Oe. There are several major achievements in this thesis namely,

1. A piezoelectric ceramic composition with high g_{33} constant of $83.136 \pm 0.84 \times 10^{-3}$ V-m/N and a high magnitude of the energy harvesting parameter ($d_{33} \cdot g_{33}$) as $18456.2 \pm 262 \times 10^{-15}$ m²/N was synthesized and formulated. A new material constant n was derived from the condition for maximization of g constant ($|d| = \epsilon^n$). According to the developed model, as the magnitude of n decreases towards unity a giant enhancement in the magnitude of the g constant can be obtained. The experimental data was found to be consistent with this prediction.
2. Effect of matrix grain size on the magnetoelectric coefficient of PZT – 20 NZF particulate composites was studied. It was found that grain size has significant effect on the piezoelectric, ferroelectric and dielectric properties of the composite and hence influences the magnetoelectric property. There is a critical grain size below which the piezoelectric charge constant (d_{33}), dielectric constant, and piezoelectric voltage constant (g_{33}) drops rapidly. This critical grain size is in the range of 100 – 150nm. Above 200nm the piezoelectric properties increases slowly and saturates at 600nm. Samples having grain size of around 100 nm show small magnitude of ME coefficient (54.4 mV/cm.Oe) while those with grain size of 600nm exhibit a value of 155 mV/cm.Oe.
3. The effect of post sintering thermal treatment of PZT – NFM composites show that there is a correlation between structural deformation in PZT matrix, presence of defects between

component phases in piezoelectric-magnetostrictive composites and the change in magnetization with changes in the ME coefficient. It was found that lattice expansion of PZT [from ($a = 3.87\text{\AA}$, $c = 4.07\text{\AA}$) to ($a = 4.07\text{\AA}$, $c = 4.09\text{\AA}$)], removal of defects and increase in magnetization contributes to the enhancement in ME coefficient after annealing and aging. There is a decrease in ferroelectric and ferromagnetic Curie temperatures by 8°C and 33°C and at least 50% enhancement was observed in magnetoelectric coefficient after annealing and aging.

4. A sintering process was introduced to fabricate NCZF – (0.9 PZT - 0.1 PZN) – NCZF trilayer composites. Soft piezoelectric phase with grain size of more than $1\text{ }\mu\text{m}$, and low coercivity magnetostrictive phase with grain size of $3\text{-}5\text{ }\mu\text{m}$ were obtained with excellent adherence to Ag-Pd electrode. Sintered and annealed samples showed ME coefficient of ~ 412 and 494 mV/cm.Oe respectively, which are quite large compared to the previously reported values. Optimization of magnetostrictive to piezoelectric thickness ratio showed a magnetoelectric coefficient of 525 mV/cm.Oe when the angle between the sample and the magnetic field direction is zero. A slightly higher value (595 mV/cm.Oe) was observed when the angle was changed to 45° . It was also found that when the intermediate piezoelectric layer is changed from single layer to trilayer stack geometry then piezoelectric and dielectric property of the composite improved remarkably from 204 pC/N and 1132 to 535 pC/N and 5500 respectively. This enhancement contributes to the high magnetoelectric response of 782 mV/cm.Oe .
5. Texturing the piezoelectric phase inside the trilayer ME composite improved the ME coefficient. X-ray diffraction and scanning electron microscopy showed that the texturing occurred inside the piezoelectric grains by using BaTiO_3 seeds. The degree of texturing was found to be 0.35 and 0.22 for (001) and (111) direction respectively. For this moderate texturing, improvement in piezoelectric and dielectric constant was by $40 - 50\%$. It improved the ME coefficient by 67% , from 526 mV/cm.Oe to 878 mV/cm.Oe .

6. Core shell particles of PZT and NFO were synthesized using chemical synthesis route with PZT as core and NFO as shell. The core - shell particles were sintered using compaction and annealed at 1025°C for 5 hours. The magnetic property (coercivity) of core shell particles was remarkably different than the as synthesized nano particles. Coercive field increased to 210 Oe, which is quite high for NFO nano particles. Due to this hard nature of NFO nano particles, high ME coefficient (> 175 mV/cm.Oe) over the wide range of field was observed with peak ME coefficient of 195 mV/cm.Oe.
7. A magnetic field sensor based on piezoelectric transformer was fabricated and characterized. The sensitivity of this sensor was excellent as a large shift in resonance peak was observed under applied magnetic field.

The goal of this thesis was to correlate the composition, microstructure with piezoelectric, magnetic and magnetoelectric properties of the ME composite system. Figure 13.1 shows the flowchart of this thesis relating composition, microstructure, geometry and properties of the magnetoelectric composite. This thesis becomes successful in presenting the fundamental concepts of ME behavior, identifying the controlling parameter and demonstrating unique synthesis techniques which are favorable to ME composites.

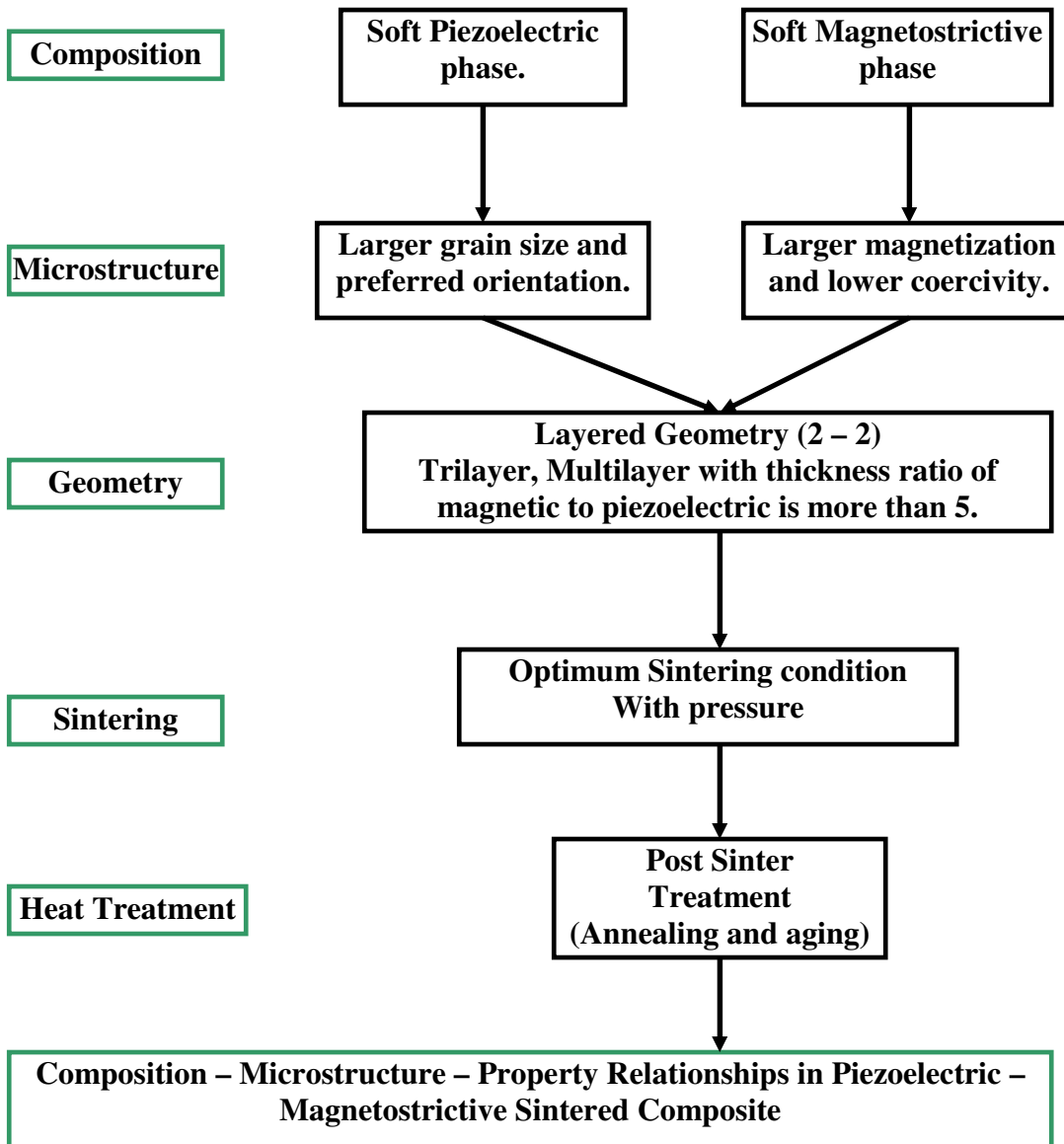


Figure 13.1: Flowchart of the thesis

CHAPTER 13

FUTURE WORKS

In this thesis, several approaches to synthesize ME composite were attempted with the goals of enhancing the resistivity, decreasing defects, restricting the interface diffusion, and understanding the fundamental parameters contributing towards ME coefficient. There is lot of scope for further improvement of the ME coefficient. The three future experiments may constitute following points:

1. Synthesis of a fully textured PZT in a trilayer or multilayer structure in order to improve the piezoelectric, dielectric and magnetoelectric properties of the composite. Other than conventional sintering, tape casting approach can be utilized.
2. Optimization of the core – shell structural composite. Optimization in terms of shell thickness, core diameter, and ratio of core diameter to shell thickness can be conducted. Shell thickness can be varied by varying the experimental parameters such as temperature, and atmosphere. For the layered structure the core shell particles can be mixed with organic binder and then either screen print or spin coated on a wafer.
3. A layered ME composite can be synthesized using sintered PZT and electroless metal deposition (Ni, Co etc.) technique. If a metal - magnetic layer can be deposited on top and bottom of thin PZT than it will work not only as magnetic phase but also as electrode layer. This is an industry oriented approach with large production rate.

APPENDIX A

PUBLICATION RELATED TO THIS RESEARCH

Submitted:

R. A. Islam, N. Basit, S. Priya, S. Dong and D. Viehland, "Microstructure - Property Relationship of Near Eutectic BaTiO₃ – CoFe₂O₄ Composites" Submitted in the Journal of Materials Science Letters.

Rashed Adnan Islam, Chuan-bing Rong, J. P Liu and Shashank Priya, "Gradient Composite Structure in Cofired Bilayer Magnetolectric Composites of Pb(Zr_{0.56}Ti_{0.44})O₃ - Ni_{0.6}Zn_{0.2}Cu_{0.2}Fe₂O₄ System" submitted in Journal of Materials Science.

Accepted:

- Rashed Adnan Islam and Shashank Priya, "Effect of Grain Size on Magnetolectric Coefficient of Pb(Zr_{0.52}Ti_{0.48})O₃ – Ni_{0.8}Zn_{0.2}Fe₂O₄ Particulate Composite", Accepted in Journal of Materials Science.

Published:

- (Rashed Adnan Islam and Shashank Priya, "Large Magnetolectric Coefficient in Co-fired Pb (Zr_{0.52}Ti_{0.48})O₃ – Pb (Zn_{1/3}Nb_{2/3})O₃ – Ni_{0.6}Cu_{0.2}Zn_{0.2}Fe₂O₄ Trilayer Magnetolectric Composites", Journal of Materials Science Letters, 43 (6), (2008).
- Review Article) S. Priya, R. Islam, S. Dong and D. Viehland, "Recent Advancement in Magnetolectric Particulate and Laminate composite", Electroceramics, 10.1007/s10832-007-9042-5
- Rashed Adnan Islam and Shashank Priya, "Doping effect on Magnetolectric Coefficient of Pb(Zr_{0.52}Ti_{0.48})O₃ - Ni_(1-x)Zn_xFe₂O₄ Particulate Composite" Journal of Materials Science, 43 (4), 1497, (2008).
- Rashed Adnan Islam and Jiechao Jiang, Feiming Bai, Dwight Viehland, and Shashank Priya, "Correlation between structural deformation and magnetolectric response in (1-x)Pb_xZr_{0.52}Ti_{0.48}O₃ – xNiFe_{1.9}Mn_{0.1}O₄ particulate composites", Appl. Phys. Lett., 91, 162905, (2007).
- Robert Myers, Rashed Adnan Islam, Makarand Karmarkar, and Shashank Priya "Magnetolectric laminate composite based tachometer for harsh environment applications", Appl. Phys. Lett. 91, 122904 (2007).
- Rashed A. Islam, Shashank Priya and Ahmed Amin, "Mn-doping effect on dielectric and electromechanical losses in the system Pb(Zr_xTi_{1-x})O₃–Pb(Zn_{1/3}Nb_{2/3})O₃", Journal of Materials Science, 10.1007/s10853-007-2051-6.
- Richard Bergs, Rashed A. Islam, Michael Vickers, Harry Stephanou, and Shashank Priya, "Magnetic field anomaly detector using magnetolectric composites", J. of Appl. Phys., 101, 024108, (2007).
- Hyeoungwoo Kim, Rashed Adnan Islam and Shashank Priya, "Working principle of voltage Controlled Differential Magnetic Field Sensor" Appl. Phys. Lett., Vol. 90, 2007, 012909.

- Rashed Adnan Islam and Shashank Priya, "Magnetoelectric Properties of the Lead-Free Co-fired $\text{BaTiO}_3 - \text{Ni}_{0.8}\text{Zn}_{0.2}\text{Fe}_2\text{O}_4$ Bilayer Composite" – J. of Appl. Phys. Lett., 89, 2006, 152911.
- Rashed A. Islam, Hyeoungwoo Kim, Shashank Priya and Harry Stephanou, "Piezoelectric Transformer Based Ultrahigh Sensitivity Magnetic Field Sensor" – Appl. Phys. Lett., 89 (1), 2006, 152908.
- Rashed Adnan Islam and Shashank Priya, "Synthesis of High Magnetoelectric Coefficient Composite Using Annealing and Aging Rote" J. of Appl. Ceram. Tech., Vol. 3(5), pp. 353 – 363, 2006.
- Rashed Adnan Islam and Shashank Priya, "Enhanced Magnetoelectric Effect in (1-x) $\text{Pb}(\text{Zr}_{0.52}\text{Ti}_{0.48})\text{O}_3 - x \text{NiFe}_{1.9}\text{Mn}_{0.1}\text{O}_4$ Particulate Composites – Electrical and Magnetic Properties", Integ. Ferroelec., Vol. 82 (1), 2006, pp. 1- 24.
- Rashed Adnan Islam and Shashank Priya, "Annealing and Aging Effect in $0.95\text{Pb}(\text{Zr}_{0.52}\text{Ti}_{0.48})\text{O}_3 - 0.5 \text{NiFe}_{1.9}\text{Mn}_{0.1}\text{O}_4$ Particulate Magnetoelectric Composites", Japn. J. of Appl. Phys. Vol. 45 (5), 2006, pp. L128 -L131.
- Rashed Adnan Islam and Shashank Priya, "High Energy Density Ceramic Composition in the System $\text{Pb}(\text{Zr,Ti})\text{O}_3 - \text{Pb}[(\text{Zn,Ni})_{1/3}\text{Nb}_{2/3}]\text{O}_3$ ", J of Am. Ceram. Soc., 89 (10), 2006, pp. 3147 – 3156.
- Chih-Ta-Chen, Rashed Adnan Islam, and Shashank Priya, "Electrical Energy Generator", Accepted in the Journal of IEEE Trans. on Ultrason., Ferroelec. and Freq. Cont., Vol. 53 (3), 2006, pp. 656-661.
- Rashed Adnan Islam and Shashank Priya, "Realization of High Energy Density Polycrystalline Piezoelectric Ceramics", J of Appl. Phys. Lett., Vol. (88), 2006, 032903.

REFERENCES

1. J. Ryu, AV. Carazo, K. Uchino and H. Kim, *J. of Electoceram*, 7, 17, (2001).
2. VC. Flores, DB. Baques, DC. Flores, *JAM. Aquino, J. Appl. Phys.*, 99, 08J503,(2006)
3. TG. Lupeiko, Lisnevskaya IV, MD. Chkheidze, and BI. Zvyagintsev, *Inorg. Mater.*, 31, 1139, (1995).
4. M. Feibig, *J.Phys. D: Appl. Phys*, 38, R123-R152, (2005).
5. C.Ederer and N. Spaldin, *Curr. Opi. Sol. Sta. & Mater. Sci.*, (2006)
6. J. Van Suchetelene, *Philips Research Report*, 27, 28 – 37, (1972).
7. G. Smolenskii and V. A. Ioffe, *Colloque International du Magnetisme, Communication No. 71*, (1958).
8. J. Wang, J.B. Neaton, H. Zheng, S. E. Lofland, Z. Ma, L.M. Ardabili, T. Zhao, L.S. Riba, S.R. Shinde, S.B. Ogale, F. Bai, D. Viehland, Y. Jia, D.G. Schlom, M. Wuttig, A. Roytburd and R. Ramesh, *Science*, 299, 1719, (2003).
9. J. Wang, H. Zheng, S. E. Lofland, Z. Ma, L.M. Ardabili, T. Zhao, L.S. Riba, S.R. Shinde, S.B. Ogale, F. Bai, D. Viehland, Y. Jia, D.G. Schlom, M. Wuttig, A. Roytburd and R. Ramesh, *Science*, 303, 661, (2004).
10. C. Ederer and N. Spaldin, *Nature Mater.*, 3, 849, (2004).
11. W. Eerenstein, N. D. Mathur and J.F. Scott, *Nature*, 442, 759,(2006).
12. N. Hur, S. Park, P.A. Sharma, J.S. Ahn, S. Guha and S-W Cheong, *Nature*, 429, 392, 3.
13. C. W. Nan, M. I. Bichurin, S. Dong, D. Viehland and G. Srinivasan, *J. Appl. Phys.*, 103, 031101, (2008).
14. S. Priya, R. Islam, S. Dong, D. Viehland, *Electroceram.*, 19, 147, (2007)
15. Harshe G. R.: Ph.D. Dissertation, Magnetolectric effect in piezoelectric – magnetostrictive composite. Pennsylvania State University, University Park, PA; 1991.

16. J.F. Herbst, T.W. Capehart and F.E. Pinkerton, *Appl. Phys. Lett.*, 70 (22), 3041, (1997).
17. C.W. Nan, M. Liu, X. Feng and S. Yu, *Appl. Phys. Lett.*, 78 (17), 2527, (2001).
18. D. N Astrov, *Sov. Phys. JETP*, 11, 708, (1960).
19. D.N. Astrov, B.I. Al'shin, R.V. Zhorin and L.A. Drobyshev, *Sov. Phys. – JETP* 28, 1123, (1968).
20. G. Smolenskii and VA. Ioffe, *Colloque International du Magnetisme, Communication*, No. 71,(1958).
21. T. Kimura, T. Goto, H. Shintani, K. Ishizaki, T. Arima and Y. Tokura, *Nature*, 426, 55, (2003).
22. T. Lottermoser, T. Lonkal, U. Amann, D. Hohlwein, J. Ihiringer and M. Fiebig, 430, 541, (2004).
23. B.B. Van Aken, T.T.A. Palstra, A. Filippetti and N.A. Spaldin, *Nat. Mater.*, 3, 164, (2004).
24. M. Fiebig, T. Lottermoser, D. Frohlich, A.V. Goltsev and R.V. Pisarev, *Nature*, 419, 818, (2002).
25. M.Zheng, J.G. Wan, Y. Wang, H. Yu, J.M. Liu, X. P. Jiang and C.W. Nan, *J. Appl. Phys.*, 95 (12), 8069, (2004).
26. J. Zhai, Z. Xing, S. Dong, J. Li and D. Viehland, *J. Amer. Ceram. Soc.*, 91 (2), 351, (2008).
27. V.C. Flores, D.B Baques, D.C. Flores, J. A. M. Aquino, *J. Appl. Phys.*, 99, 08J503, (2006).
28. R. E. Newnham, *Ferroelec.*, 68 [1/4], 1-32, (1986).
29. R. E. Newnham, *Mater. Engg*, 2 (2), 93, (1980)
30. T.H. Odell, *Electronics and Power*, 11, 266-268,(1965).
31. J.V.D. Boomgaard, AMJG. Van Run and JV. Suchtelen, 10, 295-98, (1976).
32. J.V.D. Boomgaard and RAJ. Born, *J. Mater. Sci.*, 13, 1538-1548, (1978).
33. J.V.D. Boomgaard, DR. Terrell, RAJ. Born, and HFJI. Giller, *J. Mater. Sci*, 9, 1705-

- 1709,(1974).
34. A.M.J.G. Van Run, DR. Terrell, and JH. Scholing, *J.Mater.Sci.*, 9, 1710 – 1714,(1974).
 35. J. Ryu, S. Priya, K. Uchino, D. Viehland, and H. Kim, *J. Korean Ceram. Soc.*, 39, 813-817, (2002).
 36. J. Ryu, S. Priya and K. Uchino, *J. Electroceram.*, 8, 107- 119, (2002).
 37. S. Dong, J. Li and D. Viehland, *Appl. Phys. Lett.*, 83 (11), 2265-2267, (2003).
 38. S. Dong, J. Li and D. Viehland, *IEEE Trans. Ultrason. Ferroelec. Freq. Ctrl.*, 50 [10], 1236-1239,(2003).
 39. G. Srinivasan, E.T. Rasmussen, J. Gallegos, R. Srinivasan, Y. I. Bokhan and V. M. Laletin, *Phys. Rev. B*, 64, 214408, (2001).
 40. G. Srinivasan, E.T. Rasmussen and R. Hayes, *Phys. Rev. B*, 67, 014418, (2003).
 41. V. M. Laletin, N. Paddubnaya, G. Srinivasan, C. P. De Vreugd, M. I. Bichurin, V. M. Petrov, and D. A. Filippov, *Appl. Phys. Lett.*, 87, 222507, (2005).
 42. K Zhao, K Chen, Y. R. Dai, J.G. Wan and J.S. Zhu, *Appl. Phys. Lett.*, 87, 162901, (2005).
 43. S. Dong, J. Zhai, F. Bai, J. F. Li, D. Viehland and T. A. Lograsso, *J. Appl. Phys.*, 97, 103902, (2005).
 44. N. Cai, C. W Nan, J. Zhai, and Y Lin, *Appl. Phys. Lett.*, 84 (18), 3516, (2004).
 45. Z. Xing, S. Dong, J. Zhai, L Yan, J. Li, and D. Viehland, *Appl. Phys. Lett.*, 89, 112911, (2006).
 46. S. Dong, J. Zhai, J. Li, and D. Viehland, *Appl. Phys. Lett.*, 89, 122903, (2006).
 47. S. Dong, J. Li, and D. Viehland, *Appl. Phys. Lett.*, 85 (22), 5305, (2004).
 48. J. Zhai, S. Dong, Z. Xing, J. Li, and D. Viehland, *Appl. Phys. Lett.*, 89, 083505, (2006).
 49. S. Dong, J. Zhai, N. Wang, F. Bai, J. Li, D. Viehland and T.A. Lograsso, *Appl. Phys. Lett.*, 87, 222504, (2005).
 50. S. Dong, J. Zhai, J. Li, and D. Viehland, *J. Appl. Phys.*, 100, 124108, (2006).
 51. S. Dong, J. Zhai, J. Li, and D. Viehland, *Appl. Phys. Lett.* 89, 252904, (2006).

52. G. Srinivasan, R. Hayes, C. P. De Vreugd, V. M. Laletin and N. Paddubnaya, *Appl. Phys. A*, 80, 891, (2005).
53. G. Srinivasan, E.T. Rasmussen, A. A. Bush, K.E. Kamentsev, V.F. Meshcheryakov, Y.K. Fetisov *Appl. Phys. A*, 78, 721, (2004).
54. G. Liu, C. W Nan, N. Cai and Y Lin, *J. Appl. Phys.*, 95 (5), 2660, (2004).
55. N. Zhang J. Fan, X. Rong, H. Cao, and J. Wei, *J. Appl. Phys.*, 101, 063907, (2005).
56. L. Li, Y. Q. Lin, and X. M. Chen, *J. Appl. Phys.*, 102, 064103, (2007)
57. R.V. Chpodekar, Y. Suzuki, *Appl. Phys. Lett.* 89, 182506, (2006).
58. C. Deng, Y. Zhang, J. Ma, Y. Lin, and C. W. Nan, *J. Appl. Phys.*, 102, 074114, (2007).
59. J. H. Park, H. M. Jang, H. S. Kim, C. G. Park, and S. G. Lee, *Appl. Phys. Lett.* 92, 062908, (2008).
60. Y. Zhang, C. Deng, J. Ma, Y. Lin, and C. W. Nan, *Appl. Phys. Lett.* 92, 062911, (2008).
61. H. Ryu, P. Murugavel, J. H. Lee, S. C. Chae, and T. W. Noh, Y. S. Oh, H. J. Kim, K. H. Kim, J. H. Jang, M. Kim, C. Bae and J. G. Park, *Appl. Phys. Lett.* 89, 102907, (2006).
62. Y. G. Ma, W. N. Cheng, M. Ning, and C. K. Ong, *Appl. Phys. Lett.* 90, 152911, (2007).
63. J. Zhou, H. He, Z. Shi, and C. W. Nan, *Appl. Phys. Lett.* 88, 013111, (2006).
64. H. He, J. Ma, J. Wang and C. W. Nan, *J. Appl. Phys.*, 103, 034103, (2008).
65. S. H. Xie, J. Y. Li, Y. Qiao, Y. Y. Liu, L. N. Lan, Y. C. Zhou, and S. T. Tan, *Appl. Phys. Lett.* 92, 062901, (2008).
66. H. He, J. P Zhou, J. Wang and C. W. Nan, *Appl. Phys. Lett.*, 89, 052904, (2006).
67. S. Zhao, Y. Wu, J. Wan, X. Dong, J. Liu, and G. Wang, *Appl. Phys. Lett.*, 92, 012920, (2008).
68. J. X. Zhang, J. Y. Dai, C. K. Chow, C. L. Sun, V. C. Lo, and H. L. W. Chan, *Appl. Phys. Lett.*, 91, 022901, (2008).
69. J. Li, I. Levin, J. Slutsker, V. Provenzano, P. K. Schenck, R. Ramesh, J. Ouyang, A. L. Roytburd, *Appl. Phys. Lett.*, 87, 072909, (2005).

70. J. Wan, Y. Weng, Y. Wu, Z. Li, J. Liu and G. Wang, *Nanotech.*, 18, 1, (2007).
71. X. L. Zhong, J. B. Wang, M. Liao, G. J. Huang, S. H. Xie, Y. C. Zhou, Y. Qiao and J. P. He, *Appl. Phys. Lett.*, 90, 152903, (2007).
72. Y.R. Dai, P. Bao, J.S. Zhu, J.G. Wan, H.M. Shen, J.M. Liu, *J.Appl. Phys.* 96(10), 5687, (2004).
73. G. Srinivasan, C.P. DeVreugd, C.S. Flattery, V.M. Laletsin, N. Paddubnaya, *Appl. Phys. Lett.* 85(13), 2550, (2004).
74. R.P. Mahajan, K.K. Patankar, M.B. Kothale, S.A. Patil, *Bull. Mater. Sci.* 23(4), 273, (2000).
75. K.K. Patankar, S.A. Patil, K.V. Sivakumar, R.P. Mahajan, Y.D. Kolekar, M.B. Kothale, *Mater. Chem. Phys.* 65, 97, (2000).
76. C. W. Nan, N. Cai, L. Liu, J. Zhai, Y. Ye, and Y. Lin, *J.Appl. Phys.* 94 (9), 5930, (2003).
77. J. Zhai, N. Cai, Z. Shi, Y. Lin and C. W. Nan, *J. Phys. D: Appl. Phys.*, 37, 823, (2004).
78. S. Q. Ren, L. Q. Weng, S.-H. Song, F. Li, J. G. Wan and M. Zeng, *J. of Mater. Sci.*, 40 (16), 4375, (2005).
79. R.S. Devan and B.K. Chogule, *J.Appl. Phys.* 101, 014109, (2007).
80. D. Wu, W. Gong, H. Deng and M. Li, *J. Phys. D: Appl. Phys.*, 40, 5007, (2004).
81. Y. J. Li, X.M. Chen, Y.Q. Lin and Y. H. Tang, *J. Europ. Ceram. Soc.*, 26, 2839, (2006).
82. R. A. Islam and S. Priya, *Integ. Ferroelec.*, 82 (1), 1, (2006).
83. R. A. Islam and S. Priya, *Jap. J. Appl. Phys.*, 45 (5), L128 -L131, (2006).
84. R.A. Islam and S. Priya, *J. of Appl. Cer. Tech.*, 3(5), 353, (2006).
85. W.E. Kramer, R.H. Hopkins, and M.R. Daniel, *J. Mater. Sci. Lett.*, 12 [2], 409, (1977).
86. American National Standard Institute, *IEEE Standard on Piezoelectricity* (1987). H.A. Sodano,
87. D. J. Inman and G. Park, *Shock and vibration digest*, 36 (3), May, 197, (2004).

88. H. W. Kim, A. Batra, S. Priya, K. Uchino, D. Markley, R.E. Newnham and H. F. Hofmann, *Jpn. J. Appl. Phys.*, 43 (9A), 6178, (2004).
89. H. A. Sodano, D. J Inman, G. Park, *J. Intell. Mat. Syst. Struct.*, 16, 799, (2005).
90. Kim H, Priya S, Uchino K, R. Newnham, *J. Electroceram.*, Vol. 15 (1), 27, (2005).
91. R. A. Islam, and S. Priya, *Appl. Phys. Lett.*, 88, 032903, (2003).
92. S. Priya, Ph.D. Dissertation, Pennsylvania State University, University Park, PA, 2003.
93. S. Priya and K. Uchino, *J. Appl. Phys.*, Vol. 91, (2002), 4515 – 4520.
94. S. Priya, K. Uchino and D. Viehland, *Jap. J. Appl. Phys.*, Vol. 40, (2001), L1044 – L1047.
95. S. Priya, K. Uchino and D. Viehland, *Appl. Phys. Lett.*, Vol. 81, (2002), 2430 – 2432.
96. S. Priya and K. Uchino, *Jpn. J. Appl. Phys.*, Vol. 42, (2003), 531-534.
97. S. Priya, J. Ryu, K. Uchino, C. Ahn and S. Nahm, *Appl. Phys. Lett.*, Vol. 83, (2003), 5020 – 5022.
98. N. Setter “ABC of piezoelectricity and piezoelectric materials”, *Piezoelectric Materials in Devices*, edited by N. Setter, Ceramics Laboratory, EPFL, Swiss Federal Institute of Technology, Switzerland, (2002), 1- 27.
99. B. Noheda, D. E. Cox, G. Shirane, J. A. Gonzalo, L. E. Cross and S. E. Park, *Appl. Phys. Lett.*, Vol. 74 [14], (1999), 2059-2061.
100. I. W. Chen and X. H. Wang, *Nature*, Vol. 404 (9), (2002), 168-171.
101. S. M. Li, C.B.Yoon, S. H. Lee and H. E. Kim, *J. Mater. Res.*, Vol. 19 (9), (2004), 2553-2556.
102. C. W. Ahn, H. C. Song, S. H. Park, S. Nahm, K. Uchino, S. Priya, H. G. Lee and N. K. Kang, *Jpn. J. Appl. Phys.*, Vol. 44 (3), (2005), 1314-1321.
103. S.B. Seo, S. H. Lee, C.B.Yoon, G. T. Park and H. E. Kim, *J. Amer. Ceram. Soc.*, Vol. 87 (7), (2004), 1238-1243.
104. Y.D. Hou, M.K. Zhu, H. Wang, B. Wang, H. Yan and C. S. Tian, *Mater. Lett.*, Vol. 58, (2004), 1508-1512.
105. K. Uchino, “Ferroelectric devices”, Marcel Dekker InC, 2000, New York, 57-69.

106. K. Uchino and T. Takasu, *Inspec.*, Vol. 10, (1986), 29.
107. Jaffe B, Cook WR and Jaffe H (1971) *Piezoelectric Ceramics*, Academic Press. Massachusetts, USA.
108. R.A. Islam and S. Priya, *J. Am. Ceram. Soc.*, 89 (10), 3147, (2006).
109. RE. Newnham, *Rep. Prog. Phys.*, 52, 123-156,(1989).
110. BS. Kang, DG. Choi and SK. Choi, *K. Kor. Phys. Soc.*, 32: S232 – S234,(1998).
111. HT. Martirena and JC. Burfoot, *J. Phys. C: Solid State. Phys.* 7: 3182 – 3192, (1974).
112. S. Choudhury, YL. Li, C. Krill and LQ. Chen, *Act. Mater*, 55: 1415 – 1426, (2007).
113. HM. Duiker and PL. Beale, *Phys. Rev. B* , 41 (1), 490 – 495, (1990).
114. V. Sundar, N. Kim, CA. Randall, R. Yimnirun and RE. Newnham, *Proceed. of the 10th IEEE Inter. Sym. on Appl. of Ferroelec.*, 935 – 938,(1996).
115. CJ. Lu, SB. Ren, HM. Shen, JS. Liu and YN. Wang, *J. Phys. Condens. Matter*, 8, 8011 – 8016, (1996).
116. C. Sakaki, BL. Newalkar, S. Komerneni and K. Uchino, *Jpn. J. Appl. Phys*, 40, 6907 – 6910,(2001)
117. CA. Randall, N. Kim, JP. Kucera, WW. Cao and TR. Shrout, *Am. Ceram. Soc.*, 81, 677 – 688, (1998).
118. BM. Jin, J. Kim, SC. Kim, *Appl. Phys. A: Mater. Sci. Proc.*, 65, 53 – 56, (1997).
119. TM. Shaw, ST. Mckinstry, PC. Mcintyre, *Ann. Rev. Mater. Sci.*, 30, 263,(2000).
120. Z. Zhao, V. Buscaglia, M. Viviani, MT. Buscaglia, L. Mitoseriu, A. Testino et. Al, *Phys. Rev. B*, 70, 024107,(2004).
121. S. Zhang, S. Priya, TR. Shrout and CA. Randall, *J. Appl. Phys.*, 93, 2880 – 2883, (2003).
122. Y-H.Chen, K. Uchino, D. Viehland, *J Appl. Phys.*, 89, 3928 – 3933, (2001).
123. WF. Brown Jr, R Hornreich, and S. Shtrikman, *Phys. Rev.*, 168, 574 – 577,(1968).
124. AS. Zubkov, *Elektrichestvo*, 10, 77, (1978).
125. D. C. Jiles, *Acta Mater*, 51, 5907 – 5939, (2003).

126. Data for APC 840 ceramics. Source: www.americanpiezo.com
127. W. Cao, and C. A. Randall, *J. Phys. Chem. Solids*, 57, 1499 – 1505, (1996).
128. J. Echigoya, S. Hayashi, and Y. Obi, *J. Mater. Sci.*, 35, 5587 – 5591, (2000).
129. J. Ryu, S. Priya, A. V. Carazo, K. Uchino and H. Kim, *J. Am. Ceram. Soc.* 84, 2905 (2001).
130. KI. Kobayashi, H. Morinaga, T. Araki, *J. Magn. Magn. Mater.* 104–107, 413,(1992).
131. IZ. Rahman, TT. Ahmed, L Powell, *J. Meta. Nano. Mater.*, 17, 9,(2003).
132. WC. Kim, SJ. Kim SJ, *IEEE Trans. Magn.*, 37, 2362, (2001).
133. RA. Islam and S. Priya, *J. of Amer. Ceram. Soc.*, 89(10), 3147, (2006).
134. M. Cancarevic, M. Zinkavich, and F. Aldinger, *Mater. Sci. For.*, 494, 67,(2005).
135. E. Ringgaard, ER. Nielsen and WW. Wolny, *IEEE*, (2002).
136. D. Cerovic, I. Momcilovic and SJ. Kiss, *J. Mater. Sci.*, 7, 735, (1972).
137. JJ. Shrotri, SD. Kulkarni, *J. Mater. Chem. Phys.*, 59, 1, (1999).
138. TT. Ahmed, IZ. Rahman, and MA. Rahman, *J. Mater. Proc. Tech.* 153 – 154, 797, (2004).
139. T. Okamura and Y. Kojima, *Phys. Rev.*, 86 (6), 1040, (1952).
140. JW. Martin, *Precipitation hardening*. New York: Pergamon Press,(1968).
141. MK. Griffiths, JEL. Bishop, WJ. Tucker and HA. Davies, *J. Magnet. Magnetic Mater.*, 234, 331-52, (2001).
142. Z. Sufen, J. Hanmin, W. Xuefeng and Y. Yu, *J. Magnet. Magnetic Mater.*, 247 [1], 15-18, (2002).
143. WD. Kingery, DR. Uhlmann and HK. Brown, *Introduction to Ceramics*, 2nd ed. Wiley John & Sons Inc., (1976).
144. S. Audet and J. Steigerwald, *Radiation Sensors in Semiconductor Sensor* ed. by Sze SM. John Wiley & Sons Inc., (1994).
145. B. Noheda, DE. Cox, G. Shirane, JA. Gonzalo, LE. Cross and SE. Park, *Appl. Phys. Let.*, 74 [14], 2059-2061, (1997).

146. J. Ryu, AC. Vázquez, K. Uchino, and H.E. Kim. *Jpn. J. Appl. Phys.*, 40 [8], 4948 – 4951, (2001).
147. Priya S: Ph.D. Dissertation, Characterization of Aliovalent Substituted Relaxor Ferroelectric Single Crystals for High Power Application. Pennsylvania State University, University Park, PA, (2003).
148. S. Priya, K. Uchino and D. Viehland, *Jpn. J. Appl. Phys. Pt. 2*, 40, (10A), L1044-1047, (2001).
149. M. Zheng, JG. Wan, Y. Wang, H. Yu, JM. Liu, X P. Jiang and CW. Nan. *J. Appl. Phys.*, 95 (12), 8069, (2004).
150. Z. J. Zhang, Z. L. Wang, B. C. Chakoumakos and J. S. Yin, *J. Am. Chem. Soc.*, 120, 1800, (1998).
151. C. Rath, S. Anand, R. P. Das, K. K. Sahu, S.D. Kulkarni, S.K. Date, N.C. Mishra, *J. Appl. Phys.*, 91(4), 2211, (2002).
152. J.F. Li, X. Dai, A. Chow, D. Viehland, *J. Mater. Res.*, 4, 926, (1995).
153. X. Bi, S. Chu, J. G. Zhu, D. Laughlin, *J. Appl. Phys.*, 99, 08B306, (2006).
154. Z. Xu, X. Dai, D. Viehland and D. Payne, *J. Am. Ceram. Soc.*, 78 [8], 2220, (1999).
155. RA. Islam, D. Viehland and S. Priya, *J. Mater. Sci. Lett.*, 43 (4), 1497, (2008).
156. RA. Islam, and S. Priya, *J. Mater. Sci.*, 10.1007, s10853-008-2562-9, (2007).
157. RA. Islam and S. Priya, *J. of Appl. Phys. Lett.*, 89, 152911, (2006).
158. RA. Islam, JC. Jiang, S. Priya, F. Bai and D. Viehland, *Appl. Phys. Lett.* 91, 162905, (2007).
159. APC International, *Piezoelectric Ceramics: Principle and Applications*, ISBN 0-9718744-0-9.
160. S. Priya, S. Ural, H. W. Kim, K. Uchino, and T. Ezaki, *Jpn. J. Appl. Phys. Part 1*, 43, 3503 (2004).
161. S. Dong, J. F. Li and D. Viehland, *IEEE Trans. Ultrason. Ferroelect. and Freq. Contr.*, 51 (7), 793, 2004.

162. S. Dong, J. Zhai, F. Bai, J. F. Li, D. Viehland and T. A. Lograsso, *J. Appl. Phys.*, 97, 103902, (2005).
163. S. Dong, J. F. Li, D. Viehland, J. Cheng, and L. E. Cross, *Appl. Phys. Lett.*, 85, 3534 – 3536, (2004).
164. S. Dong, J. F. Li, and D. Viehland, *Appl. Phys. Lett.*, 84, 4188 – 4190, (2004).
165. T. Takeuchi, T. Tani, and Y. Saito, *Jpn. J. Appl. Phys.*, 38, 5553, (1999).
166. S. H. Hong, S. T. Mckinstry, G. Messing, *J. Am. Ceram. Soc.*, 83 (1), 113 – 118, (2000).
167. A. Moure, L Pardo, C Alemany, P Millan and A. Castro, *J. Eu. Ceram Soc.*, 21, 1399, (2001).
168. M. Allahverdi, A. Hall, R. Brennan, M.E. Ebrahimi, N. M. Hagh and A. Safari, *J. Of Electroceram.*, 8, 129, (2002).
169. K. Watari, B. Brahmarroutu, G. Messing, S. Mckinstry and S. C. Cheng, *J. Mater. Res*, 15, (4), 846, (2000).
170. E. Sabolsky, S. Mckinstry and G. Messing, *J. Appl. Phys.*, 93 (7), 4072, (2003).
171. J. P Remeika, *Notes*, 76, 940, (1953).
172. Y.S. KooY. S. Koo, T. Bonaedy, K. D. Sung, J. H. Jung, J. B. Yoon, Y. H. Jo, M. H. JungH. J. Lee, T. Y. Koo and Y. H. Jeong, *Appl. Phys. Lett*, 91, 212903, (2007).
173. G. Rowland, *J. Phys. D: Appl. Phys*, 9, 1267, (1976).
174. K. Uestuener, M. Katter and W. Rodewald, *IEEE Trans. On. Mag.*, 42 (10), 2897, (2006).

BIOGRAPHY

Rashed Adnan Islam is a Ph.D. candidate in Material Science and Engineering Department at University of Texas at Arlington. He received his B.Sc. degree in Metallurgical Engineering and M.Sc. in Materials and Metallurgical Engineering in 2000 and 2002 respectively from Bangladesh University of Engineering and Technology (BUET). He was a lecturer in the Department of Materials and Metallurgical Engineering Department at BUET from December 2000 to December 2002. Then he joined as a Research and Development Engineering in the Center for Electronic Packaging and Assemblies, Failure Analysis and Reliability Engineering at City University of Hong Kong, Kowloon, Hong Kong. He joined UTA in Fall 2004.

Mr. Rashed was Selected (only 60 from USA) to attend for National School of Neutron and X-ray Scattering 2007 organized by Argonne National Laboratory, held from August 12 – 26, 2007. He was also selected (only 48 from North and South America) to attend for Pan American Advanced Studies Institute for Transmission Electron Microscopy in Materials Science held in University of Chile in Santiago, 9 – 22 July 2006, funded by National Science Foundation and Department of Energy of USA. His other achievements are, “ASM – Houston Chapter 2007” scholarship, “Best Graduate Student Presentation Award 2007”, “University Scholar 2006”, “3rd Prize in Ceramography Contest” etc. He has more than 25 international journal publications in the field of magnetoelectric materials, piezoelectric energy harvesting and advanced electronic packaging.

After his graduation Mr. Rashed will join Eoplex Technologies Inc. as a Sr. Materials Engineer, located in Redwood City California.